Grant Agreement No.: 226479

SafeLand

Living with landslide risk in Europe: Assessment, effects of global change, and risk management strategies

7th Framework Programme

Cooperation Theme 6 Environment (including climate change)

Sub-Activity 6.1.3 Natural Hazards

Deliverable 2.11

QRA case studies at selected "hotspots". Synthesis of critical issues

Work Package 2.3 - Development of procedures for QRA at regional scale and European scale

Deliverable/Work Package Leader: UPC

Revision: [Final]

October, 2011

Rev.	Deliverable Responsible	Controlled by	Date
Final	UPC	CNRS	

SUMMARY

The objective of this deliverable is the presentation of some examples of the quantitative risk assessment QRA for different types of landslides, at different scales and for various exposed elements (buildings and people). For every case-study, the risk is expressed using a variety of risk descriptors.Some aspects that are discussed involve the use of remote sensing data and the incorporation of the vulnerability in quantitative terms.

Note about contributors

The following organisations contributed to the work described in this deliverable:

Lead partner responsible for the deliverable:

UPC

Deliverable prepared by:

Jordi Corominas and Olga Mavrouli

Partner responsible for quality control:

CNRS

Deliverable reviewed by:

Jean-Philippe Malet

Other contributors:

AMRA: Giulio Zuccaro, Francesco Cacace, Daniela De Gregorio, Antonio Santo, Giuseppe Di Crescenzo, Anna Scotto Di Santolo

UNIFI: Filippo Catani, Veronica Tofani, Marco Uzielli, Nicola Casagli

UNIMIB: Federico Agliardi, Paolo Frattini

UNISA: Leonardo Cascini, Settimio Ferlisi, Giuseppe Sorbino, Sabatino Cuomo

LIST OF FIGURES

LIST OF TABLES

TABLE OF CONTENTS

1 INTRODUCTION

Quantitative Risk Assessment (QRA) is progressively becoming a requirement for the administrations in charge of landslide risk management. QRA aims to provide objective evaluation of risk in a reproducible and consistent way, avoiding the use of ambiguous terms, and thus favouring the comparison of risk level between distant loca- tions. The QRA may provide information on the potential loss (in €/year) due to a potential hazardous event thus allowing the interpretation based on risk acceptability criteria. The QRA results can be used by administrative authorities for urban planning and/or mitigation measure purposes, as well as by insurance companies for the application of their policies.

Although Quantitative Risk Assessment (QRA) procedures are well established for earthquakes and river floods,, in the case of landslides, QRA methodologies have been developed only recently and they are far from being routinely used by the scientific and technical community. The main reason for this is that several key components of risk are uncertain and/or difficult to obtain. On the one hand, the scarcity of data in many regions restrict the construction of frequency-magnitude relations and then the spatially-distributed character of some hazard components such as the landslide intensity (i.e. the kinetic energy of a rockfall changes along its trajectory) makes the hazard evaluation complicated. On the other hand, either the qualitative or quantitative evaluation of the vulnerability of the exposed elements is affected by a large degree of uncertainty that constraints its assessment in an objective way and makes its integration into the risk equation, a challenge.

For the risk assessment, hazard, exposure and vulnerability parameters have to be merged in order to provide qualitative, semi-quantitative or quantitative results. The expression of hazard, vulnerability and of their interaction to provide the risk results are the objectives of a QRA and it is not obvious. Factors that strongly influence the latter are amongst others the landslide type, the scale of analysis, the desired degree of detail. Another important factor that will determine the way that the QRA is performed is the risk descriptor, which refers to the terms that are used for the risk expression, as for example an expected annual loss (in monetary value), or the probability of a given state of damage, etc.

In this context, the objective of this deliverable is to present some practical applications of QRA that may serve as examples that might be followed by scientists and practitioners depending on the afore-mentioned factors (landslide type, scale, risk descriptors etc). The added value of them is that, in comparison with the current state-of-the art (see Deliverable D2.1 of the SafeLand project), they incorporate innovations, related to the calculation and hazard and vulnerability in order to incorporate them into the risk assessment. The goal of this deliverable is to cover a range of different cases as far as it concerns:

- the application scale: regional, local, site-specific;
- the landslide type: debris flow, deep-seated landslides, hyper-concentrated flows, rockfalls;
- the source of input data: empirical to remote sensing;
- the inclusion or not of the run-out modelling;
- the vulnerability assessment: buildings or people, empirical or analytical, deterministic or probabilistic, element at risk-orientated (detailed) or generalised;

- the used risk descriptors: qualitative or quantitative, and in what terms;

To this end, five-case studies are presented in this deliverable.

The first one (Section 2) refers to the debris slide- rapid earth flow that took place in the town of Castellammare di Stabia town, in the Gulf of Naples. Various slides are concerned and an important key issue is the use of vulnerability curves for the exposed buildings, considering the different structural typologies and the openings of the buildings. The risk is expressed qualitatively, in terms of the expected damage classes, for different sections of the threatened area.

Section 3 involves the case of the landslide that affected in 1982 the city of Ancona resulting in the extensive damage of many infrastructures. The scale of the study can be considered to be local to regional. The volume of the mass movement was about 180 million m^3. The large horizontal displacements were up to 8 m and the uplifts of up to 3 m. Intersting aspects of this study involve the Post-landslide PSInSAR (Permanent Scatterers radar interferometry) monitoring and the analysis of Landsat images. A main objective was the quantitative estimation of specific risk for buildings located inside the landslide area, in money terms. The intensity was back-calculated. Additionally the posterior vulnerability, or "observed degree of loss" was back-assessed from available post-event survey data in function of the intensity (ground displacements). To this end, theoretical equations were used and different building typologies and characteristics were considered.

The next case (Section 4) refers to the site of Monte Albino (Nocera Inferiore, southern Italy), characterized by multiple open slopes, where in 2005 one of them was affected by a first-failure landslide, causing three fatalities. The objective of this study was the risk assessment for the persons in the area. The slide pattern and the run-out were analytically assessed and the probability of a person being affected was calculated, assuming a range of vulnerabilities under different conditions. The risk is qualitatively assessed at a scale from 1 to 6.

An example of the rockfall risk quantification at site-specific and local scale is given at the Section 5 for the Solá d'Andorra. Important aspects of this work are the consideration of the rockfall fragmentation to use for the run-out analysis and the incorporation into the QRA of a quantitative vulnerability which is calculated analytically considering the characteristics of a given building. The calculated risk is quantitative and it expresses the annual probability of needing a complete repair of a building.

At the end, section 6 presents a second example of rockfall QRA, for the Fiumelate rockfall event, that took place in 2004, for the exposed buildings. The energies of the rock blocks impact are computed y numerical modelling, by means of back analysis. The degree of loss suffered by each building was estimated through an engineering evaluation of structure type, damaged structural elements, functional damage and repairability and a site-specific empirical vulnerability function was obtained by fitting a sigmoidal function to damage and impact energy values. The calculated risk was calculated quantitatively in terms of annual expected repair costs.

2 DEBRIS SLIDES – RAPID EARTHFLOWS AT CASTELLAMARE DE STABIA, NAPLES PROVINCE (ITALY)

(AMRA)

2.1 INTRODUCTION

Within the SafeLand European Project, a model for damage impact evaluation of the building structures hit by rapid landslides has been developed at the *PLINIVS Study Centre* of the University of Naples on behalf of AMRA.

In this Deliverable, a model application is illustrated. The case study is constituted by the Castellammare di Stabia town, located in the province of Naples, Campania region, southern Italy, between the Vesuvian area and the Sorrento Peninsula (Figure 2.1).

Figure 2.1. Castellammare di Stabia map.

Castellammare di Stabia (about 64,000 inhabitants) is characterized by an area of about 18km^2 and an altitude ranged between 0 and 1202m, respectively, along the coast and on Faito Mount.

2.2 HAZARD

Castellammare di Stabia town is subjected to a hydrogeological hazard linked to the presence of alluvial deposits of volcanic origin. The city has developed on a volcanic alluvial plain, in the Gulf of Naples, delimited by Lattari Mountains (South) and the Sarno River (East).

The landslides phenomenon has been analyzed through a numerical model, based on DAN-W calculation code (Hungr, 2002), able to assess the flow kinematic characteristics from the height and the topographical section (outline) of the relief. The calibration model has been pursued through the geometrical data related to the debris slides–rapid earth flows observed in pyroclastic deposits of the Campanian Apennines (Scotto di Santolo, 2000).

The assumed types of landslides are unchannelled and channelled debris slides as illustrated in Figure 2.2. In particular, the *channelled flows* have been schematized by a 2D model, while the *unchannelled flows* have been schematized by a 3D schema characterized by a triangular shape, with a constant section linearly increasing in function of an apical angle of 30°.

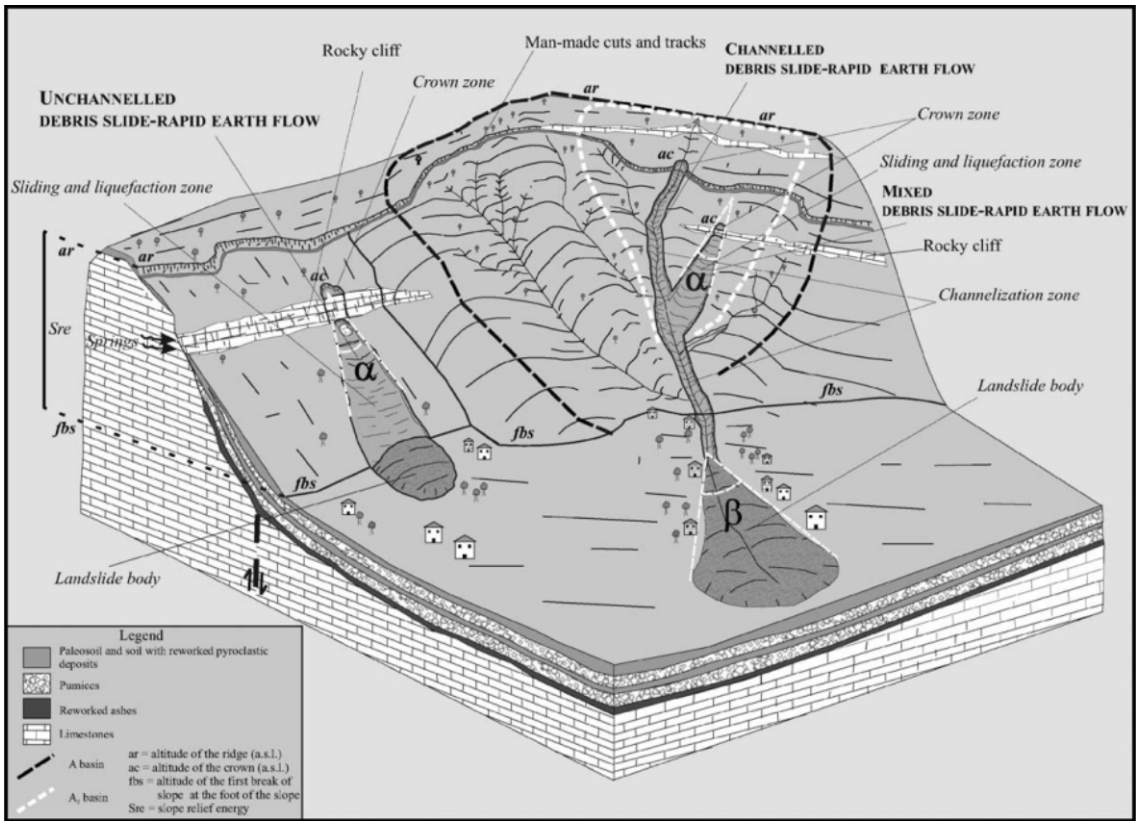

Figure 2.2. Illustration of the main morphological and morphometric parameters of a debris slide-rapid earth flow (Di Crescenzo & Santo, 2005).

Moreover, the model requires the estimation of the potential material volume that can be initially displaced in case of landslide activation. In this perspective, the empirical approach proposed by De Falco et al. (2011) has been adopted. On the basis of the morphometric data analysis (Figure 2.3) of 213 flow-like landslides occurred in

Campania in recent centuries, the study furnishes the mathematical functions between the height H (i.e. the difference in height between the top of source area and a point, the first break at the foot of the slope, where the deposition stars to take place and the landslide looses velocity) and the area $\mathbf{A_f}$ of the detachment and erosion-transport zones (Figure 2.4). The frequency distributions of the total thickness (TT) of material found on carbonatic landslide slopes and the actually displaced part (MT) during the propagation phase or post-failure movement are indicated in Figure 2.5.

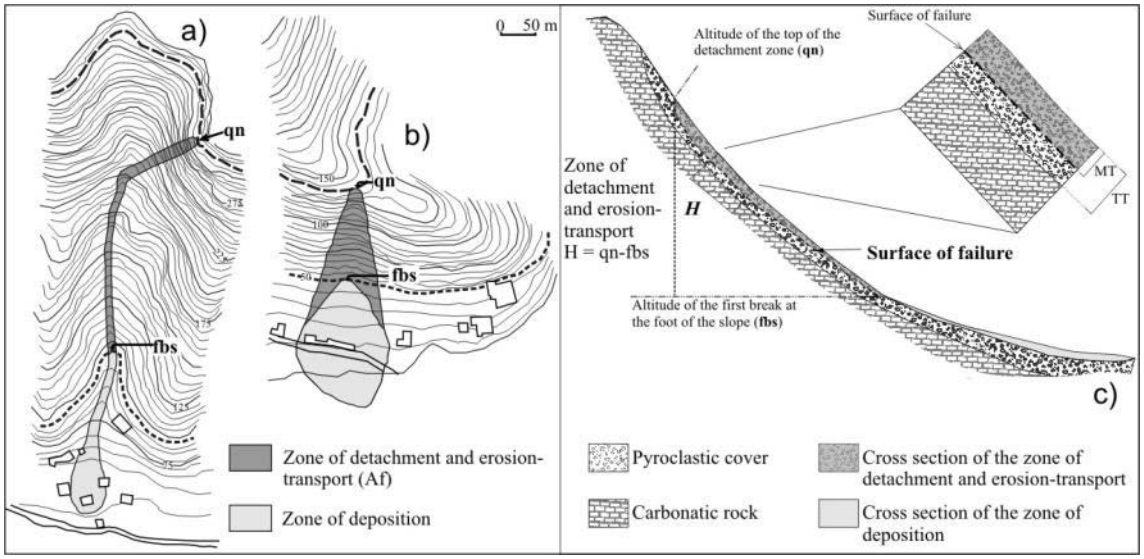

Figure 2.3. A schematic representation of the main morphometric parameters considered for the evaluation of the detachment and erosion-transport zones: on topographic maps with a poorly hierarchized drainage basin (*channelled landslide*) (a) or regular slope (*unchannelled landslide* with a particular subtriangular shape) (b); on cross-section of the sliding slope (c) with a detail that shows the total thickness of pyroclastic material (TT) and the thickness actually displaced (MT).

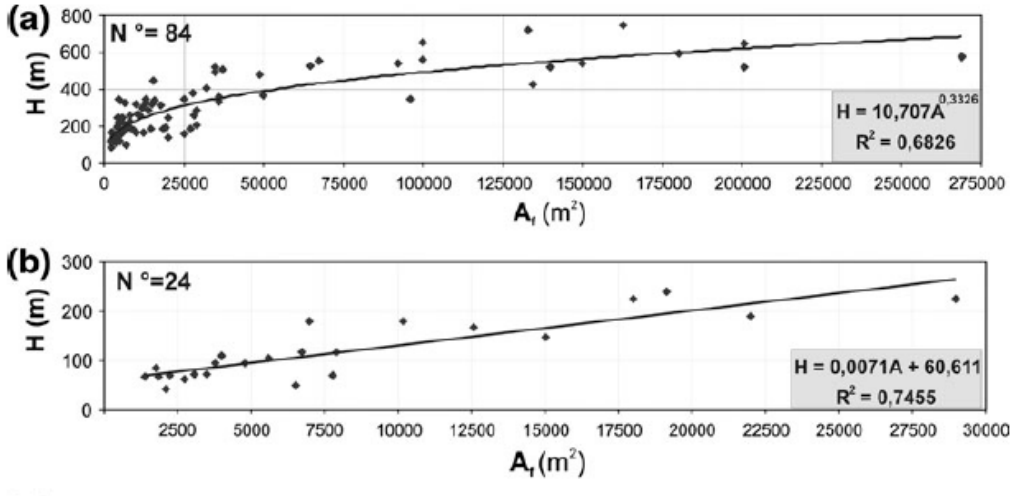

Figure 2.4. Relations between A_f and H for *channelled* (a) and *unchannelled* (b) flow-type landslides in the carbonatic context.

The most susceptible areas are identified by using a landslide-triggering susceptibility map, and then in each case the height H was estimated (Figure 2.6). This height is the

difference in level between the point on the slope with highest susceptibility and the first break at the foot of the slope. Using the statistical correlation between H and Af, calculated for historical landslides, it is possible to evaluate the area of a potential landslide on a slope. Finally, potential volumes are calculated by using $\mathbf{A_f}$ and a constant thickness of the pyroclastic cover for the whole slope (Table 2.1; Table 2.7; Figure 2.6c)

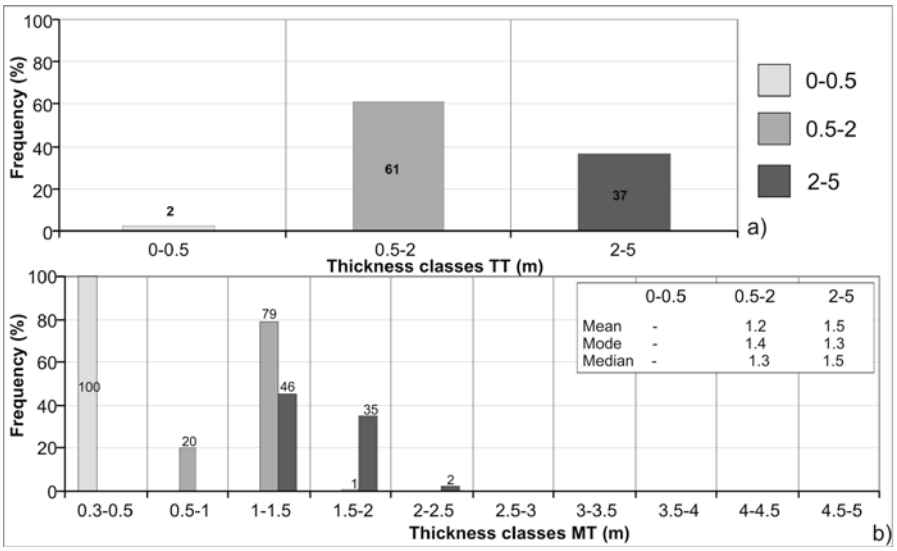

Figure 2.5. Frequency distribution of the total thickness (TT) of material found on carbonatic landslide slopes (a) and of the actually displaced part (MT) during the propagation phase or post-failure movement (b).

Table 2.1. Maximum and minimum cover thickness classes on the strength of dominant basin and interfluve pyroclastic cover thickness of the carbonatic context.

Cover thickness classes (TT) [m]	Minimum pyroclastic cover thickness MT_m [m]	Maximum pyroclastic cover thickness MT_M [m]
0-0.5	0.3	0.5
0.5-2	0.5	1.5
2-5	1	2
0.5-20	0.5	1

The landslide dimensions have been determined for the *Voellmy rheological model*, with a constant *turbulence coefficient* ξ equals to 100 $m.s^{-2}$ and a *friction coefficient* μ equals to 0.03 (M1 Model) and 0.06 (M2 Model). The entrainment phenomenon has been neglected. For the landslide geometry, the following hypotheses have been adopted:

- hypothesis A: Ha = H;
- hypothesis B: Ha = H/2;
- hypothesis C: Ha = H/3;
- hypothesis A1: Ha = 2/3H.

where Ha and H are, respectively, the landslide and the slope heights with reference to the altitude of the top of the detachment zone (crown level).

The results are furnished through diagrams which allow to determine, in function of the distance x_f between the landslide front and the crown, the speed v_f and the height h_f of the front and the maximum height h_{max} of the landslide between the front and the crown, (Figure 2.7; Figure 2.8; Figure 2.9; Figure 2.10). On the basis of the model illustrated, a hazard map relating to Castellammare di Stabia town has been produced (Figure 2.11). In this map, the basin (orange) for the channelled flows, the slope for the unchannelled ones (green) and the relative invasion sectors (sky-blue) are identified. The geometrical parameters are indicated in Table 2.7.

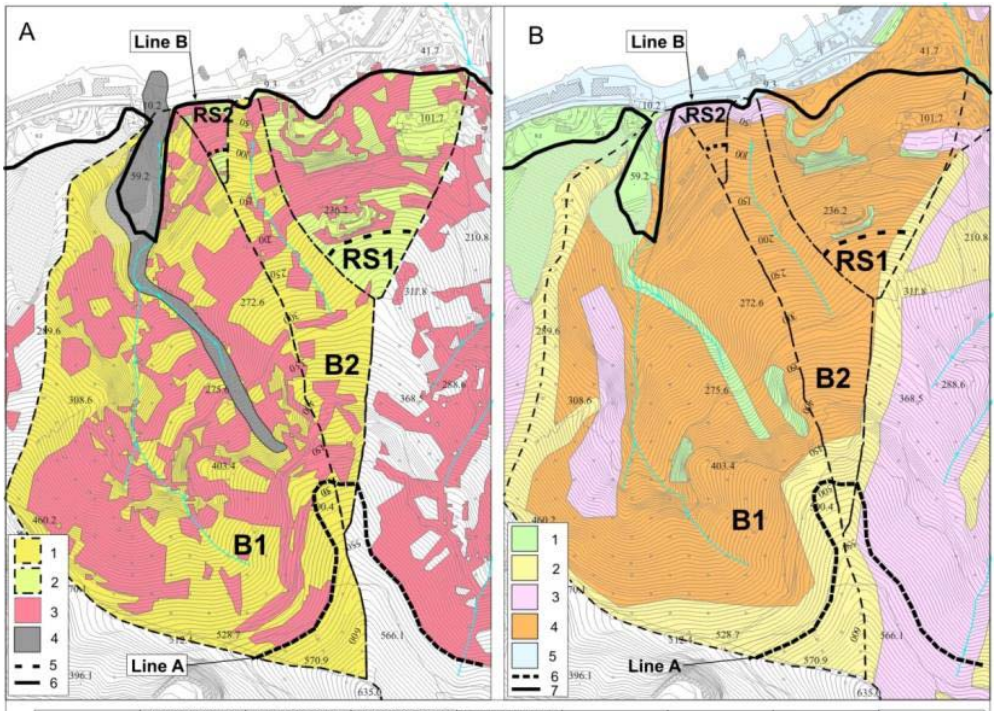

C

Drainage Basin/ Regular Slope	Altitude of the very high triggering suscettibility (Line A) (m a.s.l.)	Altitude of the first break of slope at the foot of the slope (Line B) (m a.s.l.)	Height of detachment and erosion-trasport zone H (m)	Area of detachment and erosion-trasport zone A_r (m²)	Cover thickness min MT_{min} (m)	Cover thickness max MT_{max} (m)	Volume min (m³)	Volume max (m³)
RS1	250	40	210	21100	1	2	22000	44000
RS2	95	25	70	1400	1	2	2000	4000
B1	540	150	390	49500	1	2	50000	100000
B2	450	150	300	22500	1	2	23000	46000

Figure 2.6. Sketch maps of a sector of Castellammare di Stabia (Naples). A) High triggering susceptibility and geomorphometric parameter map: 1) drainage divide of the basin; 2) regular slope boundary; 3) very high triggering susceptibility; 4) The 1997 Pozzano flow-type landslide; 5) line unites the highest susceptibility points (line A); 6) line follows the first slope break at the foot of the slope (line B). b) Pyroclastic cover thickness map: 1) outcropping carbonate bedrock; 2) carbonate bedrock with discontinuous pyroclastic cover (0–0.5 m); cover thickness: 3) 0.5–2 m; 4) 2–4) m; 5[4 m; 6) line A; 7) line B. c Table of parameters takes minimum and maximum volume evaluation into account

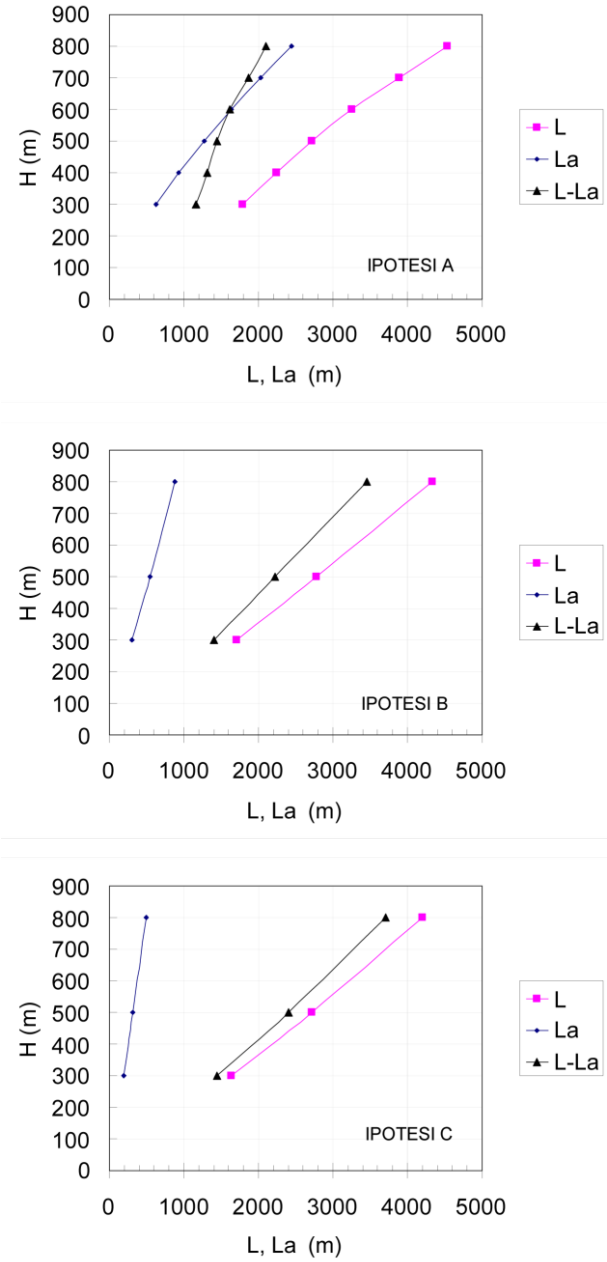

Figure 2.7. Channelled flows. M1 Model: maximum distance between the landslide front and the crown, in function of height H and the extension of the triggered zones La for the different hypoteses (A, B, C).

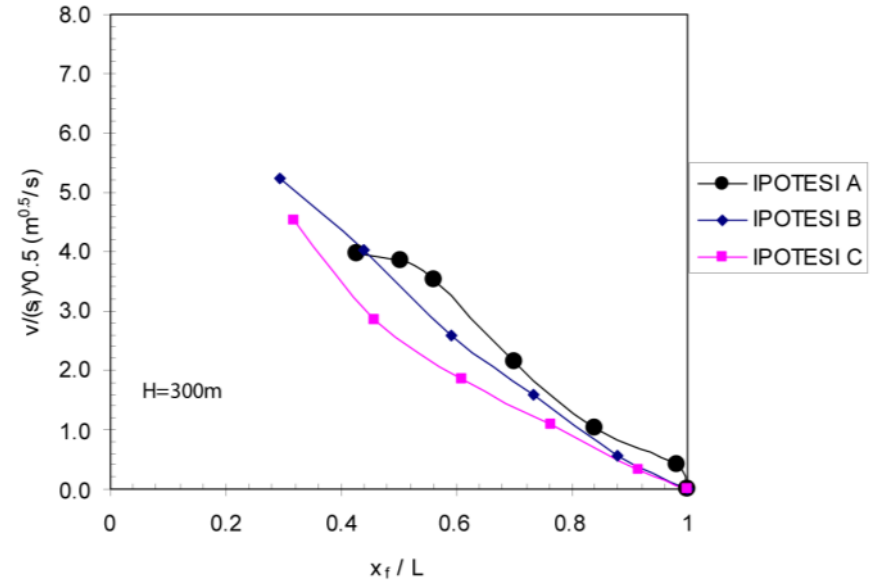

a)

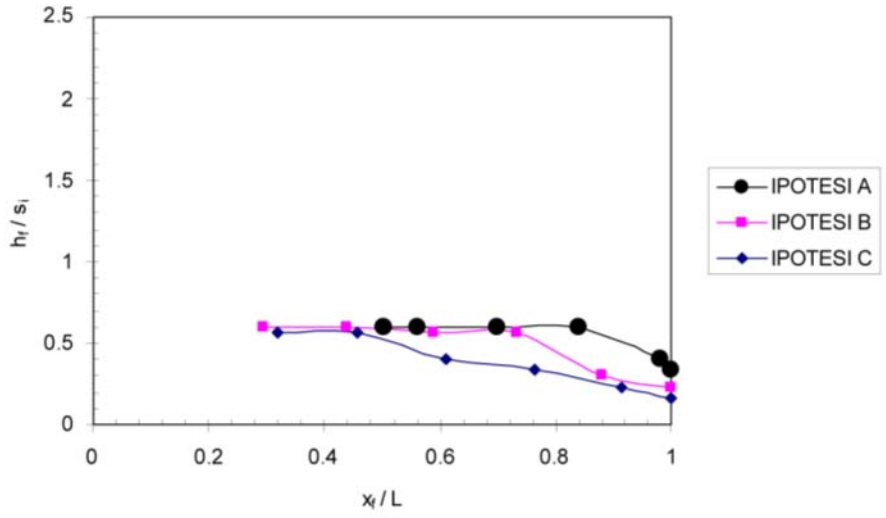

b)

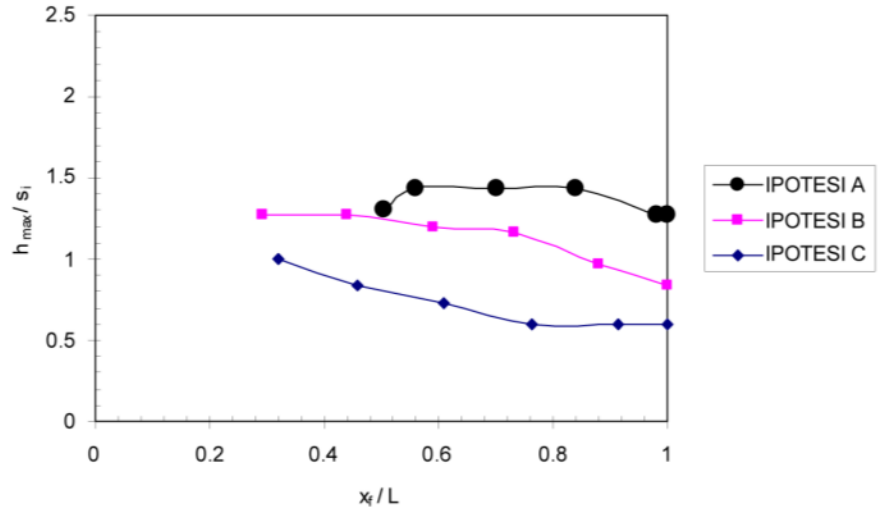

c)

Figure 2.8. Channelled debris slide- rapid earth flow. H=300m, M1 model: a) front speed v_f; b) front height h_f; c) maximum height h_{max} of the landslide between the front and the crown.

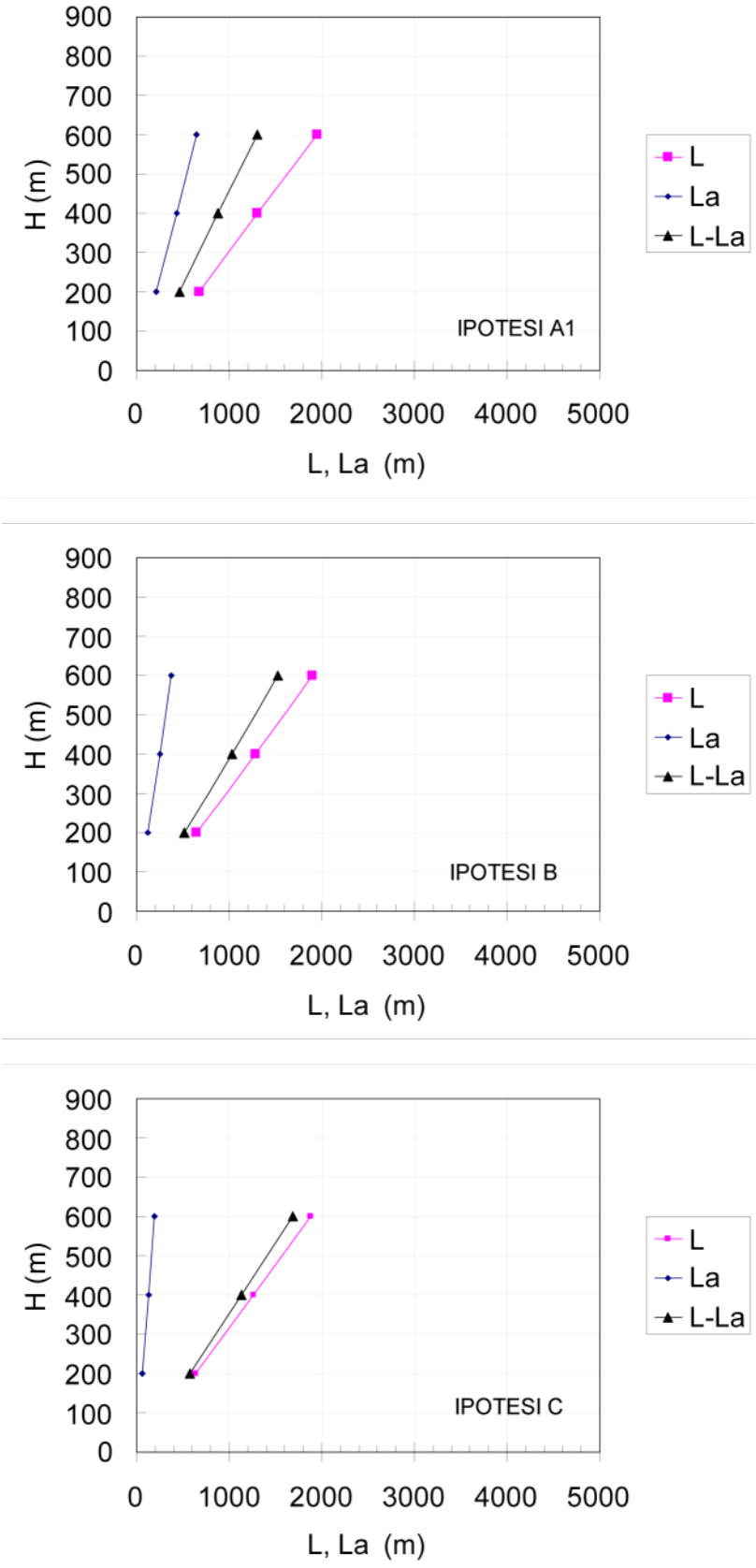

Figure 2.9. Unchannelled flows. M2 Model: maximum distance between the landslide front and the crown, in function of height H and the extension of the triggered zones La for the different hypoteses (A1, B, C).

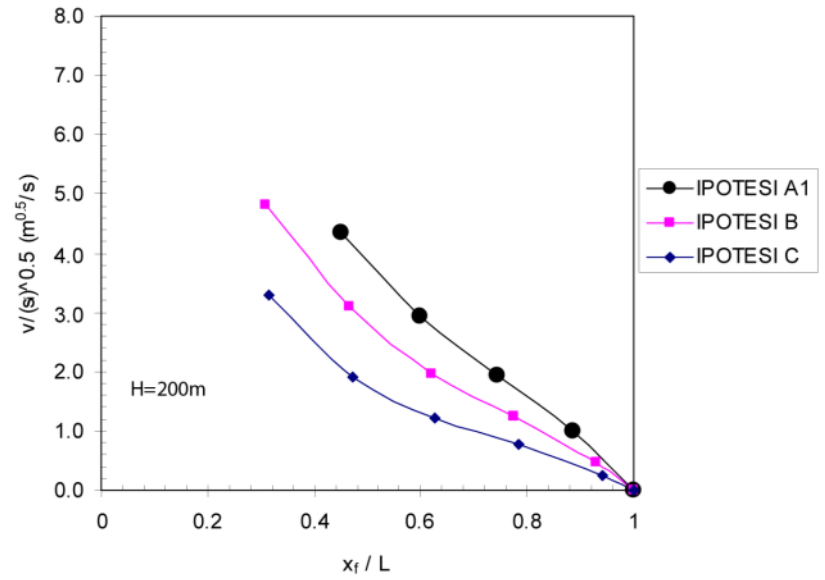

a)

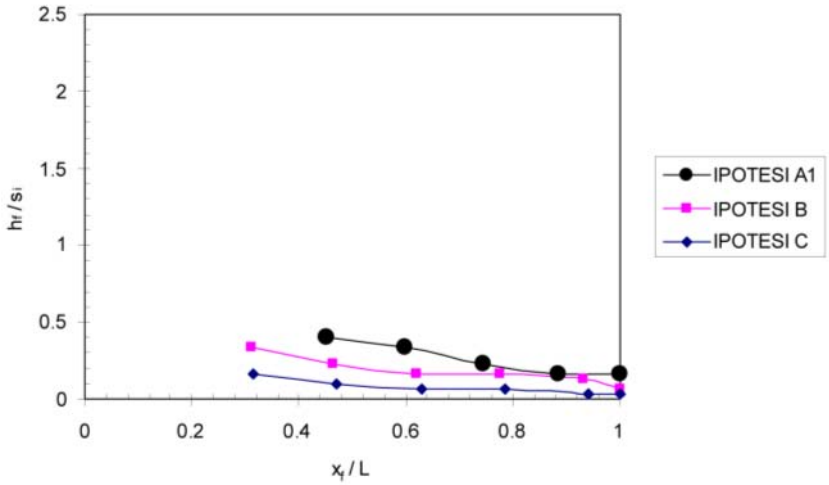

b)

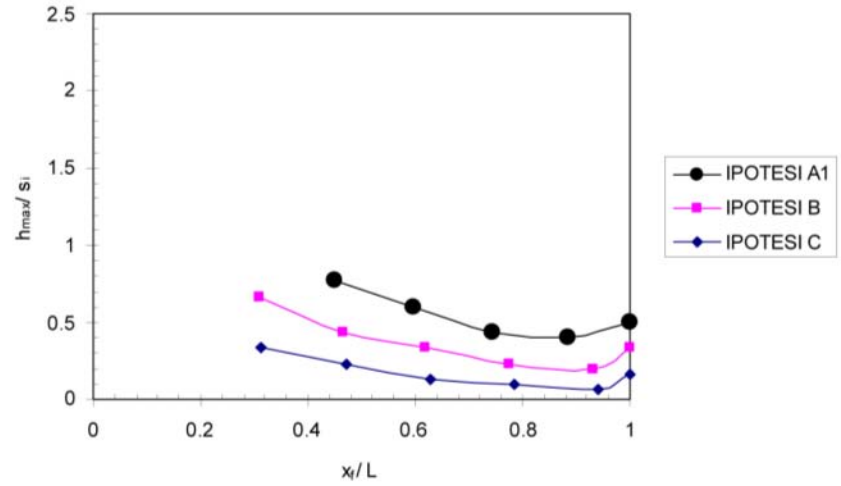

c)

Figure 2.10. Unchannelled debris slide- rapid earth flow. H=200m, M2 model: a) front speed vf; b) front height hf; c) maximum height hmax of the landslide between the front and the crown.

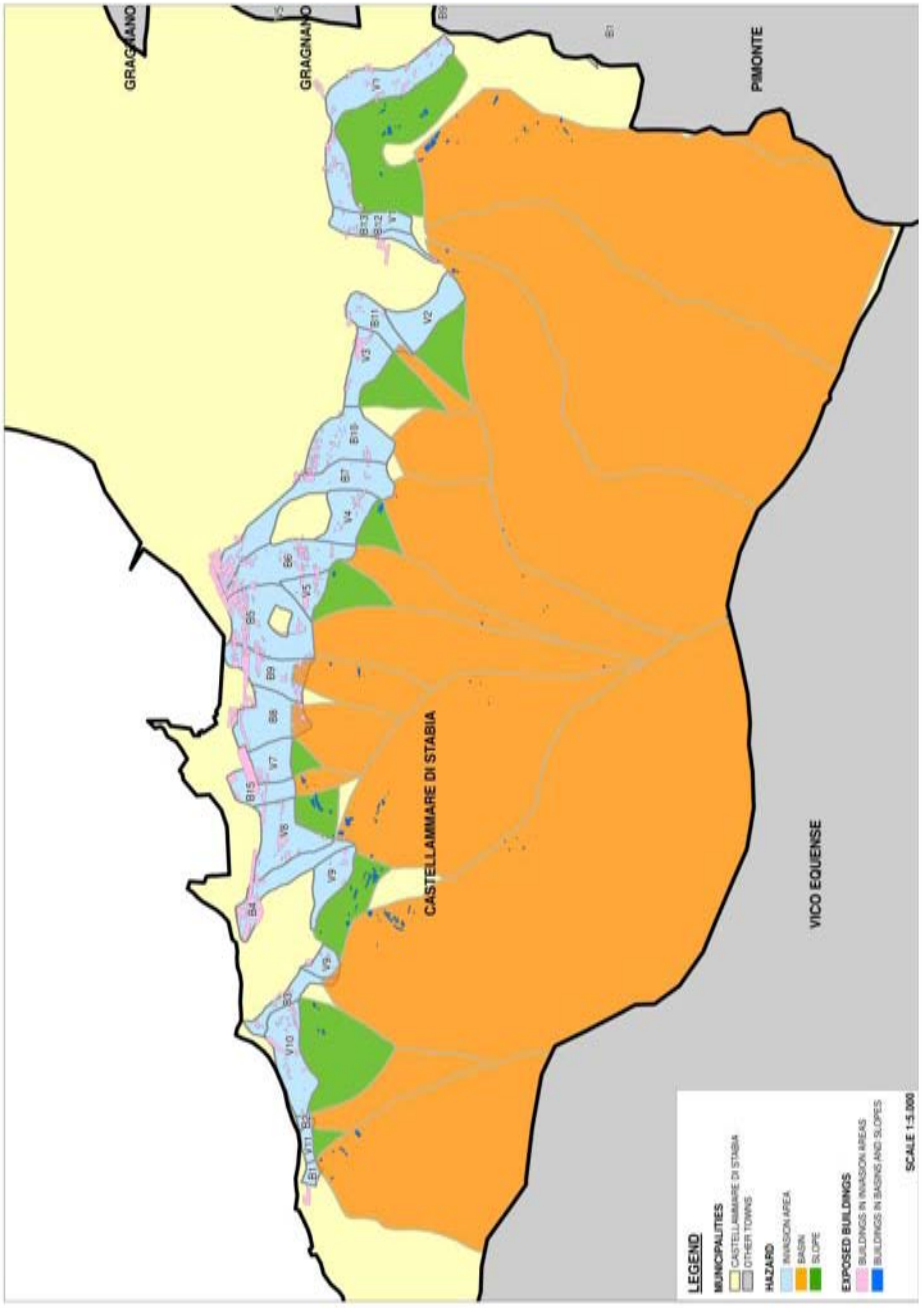

Figure 2.11. Castellammare di Stabia town: Hazard map.

2.3 VULNERABILITY

The pressure exerted by the landslides on the walls of the affected buildings is almost always able to cause, even at the limits of the affected area, the collapse of non-structural elements and damages due to the invasion of the flow inside the building, while in the presence of high velocity a strong probability of serious damage to structures is likely to occur, which in some cases leads to the collapse of the building.

It has been observed from previous events that the buildings response to the stress induced by a landslide does not depend only on the strength characteristics of the structure, but also by the *resistance hierarchy* between structure and *secondary element*, such as windows and infill panels.

In order to simulate the real behaviour of buildings, it should be therefore investigated at first the individual elementary vulnerability (structure, buffering, window) and then to trace vulnerability curves corresponding to different combinations of the element resistance. In this perspective, the three vulnerability elements categories and the respective vulnerability classes have been identified:

1. Main structures vulnerability classes category (Table 2.2), classified in buildings with continuous structure (A, B, C) and buildings with framed-structure and infill walls (D, F, G).
2. Infill walls in framed buildings vulnerability classes category (Table 2.3), classified on the basis of material, thickness (typically between 25 and 40cm) and joint to the structural frame.
3. Openings vulnerability classes category (Table 2.4), classified in function of size, material and presence of a protection screen.

Table 2.2. Vulnerability classes for main structures.

MAIN STRUCTURES	
CLASS	**TYPOLOGY**
A	Weak smoll buildings wood-structurea, seasonal or permanent, with da low-stiffness walls Masonry buildings with load-bearing walls badly connected and/or with thickness less then 25 cm, made with air bricks or irregular stone and bad quality mortar. Light precast buildings with corrugated or insulated steel sheet bearing panels
B	Strong wood buildings, permanent with stiff walls Masonry buildings with strong, well joined walls with thickness more then 30 cm and less then 50cm
C	Masonry buildings with strong, well joined walls with thickness more then 50 cm made with strong terra-cotta bricks or tuff or irregular stone and good quality morter. Rigid ceilings
D	Light precast buildings with corrugated or insulated steel sheet infill panels and steel frame not braced R.c. buildings not-aseismic, designed for vertical loads, with weak frame, bad quality concrete and low pe rcent of reinforcing steel bars
E	Light precast buildings with corrugated or insulated steel sheet infill and steel braced frame. R.c. buildings not-aseismic, designed for vertical loads. R.C. buildings with lighi frame and beams with span larger than 4 m
F	Strong steel breced frame structures Strong r. c. Buildings, a-seismic or not, with max 5m span and distance between floors less than 4 m

With the aim to analyze the effects of the landslides on the buildings, the flows impact has been schematized as a horizontal pressure evenly distributed along the hit area with

a flow front equals to the inter-storey height and the intensity furnished by the following relation:

$$p=1/2\rho v^2$$

where: ρ is the flow density, assumed equals to 15kgm^{-3}; and v is the flow speed, determined according to the hazard model illustrated in paragraph 2.2.

Table 2.3. Vulnerability classes for infill walls in framed buildings.

INFILL WALLS	
CLASS	**TYPOLOGY**
A	Corrugated or insulated steel sheet infill panels. Wood panels . Light brick walls with less then 25cm thick
B	Terra-cotta air brick walls with more then 25 and less then 35cm thick Lightweight concrete brick walls with more then 25 and less then 35cm thick Tuff walls with more then 25 cm thick , non-regular elements and ineffective connections to the frame
C	Not-reinforced or weakly reinforced concrete walls, well connected to the frame Air brick or full brick walls , more then 35 cm thick and well connected to the frame Lightweight concrete brick walls , more then 35 cm thick and well connected to the frame Tuff walls , more then 35 cm thick , with regular joint texture and well connected to the frame

Table 2.4. Vulnerability classes for openings.

OPENINGS		
CLASS	**TYPOLOGY**	**SIZE**
A	Weak Pvc (not protected or in bad condition)	large or medium
	Weak wood (not protected or in bad condition)	large or medium
	Weak aluminium (not protected or in bad condition)	large or medium
B	Weak Pvc (not protected or in bad condition)	small
	Weak wood (not protected or in bad condition)	small
	Weak aluminium (not protected or in bad condition)	small
	Strong Pvc manteined	large
	Strong wood mainteined	large
	Strong aluminium manteined	large
	wood + aluminium	large
C	Strong Pvc manteined	medium or small
	Wood + aluminium	medium or small
	Aluminium manteined	small
	Strong aluminium manteined	medium or small
	steel	any

In addition, the impact produced by the dragged objects (boulders, garbage bins, vehicles, etc.) has been taken into account, assuming a contact area of 25×25cm^2.

The study of the main structures and the infill panels has been conducted through limit state Theoretical Calculation Model (Zuccaro et al. 2000), modifying geometrical parameters (number of floors, distance between walls, height of intermediate landing, inter-story height, reinforcement percentage, thickness of infill panels, etc.) and construction characteristics (material, floor's stiffness, connections between walls frame stiffness etc.). On the other hand, for the openings, a serie of experimental breakthrough tests has been performed (Zuccaro et al 2000, Spence et al. 2004a, b, Zuccaro et al. 2008). The obtained results have been combined in a specific computational procedure, based on the probability of triggering of the most common mechanisms of collapse as a function of lateral pressure and typological characteristics.

The final outcome of the numerical and experimental analyses are constituted by the vulnerability curves detailed in Figure 2.12. For each combination of the three

vulnerability classes categories (main structures, infill panels and openings), they relate the flow speed (0-5ms^{-1}) and the expected damage, according to the descriptive scale indicated in Table 2.5. In particular, each vulnerability curve is valued as the average distribution among the ones related to all considered cases.

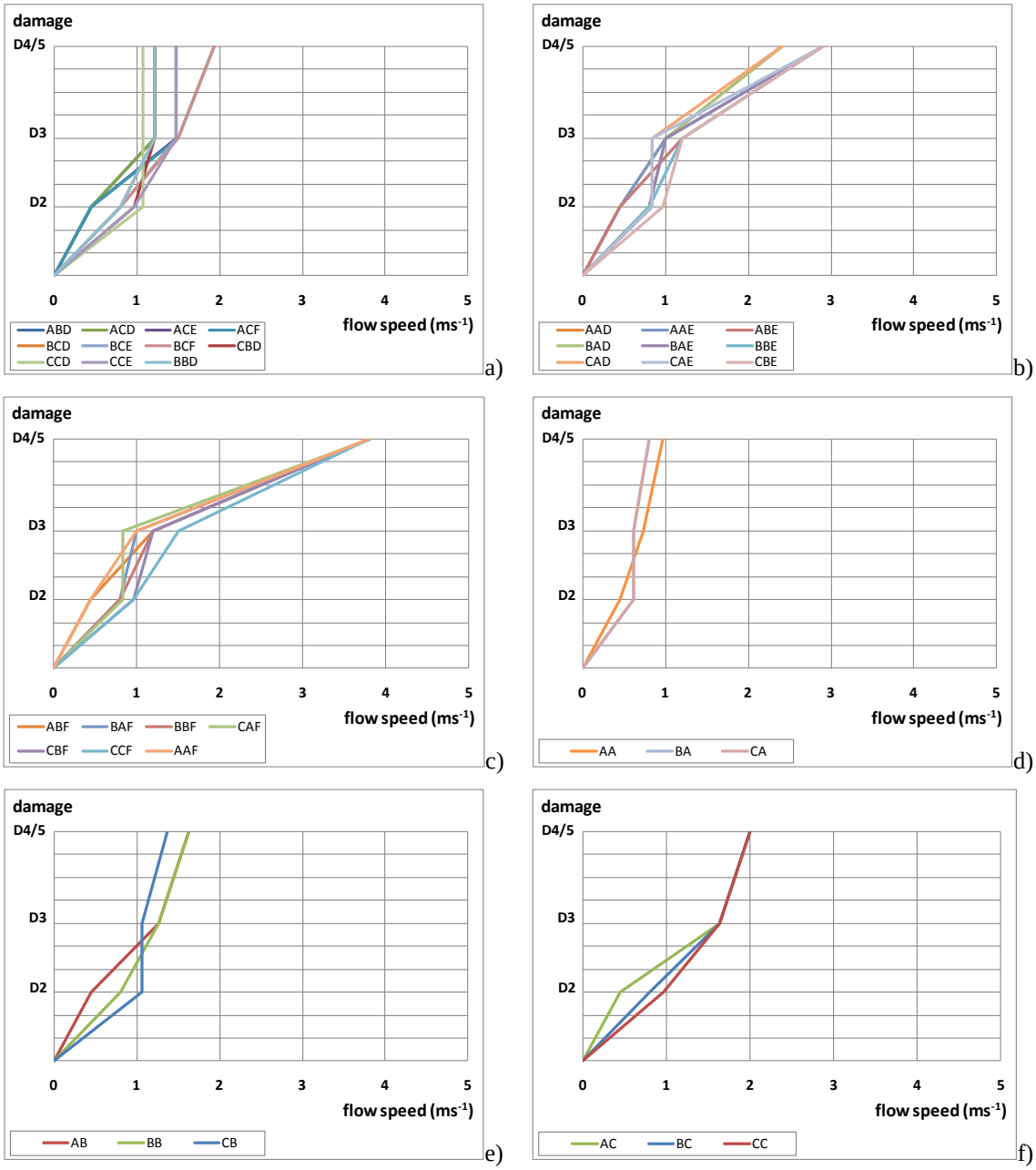

IJK code: a-c) I = openings class, J = infill panels class, K = main structures class; d-f) I = openings class, J = main structures class.

Figure 2.12. Vulnerability curves of each group of combinations among the three vulnerability categories - main structures vulnerability classes (**Table 2.2**), infill panels in framed buildings (**Table 2.3**) and openings (**Table 2.4**) - with reference to the damage scale indicated in **Table 2.5**.

In the perspective of a scenario analysis useful to plan the emergency management and the mitigation strategies, the three vulnerability classes categories have been summarized in the unified category indicated in Table 2.6. The aim is to make the more reliable and less fragmented results, which facilitates the decision-making. The results

obtained for the case study are illustrated in Figure 2.13. They show the absence of buildings of A class and the preponderance of constructions of B class (Table 2.7).

Table 2.5. Damage scale.

DAMAGE SCALE				
damage level		damage description	works needed to rehabilitate	time to rehabilitate
0	NO DAMAGE			
1	NEGLIGIBLE SLIGHT	Negligible structural damage: tiny lesions, detachment of small pieces of plaster, falling of small stones. Breakthrough of large or weak window frames badly manteined. Mild localized invasion of flow within the building. Moderate damage to furniture, furnishings andand any object is in the first floor	No extraordinary repairs	Within 24 hours after the event
2	MODERATE	Moderate structural damage: large and deep lesions, detachment of large parts of plaster. Severe damage to nonstructural elements. Breakthrough of windows mildly resistant Flooding inside the building. Major flooding in basements if any. Moderate damage to the infill in r.c. buildings Damage to interiors (flooring, fixtures etc) Major damage to furniture and and any object is in the first floor	Removal of debris seeped into the building Low maintenance works Repair or replacement of damaged windows Check and repair facilities. Repair or replacement of damaged furniture	Within 7÷15 days after the event
3	HEAVY	Severe structural damage: Many wide and deep lesions, local plasticity of the structural elements. Possible collapse of non-structural elements Breakthrough of windows aeven if strong. Severe damage to the infill walls in reinforced concrete buildings, in a few cases total collapse of infill walls. Major flooding inside the building. Total invasion of any full basements Severe damage to interior finishes (flooring, fixtures, equipment) Severe damage to furniture, facilities, furnishings and any object is in the first floor	Removal of debris seeped into the building Major maintenance works. Structural repair and reinforcement. Checking and/or partial installation of the facilities. Replacement of windows. Repair or replacement of damaged furniture	Within 15÷45 days after the event
4 - 5	VERY HEAVY DESTRUCTION	Very serious structural damage. Many severe injuries, partial or total collapse of the structure. Even total collapse of the building. Breakthrough of infill walls even if strong. Major flooding with total invasion of ground floor and basements. Total destruction of facilities, finishes and everything is in the ground floor, in some cases even in the first floor. In some cases collapse of the ceiling between ground level and basement.	Total or partial demolition. New building construction Removal of debris and area arrangement with no rebuilding.	More then 45 days (even several months) after the event.

Table 2.6. Unified vulnerability classes.

CLASS	STRUCTURE and INFILL PANELS	OPENINGS	
	TYPOLOGY	TYPOLOGY	%
A	Weak timber structures, of seasonal or permanent use, with low-stiffness walls and not braced frames. Masonry buildings of 1 or 2 storeys, with thickness walls <25 cm, made of air bricks or irregular stone and bad quality mortar. Light precast buildings with corrugated or insulated steel sheet without frame or with not braced steel frame. Steel structures with weak frames and high percentage of glass panels.	A	any
B	Strong timber structures, of seasonal or permanent use, with stiff walls and braced frames. Masonry buildings of 1, 2 or 3 storeys, with thickness walls ranged between 30 and 50cm, made of air bricks or tuff. Light precast buildings with corrugated or insulated steel sheet with braced steel frame. Not-aseismic R.C. buildings with weak infill panels of thickness < 25cm Steel structures with strong frames and high percentage of glass panels.	A, B	>30%
C	Masonry buildings of more than 3 storeys, with strong, well joined walls with thickness ranged between 30 and 50cm, made with strong terra-cotta bricks or tuff or irregular stone and good quality mortar. Braced steel frames with strong and well joined infill panels. Not-aseismic R.C. buildings with strong infill panels.	C	10-30%
D	Masonry buildings of more than 3 storeys, with strong, well joined walls with thickness >50cm, made with strong terra-cotta bricks or tuff or irregular stone and good quality mortar. Braced steel frames with strong and well joined infill panels. Aseismic R.C. buildings with strong infill panels.	D	<10%

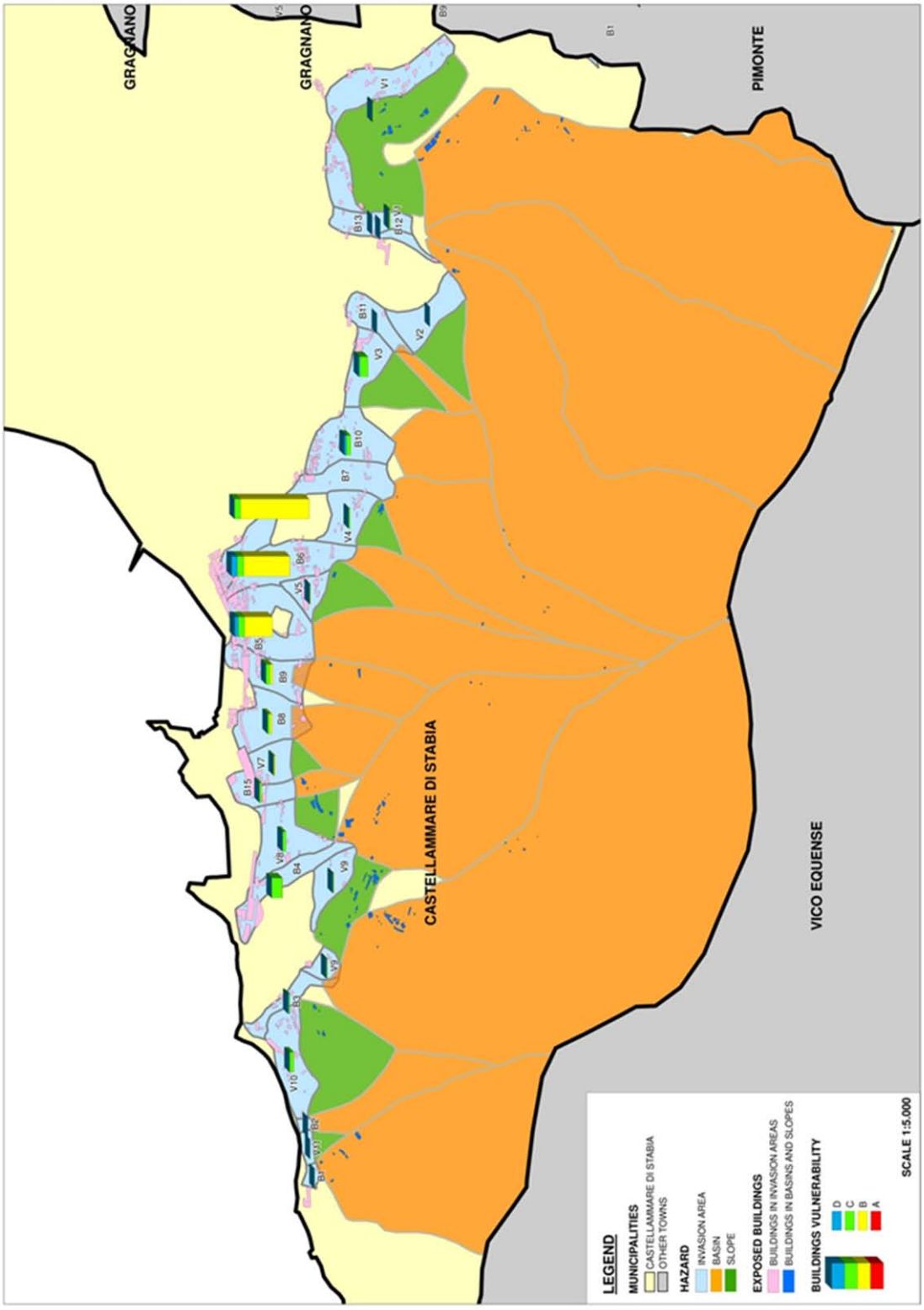

Figure 2.13. Castellammare di Stabia: Vulnerability map.

2.4 SCENARIO ANALYSIS

For the study case, the expected damage on the buildings has been determined (Table 2.7; Figure 2.14).

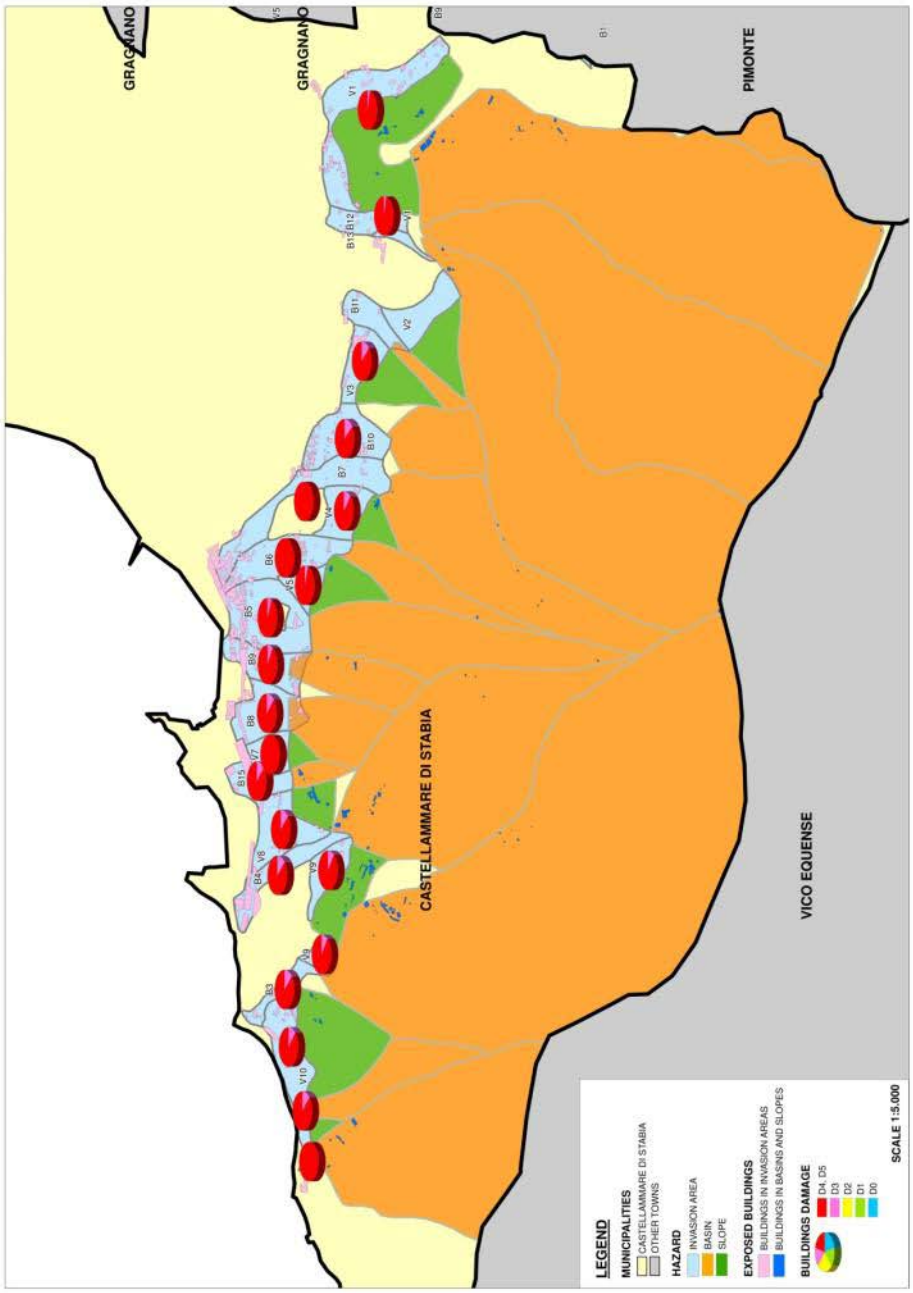

Figure 2.14. Castellammare di Stabia: Damage map.

Table 2.7. Castellammare di Stabia case study: Hazard parameters, Vulnerability classes and Damage classes with reference to each affected sector indicated in Figure 2.11.

AFFECTED SECTORS	HAZARD PARAMETERS											VULNERABILITY CLASSES				DAMAGE CLASSES				
	Qn	fbs	H	Vmin	Vmax	L	Lf	MT_m	MT_M	v	p	A	B	C	D	D0	D1	D2	D3	D4-5
	[m]	[m]	[m]	[m^3]	[m^3]	[m]	[m]	[m]	[m]	[ms^{-1}]	[kPa]	(Table 2.6)				(Table 2.5)				
B1	540	150	390	50000	99000	0	0	1	2	9,3	686,3	0	1	0	0	0	0	0	0	1
B2	450	150	300	23000	45000	0	0	1	2	9,4	711,6	0	0	1	0	0	0	0	0	1
B3	545	250	295	11000	43000	0	0	0,5	2	8,4	568,5	0	0	7	6	0	0	0	2	13
B4	650	200	450	77000	153000	0	0	1	2	8,2	531,9	0	3	80	2	1	0	0	8	77
B5	550	200	350	36000	72000	0	0	1	2	-	-	0	214	49	28	0	0	0	0	6
B6	550	200	350	36000	72000	0	0	1	2	8,1	529,7	0	354	51	44	0	0	0	1	192
B7	620	240	380	46000	92000	0	0	1	2	9,1	665,3	0	529	48	0	0	0	0	3	317
B8	400	110	290	21000	41000	0	0	1	2	9,2	681,9	0	16	16	1	0	0	0	0	1
B9	440	125	315	27000	53000	0	0	1	2	9,2	676,8	0	19	32	0	0	0	0	3	41
B10	550	275	275	18000	35000	0	0	1	2	8,4	569,4	0	0	32	16	0	0	0	6	42
B11	500	250	250	13000	26000	0	0	1	2	-	-	0	0	0	0	0	0	0	0	0
B12	480	275	205	4000	15000	0	0	0,5	2	-	-	0	0	0	0	0	0	0	0	0
B13	450	250	200	7000	14000	0	0	1	2	-	-	0	0	0	0	0	0	0	0	0
B15	250	100	150	2500	5000	0	0	1	2	8,0	505,6	0	5	12	0	0	0	0	0	2
V1	300	200	100	6000	12000	155	110	1	2	7,5	446,5	0	5	6	2	0	0	0	1	32
V2	370	250	120	9000	17000	160	120	1	2	6,7	361,7	0	0	0	0	0	0	0	0	0
V3	350	195	155	14000	27000	220	160	1	2	6,0	291,4	0	0	64	8	0	0	0	8	64
V4	290	200	90	5000	9000	115	80	1	2	7,6	459,7	0	0	10	0	0	0	0	1	10
V5	275	145	130	10000	20000	175	130	1	2	5,3	226,5	0	3	3	0	0	0	0	0	8
V7	180	105	75	3000	5000	90	70	1	2	7,9	495,6	0	10	3	0	0	0	0	0	11
V8	190	110	80	3000	6000	145	110	1	2	6,0	286,3	0	0	24	3	0	0	0	3	24
V9	200	125	75	3000	5000	130	95	1	2	7,3	430,9	0	3	4	2	0	0	0	1	8
V10	250	40	210	22000	43000	290	210	1	2	-	-	0	3	29	2	0	0	0	3	31
V11	95	25	70	2000	3000	90	70	1	2	9,3	686,3	0	0	0	0	0	0	0	0	0

REFERENCES

De Falco, M., Di Crescenzo, G., Santo, A. (2011). Volume Estimate of Flow-type Landslides along Carbonate and Volcanic Slopes in Campania (Southern Italy). Nat. Hazards. DOI 10.1007/s11069-011-9782-z

Di Crescenzo, G., Santo A. (2005). Debris slides-rapid earth flows in the carbonate massifs of the Campania region (southern Italy): morphological and morphmetric data for evaluating triggering susceptibility. Geomorphology 66 (2005) 255-276.

Hungr, O. (2002). Analytical models for slides and flows. In: Proceedings of the International Symposium on Landslide Risk Mitigation and Protection of Cultural and Natural Heritage, Kyoto, 21–25 January 2002. Edited by K. Sassa. Kyoto University.

Scotto di Santolo, A. (2002). Le colate rapide. Hevelius Edizioni srl, Benevento 2002, ISBN 88-86977-42-5.

Spence, R.J.S., Baxter, P.J., Zuccaro, G. (2004a). Building vulnerability and human casualty estimation for a pyroclastic flow: a model and its application to Vesuvius. J. Volcanol Geotherm Res. 133: 321–343.

Spence, R.J.S., Zuccaro, G., Petrazzuoli, S., Baxter, P.J. (2004b). The resistance of buildings to pyroclastic flows: analytical and experimental studies and their application to Vesuvius. Natural Hazards Review 5: 48–59.

Zuccaro, G. (2000). Final Report European Project ENV4-CT98 0699: Human and Structural Vulnerability Assessment for Emergency Planning in Future Eruptions of Vesuvius using Volcanic Simulations and Casualty Modeling. Directorate XII Commission. EU. June, 2000.

Zuccaro, G., Cacace, F., Spence, R.J.S., Baxter, P.J.(2008) Impact of explosive eruption scenarios at Vesuvius, Journal of Volcanology and Geothermal Research 178 416–453.

3 DEAP-SEATED LANDSLIDE IN ANCONA (ITALY)

(UNIFI)

3.1 INTRODUCTION

On the night of December 13th, 1982 (according to the notation for dates employed herein: 1982-12-13), the city of Ancona has been affected by a large landslide that occurred along the coast to the north of the town, in the adjacent slopes of the Montagnolo Hill (Figure 3.1). The volume of the mass movement was about 180 million m^3, while the affected surface area was 220 hectares, accounting for 11% of the total urban area of the Ancona municipality (Cardellini & Osimani, 2008).

No casualties were recorded during the event. Nonetheless, the landslide caused extensive damage to structures and infrastructure, such as the University Medical Faculty and the local hospital (Anon, 1986; Cotecchia, 1997a, b). As described by Cardellini and Osimani (2008), in the morning of December 13th, "after a night of uninterrupted movements and noises due to the opening and widening of fractures in buildings", a total of 3661 people (1071 families) were evacuated from the residential districts named Posatora and Borghetto. Of these, 1562 people were moved to hotels and other residences by the Ancona municipality, and remained in that situation for a long time. Gas and water supplies were interrupted and the city remained for some days without the essential gas and water services. 280 structures (out of a total 865) suffered non-negligible to irreparable damage (or were destroyed). Among these, the highly strategic buildings of the Faculty of Medicine, the Oncological Hospital, the Geriatric Hospital and the Tambroni retirement home. 31 farms, 101 SMEs, 3 industries and 42 shops were significantly damaged, and 500 people lost their jobs. The Adriatic railway and Flaminia road were shifted laterally 10 m towards the sea.

During the event, displacements started at the toe of the slope, spreading upwards. Cotecchia (2006) reported that "large horizontal displacements of up to 8 m and uplifts of up to 3 m affected the lower parts of the slope. In the upper parts of the slope area, large horizontal displacements (up to 5 m) and vertical settlements (up to 2.5 m) were recorded. The effects of the landslide movements were not restricted to on-shore areas; large displacements also occurred in the seabed adjacent to the main landslide".

Though the 1982-12-13 event can be described as prevalently slow, rapid mudslides occurred in highly saturated colluvial soils in some areas of the landside, (Cardellini & Osimani 2008). The Ancona landslide can be described as a deep-seated, complex, composite landslide according to the Cruden & Varnes (1996) classification.

The Ancona landslide is an important case-study for multiple reasons: first, it is an active (though slow) landslide; second, it affects a strategic urban location; third, a considerable amount of monitoring data are available.

Because of the significance of the Ancona landslide event, local authorities were interested in assessing the possibility to stabilize the affected area. An extensive campaign of geological, lithological, geophysical, geomorphologic, geotechnical, interferometer, topographic and hydrologic analyses, aimed at supporting a preliminary design for remediation, was initiated. A wide range of both intrusive and non-intrusive investigative techniques were used to assess the geological and geotechnical

characteristics of the mass involved in the 1982 landslide, the failure mechanisms and the factors that triggered the event. These are reported in detail in Cotecchia, (2006).

The preliminary design of slope stabilization measures envisaged:

- A large stabilization embankment, consisting of an earth embankment and a protective reef to improve the static equilibrium of the slope by increasing the load at the toe;
- A deep drainage system, comprising a network of permeable, parallel drainage trenches perpendicular to the coastline and crossing the lowest part of the landslide area as well as deep drainage wells constructed at regular intervals within the trenches to reduce the pore water pressures in the soil;
- A bio-stabilization and slope re-profiling strategy to improve the drainage of surface waters and minimize areas of excessive accumulation or ponding, thereby reducing infiltration into the slope.

In the intentions of the designers, the main beneficial effects of the stabilization measures should have been on the superficial and intermediate sliding surfaces. These were deemed to be crucial to the global stability of the slope as they restricted the progressive retrogressive failure mechanisms, which were thought to be the most likely mode of long-term slope degradation.

Local Authorities concluded that a comprehensive consolidation was would have entailed very large expenses and would have brought a very severe environmental and socio-economical impact on the area. Hence, The Ancona Municipality decided to live with the landslide while striving to ensure the safety of local residents.

In 2002, the Regione Marche assigned the Ancona Administration the responsibility of creating an Early Warning System and an Emergency Plan for people who are still today living in the landslide area. The Early Warning System, which is currently being improved by additional instrumentation, aims to provide an integrated and continuous control at a superficial and deep level of the entire landslide area. Details are given in Cardellini & Osimani (2008). Nonetheless, the planned remedial scheme was partially carried out, when some stabilization works were conducted between 1999 and 2003 on the eastern part of the landslide area (between the Barducci and Palombella districts)[1]. A more superficial drainage system was also completed; reinforced bulkheads were built, and some parts of the landslide area were reforested.

[1] The stabilization works involved the construction of two substantial drainage trenches uphill of Via della Grotta. These were located largely within the major existing natural trenches and had the function of intercepting surface water infiltrating into the slope through these natural features and generally lowering pore water pressures within the slope. After this initial work, priority was given to the stabilization of the slope between Via della Grotta and the main road SS16. This was the location of the superficial but extensive “Barducci” landslide which occurred in 1982, with an approximately NNE direction of propagation. These works consisted of: (a) two anchored concrete diaphragm walls; (b) one anchored bored cast in situ concrete pile wall; (c) a system of drainage trenches; (d) a surcharge fill at the toe of the slope; (e) a bio-stabilization program comprising the planting of a large forested area; and (f) associated slope re-profiling and drainage improvements. Details are given in Cotecchia (2006).

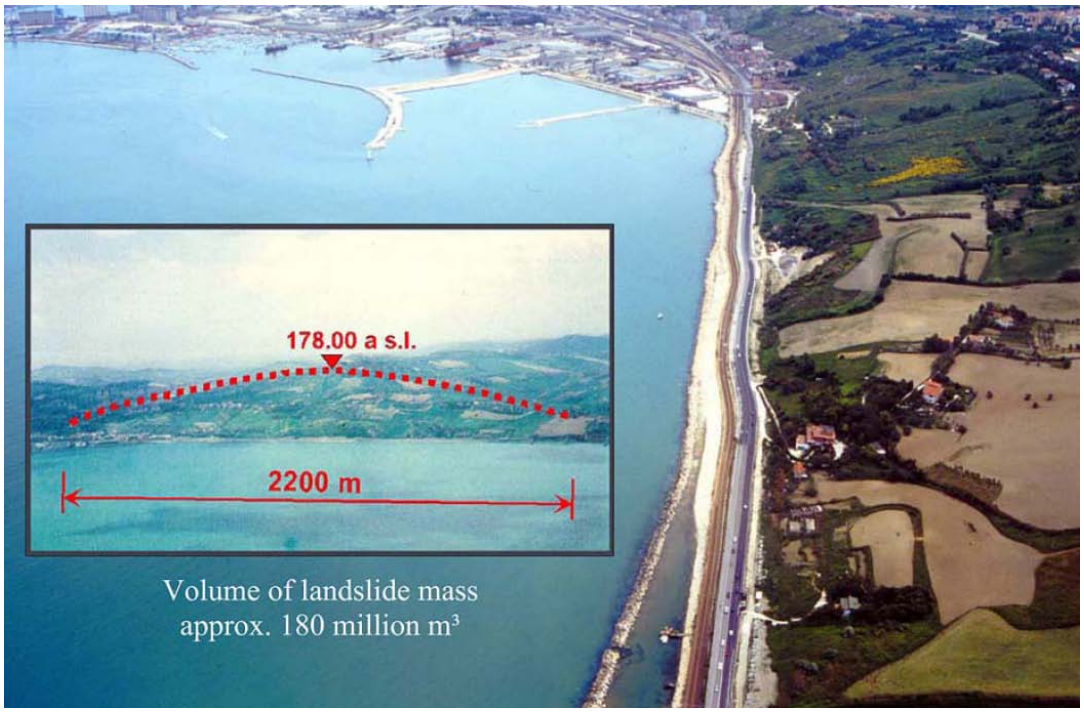

Figure 3.1. Panoramic view of the Ancona landslide area (from Cotecchia 2006)

3.1.1 Reference risk model

It is generally accepted that quantitative risk estimation for natural hazards is to be preferred over qualitative estimation whenever possible, as it allows for a more explicitly objective output and an improved basis for communication between the various categories involved in technical and political decision-making. The considerable heterogeneity in conceptual approaches to risk estimation is a well-known fact. No univocal definition is available at present, and the conceptual unification of risk analysis methods currently appears to be a practically unattainable goal. A consistent quantitative risk estimation analysis must rely on a reference risk framework. UNDRO (1979), for instance, proposed the following model, in which risk is calculated as the product of three macro-factors:

$$R = H \cdot V \cdot E$$

in which R=risk; H=hazard; V=vulnerability and E=value of elements at risk.

To avoid the undesirable consequences of misinterpretations of risk estimates and assessment due to the aforementioned terminological fragmentation, it is essential to provide reference definitions explicitly. In the ISSMGE TC304 "*Engineering Practice of Risk Assessment & Management" Glossary*" (e.g. http://jyching.twbbs.org/issmge/2004Glossary_Draft1.pdf), hazard is "the probability that a specific hazardous event occurs within a given period of time"; vulnerability is defined as "the degree of expected loss (from 0: no loss expected; to 1: total loss expected) in an element or system in relation to a specific hazardous event", while the "elements at risk" macro-component parameterizes the value of vulnerable physical or non-physical assets in a reference system. Consequently, risk can be defined as "the probability of the manifestation of a given level of loss in physical or non-physical assets within a given time period as the result of the occurrence of a specific hazardous event". The measurement units of elements at risk are not univocal, and depend on the

typology of elements at risk. The value of physical assets, for instance, is usually measured and expressed in financial units, while the value of lives has been parameterized in the risk analysis literature using both financial and non-financial units (e.g. 'equivalent fatalities').

The reference risk equation in can be rewritten as

$$R = R_s \cdot E$$

in which:

$$R_s = H \cdot V$$

is the specific risk, i.e. the probability of adverse degree of loss related to a hazardous event of a given magnitude.

3.1.2 Objectives of the study

Reliable estimates of the value of the buildings located inside the landslide area are not available. Hence, only specific risk can be estimated to an acceptable degree of confidence. The objectives of the present study are: (1) the quantitative characterization of slope kinematics from monitoring data; and (2) the quantitative estimation of specific risk for a set of 60 buildings located inside the landslide area.

3.1.3 Knowledge from previous investigations

The present analysis approaches the case-study from a quantitative point of view, and relies on previous investigations which contents are reported synthetically in the following.

3.1.3.1 Geological, lithological and bio-stratigraphic setting

The geological setting of the area involved in the 1982 landslide was deduced from a detailed geological, lithological and micropalaeontological survey and also from the structural and stratigraphic analyses of cores from more than 60 boreholes drilled from 1983 to 1999, both on-land and off-shore. From a structural point of view, the Ancona area lies on the external margin of the Apennines, which tectonic history is directly connected to the evolution of the Adriatic foredeep (Bally et al. 1988). Figure 3.2 (Cotecchia 2006) shows a geological map of the area, together with a representative geological cross section. Underlying the recent superficial cover of elluvium, colluvium and associated landslide debris, a succession of strata belonging to the Lower, Middle and Upper Pliocene and the Lower Pleistocene were identified. Also depicted on the geological map are traces of the Tavernelle syncline, NE–SW transcurrent faults and

EW normal faults, which were formed principally as a result of several tectonic phases from the Pliocene to the Quaternary (see Cotecchia 2006 for relevant references).

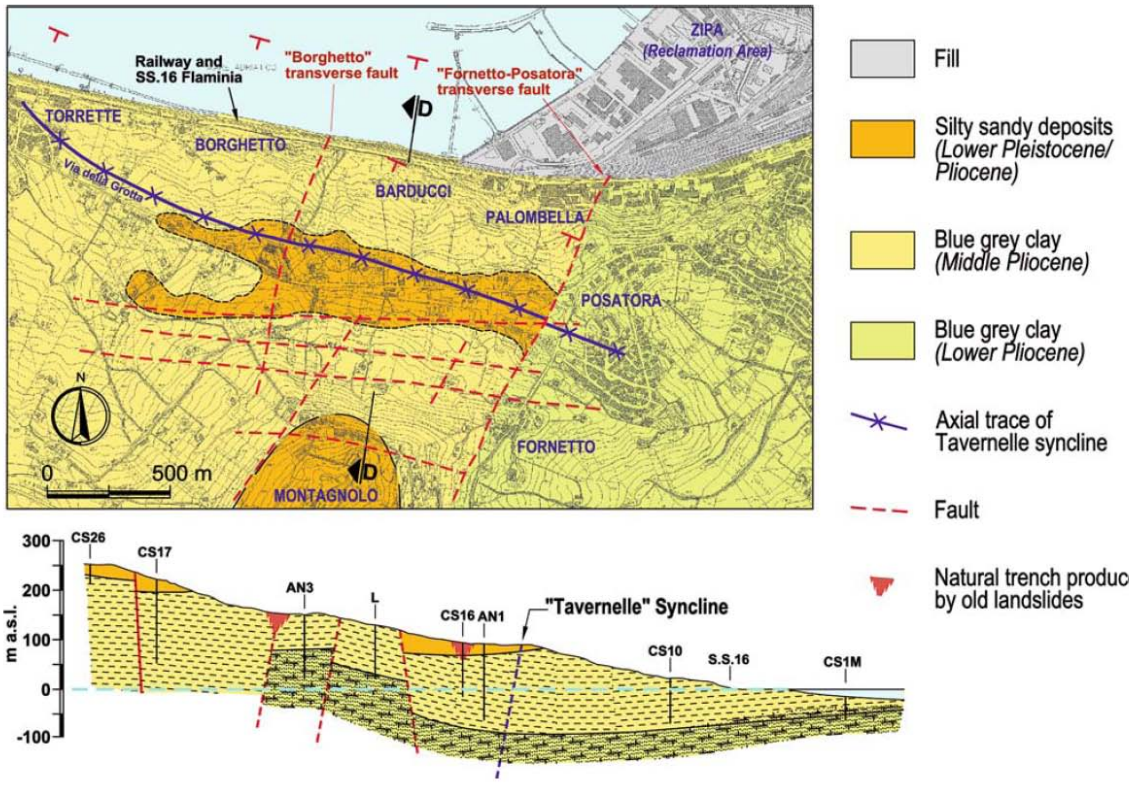

Figure 3.2. Geological map and cross section of the Ancona landslide area (from Cotecchia 2006)

3.1.3.2 Tectonic and seismic setting

The Ancona zone is still affected by tectonic activity, as shown by neo-tectonic variations in ground levels. The tectonic and structural setting of the Ancona area derives from several tectonic phases along the peri-Adriatic belt (Cotecchia 2006)[2]. Such tectonic movements, both parallel and transverse to the coastline, generated

[2] The oldest recognised phase is the Lower and Middle Pliocene compressive phase, having a maximum direction of compression around 50° N–60° E. During this phase, reverse faults and fold structures developed, having a direction parallel to the Apennine Chain (NNW-SSE). The Tavernelle syncline was also formed during this tectonic phase. From the Upper Pliocene until the present, the prevalent direction of tectonic movements at Ancona has remained north-easterly. In the northern part of the Apennine arc (which includes the Ancona area), some authors (e.g. Patacca et al. 1990) distinguished zones of lithospheric ruptures having an anti-Apenninic direction, corresponding to normal and transcurrent faults at the surface. These anti-Apenninic faults have produced, in some places, the dislocation of the Lower Pleistocene fluvial terraces, supporting the idea that these faults developed mainly after the Lower Pleistocene. At Ancona the main anti-Apenninic faults attributed to this period are the Fornetto-Posatora and the Borghetto transcurrent faults, which are associated with the concentration of normal faults running NE–SW across the slope. The Fornetto-Posatora fault, which delimits the eastern margin of the Montagnolo Hill, also dislocates the Tavernelle Syncline, juxtaposing laterally the Lower and Middle Pliocene at the surface. The throw of the fault displaces the Lower Pliocene by up to 150 m.

discontinuities or zones of weakness in the slope which strongly influenced the development of the failure mechanisms and movements observed at Ancona. Crescenti et al. (1977) related the seismic activity that occurred in the area between 1972 and 1975 to movements along the existing anti-Apenninic transcurrent faults. As shown in Figure 3.3, the 1982 landslide area is located within the isoseismic line VIII (Mercalli-Sieberg scale) of the 1972 earthquake, towards the epicentre. During the seismic events, some deep fractures developed in the area between the main scarp of the 1982 landslide and the upper trench (Cotecchia 2006).

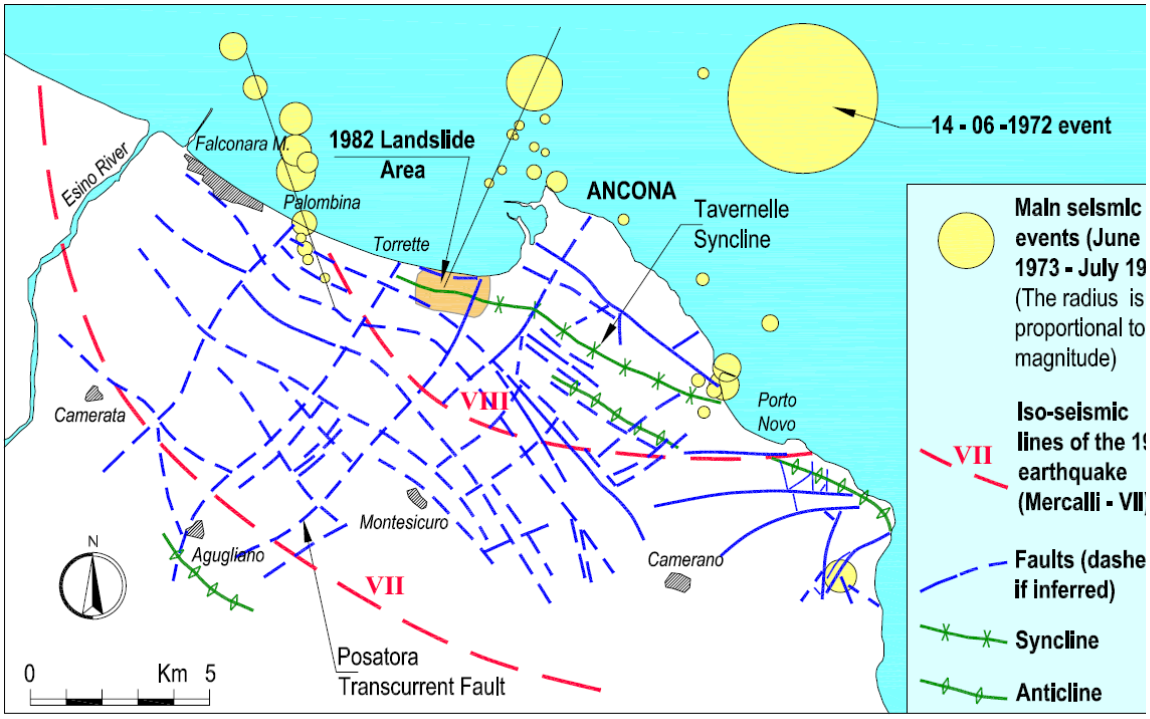

Figure 3.3. Ancona landslide: seismic events (1972 and subsequent 1973-1980). Figure from Cotecchia (2006)

3.1.3.3 Geomorphologic features of the ancona landslide

The coastal slopes in the Ancona area are known to have been unstable for centuries. Historical records document significant movements which occurred in the same slope in 1578, 1774, 1858 and 1919 (see Cotecchia 2006 for relevant references). The 1982 event caused the partial or total reactivation of the majority of the pre-existing geomorphological discontinuities, as well as the activation of several new sliding surfaces and deformation zones. A general subsidence of the central and upper part of the slope was observed, with a partial reactivation and extension of the pre-existing natural trenches (Cotecchia 2006). The geomorphological map of deep mass movements (Figure 3.4) shows the outcropping morphology of the deeper landslide bodies present in the slope.

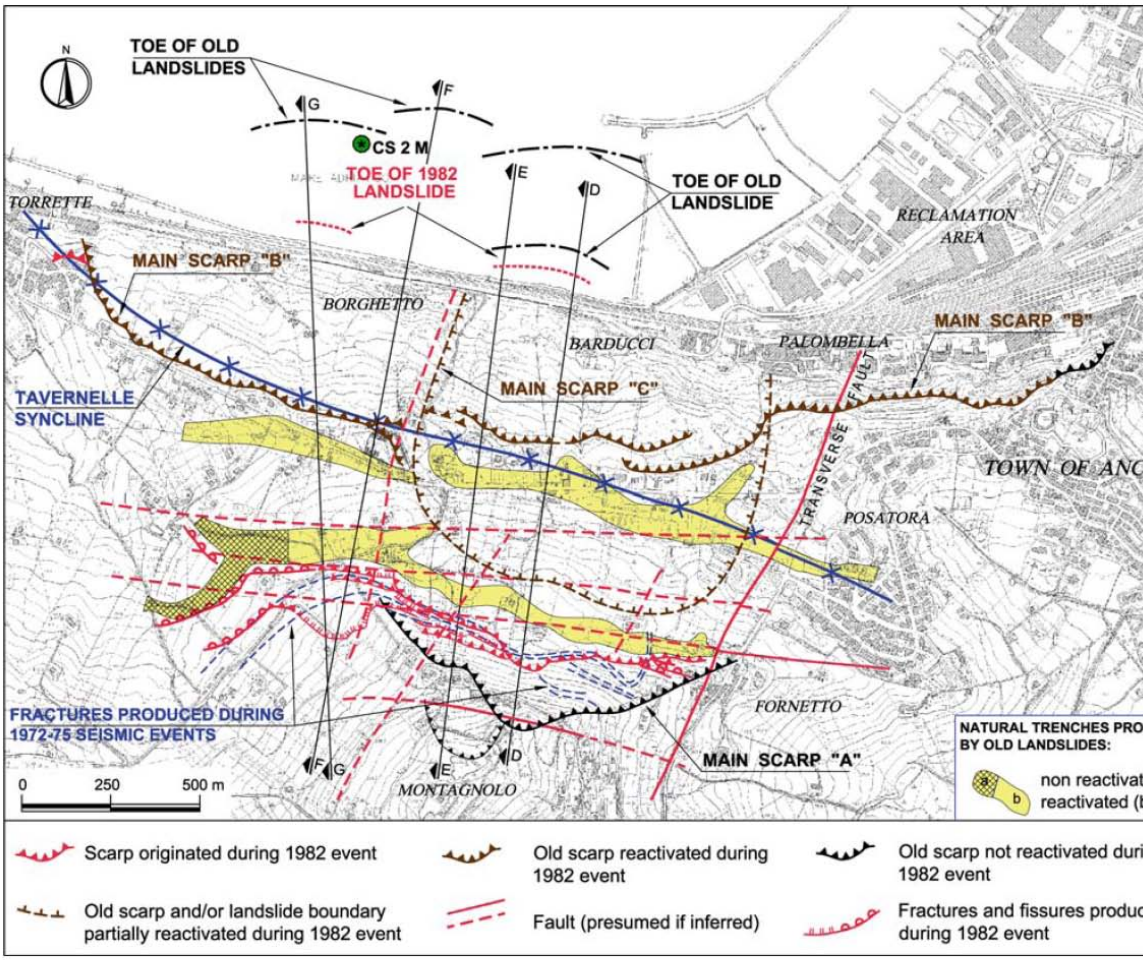

Figure 3.4.Ancona landslide: geomorphological map of deep mass movements (Cotecchia 2006)

The main geomorphological features of the Ancona 1982 landslide were outlined by Cotecchia (2006):

- The principal scarp of the slide runs approximately sub-parallel to the coastline;
- Three pre-existing deep compound landslides (A, B and C, respectively) have been identified in the area.
- The main scarp of Body A, not reactivated in 1982, is located at the top of the slope and is related to a sliding surface that reaches the sea and has a maximum depth of 120 m bgl
- Body B, with a maximum depth of 80 m bgl, is in the middle part of the slope.
- Numerous shallow slips have been observed within Body B (e.g. the ‘‘Barducci’’ landslide in the central part of the slope).
- Body C, with a maximum depth of 120 m bgl, involves the slope below the main scarp ‘‘A’’ and is bounded by two NNE–SSW faults and one EW fault.
- The sliding surfaces of the three deep landslides converge into a single shear band at the base which, in the past, emerged offshore at a distance of 100 m from the present coastline.

- Two systems of natural trenches produced by the different displacements downhill of old landslide bodies are present on the slope (shown in yellow on the map).
- Uplift movements were observed for a distance of 50 m from the coastline.

3.1.3.4 Geotechnical estimation of post-sliding strength parameters

Geotechnical in situ and laboratory testing were carried out by Cotecchia on soils in the investigated area in order to determine the input parameters for the stability analyses. The colluvial soils which are generally found at shallow depths within the slope area are generally less homogeneous and plastic than the underlying Pliocene clays. Direct shear and triaxial tests, for both the on-land clays and off-shore clays indicate that the friction angles and cohesion intercept vary with increasing vertical effective stress, associated with the consolidation pressure and reducing void ratio. At medium to high pressures, the range where the on-land samples were mostly tested, the intercept cohesion reaches 100 kPa and the friction angle 21°. The residual friction angles obtained from direct shear testing are around 15° for the over-land samples, decreasing to 13° for the offshore samples. The results of triaxial and direct shear tests were in good accordance, though the former gave slightly higher strength values. Details are given in Cotecchia (2006).

3.1.3.5 Hydrogeologic setting

The ground water system in the area is influenced by the complex structural setting including natural trenches, fractures and discontinuities (generated both by landsliding and tectonic movements). Based on readings from 35 piezometers installed in the area of the landslide, Cotecchia (2006) suggested the presence of a prevalent seepage domain in most of the slope, probably as a result of the high degree of fissuring of the clays and the presence of sandy interbeds, despite the presence of independent deep groundwater levels. The Great Ancona Landslide of 1982 occurred during a rainy season characterized by six consecutive days of rain with an average intensity of 30 mm/day. Cotecchia (2006) described this rainfall intensity as “heavy, but not exceptional”. A statistical analysis yielded a return period of less than 10 years[3].

3.1.4 Presumed causes of landslide triggering

The mechanical behavior of a slope formed by fractured clays and containing numerous zones of reworked material (due to the presence of preexisting sliding surfaces) is not controlled by the intrinsic strength of the undisturbed clay, but mainly by the geometry, frequency and kind of discontinuities crossing the slope and by the strength characteristics of the clay along these discontinuities. Landslides in stiff jointed clays often occur along existing preferential surfaces produced by previous landslide or tectonic processes, where shear strength attains the residual value.

---

[3] A much higher return period of more than 50 years was obtained for the rainfall events which, in 1919, resulted in mass movements similar to those of 1982 (Cotecchia 2006).

Though not exceptional, the precipitation preceding the 1982 event was the highest and most unfavorable since the 1972–1973 earthquakes. Cotecchia (2006) opined that such a period of sustained heavy rainfall, may have caused a significantly higher net infiltration than would have been caused by a more intense but temporally limited precipitation period. Consequently, the triggering mechanism of the 1982 landslide may not have been the amount and duration of precipitation; rather, the increased permeability due to the fissuring of the clay produced by the 1972 earthquake and the probable contemporaneous re-opening of the natural trenches. According to Cotecchia (2006), the sub-vertical man-made cuts for clay quarrying also played a relevant role in accelerating slope instability processes by significantly altering slope geometry[4].

3.2 PARAMETERIZATION OF LANDSLIDE INTENSITY

Landslide intensity parameterizes the damaging potential of a landslide through its kinetic, and/or geometric attributes. This section illustrates the procedure used for the quantitative parameterization of landslide intensity. The output intensity parameter will be used in Section 3.4.2 in the quantitative estimation of vulnerability.

No univocal set of intensity parameters are available, though a variety of kinetic and geometric attributes have been used in previous studies (e.g. Hungr, 1997; Uzielli et al., 2008). As the Ancona landslide is a slow landslide, it is suitable to define an intensity parameter in terms of ground displacement (geometric attribute) rather than velocity (kinetic attribute). The back-calculation of intensity is used herein for the formulation of an intensity function as detailed in Section 3.2.4. The expression for posterior (i.e. back-calculated) intensity at the spatial location of a building is calculated by inverting the reference vulnerability model given in Uzielli (2012):

$$I_p = \begin{cases} \Omega\sqrt{\dfrac{V_p}{2}} & \text{for } V_p \le 0.50 \\ \Omega\left(1-\dfrac{\sqrt{2-2V_p}}{2}\right) & \text{for } V_p > 0.50 \end{cases} \tag{3.1}$$

in which I_p is the posterior landslide intensity, V_p is the posterior vulnerability and Ω is the resilience of vulnerable elements. The resilience index Ω expresses the inherent capacity of vulnerable assets to preserve integrity, functionality and desired performance in the course of the interaction with a reference hazardous event. The general resilience index model is detailed in Section 3.2.2.

[4] The quarrying of clay along the coast was a very old practice, which was abandoned in the 1950s. Numerous quarries at the toe of the slope between Palombella and Torrette are documented. Not all of them are still visible today because many have been covered by subsequent landsliding events. During the execution of the first phase of planned remedial works, a number of old brick kilns were found buried by landslide debris, thus confirming this process.

3.2.1 Quantitative estimation of posterior vulnerability

Posterior vulnerability, or “observed degree of loss” was back-assessed from available post-event survey data compiled by the Ancona municipality (Comune di Ancona) on 70 buildings located inside the landslide perimeter. Of the 70 buildings, 60 are still existing and 10 have been demolished. Figure 3.6 shows the location of the buildings.

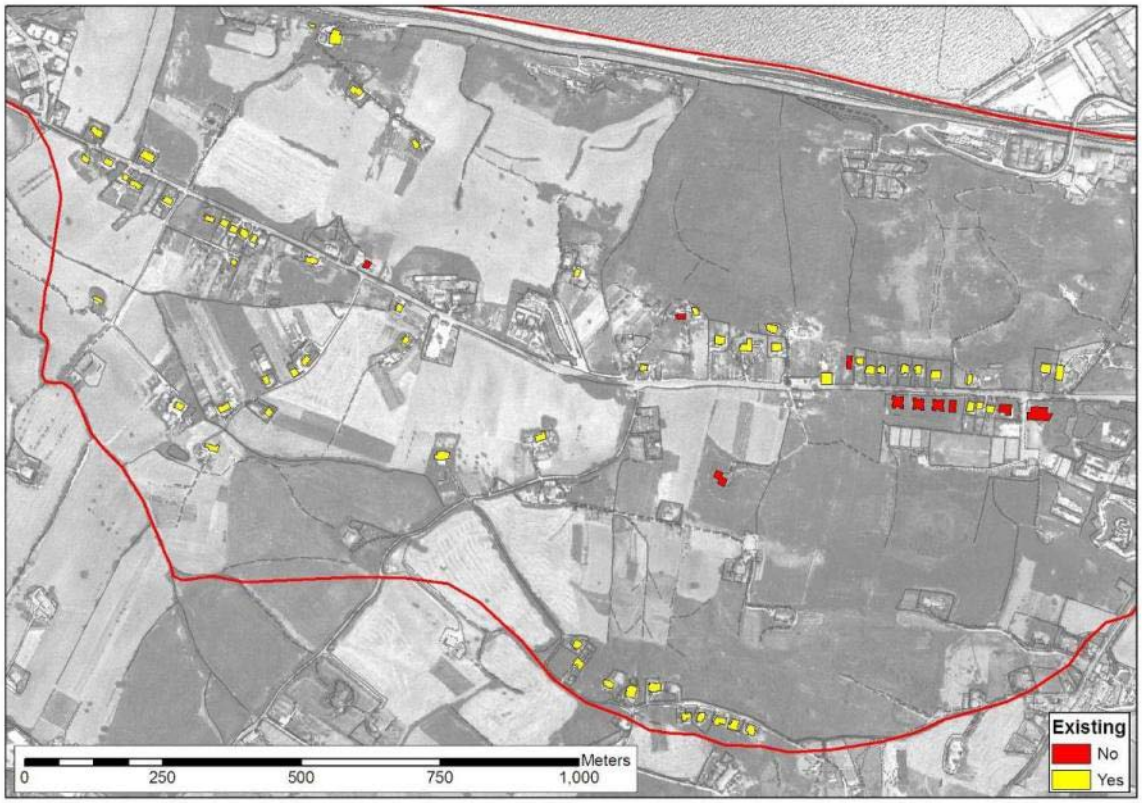

Figure 3.5. Buildings at present: existing vs. non-existing

A set of 3 typological attributes (structural typology, age of building, foundation type) and 7 damage categories were selected as relevant indicators for the quantitative estimation of posterior vulnerability. The damage indicators expressed the damage observed to: (1) main structures; (2) floors; (3) perimetral walls; (4) internal walls; (5) internal stairs; (6) external stairs; and (7) retaining structures. The complete set of the selected typological attributes and damage indicators was available for 70 buildings. Tables 1, 2 and 3 detail the categories of the structural typology, building age and foundation type attributes, respectively.

Table 3.1 Categorization of structural typology

Category	Structural typology
1	stone masonry
2	tuff masonry
3	brick masonry
4	reinforced concrete
5	mixed structure
6	retrofitted building

Table 3.2 Categorization of building age

Category	construction year
1	< 1900
2	1901-1943
3	1944-1962
4	1963-1971
5	1972-survey
6	unknown

Table 3.3 Categorization of foundation type

Category	Foundation type
1	plinths
2	strip footing
3	mat footing
4	piles

Table 3.4 contains the post-damage survey data for the 70 selected buildings. The damage indicators for main structures (D-MS), floors (D-FL), perimetral walls (D-PW), internal walls (D-IW)and internal staircases (D-IS) are expressed on a scale from 1 (no damage) to 5 (complete destruction). The damage indicators for external staircases (D-ES) and retaining walls (D-RW) are expressed on a binary scale (0: no damage; 1: damage).

Table 3.4 Post-damage survey data

				Attributes			Surveyed damage levels						
building ID	ID in damage survey	existing	use	structural typology	foundation type	age of building	main structures	floors	perimetral walls	internal walls	external stairs	internal stairs	retaining structures
001	11	1	3	4	1	4	1	1	1	1	1	1	1
002	10	1	3	4	2	4	1	2	1	1	0	1	0
003	9	1	1	3	2	4	1	1	3	1	0	1	0
004	8	1	1	4	2	5	1	1	1	1	0	1	0
005	7	1	3	4	2	5	1	1	1	1	0	1	0
006	4	1	3	4	1	5	1	1	1	1	1	1	0
007	3	1	3	4	1	4	1	1	2	2	1	1	0
008	5	1	3	4	1	4	2	1	2	2	0	1	0
011	82	1	2	2	2	1	5	5	5	5	0	5	0
018	53	0	3	5	2	5	5	4	5	5	0	1	0
019	52	0	1	4	4	6	5	3	4	4	0	4	0
027	44	0	7	4	2	4	4	4	4	4	1	4	1
028	45	0	7	4	2	4	3	3	3	4	0	2	0
029	46	1	1	5	2	3	3	3	3	3	0	3	0
030	47	1	1	3	3	4	1	1	1	1	0	1	0
031	48	1	1	4	4	4	4	4	3	3	0	3	0

032	49	0	1	4	4	5	4	4	4	4	0	4	1
033	50	0	1	4	4	6	5	3	4	4	0	4	0
034	51	0	1	4	4	6	5	3	4	4	0	4	0
055	38	1	3	4	4	4	3	3	3	3	1	2	1
056	39	1	3	4	4	4	5	5	5	5	1	5	1
057	40	1	3	4	2	4	3	1	3	1	1	1	1
058	41	1	2	2	2	1	5	5	5	5	1	5	0
059	42	1	3	6	2	1	1	1	1	1	0	1	0
060	27	1	3	4	2	5	1	1	3	3	0	1	1
061	28	1	3	4	2	5	1	1	1	1	0	1	1
062	261	1	3	4	2	5	3	1	3	1	1	1	1
063	25	1	3	4	2	5	3	1	1	3	1	1	1
064	24	1	3	4	1	4	2	1	2	1	0	1	1
065	32	1	1	6	3	5	2	2	4	2	0	2	0
067	34	1	3	4	1	4	3	4	3	3	1	3	1
068	35	1	3	4	4	4	4	4	4	4	1	5	1
069	36	1	3	4	4	4	2	2	3	2	1	2	1
071	33	0	3	4	4	4	4	4	4	4	1	4	1
073	22	0	2	3	2	3	4	4	4	4	0	3	0
077	20	1	2	4	4	5	1	1	1	1	0	1	1
078	105	1	3	4	1	4	1	1	1	2	0	1	1
079	104	1	3	4	1	4	1	1	2	1	0	1	0
081	106	1	3	4	1	4	1	2	1	1	0	1	1
082	88	1	2	1	2	1	1	1	1	1	0	1	0
083	92	0	2	3	2	6	5	5	5	5	0	5	0
084	102	1	1	3	2	4	1	2	1	1	0	1	1
085	98	1	1	4	1	4	2	3	2	3	0	2	0
086	89	1	2	3	2	4	1	1	2	1	0	1	1
087	83	1	2	3	2	3	3	1	3	2	0	1	0
089	87	1	2	5	2	3	3	3	3	3	1	3	1
090	116	1	3	4	1	4	5	4	3	3	1	3	1
091	262	1	3	4	3	4	1	3	3	3	0	1	1
092	108	1	3	4	1	5	1	1	1	2	0	1	1
093	114	1	1	4	1	4	3	2	3	2	0	1	1
094	112	1	1	4	1	4	1	1	1	1	0	1	1
095	118	1	3	4	4	4	1	1	1	1	1	1	1
096	107	1	3	2	2	1	3	3	3	1	0	3	0
097	119	1	3	4	2	4	3	1	1	1	0	1	1
098	95	1	2	3	2	2	5	5	5	5	1	5	0
099	109	1	3	4	1	4	5	5	5	3	0	1	1
100	90	1	2	2	2	1	5	5	5	5	0	5	0
101	91	1	2	2	2	1	1	3	3	1	0	1	1
103	93	1	2	2	2	1	1	1	1	1	0	1	0
105	84	1	2	2	2	6	5	5	5	5	1	3	0
106	85	1	2	4	1	5	4	4	4	4	0	4	0
108	94	1	2	4	2	5	1	1	1	1	0	1	0
109	96	1	2	3	2	1	1	1	1	2	0	1	0
110	97	1	3	4	1	5	5	3	4	2	1	3	1
111	99	1	1	4	1	4	1	1	2	1	0	1	0
112	101	1		3	2	3	2	2	2	2	1	3	0
113	113	1	3	4	2	5	1	1	2	2	1	1	1
114	1	1	3	4	1	4	1	1	1	1	0	1	1
115	2	1	3	4	1	4	1	2	1	1	0	1	1
117	43	1	3	4	3	5	1	1	1	1	0	1	1

Figure 3.7 illustrates the building use. Figures 3.8, 3.9 and 3.10 plot the typological attributes by building, as given in the post-landslide survey. Figures 3.11, 3.12, 3.13, 3.14, 3.15, 3.16 and 3.17 plot the observed damage assessed in the survey.

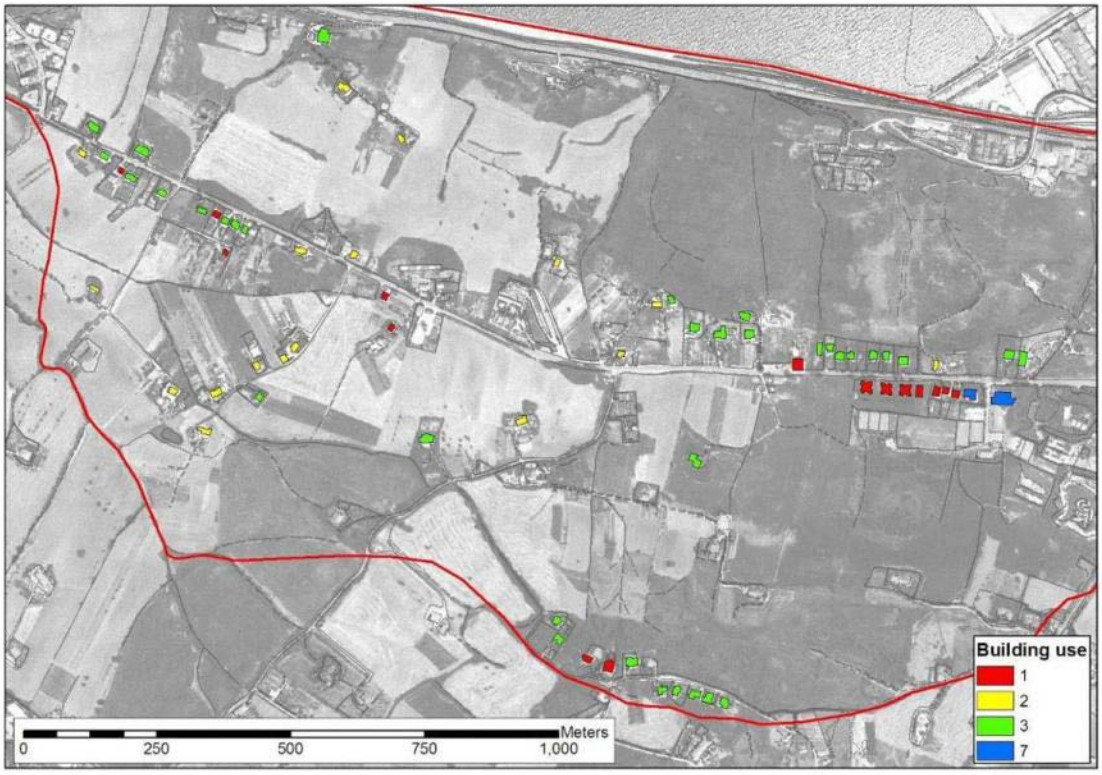

Figure 3.6. Building use

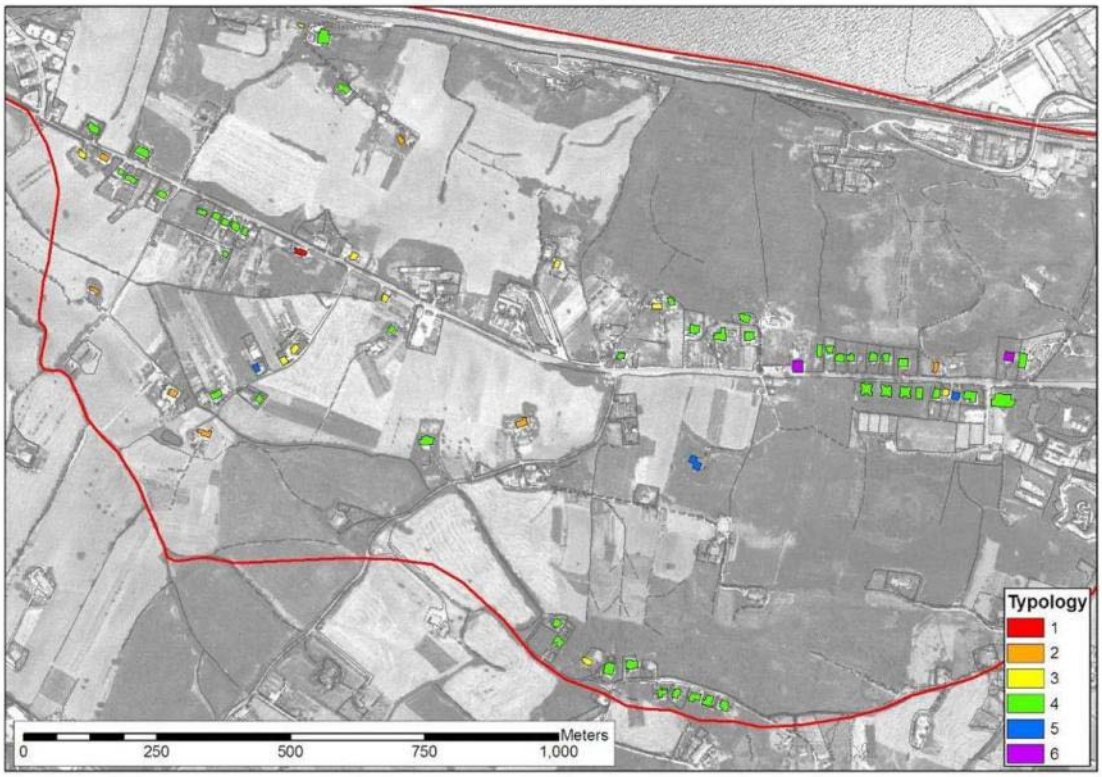

Figure 3.7. Structural typology

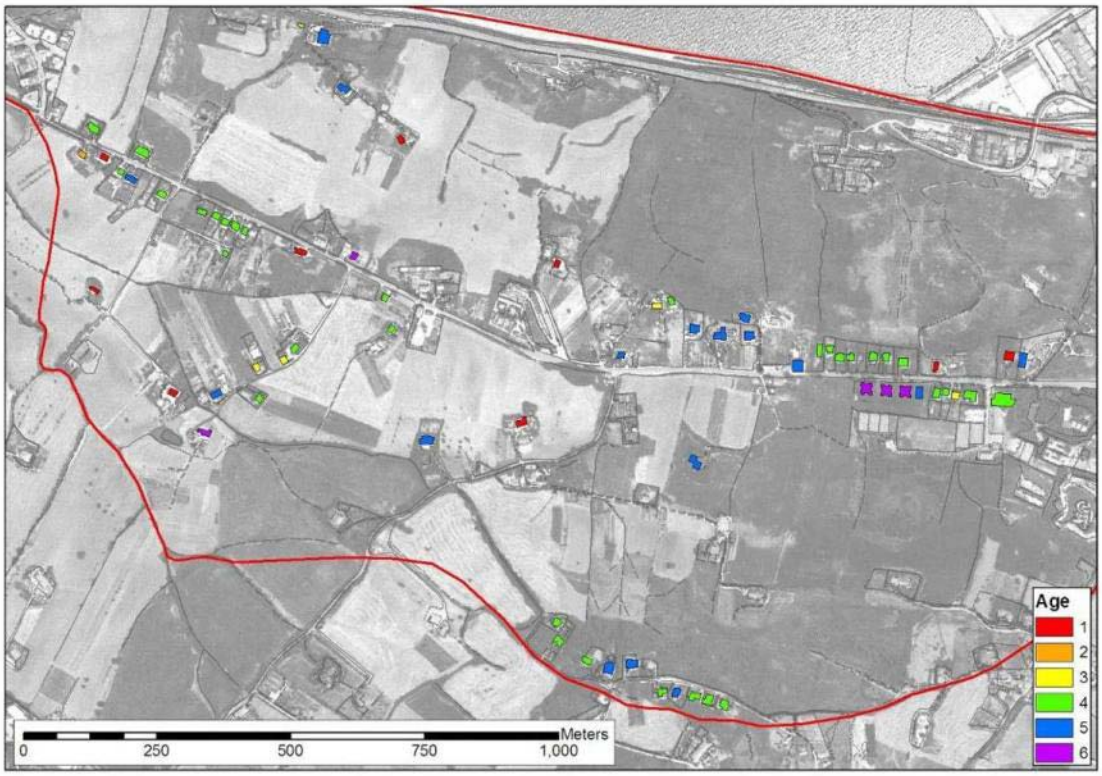

Figure 3.8. Age of building

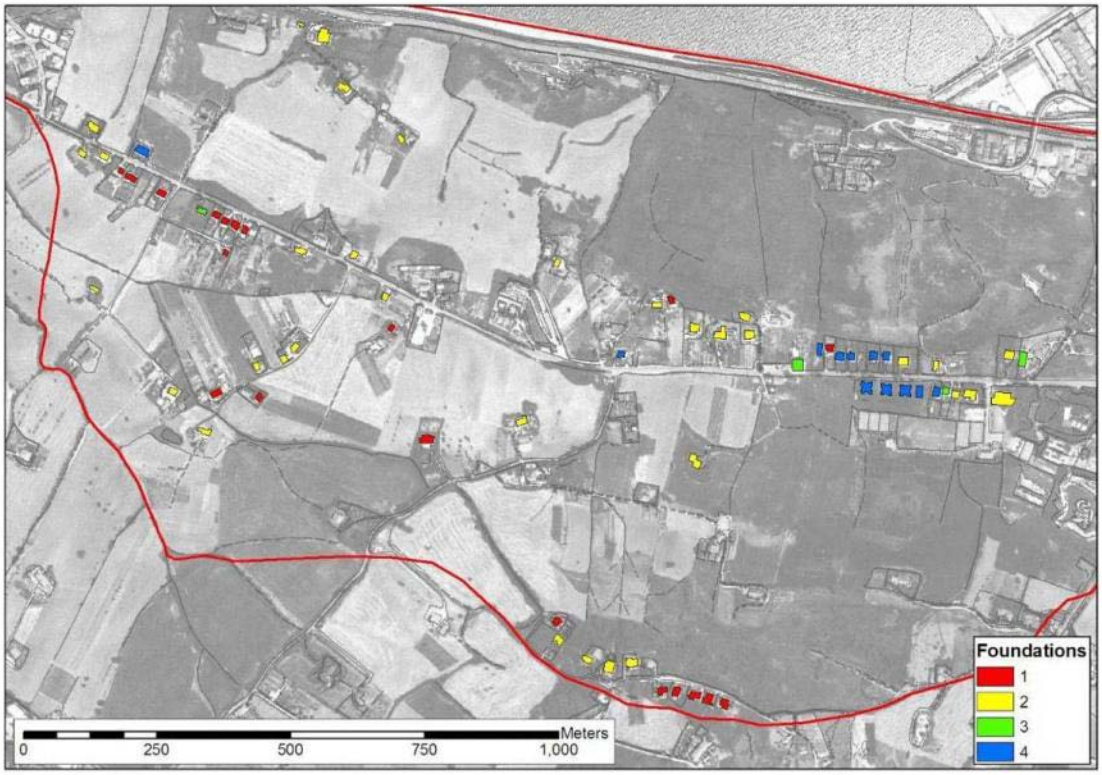

Figure 3.9. Foundation type

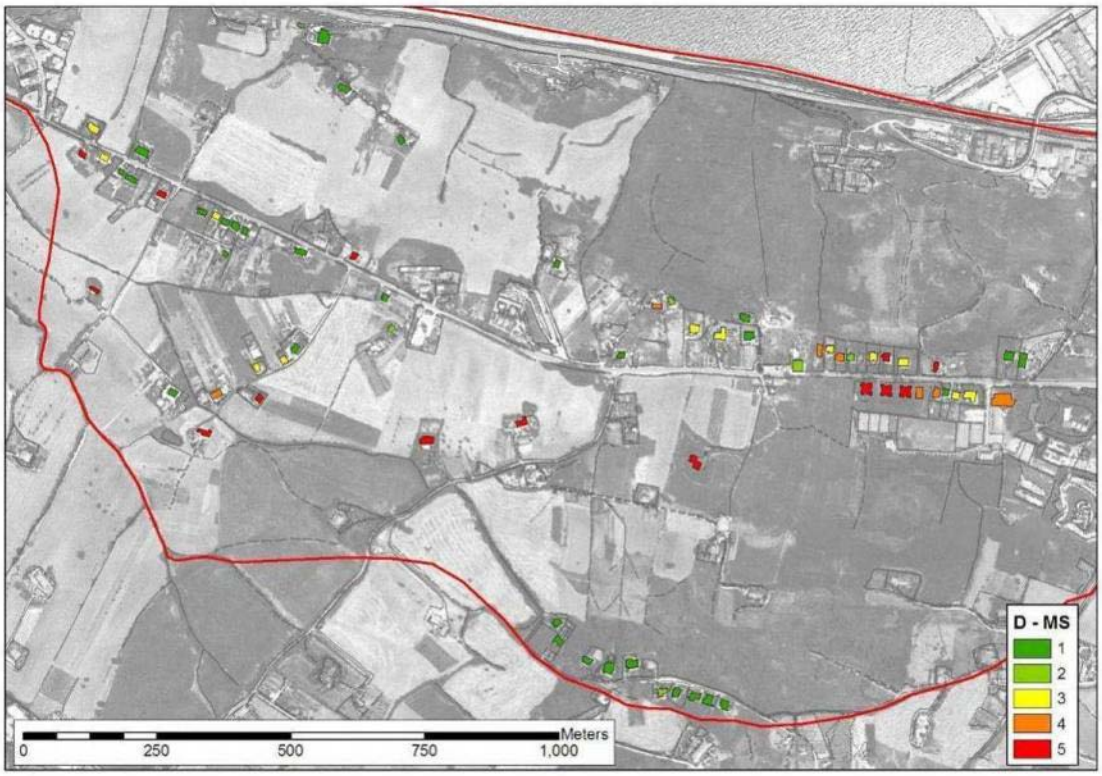

Figure 3.10. Observed damage to main structures

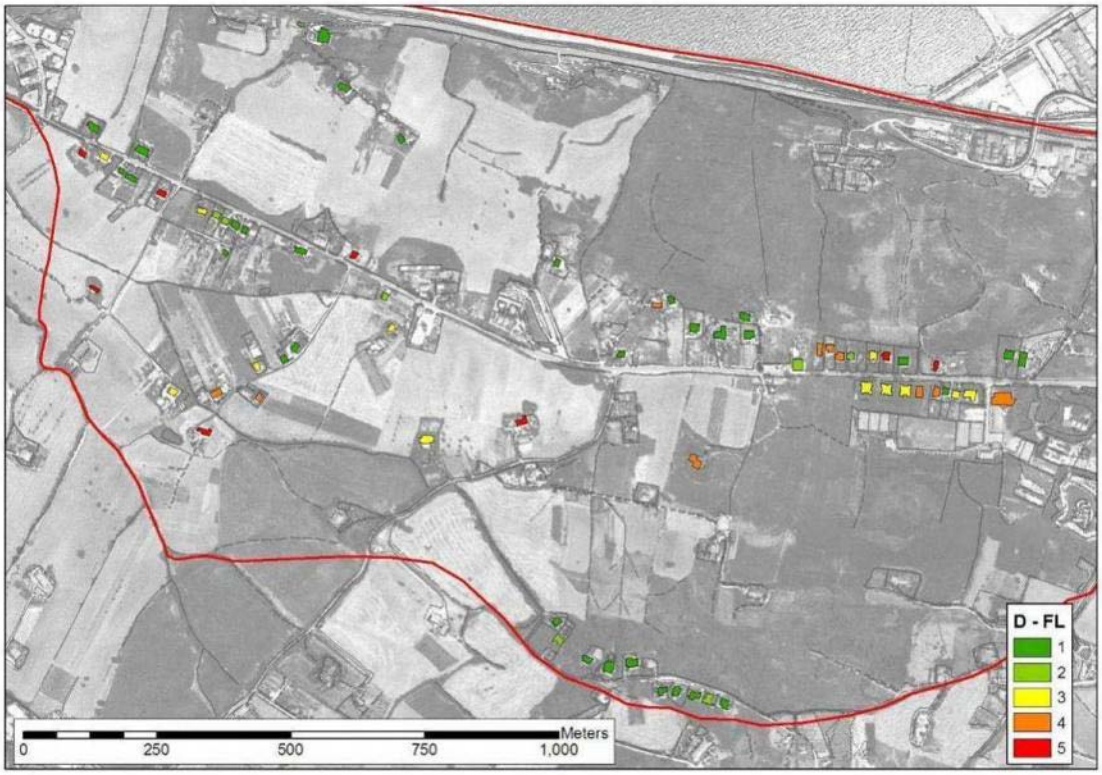

Figure 3.11. Observed damage to floors

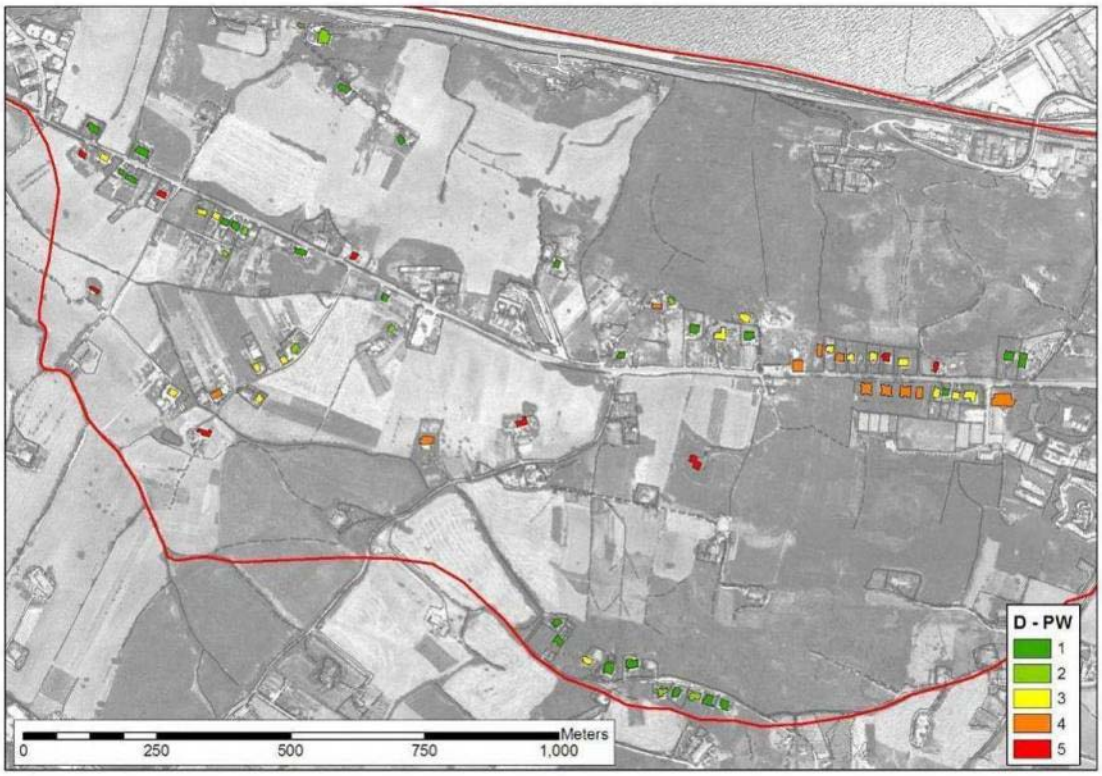

Figure 3.12. Observed damage to perimetral walls

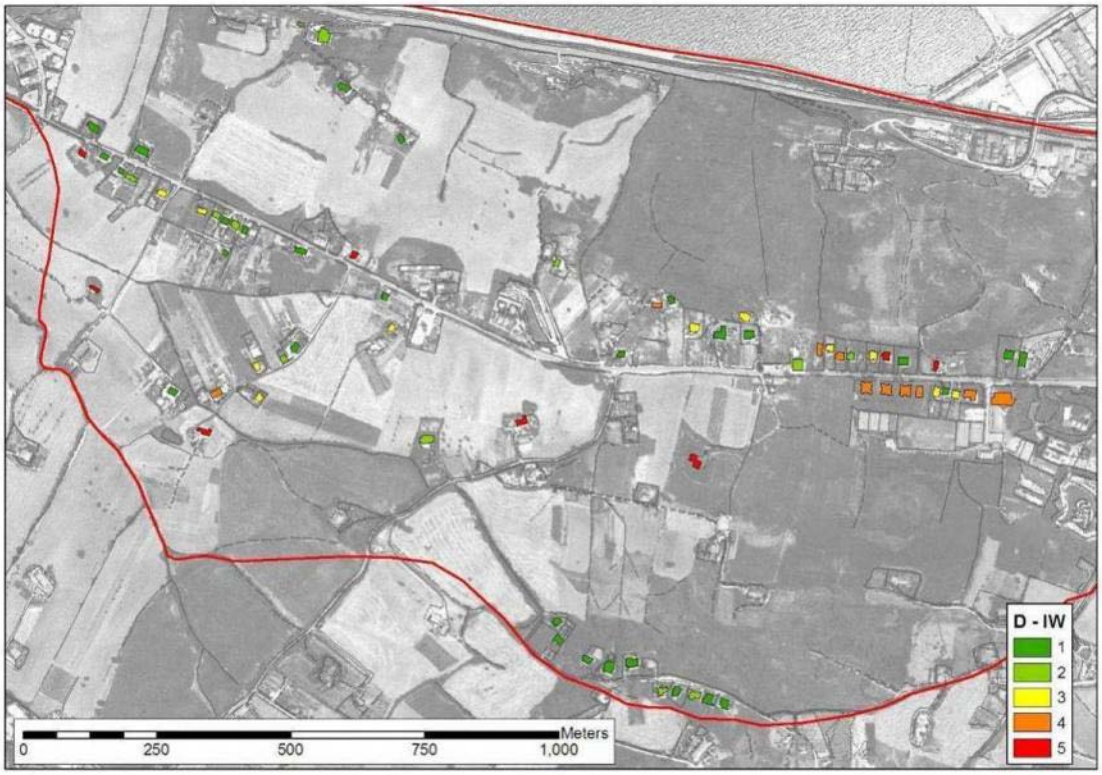

Figure 3.13. Observed damage to internal walls

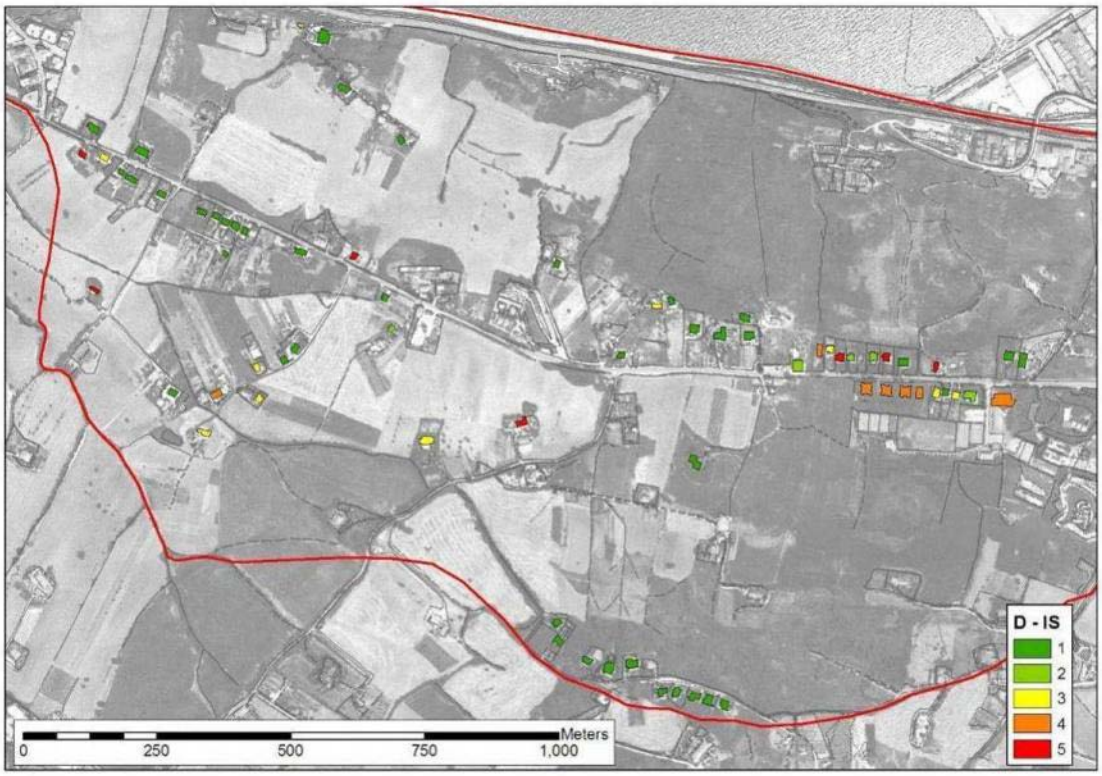

Figure 3.14. Observed damage to internal staircases

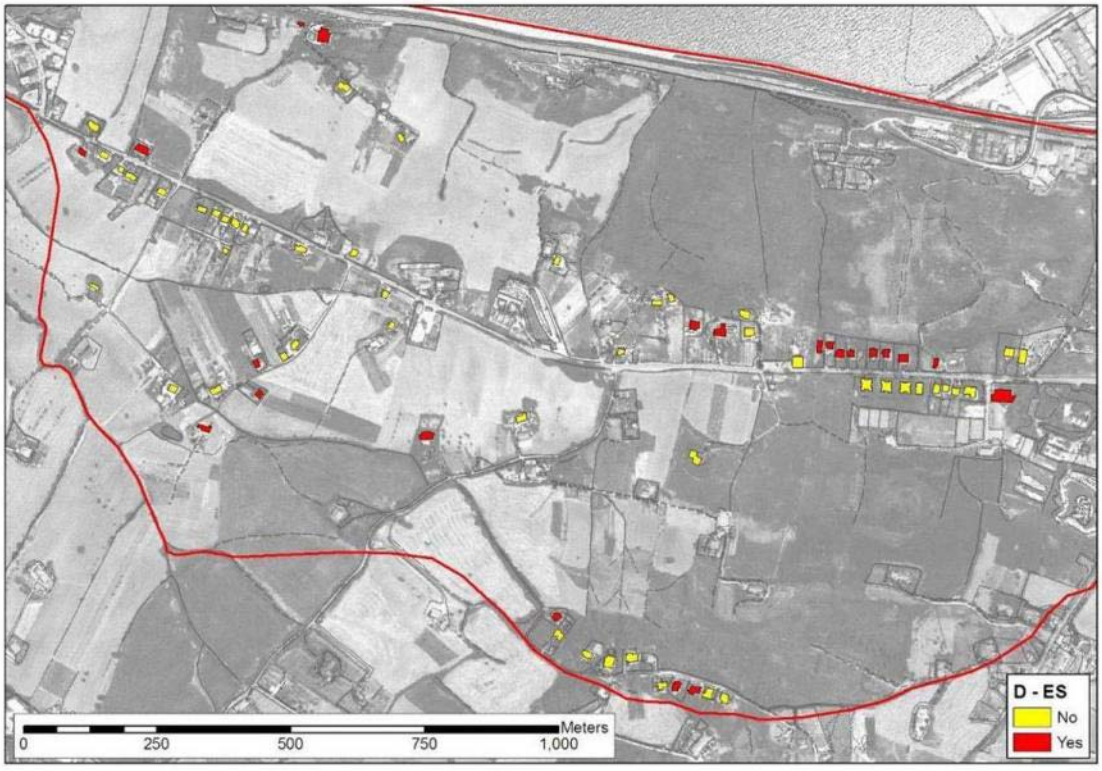

Figure 3.15. Observed damage to external staircases

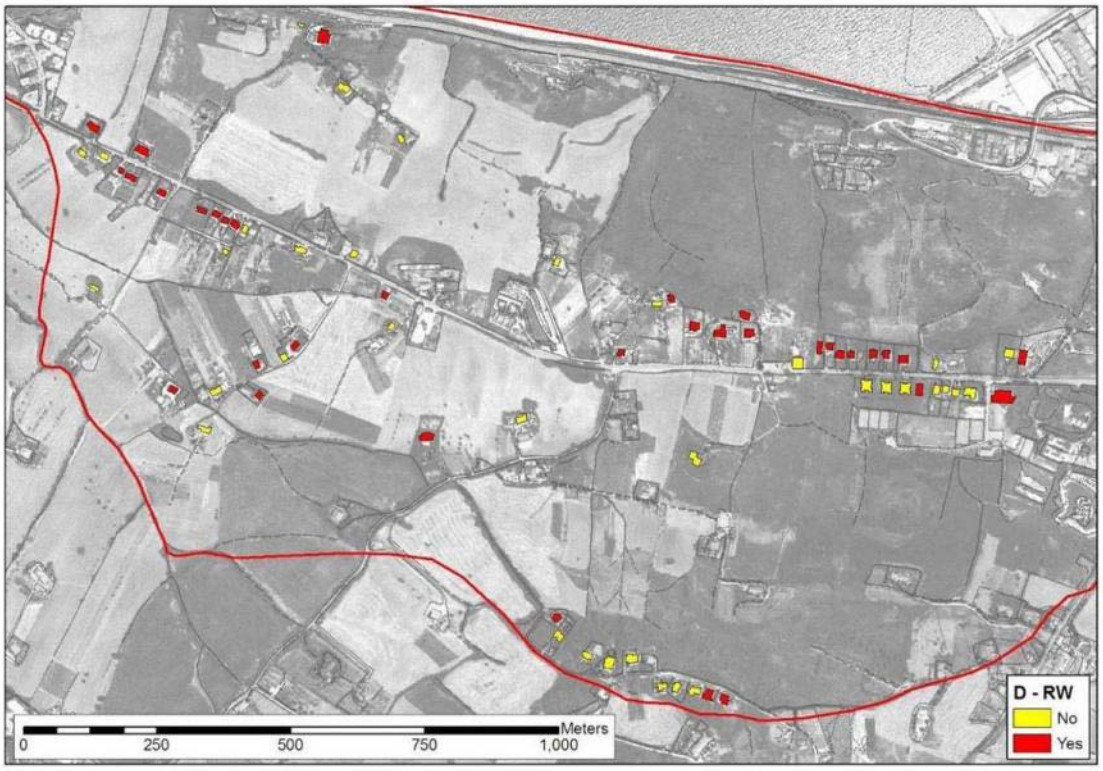

Figure 3.16. Observed damage to retaining walls

The reference model for posterior vulnerability is

$$V_p = \sum_{k=1}^{m} \left(\varepsilon_k \cdot \eta_k \cdot \Gamma_k \right)$$

in which:

m is the number of vulnerability indicators; $\Gamma_k \in [0,1]$ is the *k*-th vulnerability indicator and $\psi_k \in [0,1]$ representes the relevance coefficient for the *k*-th vulnerability indicator

$$\eta_k = \frac{\psi_k}{\sum_{k=1}^{m} \psi_k}$$

$$\varepsilon_k = \text{sign}\left(\psi_k \cdot \Gamma_k \right)$$

To obtain vulnerability factors Γ_k, ratings G_k from the damage survey [expressed on a 1-5 scale] were converted to the [0,1] scale by $\Gamma_k = 0.25(G_k - 1)$ as formulated in Table 3.5. Relevance factors were assigned subjectively.

Table 3.5 Structural damage to Ancona buildings (categories from survey)

	Structural component	Γ_k	ψ_k
MS	main structure		1.00
FL	floors		0.90
PW	perimetral walls		0.80
IW	internal walls	$\Gamma_k = 0.25(G_k - 1)$	0.70
IS	internal stairs		0.60
ES	external stairs		0.30
RW	retaining walls		0.40

Figure 3.18 plots the posterior vulnerability for the buildings under investigation.

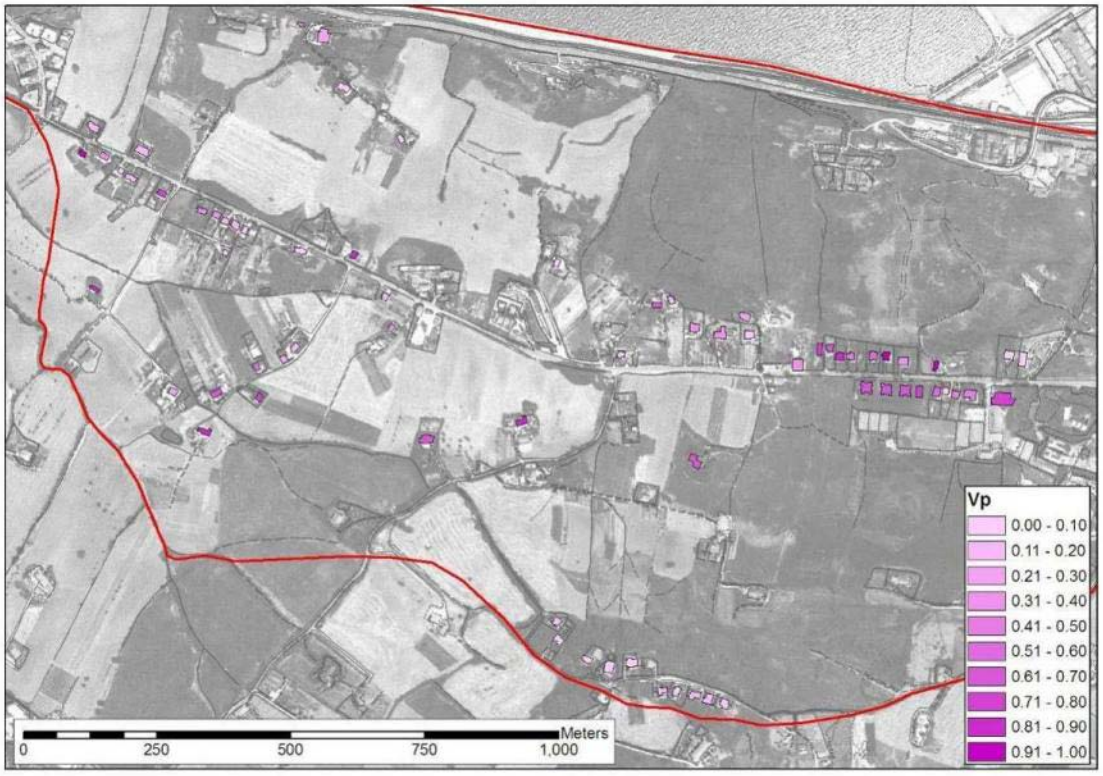

Figure 3.17. Posterior vulnerability

3.2.2 Quantitative estimation of building resilience

The resilience index proposed by Uzielli (2012) is:

$$\Omega = \sum_{j=1}^{n} \left(\delta_j \cdot \rho_j \cdot \Theta_j \right)$$

in which:

n is the number of resilience indicators; $\Theta_j \in [0,1]$ is the j-th resilience indicator and $\varphi_j \in [0,1]$ represents the relevance coefficient for the j-th resilience indicator

$$\rho_j = \frac{\varphi_j}{\sum_{j=1}^{n} \varphi_j}$$

$$\delta_j = \text{sign}\left(\varphi_j \cdot \Theta_j\right)$$

Relevance coefficients are user-defined in the range [0,1], and reflect available knowledge or belief regarding the relevance of each indicator in concurring to damage. As the total resilience must be defined in the range [0,1], at least one of the resilience coefficients must be greater than zero. Detailed specification of relevance coefficients for intensity and resilience is optional. If, due to insufficient information, it is not possible to define a hierarchy in intensity and resilience indicators, relevance coefficients can be set uniformly equal to unity. Relevance coefficients are event-specific and category-specific. For instance, it could be known (or assumed) that the damage caused by a slow-moving landslide on a building is mainly due to the displacement (i.e. kinematic parameter), while kinetic characteristics could be predominant in case of a rapid movement. A set of three resilience indicators (for the relevant attributes available in the damage survey) for landslide risk to structures is proposed, namely:

- structural typology indicator Θ_{STY};
- building age indicator Θ_{AGE};
- foundation type Θ_{FNT}.

The depth of sliding surfaces cannot be estimated confidently due to the fact that inclinometers are not located in the proximity of buildings. Hence, the resilience indicator for foundation type does not refer conceptually to the ability of the foundation system to resist displacement; rather, its capability of preserving a rigid-body behavior of the superstructure. Resilience indicators and relevance factors were assigned subjectively as detailed in Tables 3.6, 3.7 and 3.8.

Table 3.6 Structural types for the Ancona buildings as categorized in the damage survey (1985-1986)

	Structural typology	Θ_{STY}	φ_{STY}
1	stone masonry	0.30	1.00
2	tuff masonry	0.40	1.00
3	brick masonry	0.50	1.00
4	reinforced concrete	0.70	1.00
5	mixed structure	0.30	1.00
6	retrofitted building	0.80	1.00

Table 3.7 Age of the Ancona buildings as categorized in the damage survey (1985-1986)

	construction year	age at survey	Θ_{AGE}	φ_{AGE}
1	< 1900	>80	0.20	0.80
2	1901-1943	40-80	0.40	0.80
3	1944-1962	25-40	0.70	0.80
4	1963-1971	15-25	0.80	0.80
5	1972-survey	<15	0.90	0.80
6	unknown	unknown	0.20	0.80

Table 3.8 Foundation type as categorized in the damage survey (1985-1986)

	Foundation type	Θ_{FNT}	φ_{FNT}
1	plinths	0.10	0.90
2	strip footing	0.30	0.90
3	mat footing	0.50	0.90
4	piles	0.70	0.90

Figure 3.19 plots the resilience for the buildings under investigation (at the time of the survey).

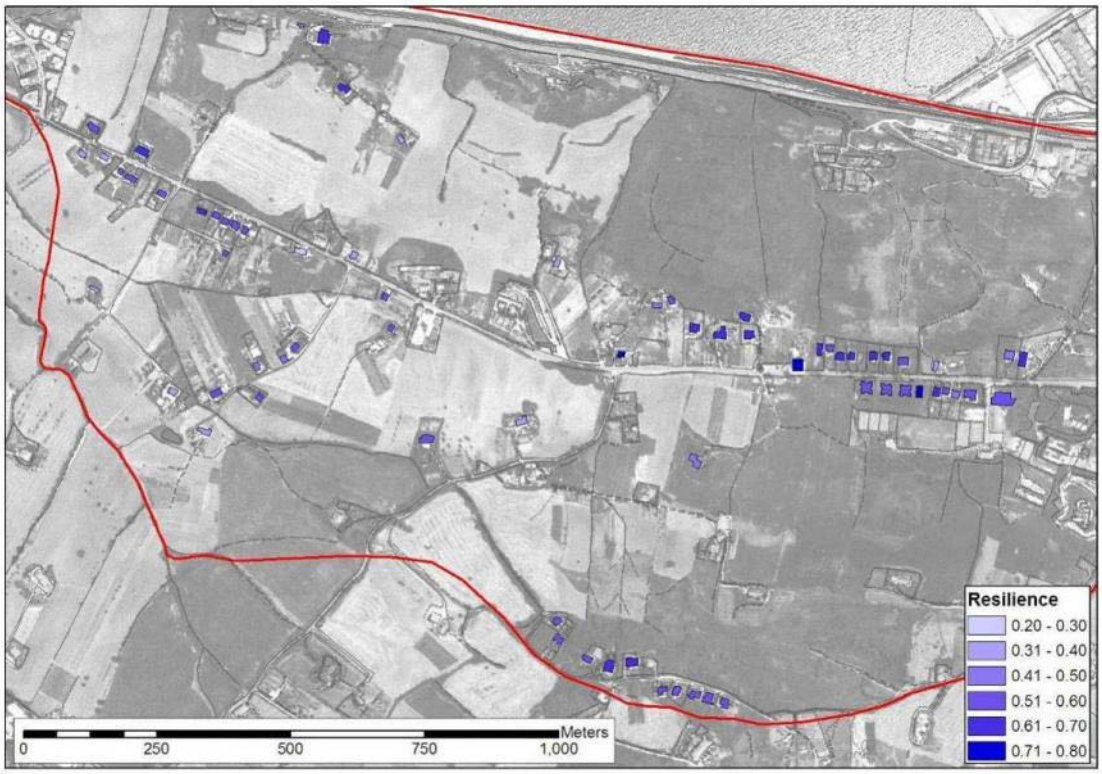

Figure 3.18. Resilience of buildings at time of survey

3.2.3 Back-calculation of landslide intensity

The intensity model implemented for the set of 70 buildings. Table 3.9 reports the inputs and output values.

Table 3.9 Posterior vulnerability indicators and index, resilience factors, resilience index and posterior intensity for the set of 70 buildings.

building ID	Vulnerability indicators							V_p	Resil. indicat.			Ω	I_p
	main structures	floors	perimetral walls	internal walls	external stairs	internal stairs	retaining structures		structural type	age	foundation type		
001	0.00	0.00	0.00	0.00	1.00	0.00	1.00	0.15	0.70	0.80	0.10	0.53	0.14
002	0.00	0.25	0.00	0.00	0.00	0.00	0.00	0.05	0.70	0.80	0.30	0.59	0.09
003	0.00	0.00	0.50	0.00	0.00	0.00	0.00	0.09	0.50	0.80	0.30	0.51	0.11
004	0.00	0.00	0.00	0.00	0.00	0.00	0.00	0.00	0.70	0.90	0.30	0.61	0.00
005	0.00	0.00	0.00	0.00	0.00	0.00	0.00	0.00	0.70	0.90	0.30	0.61	0.00
006	0.00	0.00	0.00	0.00	1.00	0.00	0.00	0.06	0.70	0.90	0.10	0.56	0.10
007	0.00	0.00	0.25	0.25	1.00	0.00	0.00	0.14	0.70	0.80	0.10	0.53	0.14
008	0.25	0.00	0.25	0.25	0.00	0.00	0.00	0.13	0.70	0.80	0.10	0.53	0.14
011	1.00	1.00	1.00	1.00	0.00	1.00	0.00	0.85	0.40	0.20	0.30	0.30	0.22
018	1.00	0.75	1.00	1.00	0.00	0.00	0.00	0.68	0.30	0.90	0.30	0.47	0.28
019	1.00	0.50	0.75	0.75	0.00	0.75	0.00	0.64	0.70	0.20	0.70	0.53	0.30
027	0.75	0.75	0.75	0.75	1.00	0.75	1.00	0.79	0.70	0.80	0.30	0.59	0.39
028	0.50	0.50	0.50	0.75	0.00	0.25	0.00	0.43	0.70	0.80	0.30	0.59	0.27
029	0.50	0.50	0.50	0.50	0.00	0.50	0.00	0.43	0.30	0.70	0.30	0.41	0.19
030	0.00	0.00	0.00	0.00	0.00	0.00	0.00	0.00	0.50	0.80	0.50	0.57	0.00
031	0.75	0.75	0.50	0.50	0.00	0.50	0.00	0.53	0.70	0.80	0.70	0.70	0.36
032	0.75	0.75	0.75	0.75	0.00	0.75	1.00	0.72	0.70	0.90	0.70	0.73	0.46
033	1.00	0.50	0.75	0.75	0.00	0.75	0.00	0.64	0.70	0.20	0.70	0.53	0.30
034	1.00	0.50	0.75	0.75	0.00	0.75	0.00	0.64	0.70	0.20	0.70	0.53	0.30
055	0.50	0.50	0.50	0.50	1.00	0.25	1.00	0.54	0.70	0.80	0.70	0.70	0.37
056	1.00	1.00	1.00	1.00	1.00	1.00	1.00	1.00	0.70	0.80	0.70	0.70	0.70
057	0.50	0.00	0.50	0.00	1.00	0.00	1.00	0.34	0.70	0.80	0.30	0.59	0.24
058	1.00	1.00	1.00	1.00	1.00	1.00	0.00	0.91	0.40	0.20	0.30	0.30	0.24
059	0.00	0.00	0.00	0.00	0.00	0.00	0.00	0.00	0.80	0.20	0.30	0.44	0.00
060	0.00	0.00	0.50	0.50	0.00	0.00	1.00	0.24	0.70	0.90	0.30	0.61	0.22
060	0.00	0.00	0.00	0.00	0.00	0.00	1.00	0.09	0.70	0.90	0.50	0.67	0.14
061	0.00	0.00	0.00	0.00	0.00	0.00	1.00	0.09	0.70	0.90	0.30	0.61	0.13
062	0.50	0.00	0.50	0.00	1.00	0.00	1.00	0.34	0.70	0.90	0.30	0.61	0.25
063	0.50	0.00	0.00	0.50	1.00	0.00	1.00	0.33	0.70	0.90	0.30	0.61	0.25
064	0.25	0.00	0.25	0.00	0.00	0.00	1.00	0.18	0.70	0.80	0.10	0.53	0.16
065	0.25	0.25	0.75	0.25	0.00	0.25	0.00	0.30	0.80	0.90	0.50	0.71	0.27
067	0.50	0.75	0.50	0.50	1.00	0.50	1.00	0.62	0.70	0.80	0.10	0.53	0.30
068	0.75	0.75	0.75	0.75	1.00	1.00	1.00	0.82	0.70	0.80	0.70	0.70	0.49
069	0.25	0.25	0.50	0.25	1.00	0.25	1.00	0.40	0.70	0.80	0.70	0.70	0.32
071	0.75	0.75	0.75	0.75	1.00	0.75	1.00	0.79	0.70	0.80	0.70	0.70	0.47
073	0.75	0.75	0.75	0.75	0.00	0.50	0.00	0.61	0.50	0.70	0.30	0.48	0.27
077	0.00	0.00	0.00	0.00	0.00	0.00	1.00	0.09	0.70	0.90	0.70	0.73	0.15
078	0.00	0.00	0.00	0.25	0.00	0.00	1.00	0.12	0.70	0.80	0.10	0.53	0.13
079	0.00	0.00	0.25	0.00	0.00	0.00	0.00	0.04	0.70	0.80	0.10	0.53	0.08
081	0.00	0.25	0.00	0.00	0.00	0.00	1.00	0.13	0.70	0.80	0.10	0.53	0.14
082	0.00	0.00	0.00	0.00	0.00	0.00	0.00	0.00	0.30	0.20	0.30	0.26	0.00
083	1.00	1.00	1.00	1.00	0.00	1.00	0.00	0.85	0.50	0.20	0.30	0.33	0.24
084	0.00	0.25	0.00	0.00	0.00	0.00	1.00	0.13	0.50	0.80	0.30	0.51	0.13

085	0.25	0.50	0.25	0.50	0.00	0.25	0.00	0.30	0.70	0.80	0.10	0.53	0.20
086	0.00	0.00	0.25	0.00	0.00	0.00	1.00	0.13	0.50	0.80	0.30	0.51	0.13
087	0.50	0.00	0.50	0.25	0.00	0.00	0.00	0.23	0.50	0.70	0.30	0.48	0.16
089	0.50	0.50	0.50	0.50	1.00	0.50	1.00	0.57	0.30	0.70	0.30	0.41	0.22
090	1.00	0.75	0.50	0.50	1.00	0.50	1.00	0.73	0.70	0.80	0.10	0.53	0.33
091	0.00	0.50	0.50	0.50	0.00	0.00	1.00	0.34	0.70	0.80	0.50	0.64	0.27
092	0.00	0.00	0.00	0.25	0.00	0.00	1.00	0.12	0.70	0.90	0.10	0.56	0.14
093	0.50	0.25	0.50	0.25	0.00	0.00	1.00	0.36	0.70	0.80	0.10	0.53	0.22
094	0.00	0.00	0.00	0.00	0.00	0.00	1.00	0.09	0.70	0.80	0.10	0.53	0.11
095	0.00	0.00	0.00	0.00	1.00	0.00	1.00	0.15	0.70	0.80	0.70	0.70	0.19
096	0.50	0.50	0.50	0.00	0.00	0.50	0.00	0.35	0.40	0.20	0.30	0.30	0.12
097	0.50	0.00	0.00	0.00	0.00	0.00	1.00	0.19	0.70	0.80	0.30	0.59	0.18
098	1.00	1.00	1.00	1.00	1.00	1.00	0.00	0.91	0.50	0.40	0.30	0.39	0.31
099	1.00	1.00	1.00	0.50	0.00	0.00	1.00	0.73	0.70	0.80	0.10	0.53	0.33
100	1.00	1.00	1.00	1.00	0.00	1.00	0.00	0.85	0.40	0.20	0.30	0.30	0.22
101	0.00	0.50	0.50	0.00	0.00	0.00	1.00	0.27	0.40	0.20	0.30	0.30	0.11
103	0.00	0.00	0.00	0.00	0.00	0.00	0.00	0.00	0.40	0.20	0.30	0.30	0.00
105	1.00	1.00	1.00	1.00	1.00	0.50	0.00	0.85	0.40	0.20	0.30	0.30	0.22
106	0.75	0.75	0.75	0.75	0.00	0.75	0.00	0.64	0.70	0.90	0.10	0.56	0.32
108	0.00	0.00	0.00	0.00	0.00	0.00	0.00	0.00	0.70	0.90	0.30	0.61	0.00
109	0.00	0.00	0.00	0.25	0.00	0.00	0.00	0.04	0.50	0.20	0.30	0.33	0.05
110	1.00	0.50	0.75	0.25	1.00	0.50	1.00	0.69	0.70	0.90	0.10	0.56	0.34
111	0.00	0.00	0.25	0.00	0.00	0.00	0.00	0.04	0.70	0.80	0.10	0.53	0.08
112	0.25	0.25	0.25	0.25	1.00	0.50	0.00	0.31	0.50	0.70	0.30	0.48	0.19
113	0.00	0.00	0.25	0.25	1.00	0.00	1.00	0.23	0.70	0.90	0.30	0.61	0.21
114	0.00	0.00	0.00	0.00	0.00	0.00	1.00	0.09	0.70	0.80	0.10	0.53	0.11
115	0.00	0.25	0.00	0.00	0.00	0.00	1.00	0.13	0.70	0.80	0.10	0.53	0.14

Figure 3.20 plots the back-calculated intensity for each building. Such parameter was compared with the displacements induced by the main 1982 landsliding event to attempt the formulation of an analytical intensity model as detailed in Section 3.2.4.

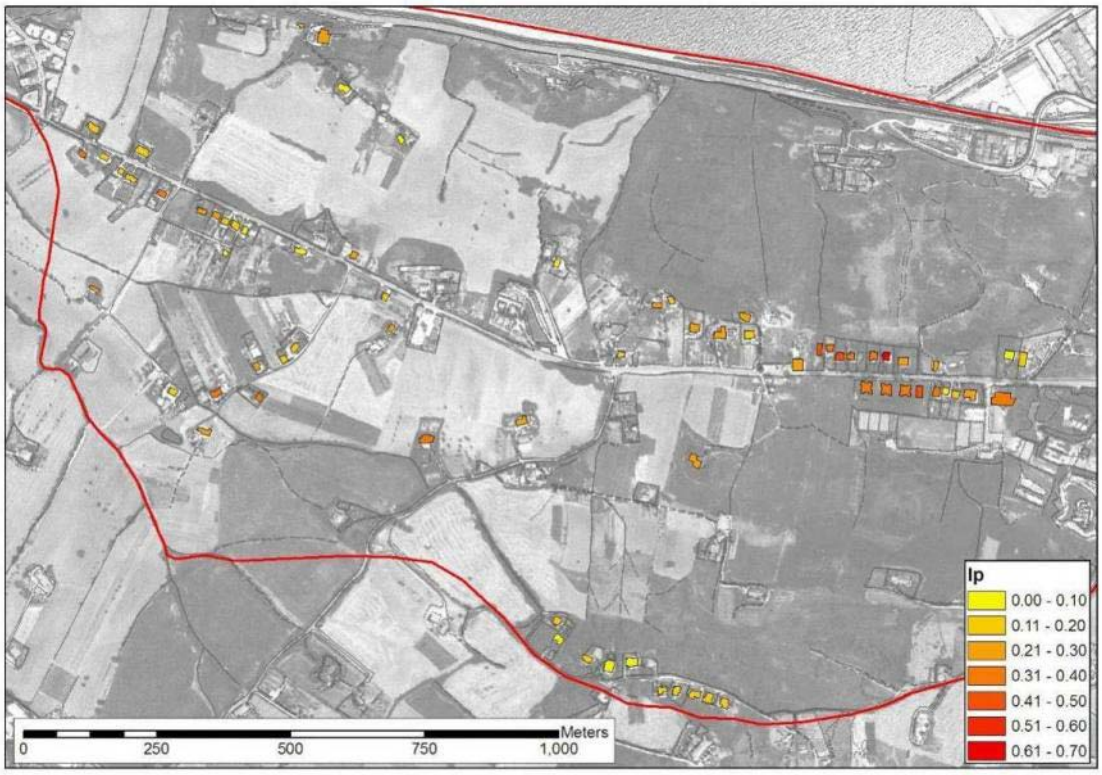

Figure 3.19. Back-calculated intensity

3.2.4 Formulation of the intensity function

No univocal quantitative model relating the intensity measure (i.e. ground displacement) to building damage is available. The parameterization of the intensity function was then pursued empirically. As described in the following, an analytical intensity model was constructed by comparing landslide-induced ground displacements and the effects on the set of buildings for which post-landslide damage was surveyed.

Figure 3.21 (Anon, 1986) plots the principal horizontal and vertical displacements which occurred in the hours immediately following the reactivation of the slide on December 13th, 1982. The ground displacement estimates were obtained by comparing pre- and post-landslide aerial photographs. The ground displacements illustrated graphically in Figure 3.21 were digitized and processed in a GIS environment to retrieve approximate numerical values, which were subsequently examined jointly with the estimates of posterior intensity obtained in Section 3.2.3.

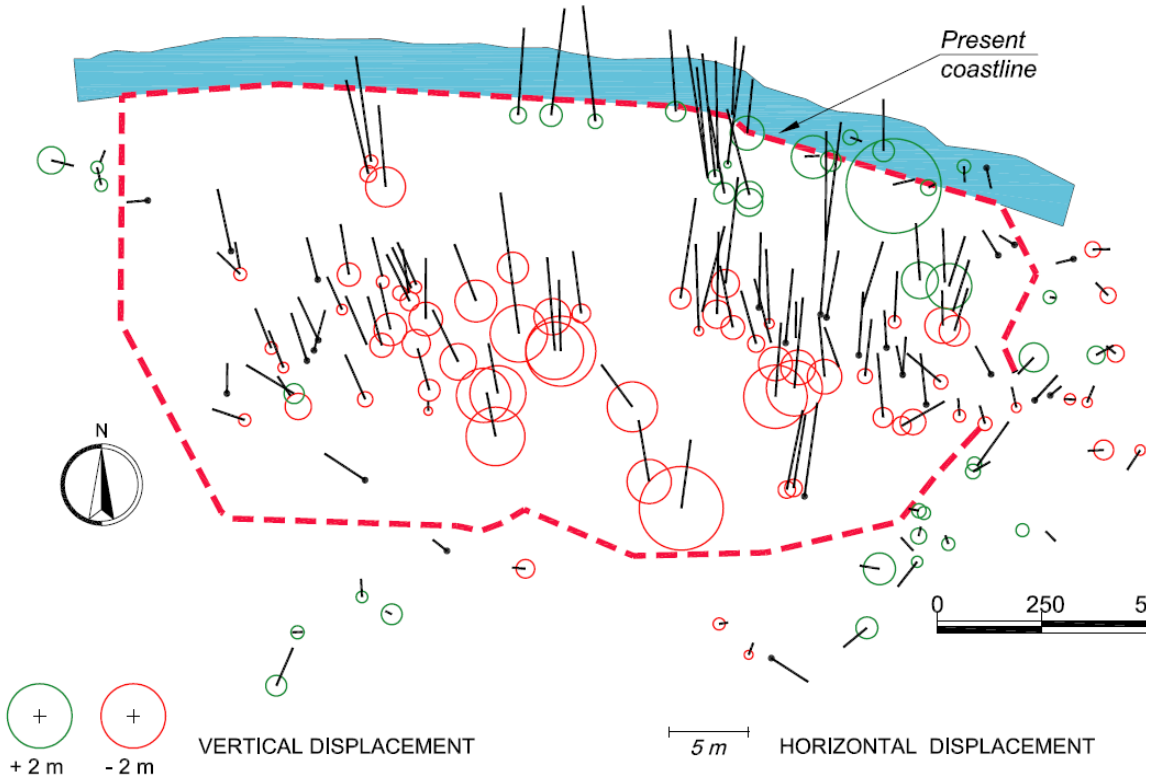

Figure 3.20. Principal horizontal and vertical displacements caused by the December 13th, 1982 landslide (Anon,1986; Cotecchia, 2006)

In order to related ground displacement to building damage, it is necessary to quantify at least approximately the magnitude of vertical and horizontal ground displacements at building locations. As building locations generally do not correspond to displacement measurement locations, it is necessary to spatialize horizontal and vertical measurements through interpolation of measured values. Here, this is achieved by geostatistical interpolation using radial basis functions (RBF) with regularized splines. RBFs are exact deterministic interpolators. They provide prediction surfaces that are comparable to the exact form of geostatistical kriging. However, they do not require investigation of the autocorrelation of the data, nor do they require assumptions about the statistical distribution of the data.

The magnitude of the total ground displacement vector is calculated as:

$$D_{G,tot} = \sqrt{D_{G,ver}^2 + D_{G,hor}^2}$$

in which $D_{G,ver}$ and $D_{G,hor}$ are the vertical and horizontal ground displacement, respectively.

The RBF-interpolated vertical, horizontal and total ground displacements are shown in Figures 3.22, 3.23 and 3.24, respectively. It should be noted that only the magnitude of displacement vectors is of interest, as damaging potential to buildings is assumed to be invariant to the direction of ground displacement.

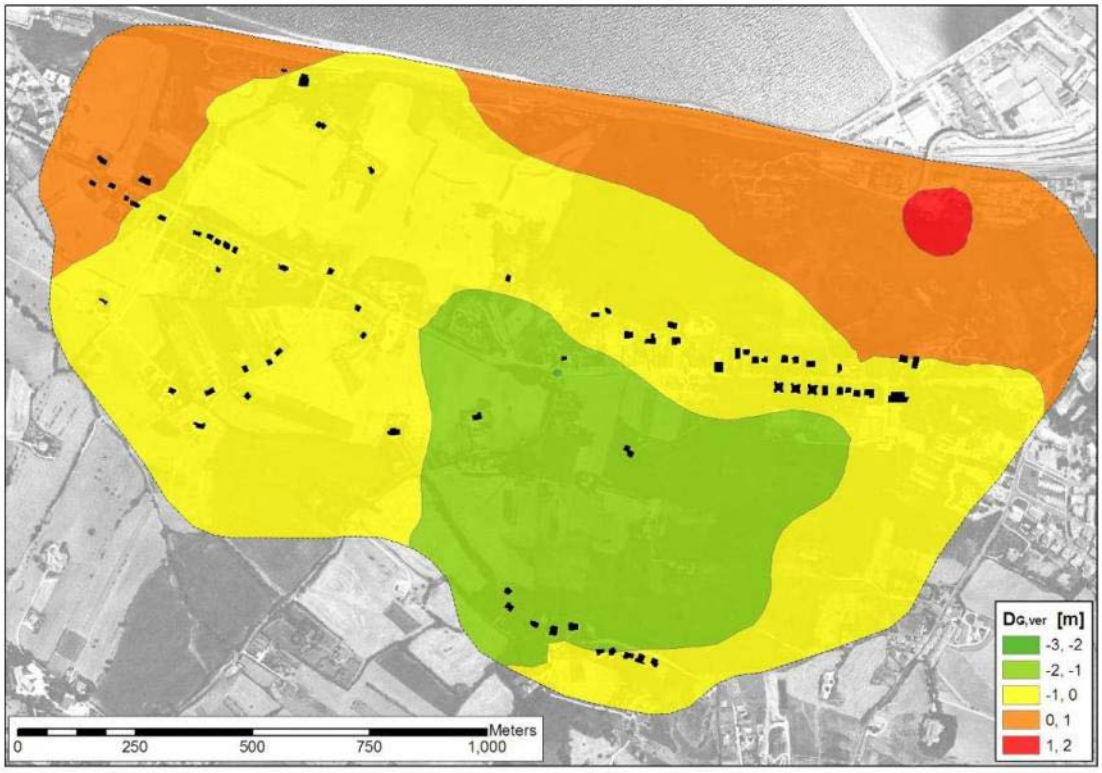

Figure 3.21. RBF interpolations of landslide-induced vertical ground displacements by RBF

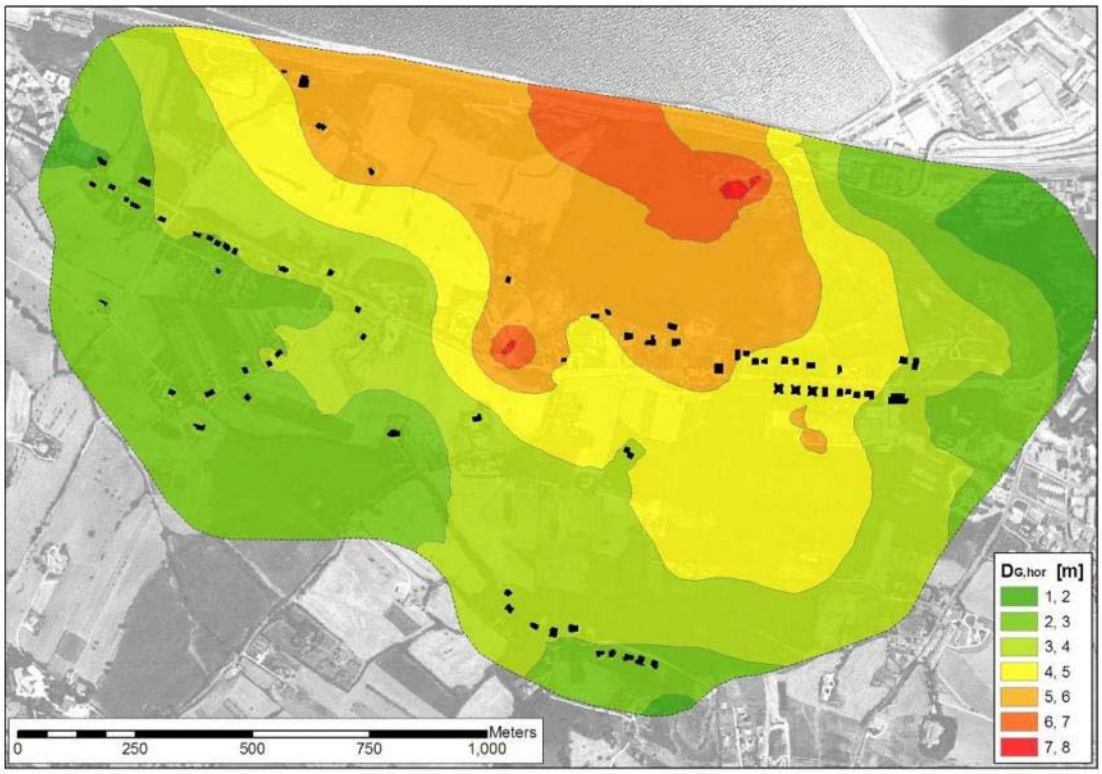

Figure 3.22. RBF interpolations of landslide-induced horizontal ground displacements by RBF

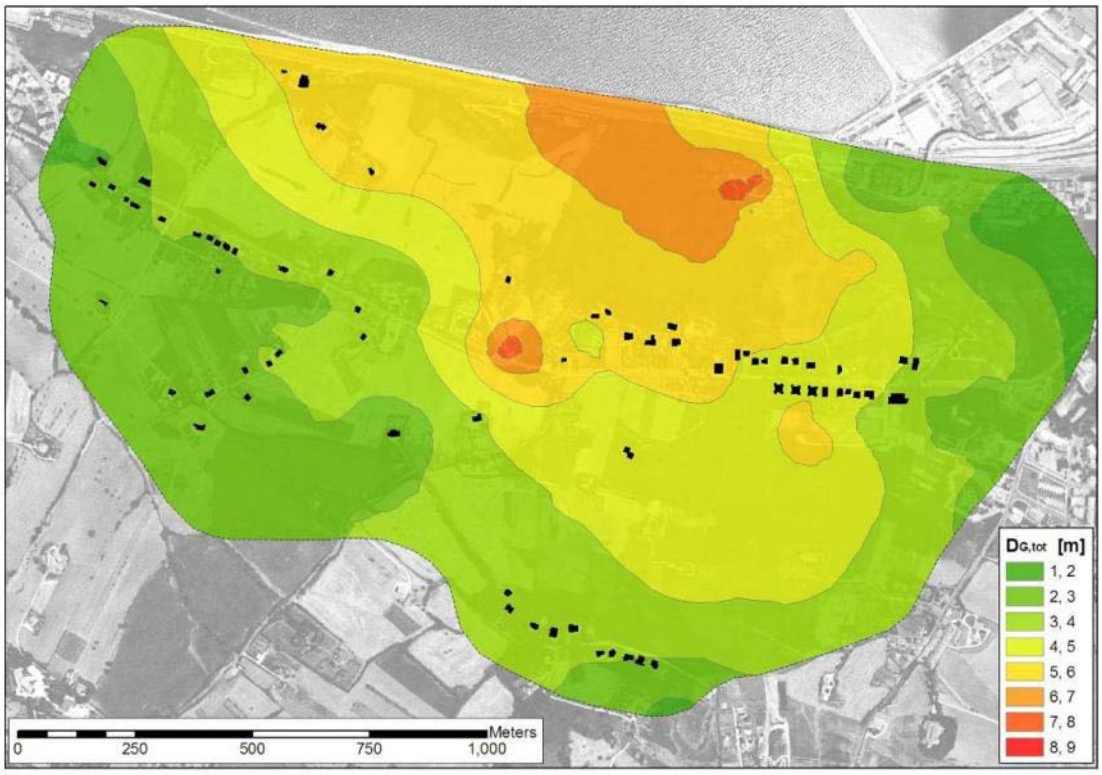

Figure 3.23. RBF interpolations of total landslide-induced ground displacements

Two analytical intensity models were obtained by the maximum likelihood fitting of power law models to total displacement and posterior intensity data for the 70 buildings. The two models are namely:

1) a "best-fit" intensity model I_{bf}, obtained by generalized least-squares regression;
2) an upper-bound "specific" intensity model I_{ub}, which encloses all posterior intensity values, obtained through a constrained optimization procedure.

While the best-fit model parameterizes the presumed central trend of the displacement-intensity relation, the analytical model for specific intensity is conservative with respect to available sample data of back-calculated intensity and interpolated ground displacement. A conservative model is warranted by the presence of uncertainties in at least: (a) the magnitude of ground displacement at building locations; and (b) the kinematic interaction between ground and buildings.

The resulting analytical expressions for I_{bf} and I_{ch} are

$$I_{bf} = 0.11 \cdot D_{G,tot}^{0.45}$$

$$I_{ch} = 0.22 \cdot D_{G,tot}^{0.73}$$

Figure 3.25 plots the posterior intensity I_p obtained in Section 3.2.3 versus interpolated estimates of total ground displacement at the spatial locations of the 70 buildings, as well as the best-fit and sprcific intensity power law models.

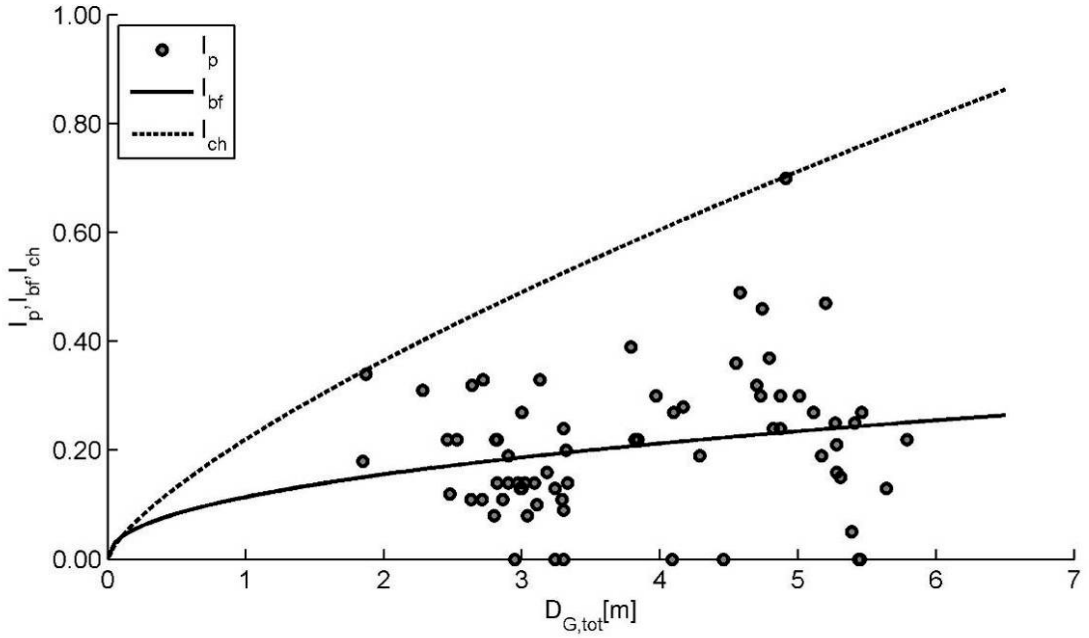

Figure 3.24. Posterior intensity versus total ground displacement at the spatial location of the 70 buildings, best-fit and upper-bound intensity models

Due to the complexity of the physical interaction between sliding masses and vulnerable elements, it is very difficult to assess the relative displacement between ground and buildings. Based on available data, it is not possible to formulate a quantitative model relating total ground displacement $D_{G,tot}$ and the total displacement of a building, D_B, even by assuming a simplified rigid body translational displacement behavior for the latter. In absence of specific information, the proportionality model is proposed:

$$D_B = \frac{D_{G,tot}}{k_D} \tag{3.2}$$

In the case of the Ancona landslide, it is presumable that $k_D \geq 1$, so it can be supposed that the simplified, translational, rigid body movement of a building does not exceed that of its underlying foundation ground, and so intensity can be related directly to building displacement.

3.3 QUANTITATIVE CHARACTERIZATION OF SLOPE KINEMATICS

The quantitative characterization of slope kinematic is pursued preliminarily to the parameterization of hazard and vulnerability. Modeling of slope kinematics is attempted using PSInSAR data and inclinometric measurements.

3.3.1 Characterization of slope kinematics from inclinometer data

Data from 59 inclinometers located inside and around the landslide area were available. Of the 59 inclinometers, 38 are still functioning, while 21 were dismissed between 2002 and today. Inclinometers BA05, BA07 and BA08 were replaced by BC05, BC07 and BC08, respectively. The former set were discarded as the latter are more representative of current behavior. Data from inclinometers GA01, GH01, MA01, MA02, PC01 and PC02 comprised less than five measurements following the zero-reading, which did not allow meaningful statistical processing. Moreover, these inclinometers are located far outside the landslide perimeter. Hence, such inclinometers were also discarded.

Figure 3.26 illustrates the locations of 49 out of the 50 inclinometers which were used in the present analysis, along with the locations of the buildings which were used for the development of the intensity model. Figure 3.27 details the location of the inclinometers in the Grotta and Palombella areas.

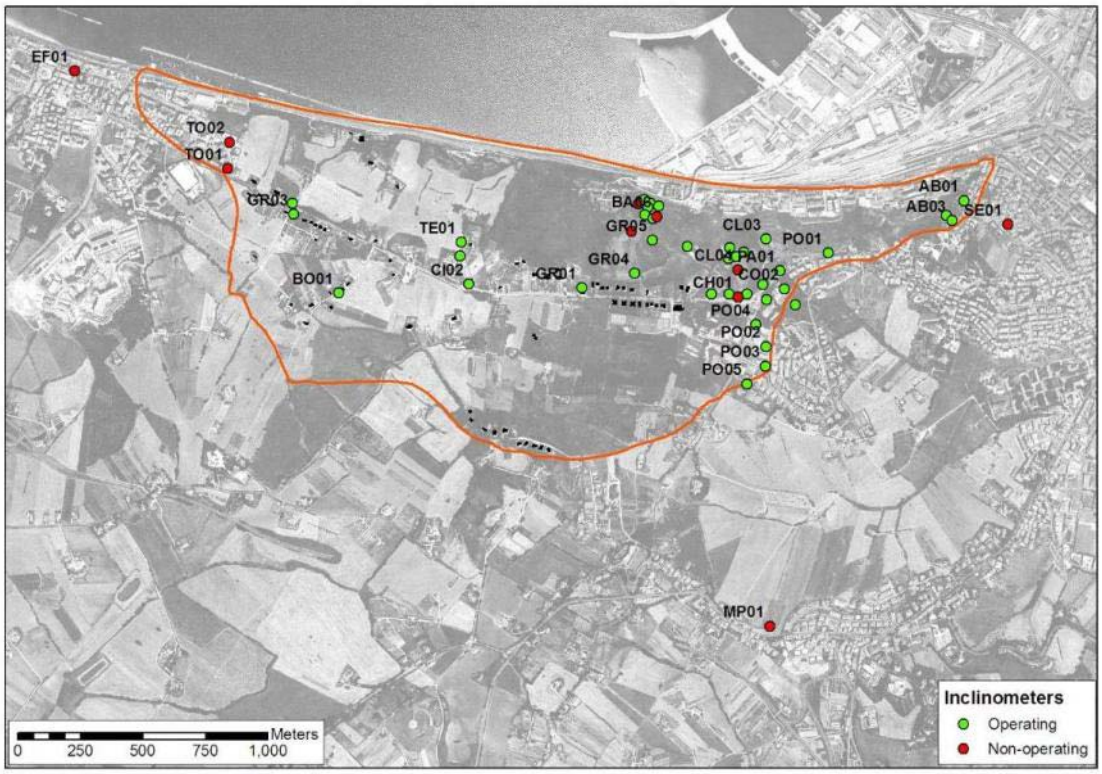

Figure 3.25. Inclinometer locations – general view

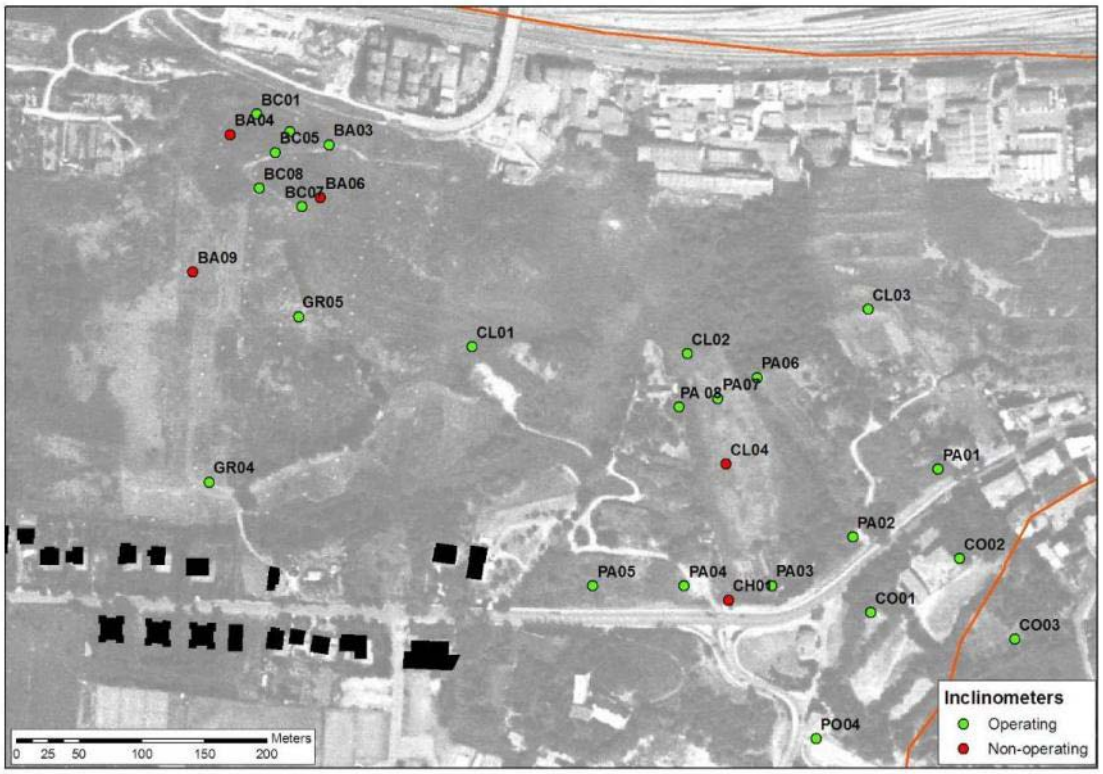

Figure 3.26. Inclinometer locations – detail of inclinometer locations in the Grotta and Palombella areas

Data obtained from inclinometer installations were used to:

- identify the sliding surfaces;
- investigate the sliding velocity.

At any given measurement depth, the cumulative displacement ($D_{IN,c}$) is the total displacement with respect to zero-reading (in mm). The incremental displacement ($D_{IN,i}$), also in mm, is the displacement with respect to previous reading. An example plot of inclinometer readings is shown in Figure 3.28 for the borehole PA02. Subplots (a)-(d) refer to cumulative displacement, incremental displacement, cumulative azimuth and incremental azimuth, respectively. In all subplots, each line refers to one reading, with darker lines corresponding to more recent readings. Positive values indicate down-slope kinematics, while negative values indicate up-slope kinematics.

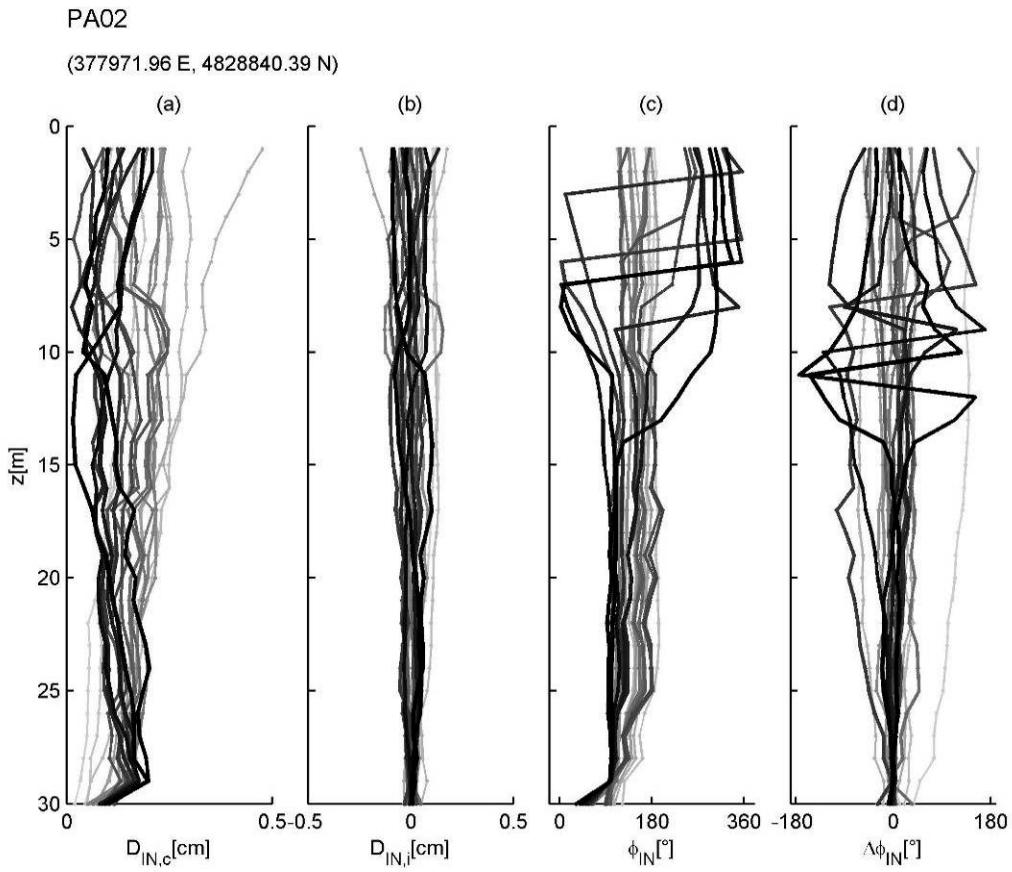

Figure 3.27. Example of inclinometer data.

As shown in the example subplots (c) and (d) of Figure 3.28, azimuth readings were found to display a high variability from one reading to another (not infrequently up to 90° approximately). Cotecchia (2006) attributed this fact to several causes, including: (a) lack of continuity in the readings over the years, resulting in a succession of different operators and equipment; (b) instrumental errors (drifting and calibration errors); and (c) operator inexperience and data processing errors.

In accordance with previous observations by Cotecchia (2006), it was seen that recorded deformation azimuths within the superficial strata tend to be influenced by factors such as slope morphology and other localized features (e.g. proximity to natural trenches, maximum slope gradients). However, azimuth readings recorded in stable deeper sections were also deemed not reliable, as the general direction of movement often resulted in complete disagreements with the global movement of the main landslide body (Body C).

From a quantitative perspective, in accordance with previous assessments by Cotecchia (2006), the epistemic fluctuation of azimuth readings resulted in the loss of any practical significance. Hence, azimuth readings were not considered in the present analysis.

The unavailability of reliable azimuth measurements does not impede the kinematics-based specific risk estimation for buildings, as the landslide damaging potential is invariant to the direction of sliding.

The average daily incremental velocity (ξ_{INd}) is given by the incremental displacement between two readings divided by the number of days occurring between the two readings, and is measured in mm.day^{-1}. The number of readings was not sufficient to allow a statistically significant analysis of temporal stationarity of displacement and velocity, i.e. to assess in rigorous statistical terms the existence of preferential seasonal periods for the occurrence of sliding. A qualitative, less formal assessment allowed to assume temporal stationarity of sliding, thus allowing the projection of the average daily incremental velocity to a yearly basis by multiplying ξ_{INd} by 365 to obtain the average yearly velocity ξ_{IN} (mm.yr^{-1}). For each inclinometer and for each pair of consecutive readings, the average velocity between consecutive readings ξ_{IN} was calculated as described above.

Figure 3.29 illustrates an example of (a) cumulative displacement vs. depth (by reading); (b) cumulative displacement by date (and reading); (c) incremental displacement by date (and reading); and (d) average velocity between consecutive readings (by date and reading) for inclinometer BA02.

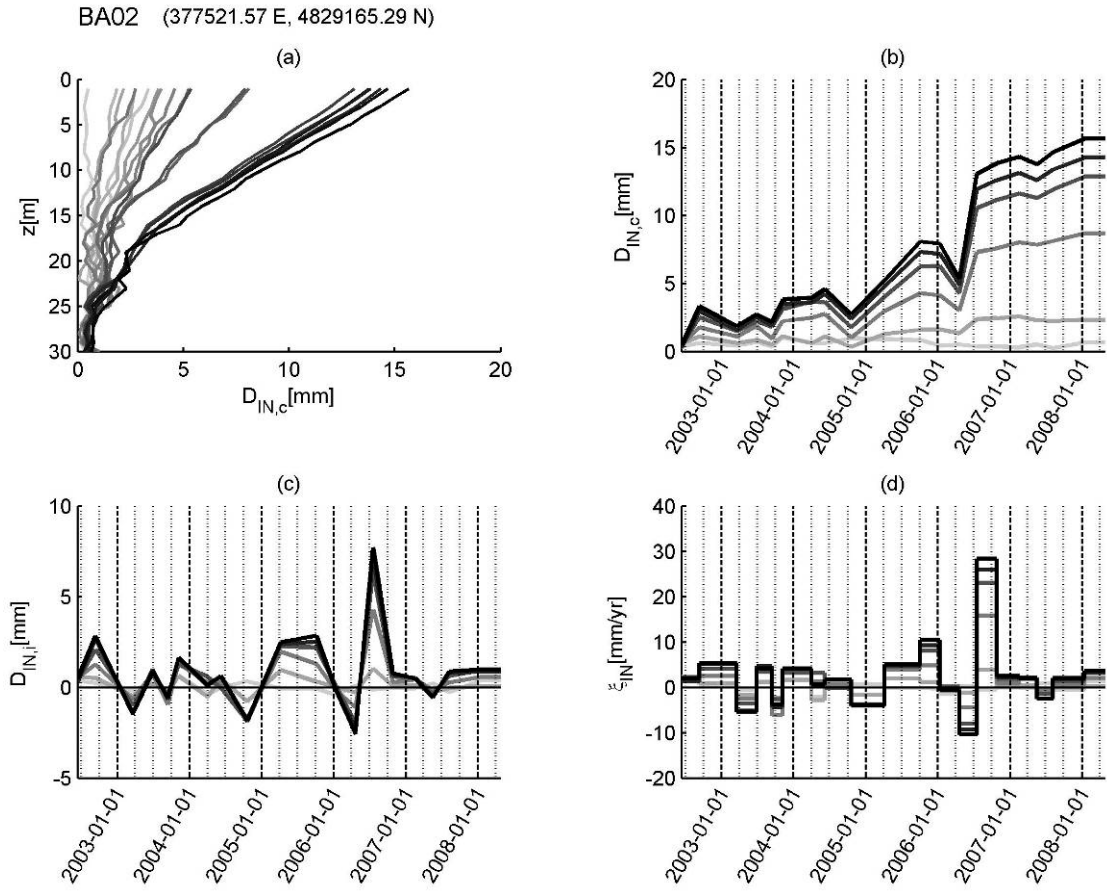

Figure 3.28. Example plot of (a) cumulative displacement vs. depth (by reading); (b) cumulative displacement by date (and reading); (c) incremental displacement by date (and reading); and (d) average velocity between consecutive readings (by date and reading)

3.3.1.1 Identification of sliding surfaces

To identify sliding surfaces, the differential velocity $\xi_{IN\Delta}$, given by the difference between the average velocity at one reading depth and at the reading depth immediately

above, was calculated. A lower differential velocity threshold $\xi_{IN\Delta t}$=1 mm.yr^{-1}, below which $\xi_{IN\Delta}$ (in absolute value) could be considered negligible for the purposes of the present analyses, was established subjectively. Instances in which $|\xi_{IN\Delta}| \geq \xi_{IN\Delta t}$ were recorded (Figure 3.30 for inclinometer BA02, in which date from more recent readings are shown in darker lines, and in which the dashed lines delimit the range $\pm\xi_{IN\Delta t}$).

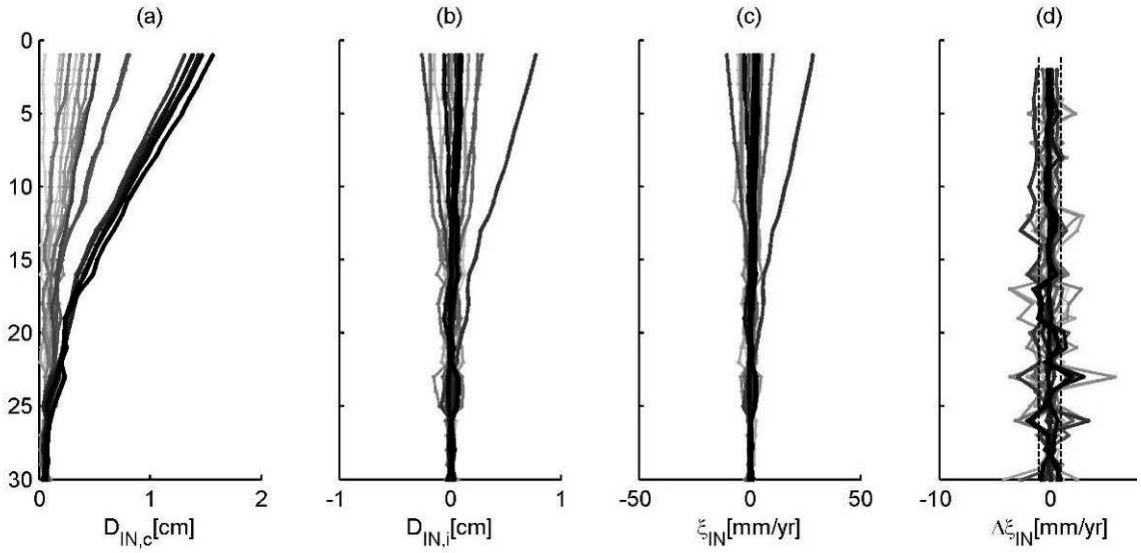

Figure 3.29. Average velocity and differential average velocity for inclinometer BA02

Chrono-plots such as the one shown in Figure 3.30 (which is related to the data shown in Figure 3.29) were obtained for all inclinometers. In the chrono-plots, significant differential velocities are plotted as filled circles by date and depth (of the lower measurement, e.g. values plotted at depth z = 15 m refer to the differential velocity between readings at 14 and 15 m). The radius of the circle indicates semi-qualitatively the magnitude (in absolute value) of differential velocity. Gray circles indicate that the differential velocity is negative, i.e. that the more surficial layer has moved down-slope with respect to the less surficial soil; black circles indicate a positive differential velocity, i.e. a situation in which a surficial stratum has moved up-slope relatively to the adjacent, less surficial stratum. In terms of landslide kinematics, negative differential velocities could be explained by gravitational translational movements, while positive differential velocities could be due to rotational kinematisms, by which the more surficial strata located above the center of rotation are projected up-slope. The example for inclinometer BA02 in Figure 3.31 shows the presence of sliding surfaces at different depths, with very relevant kinematics occurring between 12 and 30 m bgl) in 2003 and 2004 and numerous other kinematics, both shallow and surficial. A detailed qualitative analysis of the temporal distribution of differential sliding supported the hypothesis of temporal stationarity of sliding, as well as the confident projection of average velocities from a trimestral to an annual reference period as discussed previously.

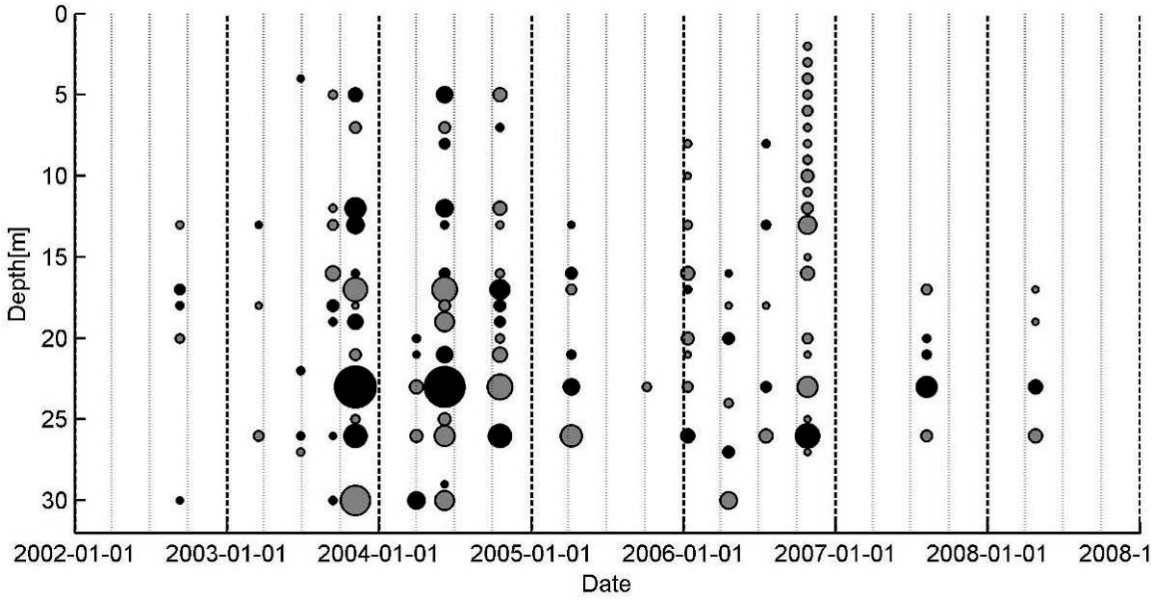

Figure 3.30. Chrono-plot of differential sliding for inclinometer BA02.

A set of 12 reference depths, which were deemed to be significant for the description of the kinematics of the Ancona landslide, were defined: 1, 3, 5, 10, 20, 30, 40, 50, 60, 70, 80 and 90 m bgl (hereinafter denoted as D01, D03, D05, D10, D20, D30, D40, D50, D60, D70, D80 and D90, respectively).

3.3.1.2 Statistical modeling of inclinometer data

Inclinometer data were analyzed statistically. The empirical cumulative distribution function (ECDF) of a sample is the cumulative distribution function associated with the empirical measure of the sample itself. ECDFs of ξ_{IN} were calculated for each inclinometer and for each reference depth.

A set of statistics were extracted from each velocity sample, namely: (a) the 0.05th sample quantile; (b) the 0.50th quantile, or sample median; and (c) the 0.95th quantile. Hereinafter, these are denoted by $\xi_{IN,05}$, $\xi_{IN,50}$ and $\xi_{IN,95}$, respectively. While the median corresponds to a central probability level, the 0.05 and 0.95 quantiles were used to represent the lower and upper bounds of the 90% range of sample values. Such range was deemed sufficiently representative of slope kinematics for engineering purposes. Characteristic sample values were also retrieved from each sample, and are defined here as

$$\xi_{ch} = \max\left[\text{abs}\left(\xi_{05}\right), \text{abs}\left(\xi_{95}\right)\right]$$

in which abs(ξ_{05}) and abs(ξ_{95}) are the absolute values of the 5th and 95th percentiles, respectively, of ξ_{IN}. Figure 3.32 shows an example plot for inclinometer BA08. In the plots, darker lines correspond to shallower reference depths.

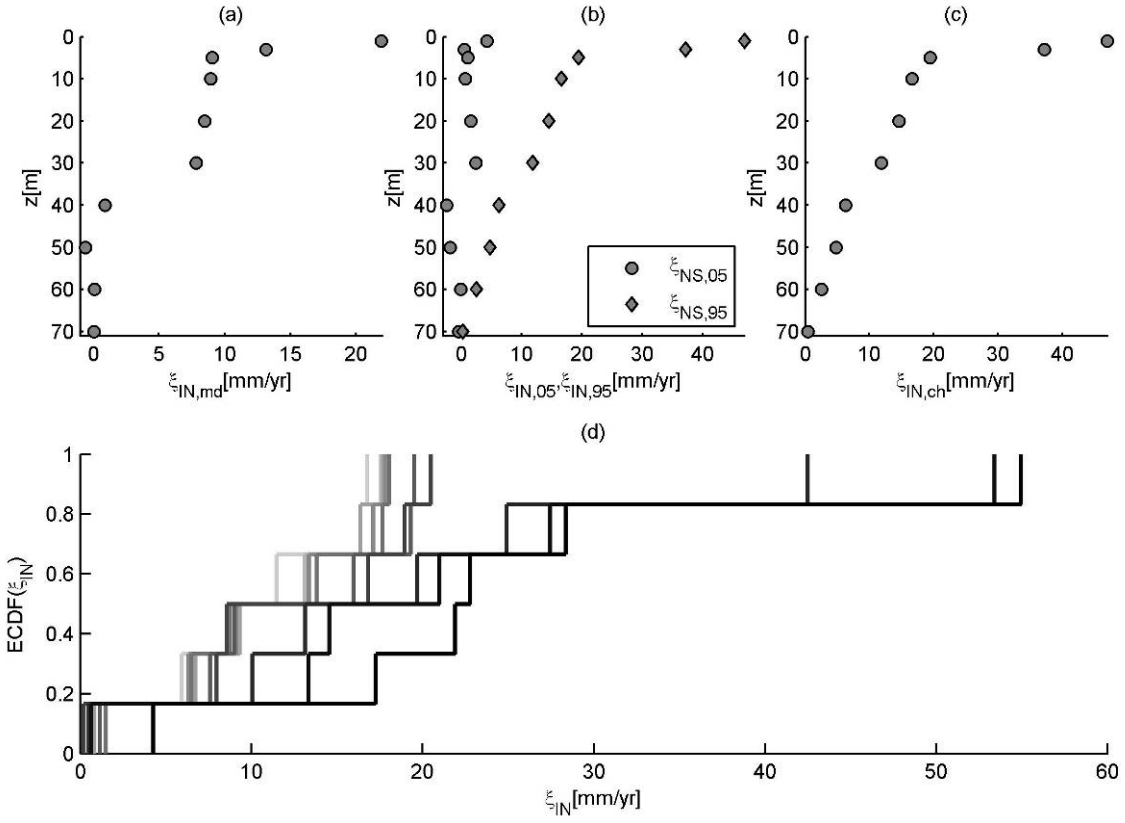

Figure 3.31. Sample statistics of ξIN at reference depths D01, D03, D05, D10, D20, D30, D40, D50, D60 and D70 for inclinometer BA08: (a) sample median; (b) 0.05 and 0.95 quantiles; (c) characteristic value; and (d) empirical cumulative distribution functions

Figures 3.33 to 3.56 plot median and characteristic values of ξ_{IN} as estimated from inclinometer data at the 12 reference depths. Figure 3.57 plots the relative frequency histograms of $\xi_{IN,md}$ and $\xi_{IN,ch}$ by reference depth for the aggregate sample obtained by merging the data from all inclinometers.

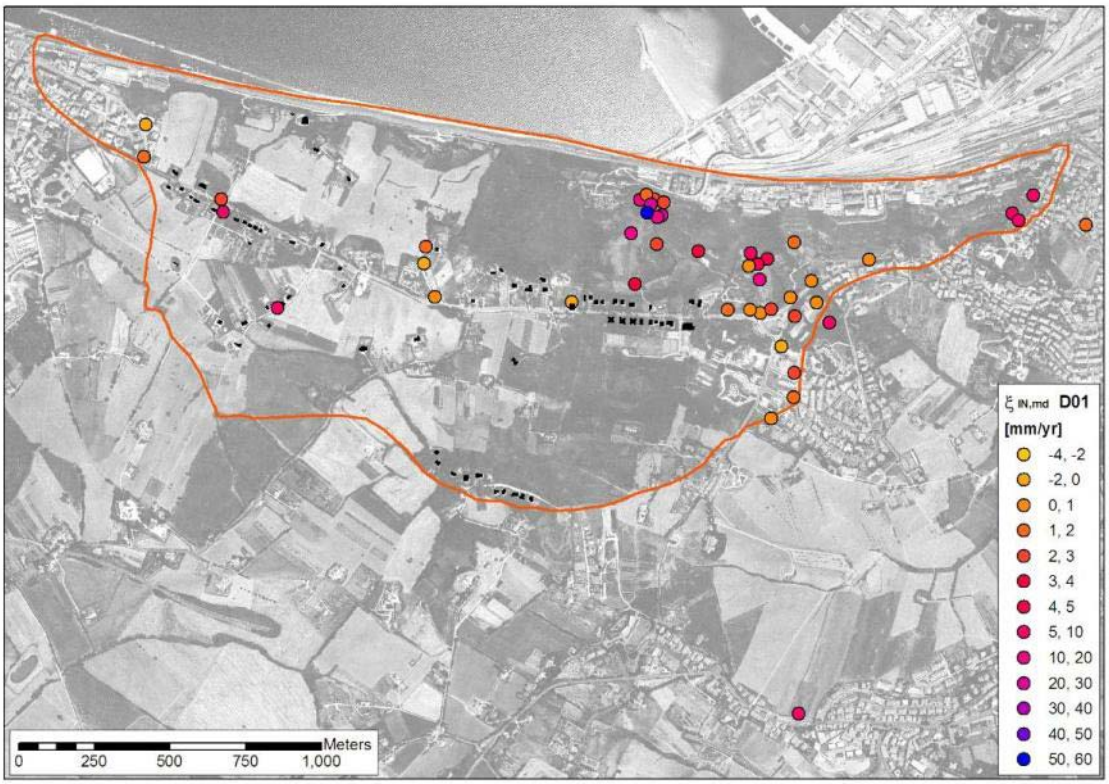

Figure 3.32. Inclinometer-based estimates of ξIN,md at reference depth D01.

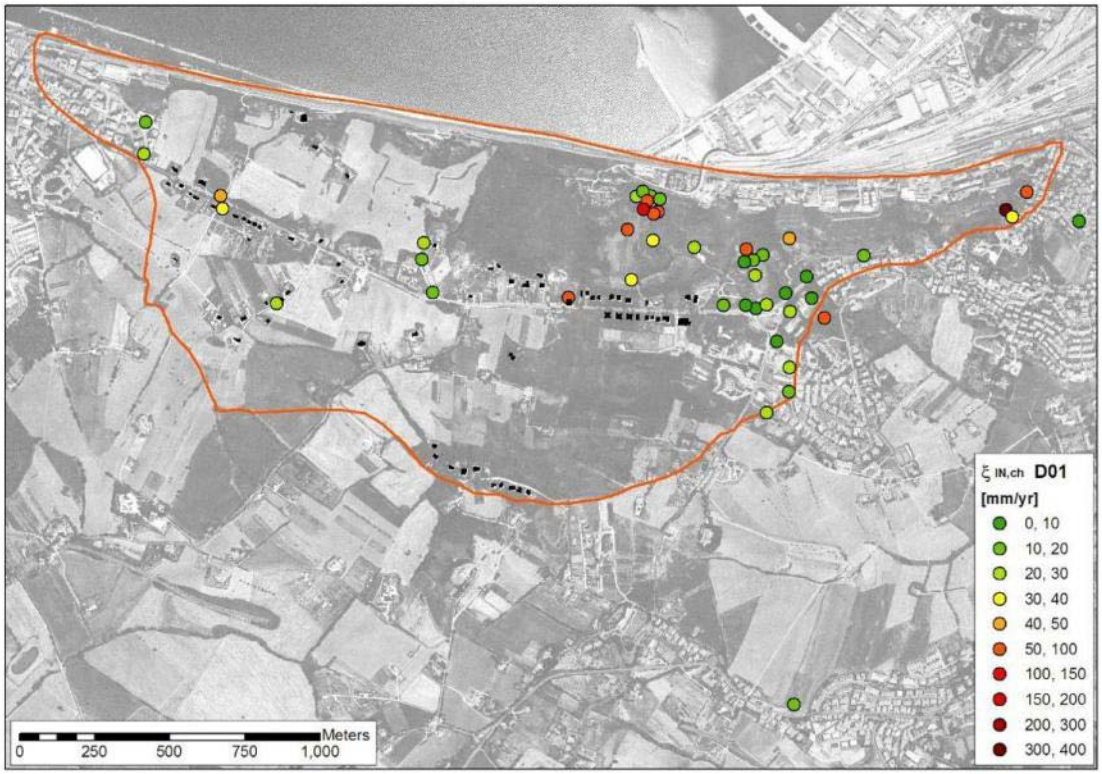

Figure 3.33. Inclinometer-based estimates of $\xi_{IN,ch}$ at reference depth D01.

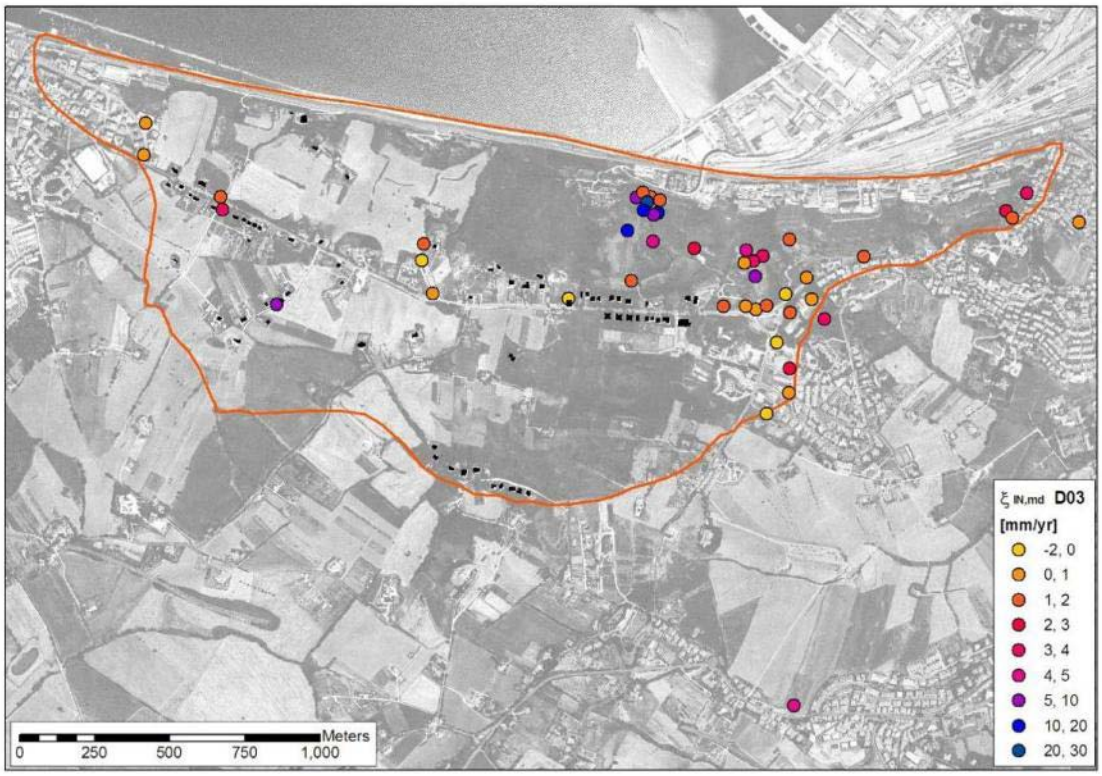

Figure 3.34. Inclinometer-based estimates of $\xi_{IN,md}$ at reference depth D03.

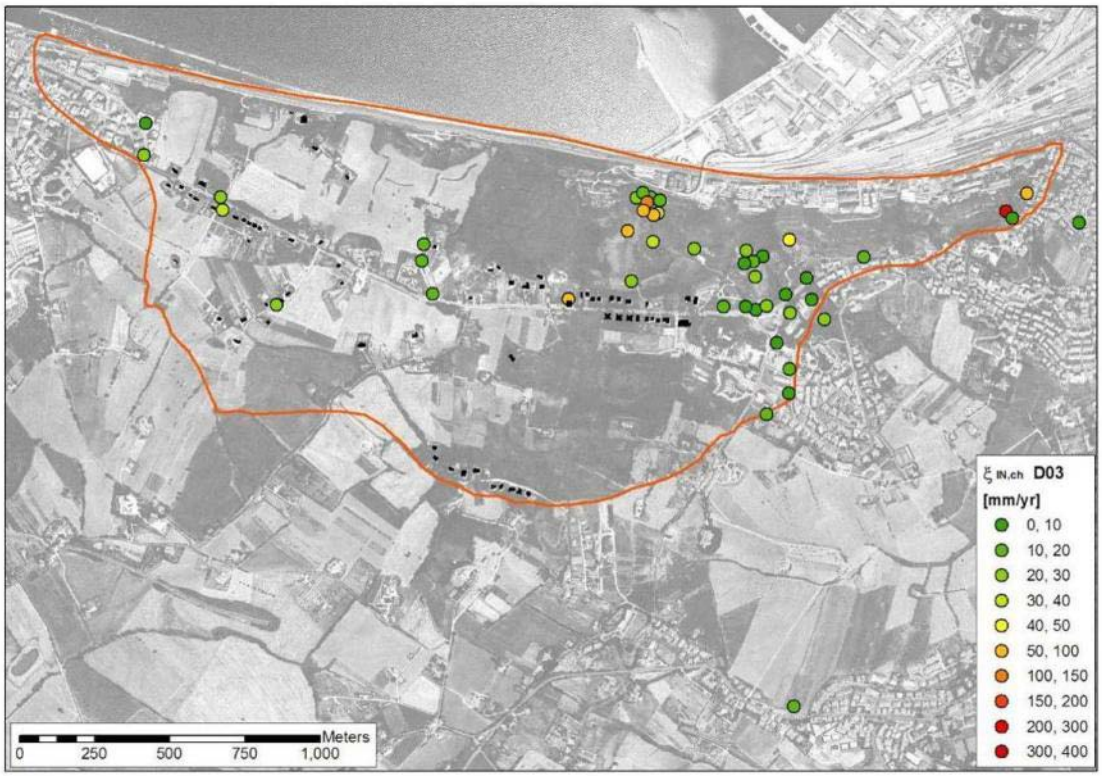

Figure 3.35. Inclinometer-based estimates of $\xi_{IN,ch}$ at reference depth D03.

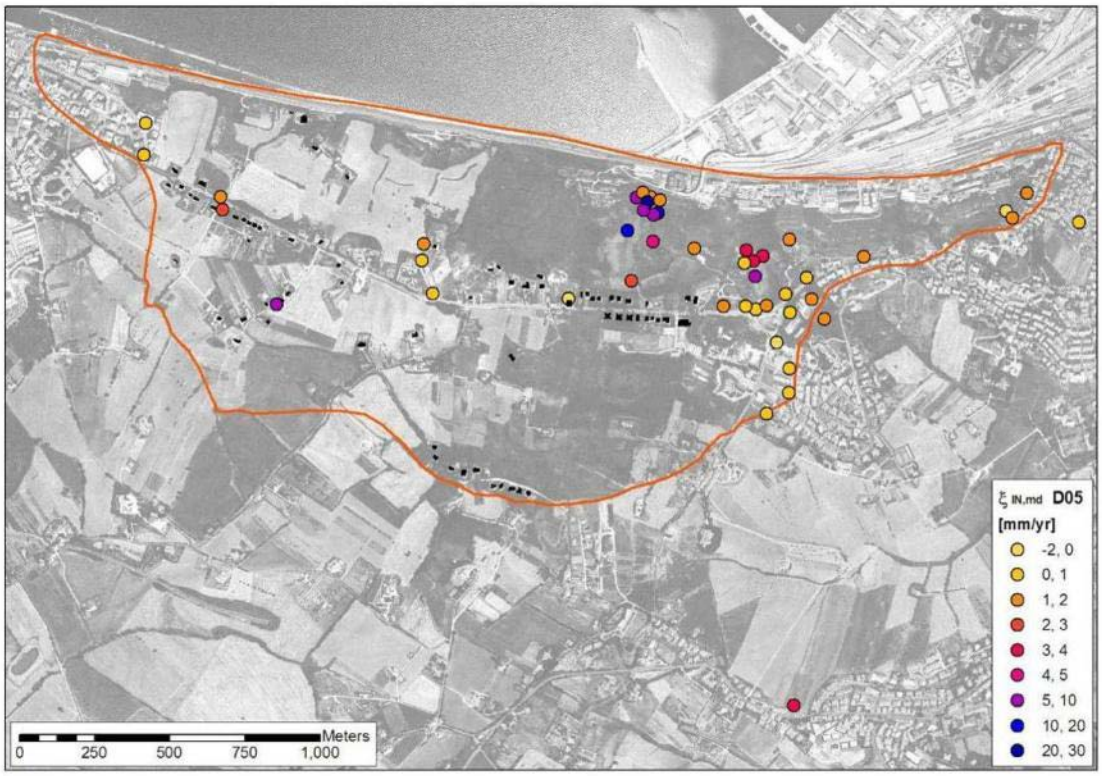

Figure 3.36. Inclinometer-based estimates of $\xi_{IN,md}$ at reference depth D05.

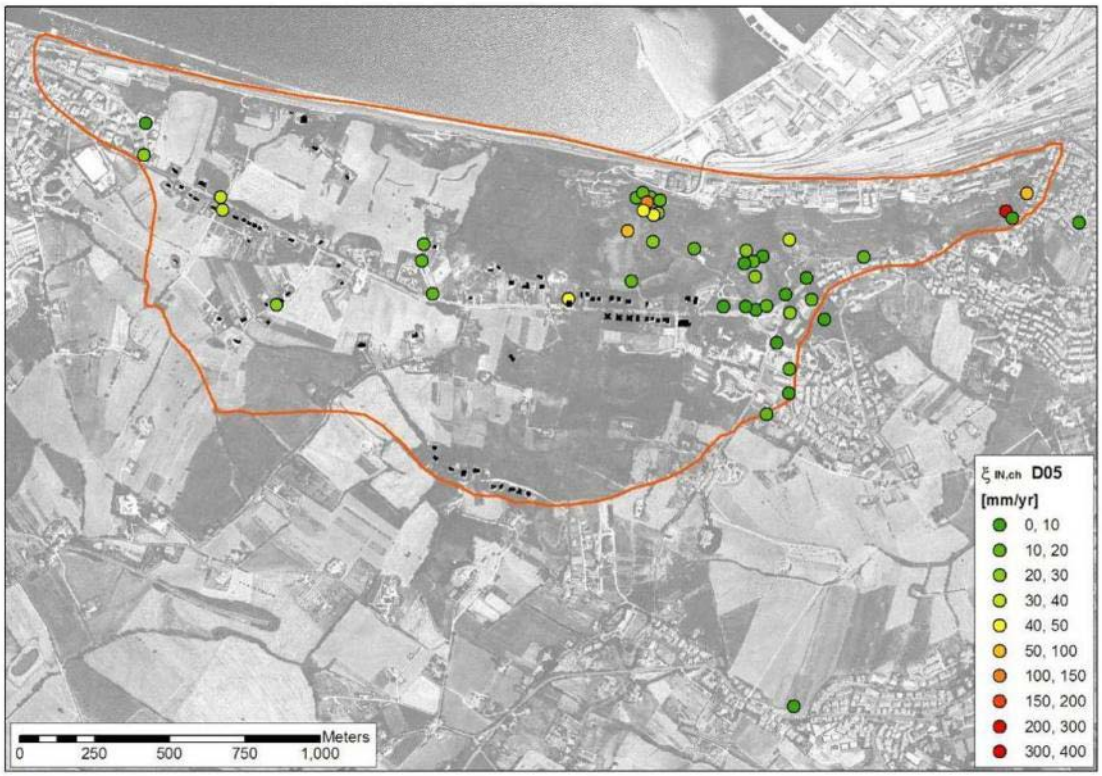

Figure 3.37. Inclinometer-based estimates of $\xi_{IN,ch}$ at reference depth D05.

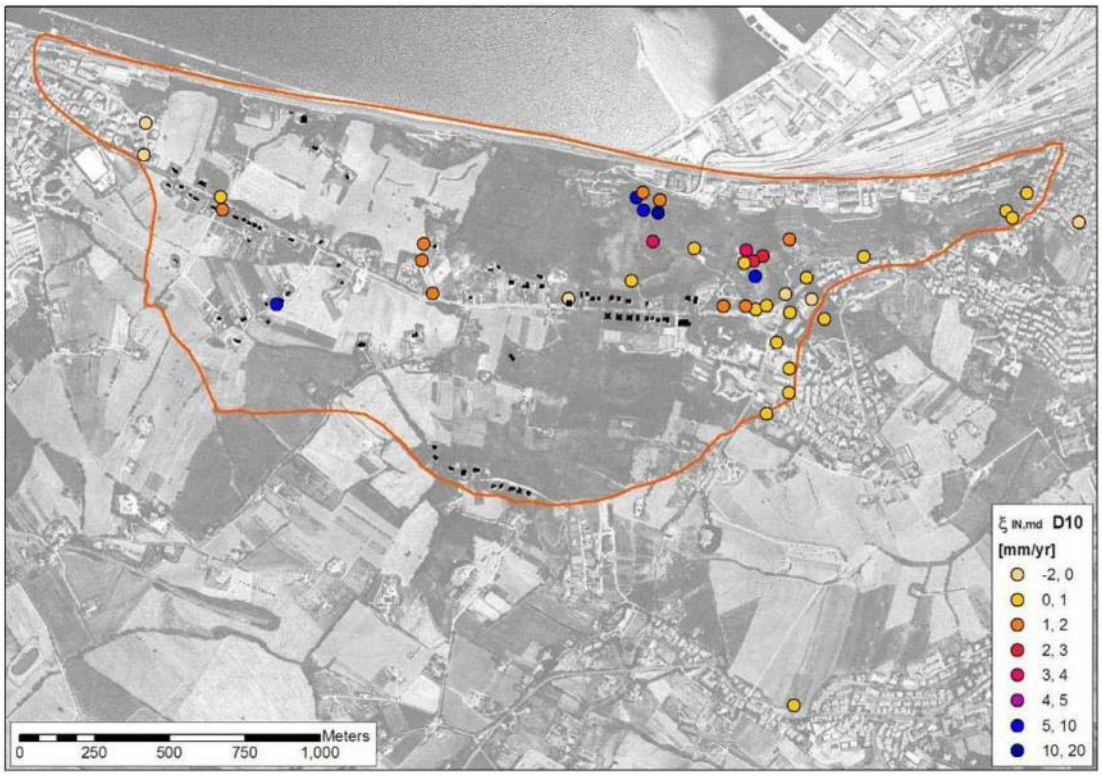

Figure 3.38. Inclinometer-based estimates of $\xi_{IN,md}$ at reference depth D10.

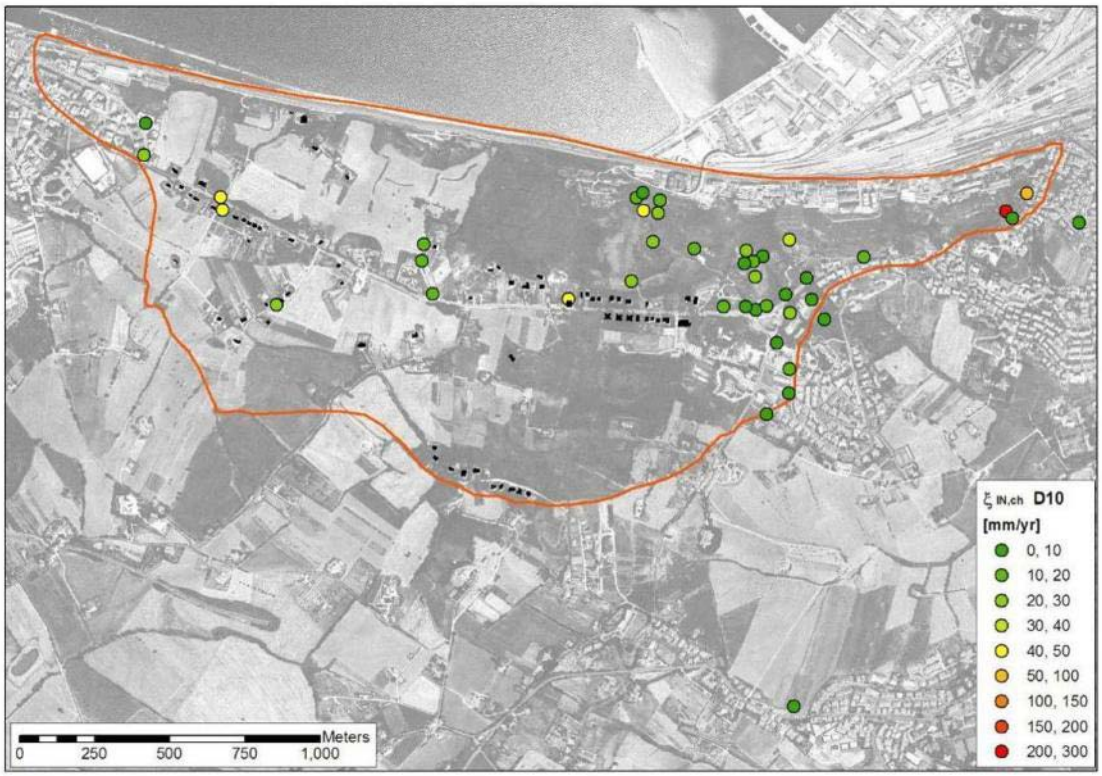

Figure 3.39. Inclinometer-based estimates of $\xi_{IN,ch}$ at reference depth D10.

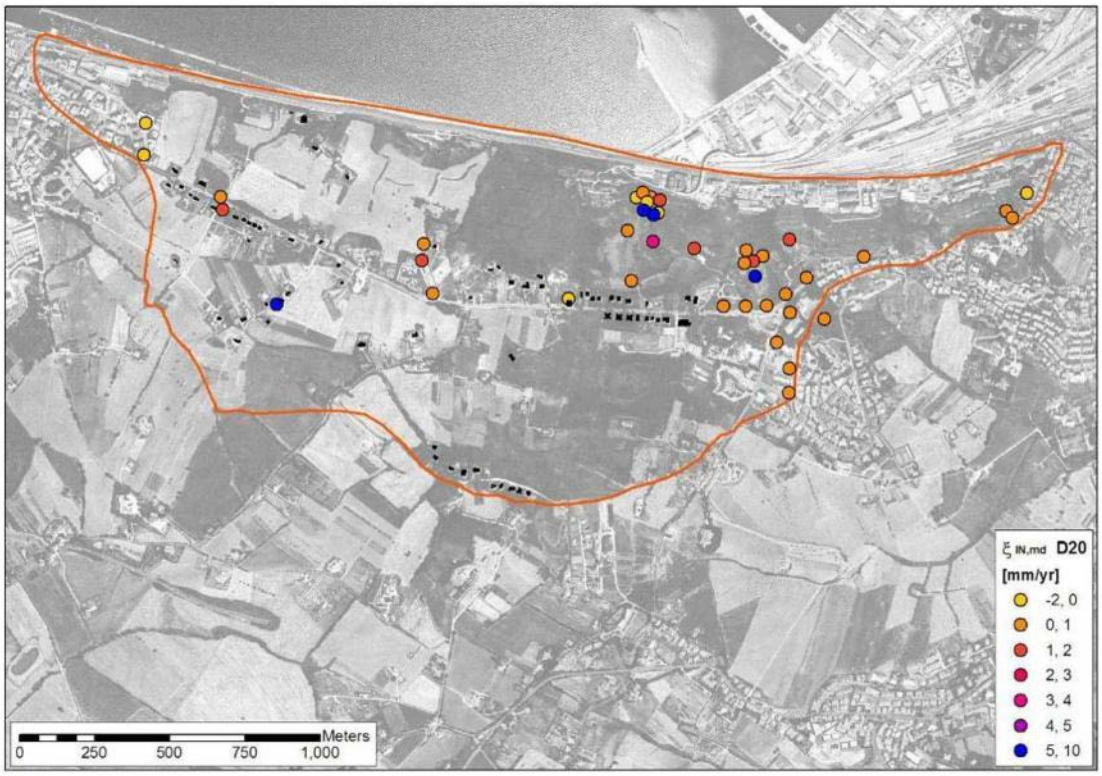

Figure 3.40. Inclinometer-based estimates of $\xi_{NS,md}$ at reference depth D20.

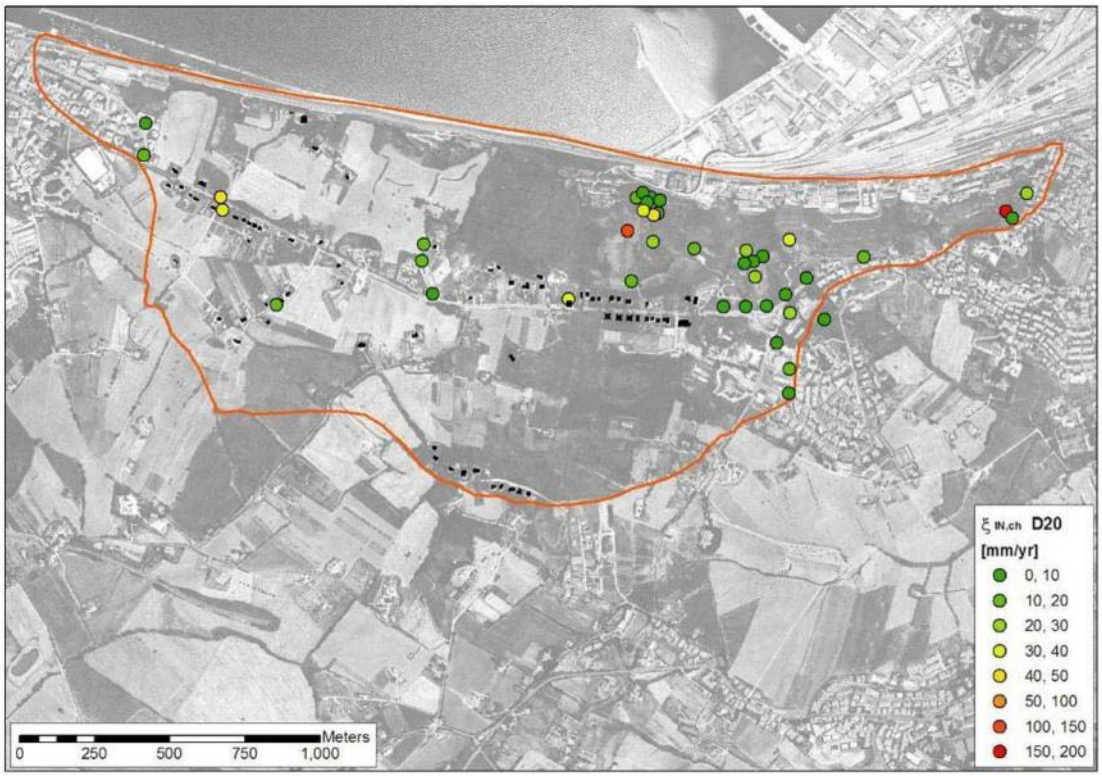

Figure 3.41. Inclinometer-based estimates of $\xi_{NS,ch}$ at reference depth D20.

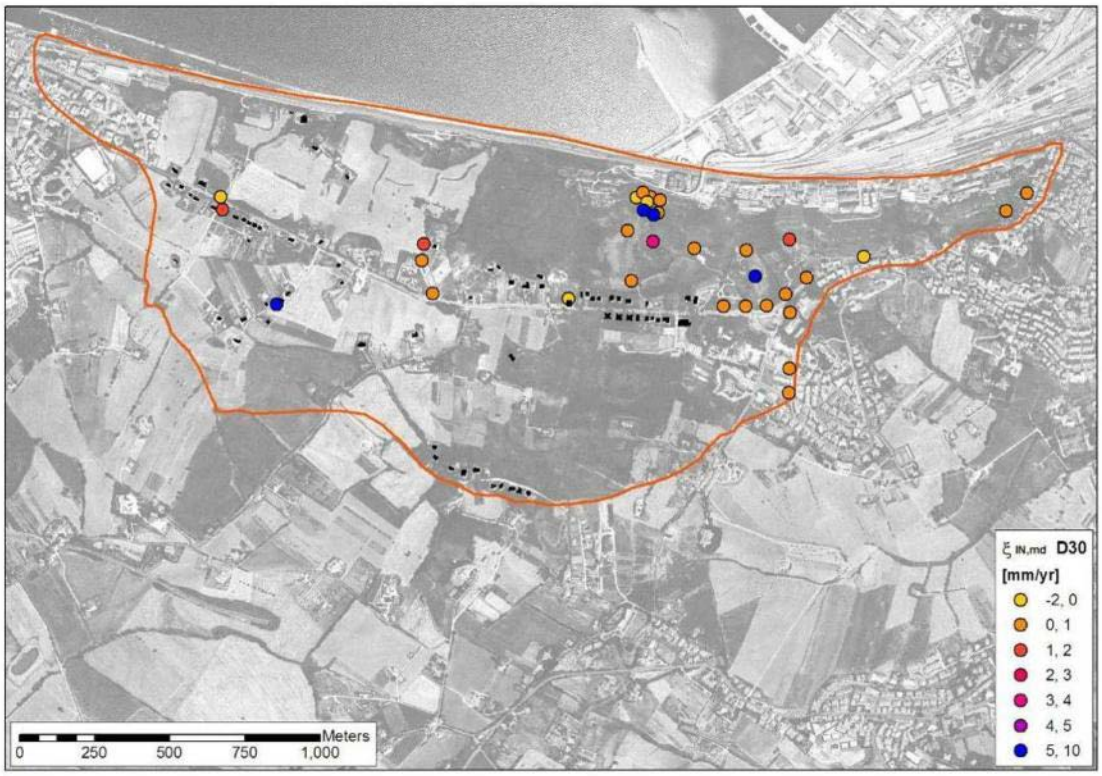

Figure 3.42. Inclinometer-based estimates of $\xi_{NS,md}$ at reference depth D30.

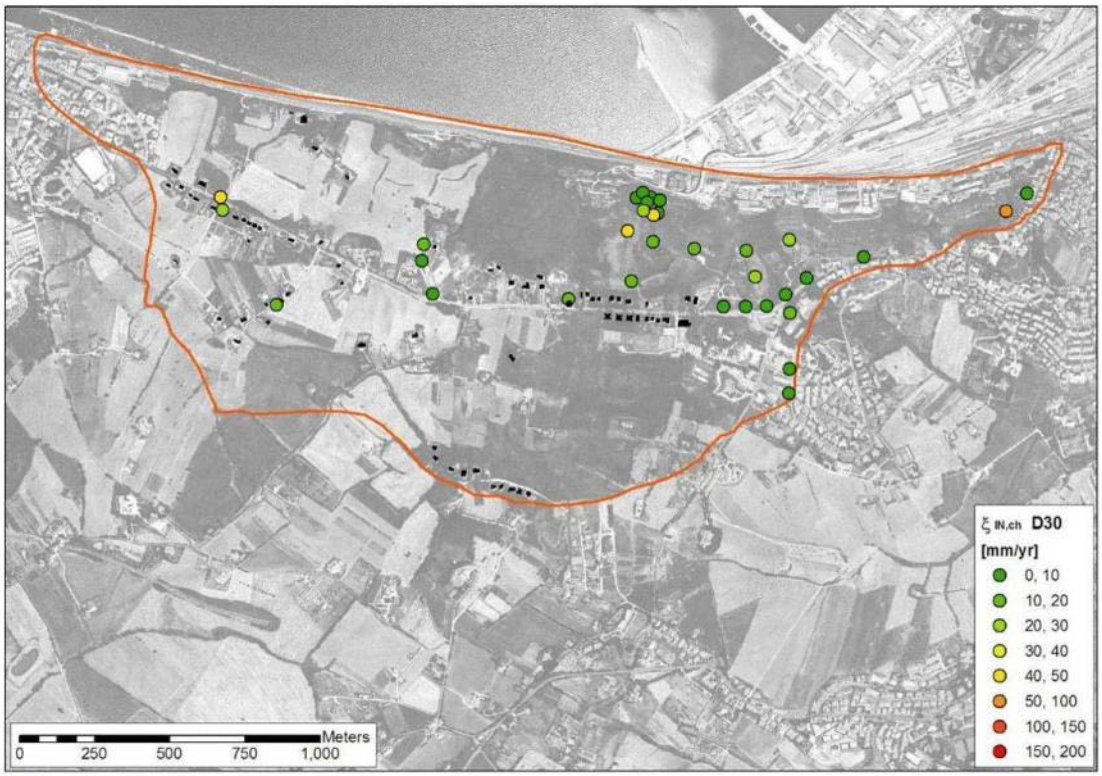

Figure 3.43. Inclinometer-based estimates of $\xi_{NS,ch}$ at reference depth D30.

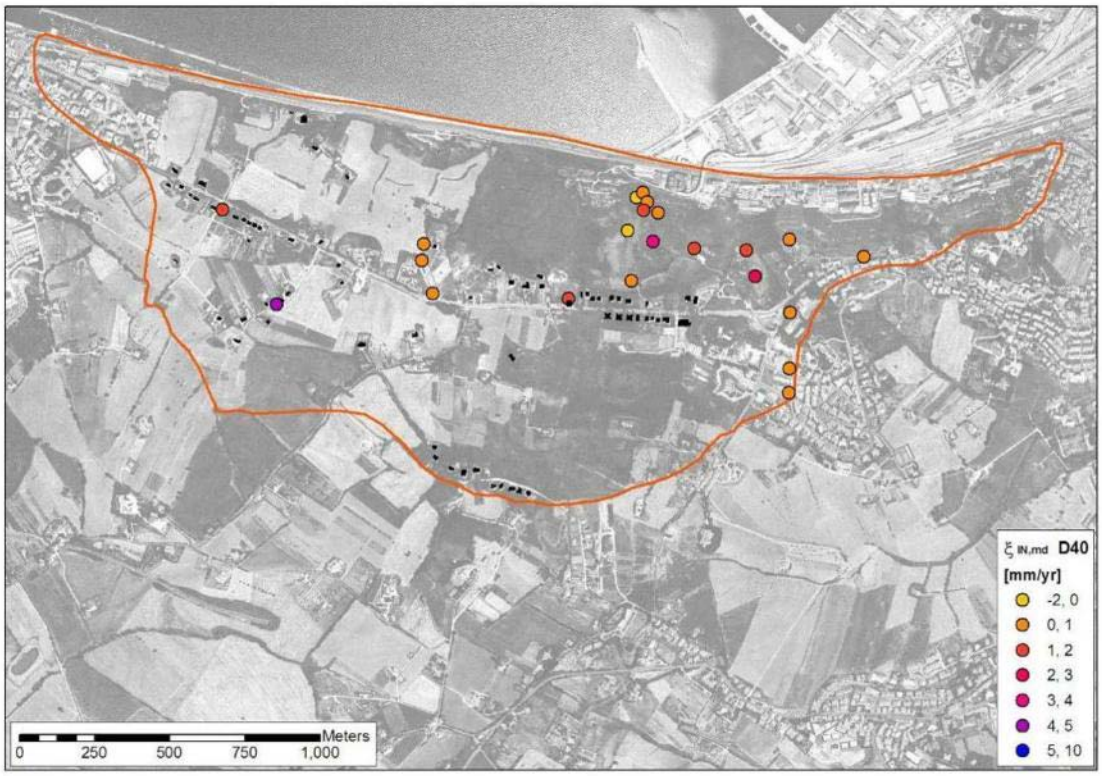

Figure 3.44. Inclinometer-based estimates of $\xi_{NS,md}$ at reference depth D40.

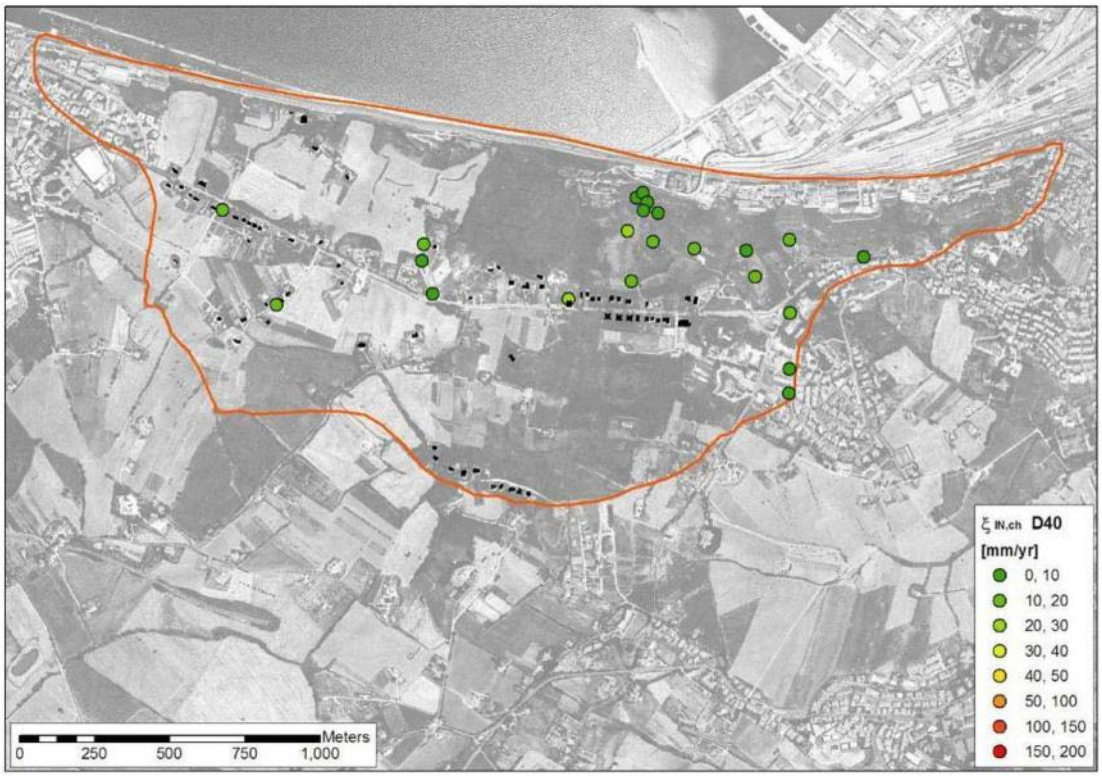

Figure 3.45. Inclinometer-based estimates of $\xi_{NS,ch}$ at reference depth D40.

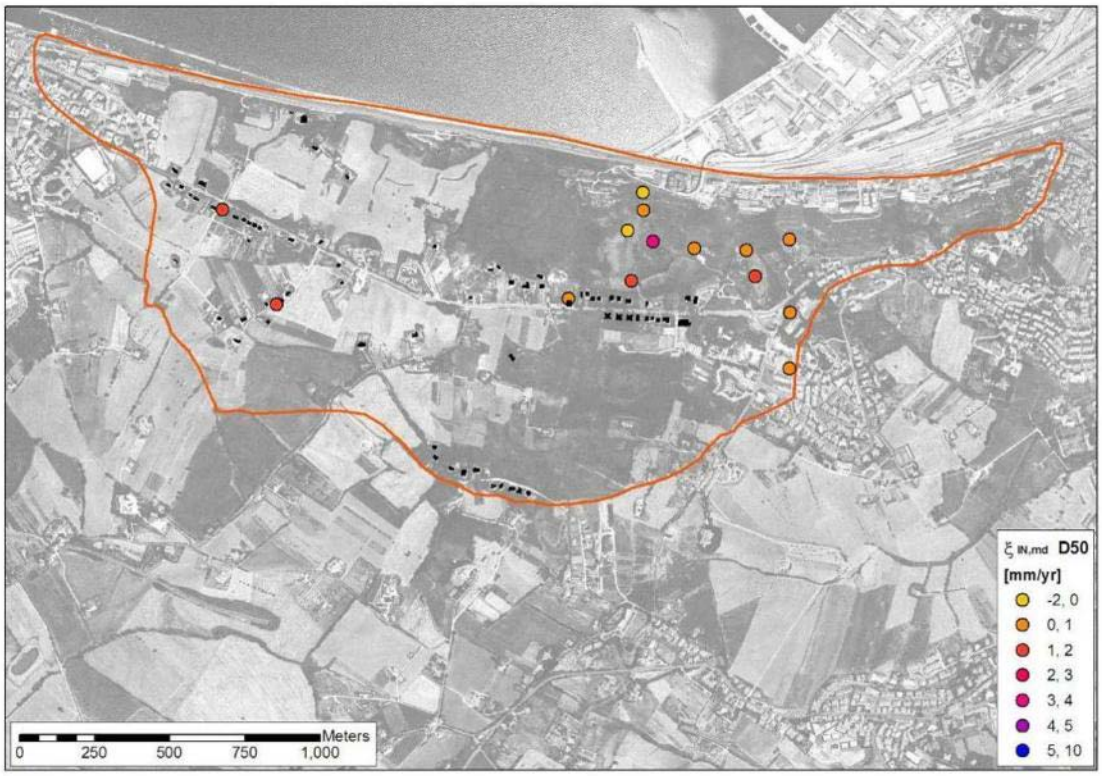

Figure 3.46. Inclinometer-based estimates of $\xi_{NS,md}$ at reference depth D50.

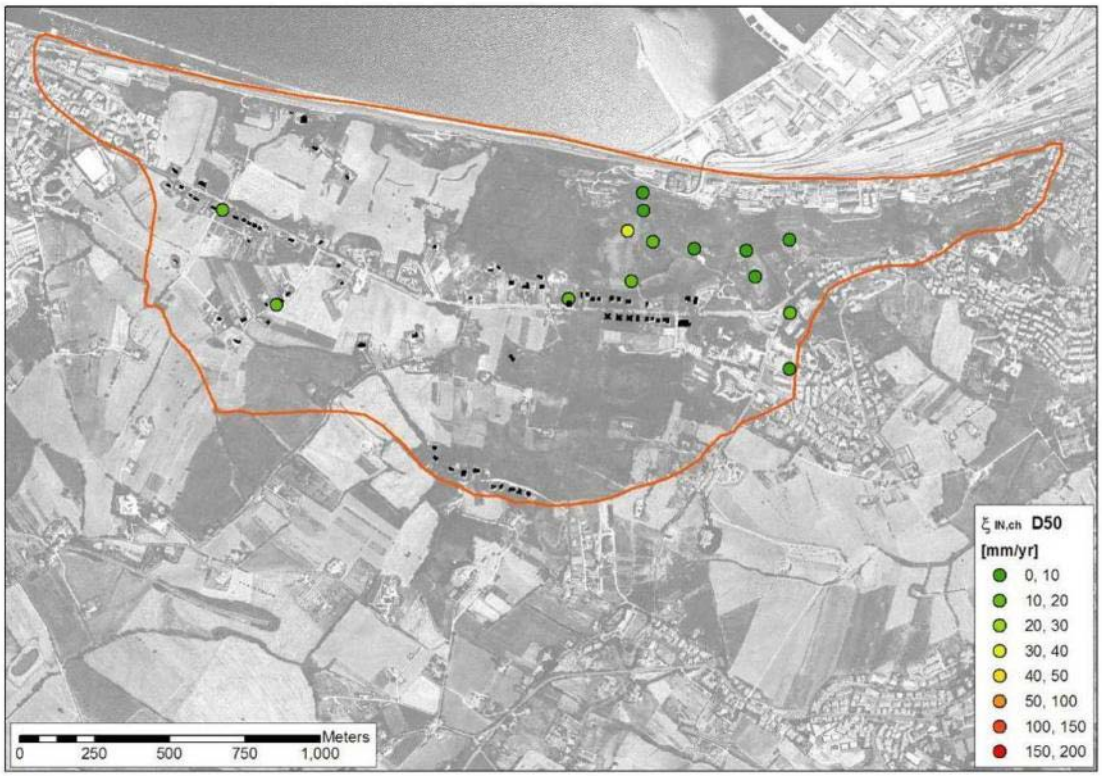

Figure 3.47. Inclinometer-based estimates of $\xi_{NS,ch}$ at reference depth D50.

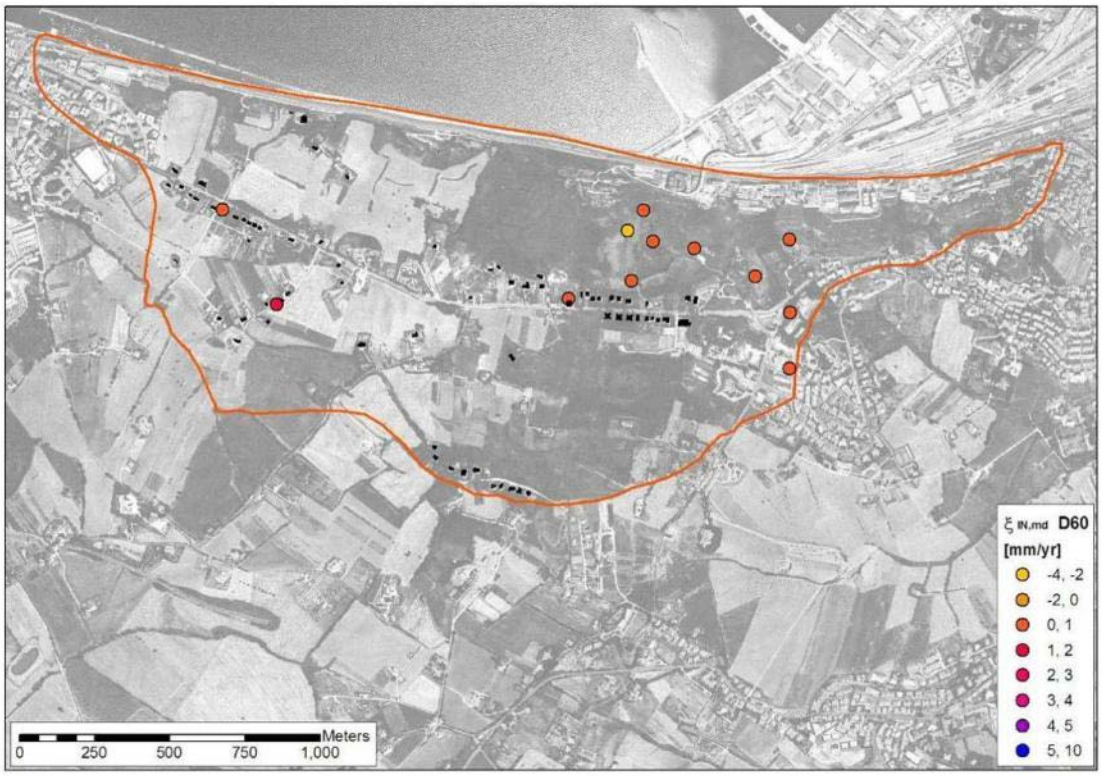

Figure 3.48. Inclinometer-based estimates of $\xi_{IN,md}$ at reference depth D60.

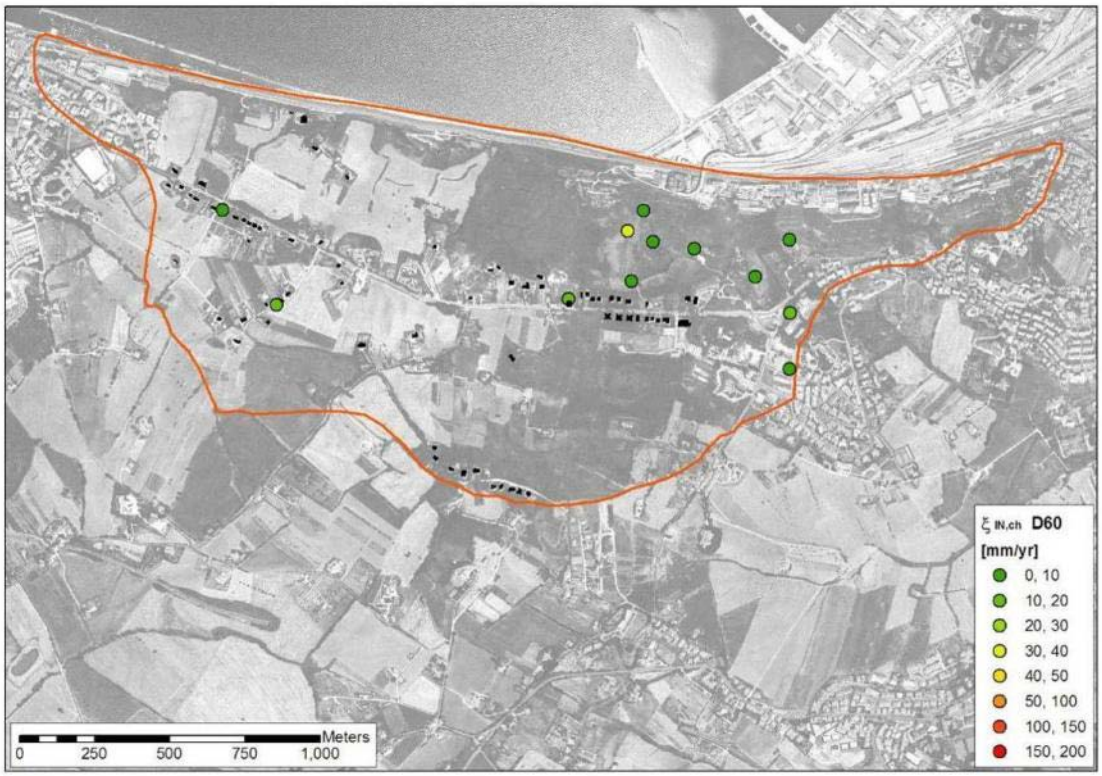

Figure 3.49. Inclinometer-based estimates of $\xi_{IN,ch}$ at reference depth D60.

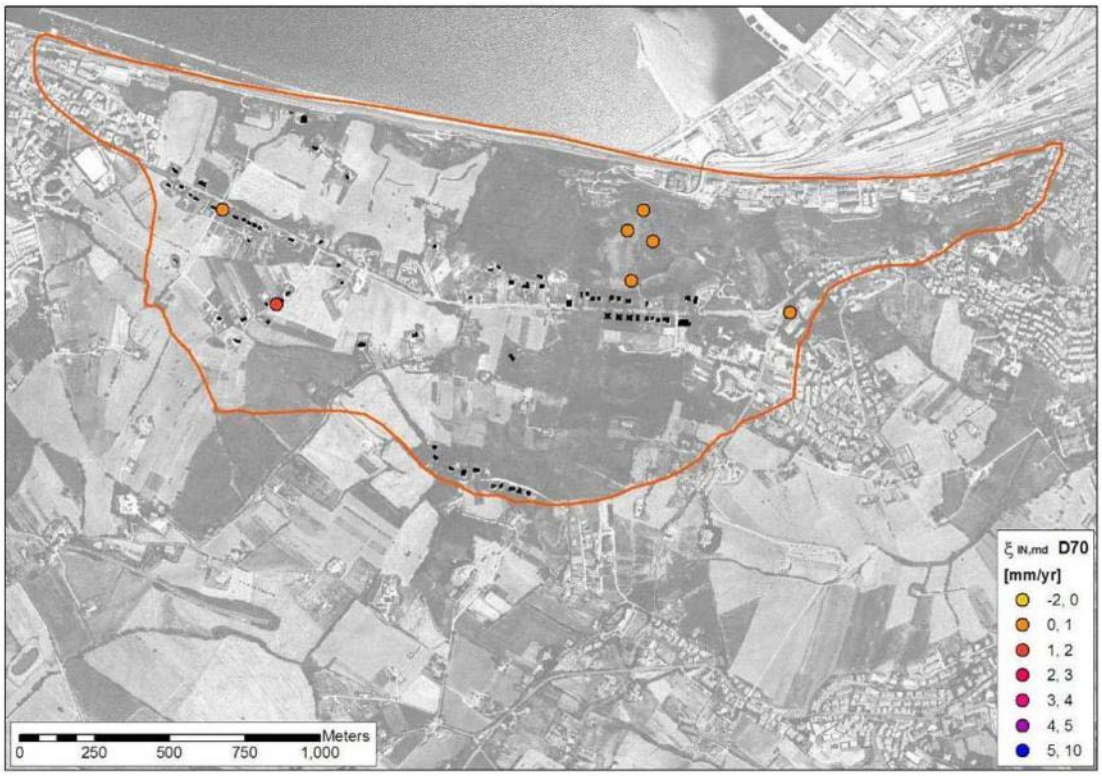

Figure 3.50. Inclinometer-based estimates of $\xi_{IN,md}$ at reference depth D70.

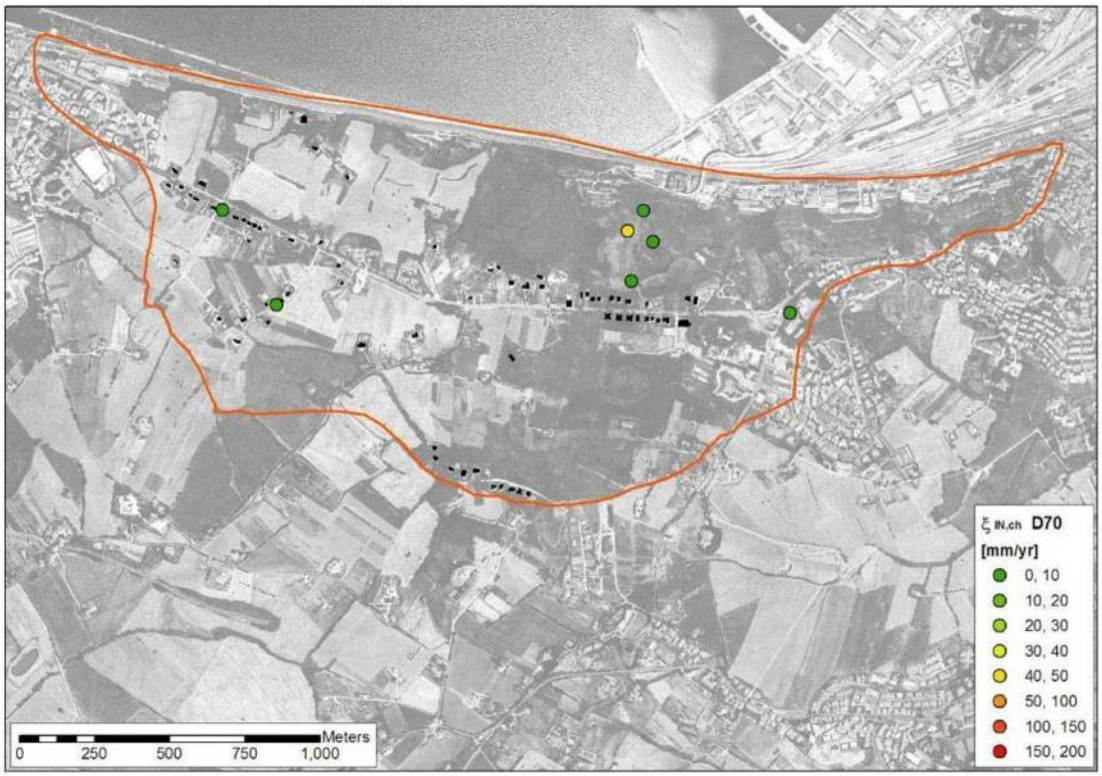

Figure 3.51. Inclinometer-based estimates of $\xi_{IN,ch}$ at reference depth D70.

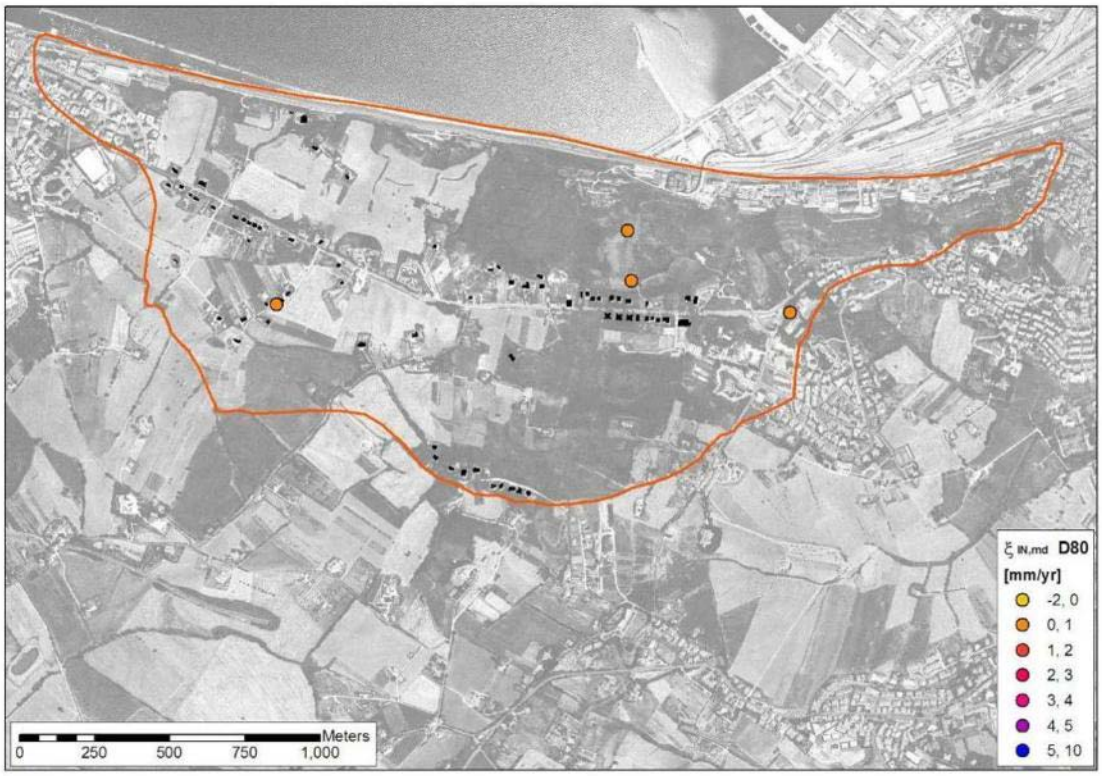

Figure 3.52. Inclinometer-based estimates of $\xi_{IN,md}$ at reference depth D80.

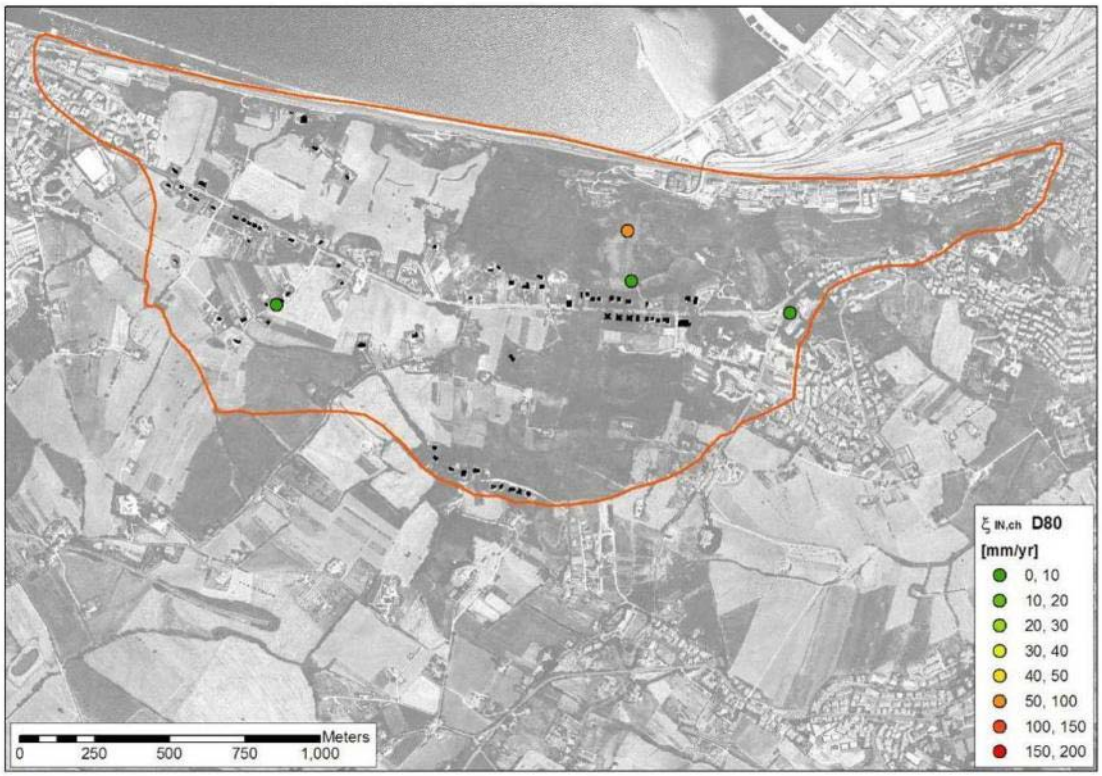

Figure 3.53. Inclinometer-based estimates of $\xi_{IN,ch}$ at reference depth D80.

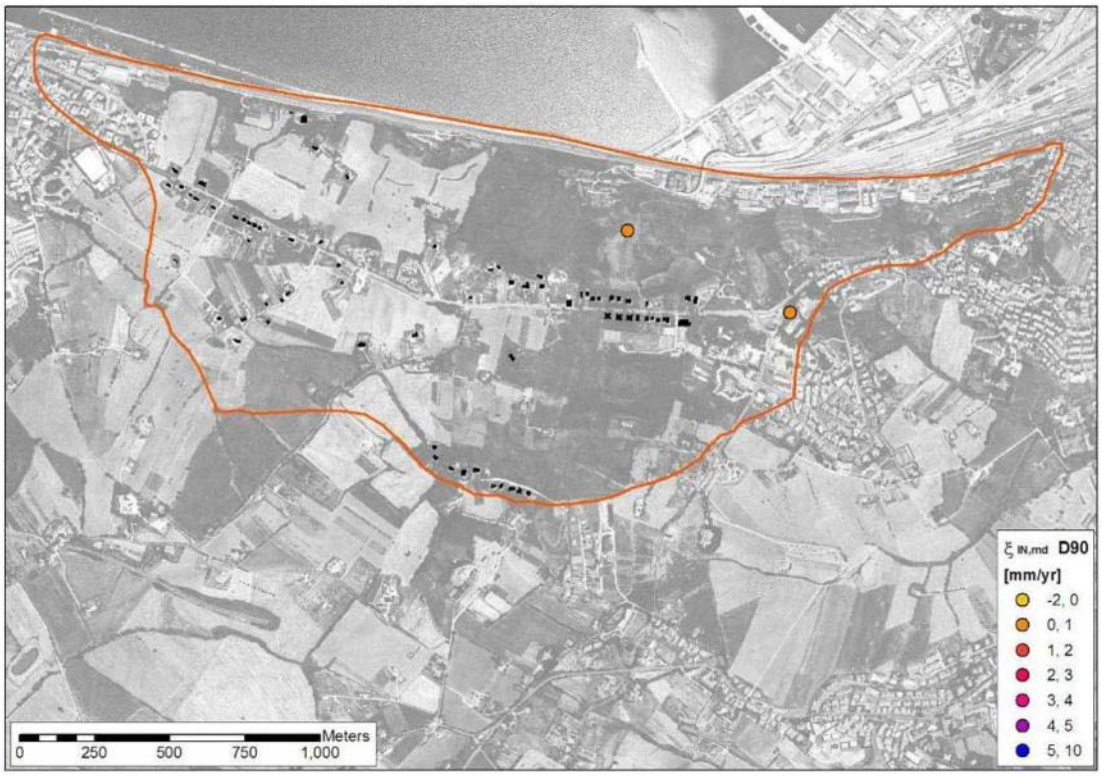

Figure 3.54. Inclinometer-based estimates of $\xi_{IN,md}$ at reference depth D90.

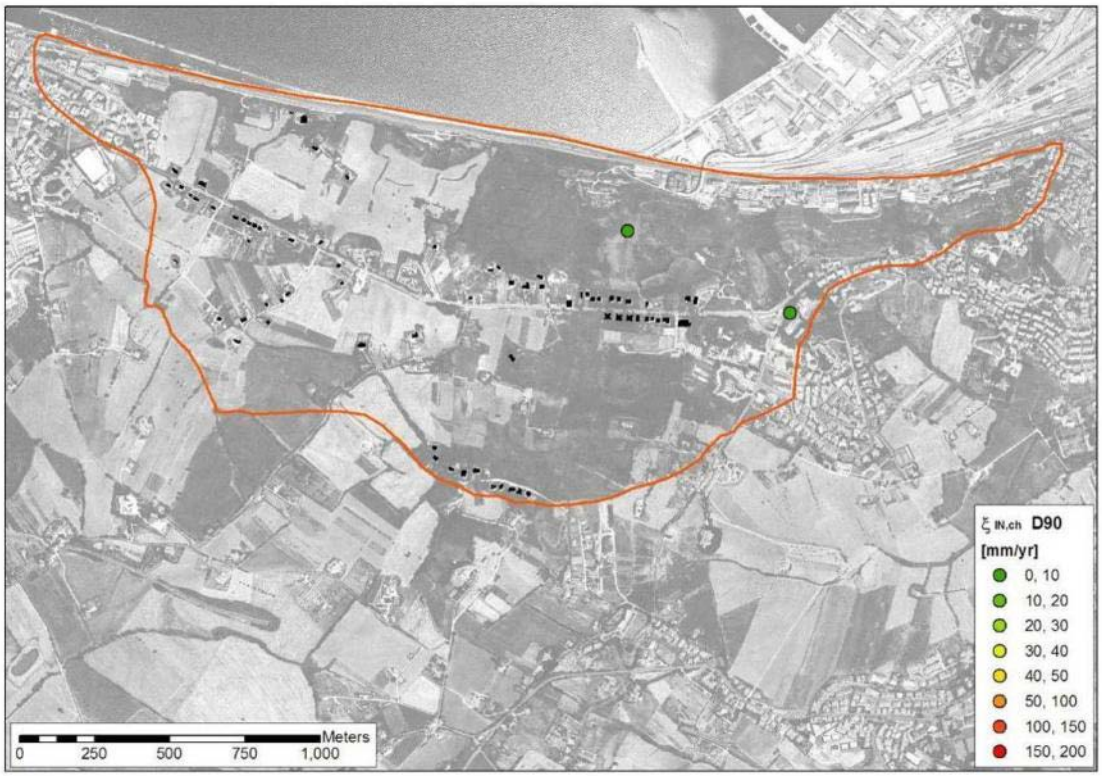

Figure 3.55. Inclinometer-based estimates of $\xi_{IN,ch}$ at reference depth D90.

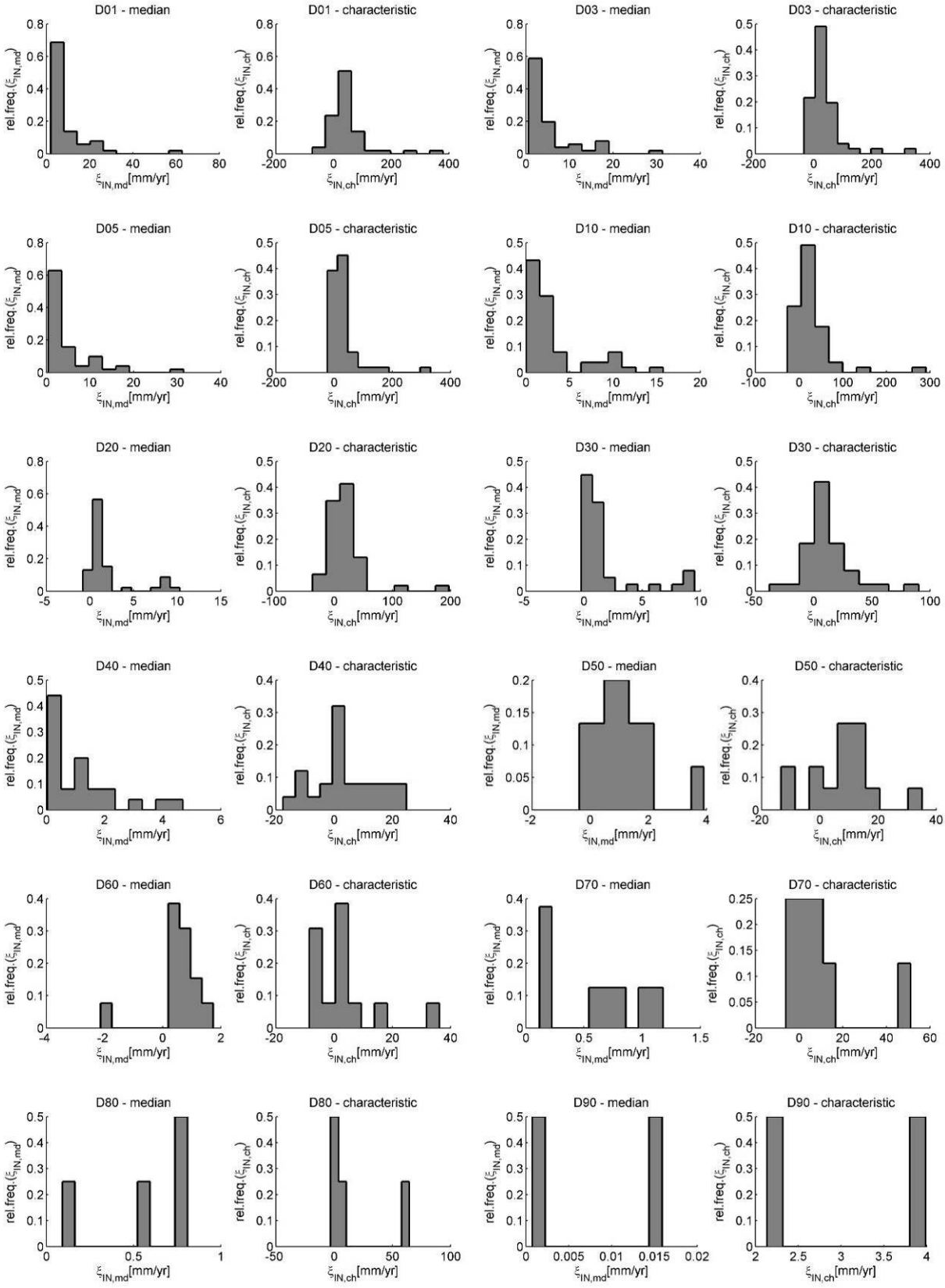

Figure 3.56. Relative frequency histograms of median and characteristic ξ_{IN} by reference depth for the aggregate estimates from all inclinometers.

As could be expected, a general decrease with depth is observed for both sample median and sample characteristic values. Significant decrease in sample statistics is noted between D10 and D20 and between D30 and D40. Sample ranges of characteristic values decrease rapidly with depth.

3.3.1.3 Gaussian modelling of inclinometer data

For the purpose of statistical characterization, it may be convenient to assess whether sets of ξ_{IN} were at least approximately Gaussian in terms of statistical distribution and, if the case, to model them as Gaussian random variables. The probability density function of a Gaussian distribution of a generic random variable x is given by:

$$f(x,\mu,\sigma)=\frac{1}{\sigma\sqrt{2\pi}}\exp\left[-\frac{(x-\mu)^2}{2\sigma^2}\right]$$

in which: μ and σ are the mean and standard deviation of the distribution, respectively.

Gaussian distributions were fitted to samples of ξ_{IN} at each inclinometer location by maximum likelihood estimation. A set of distribution statistics was extracted from each fit, namely: ξ_{05G}, ξ_{50G} and ξ_{95G}, corresponding to the 0.05, 0.50 and 0.95 quantiles of the cumulative Gaussian distribution with parameters μ and σ. Characteristic distribution values, defined as the maximum (in absolute value) between the 0.05 and 0.95 distribution quantiles, were retrieved. Figure 3.58 plots the ECDFs with superimposed fitted Gaussian distributions for inclinometer BA08. Lighter lines correspond to greater reference depths.

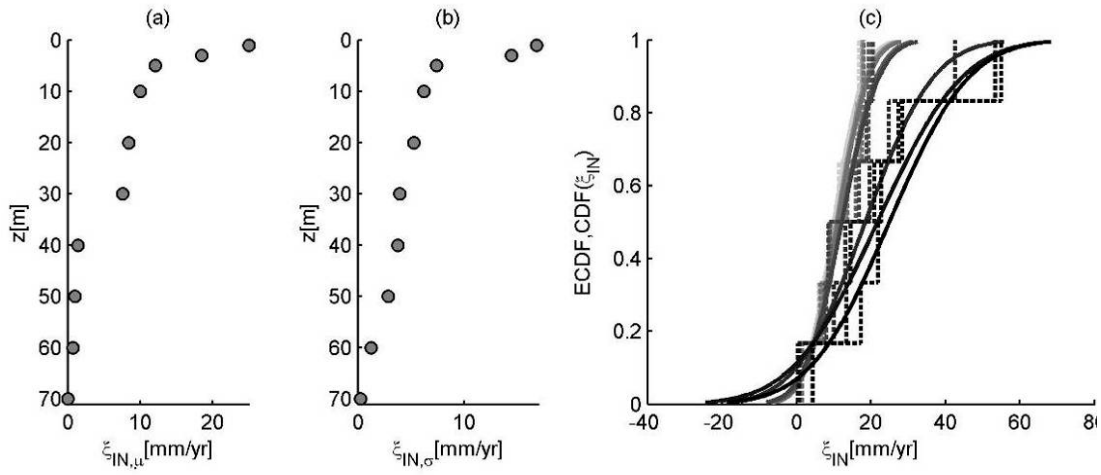

Figure 3.57. Parameters of fitted Gaussian distributions at reference depths D01, D03, D05, D10, D20, D30, D40, D50, D60 and D70 for inclinometer BA08: (a) mean; (b) standard deviation; (c) empirical and fitted Gaussian cumulative distributions

The goodness of the aforementioned maximum likelihood fitting was assessed at a 0.05 significance level, for each inclinometer, using the Anderson-Darling test (Anderson &

Darling, 1954). Such test has been shown to perform very well in comparison with other normality tests (Thode, 2002). Figure 3.59 plots the assessment of Gaussianity at 0.05 significance level of ξ_{IN} for all inclinometers at depth D01.

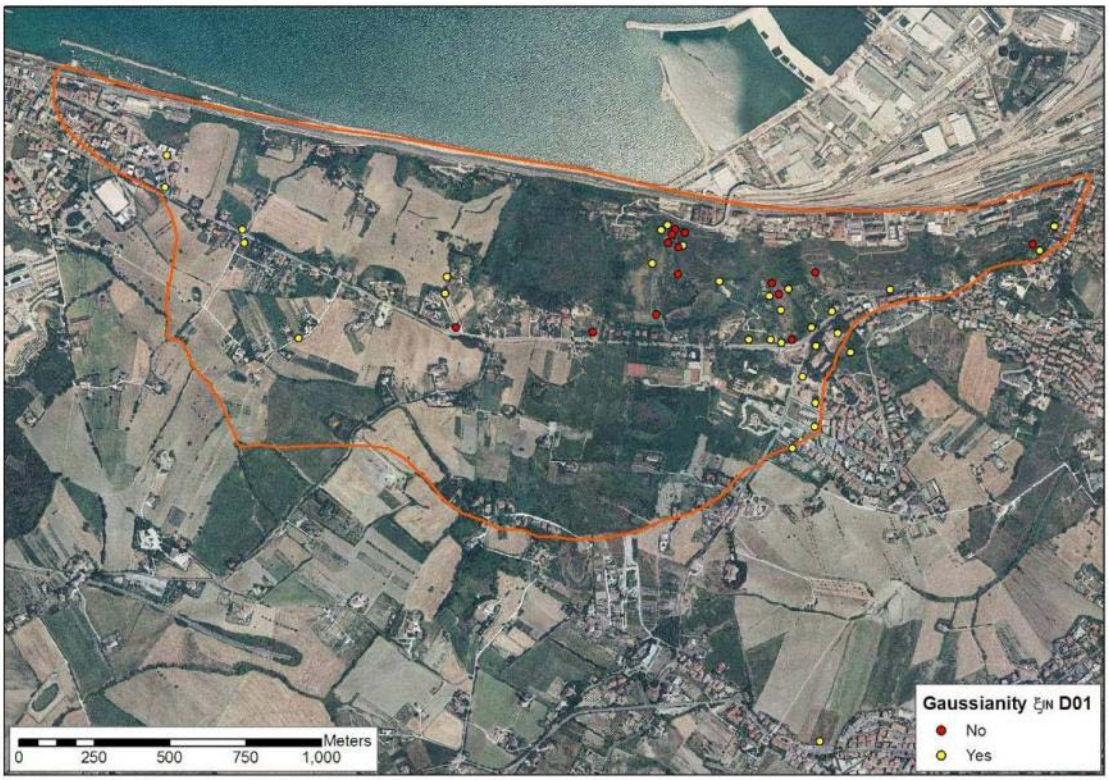

Figure 3.58. Assessment of Gaussianity of ξ_{IN} at reference depth D01

It is of interest to investigate further whether the approximation of empirical distributions by fitted Gaussian distributions is licit from an engineering perspective. Figure 3.60 plots the empirical cumulative distribution functions of the statistic $\Delta\xi_{SG}$ which equals the absolute values of the difference between the absolute values of sample median and sample characteristic quantiles and the corresponding quantiles from the fitted Gaussian distributions for all inclinometers at depth D01.

If the tolerability threshold for $\Delta\xi_{SG}$ is set at 10 mm.yr^{-1}, it may be seen in Figure 3.60 that such statistic satisfies the tolerability criterion (i.e. the difference between sample and Gaussian quantiles is less than 10 mm.yr^{-1}) for 86.1% and 38.7% of data for median and characteristic values of ξ_{IN}, respectively. The performance of Gaussian distributions in approximating sample values is deemed unsatisfactory. Hence, sample statistics of ξ_{IN} will be considered further in the analysis.

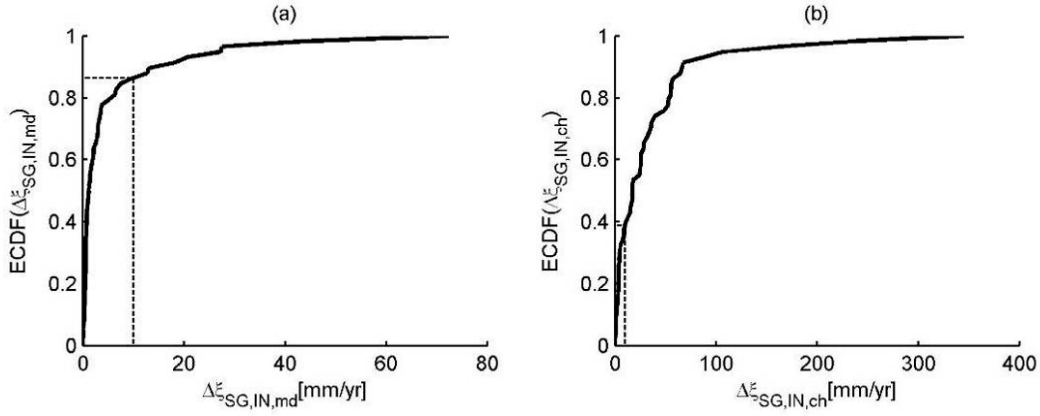

Figure 3.59. Empirical cumulative distribution functions of $\Delta\xi_{SG}$ for samples of ξ_{IN} from all inclinometers at depth D01 (median and characteristic quantiles).

3.3.1.4 Geostatistical interpolation of inclinometer data

In order to better characterize slope kinematics, it is useful to spatialize ξ_{IN} beyond the discrete set of pseudo-locations. RBFs were implemented to interpolate sample values throughout the landslide area. Figures 3.61 to 3.68 plot the RBF interpolations of median and characteristic ξ_{IN} inside the landslide perimeter at reference depths D01, D03, D05 and D10.

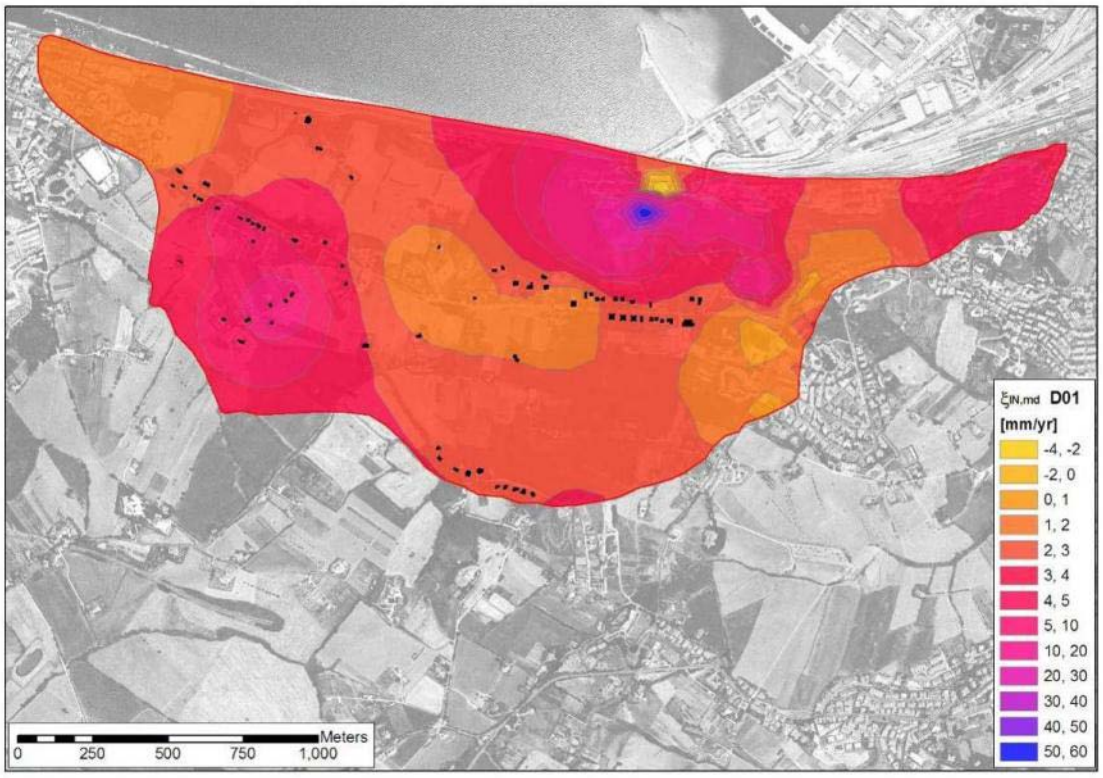

Figure 3.60. RBF interpolation of $\xi_{IN,md}$ at D01.

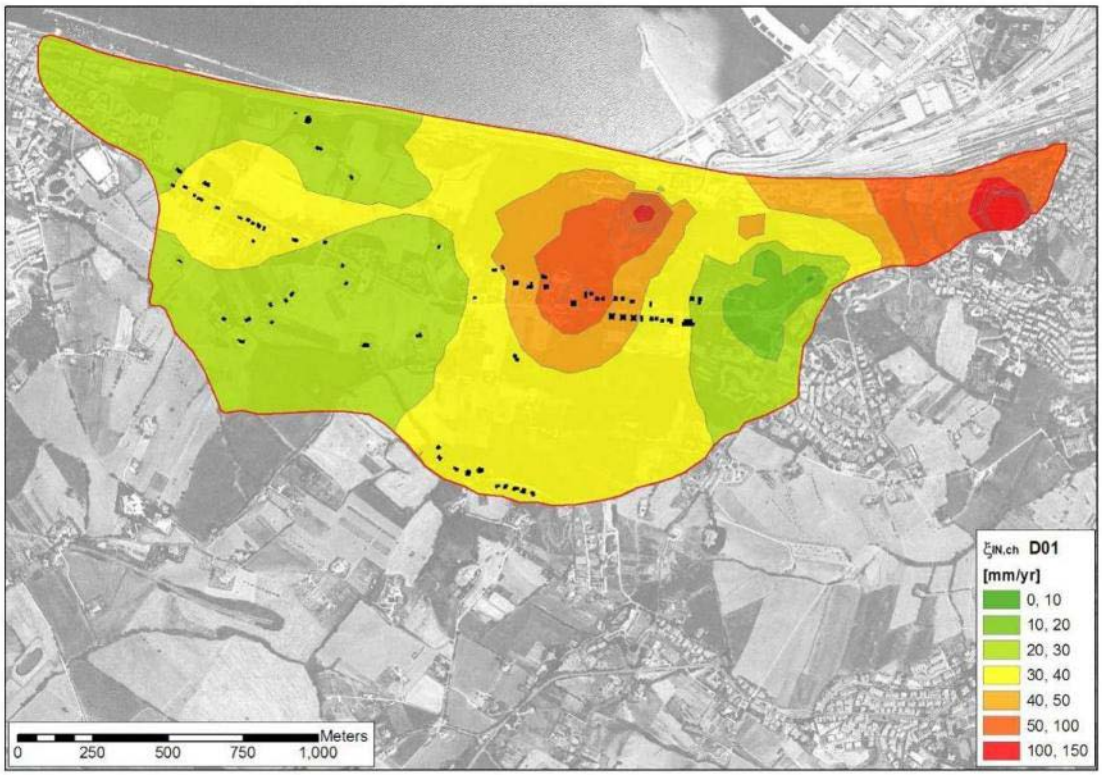

Figure 3.61. RBF interpolation of $\xi_{IN,ch}$ at D01

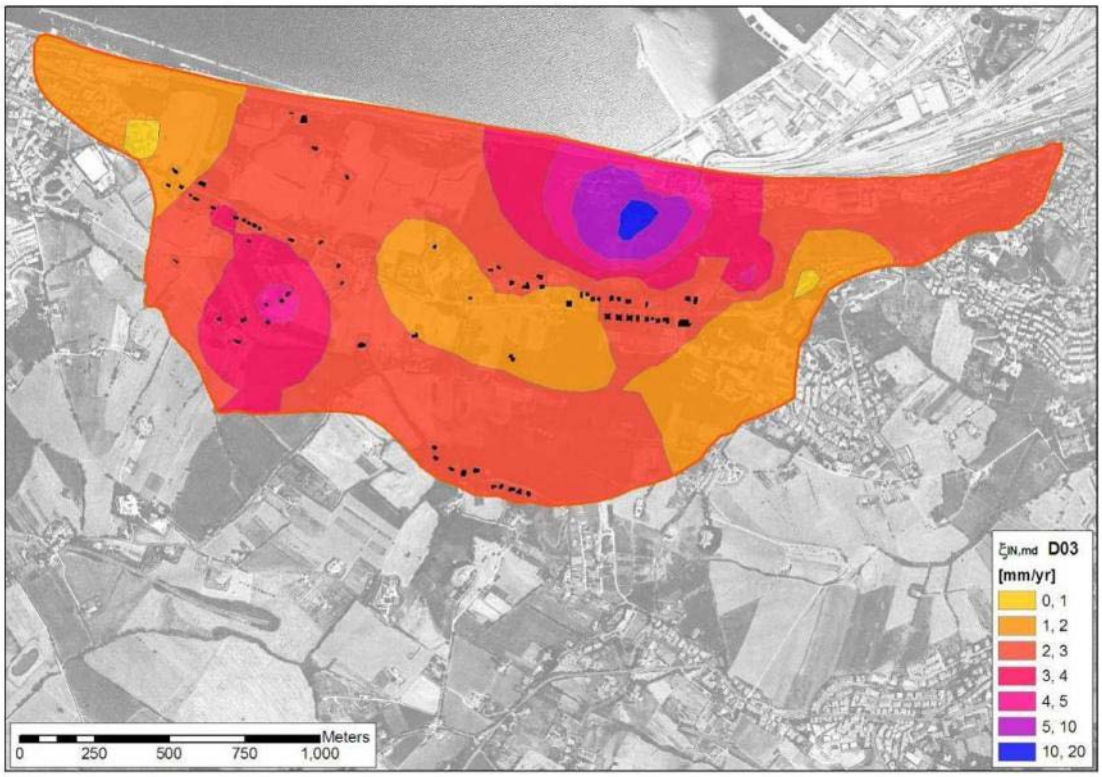

Figure 3.62. RBF interpolation of $\xi_{IN,md}$ at D03.

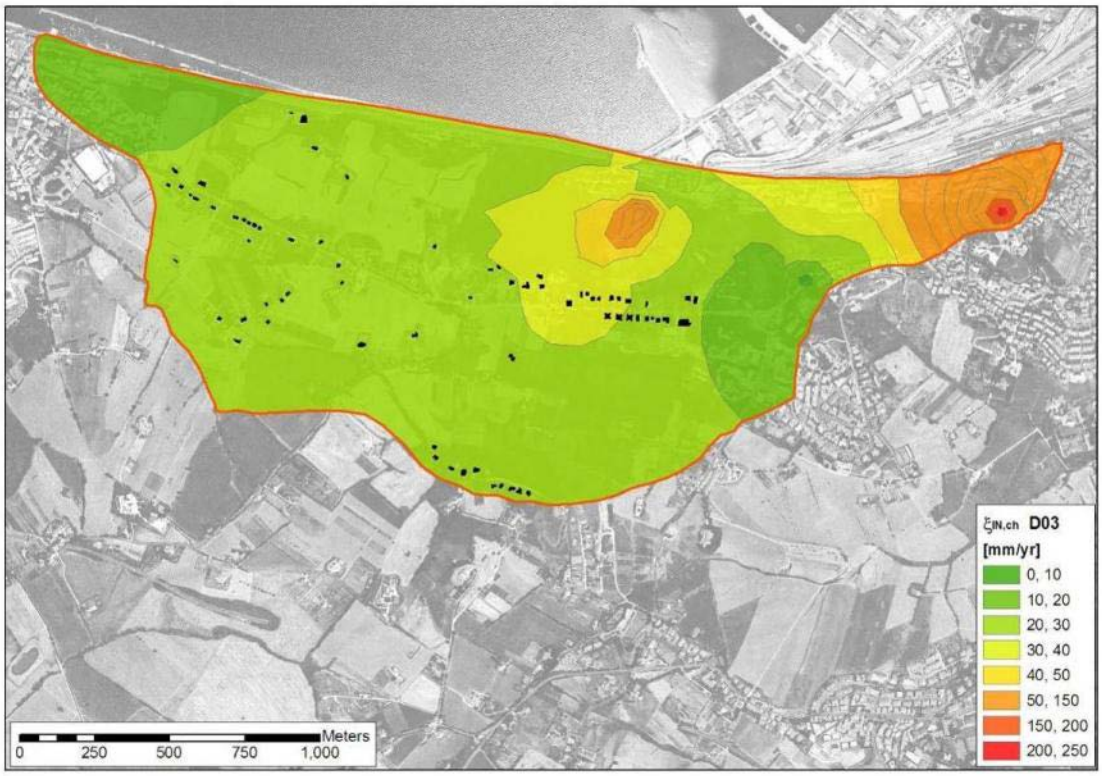

Figure 3.63. RBF interpolation of $\xi_{IN,ch}$ at D03.

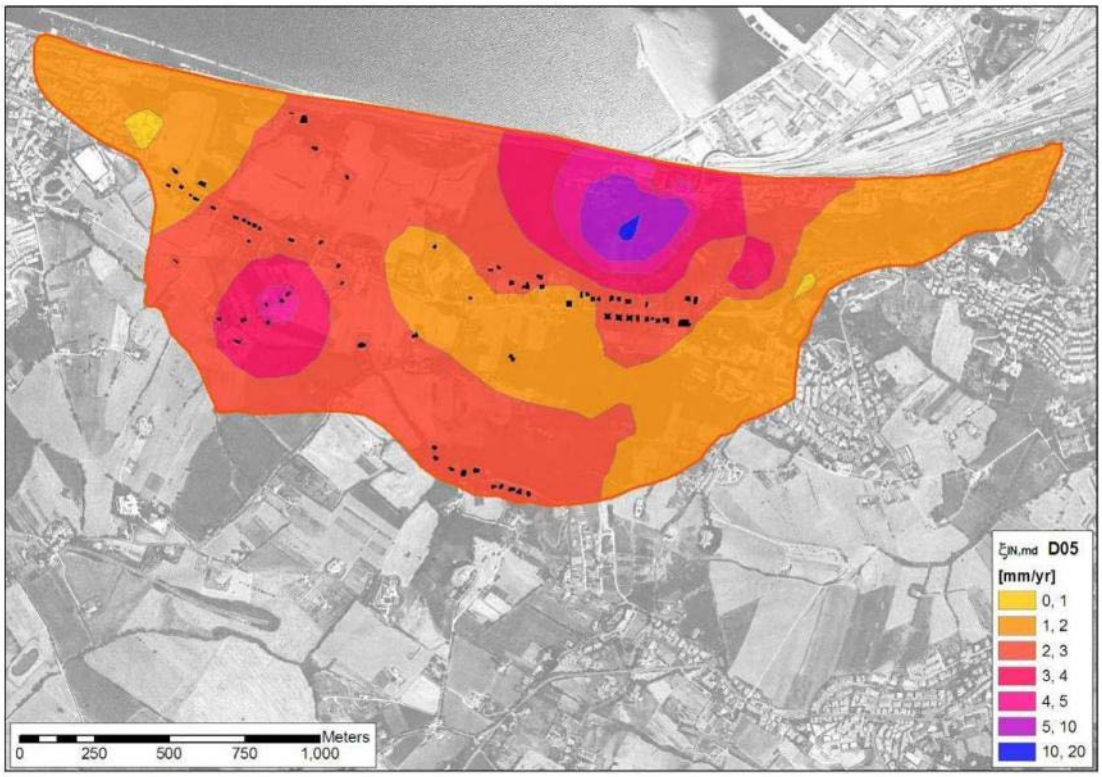

Figure 3.64. RBF interpolation of $\xi_{IN,md}$ at D05.

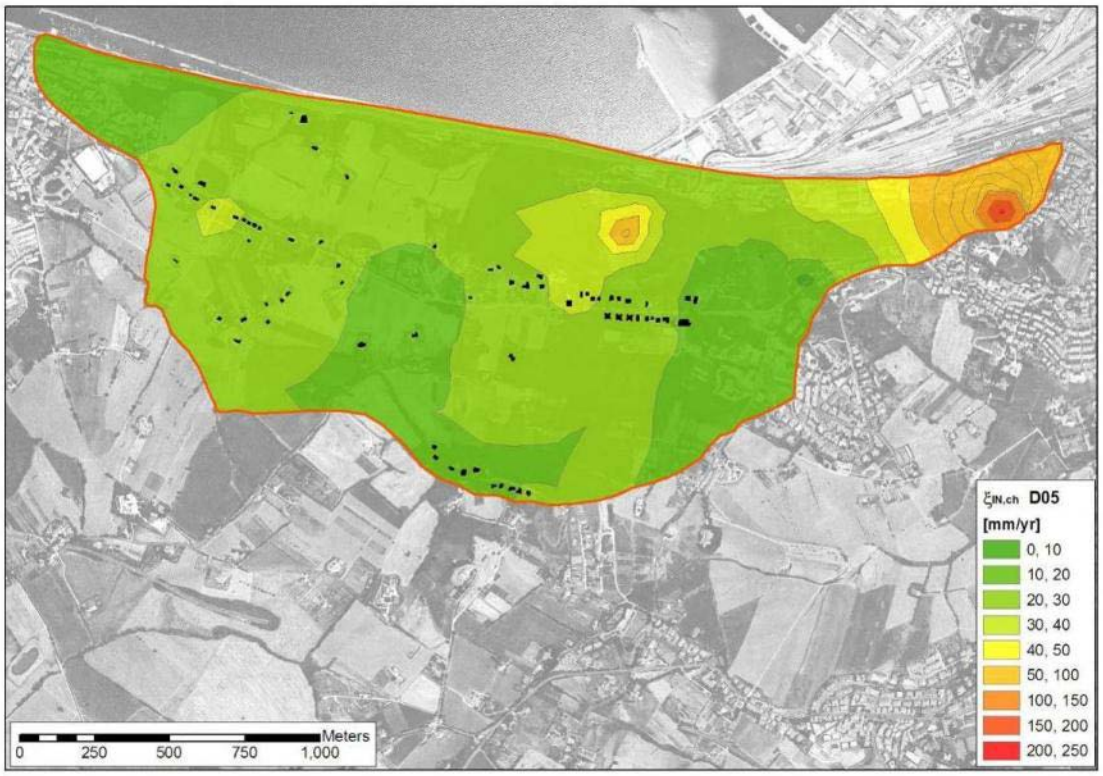

Figure 3.65. RBF interpolation of $\xi_{IN,ch}$ at D05.

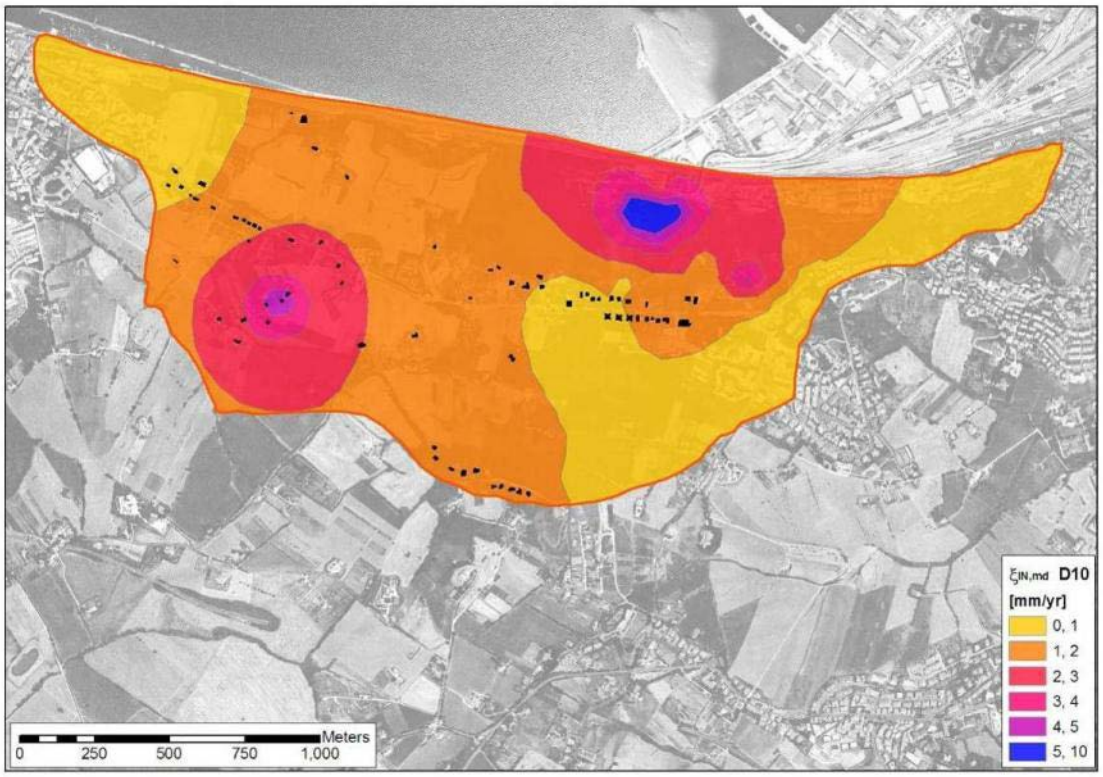

Figure 3.66.RBF interpolation of$\xi_{IN,md}$ at D10.

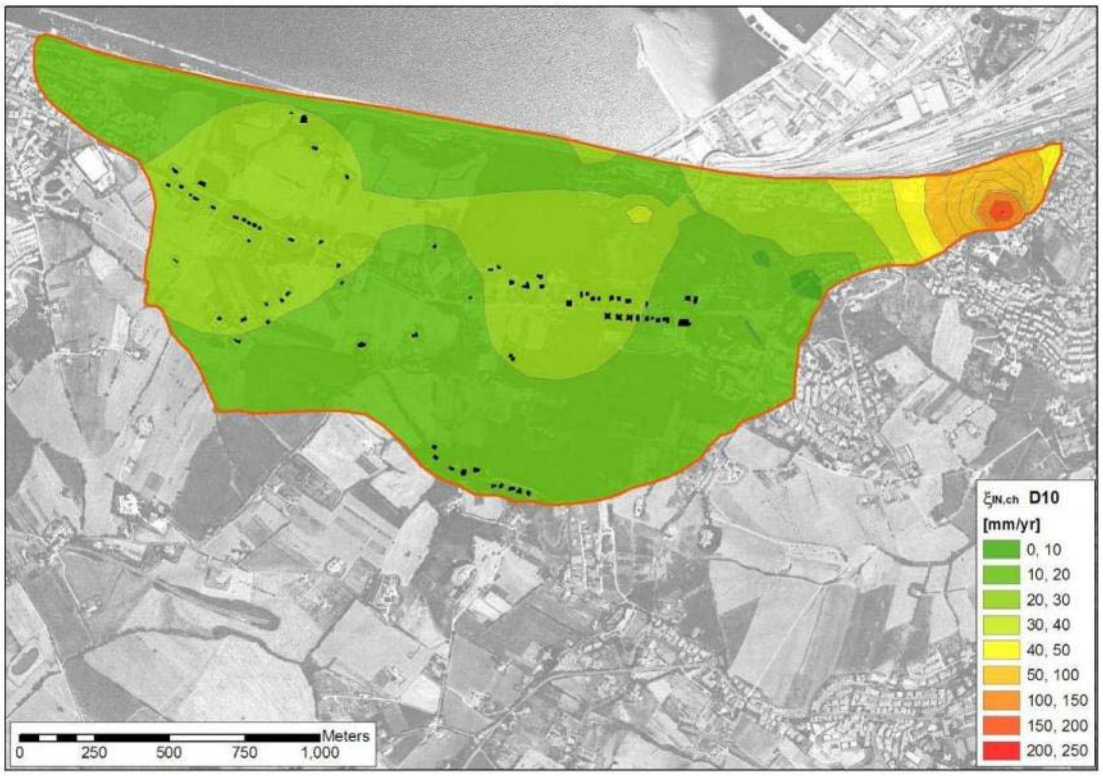

Figure 3.67. RBF interpolation of $\xi_{IN,ch}$ at D10.

3.3.2 Characterization of surficial kinematisms by radar interferometry

Interferometric Synthetic Aperture Radar (InSAR) is a remote-sensing tool capable of measuring small displacements of the earth's surface, across large areas. The PSInSAR technique (e.g. Tele-Rilevamento Europa, 2008) relies on long temporal series of SAR data of an area, acquired by the satellite on the same orbit, to filter out atmospheric artifacts. Multiple differential interferograms are generated from a set of radar scenes, and are subjected to numerical and statistical analyses from which a sub-set of image pixels, called Permanent Scatterers (PS), are identified. High precision measurements can be performed on PS because these are virtually unaffected by temporal and geometrical decorrelation. PS contain either natural objects, such as rock outcrops, man-made objects such as statues, lamp standards, heating and ventilating structures on the roofs of buildings, or specially fabricated reflectors. As anticipated, by the PSInSAR technique it is possible to measure displacements in the vertical and East-West directions, while it is not possible to measure displacements in the North-South direction. In the present study, PSInSAR data are analyzed to assess, both qualitatively and quantitatively, surficial kinematisms in the vertical and East-West directions.

3.3.2.1 Calculation of vertical and East-West displacements

Two data sets of satellite images were available for each satellite; the first acquired during the satellite's descending orbit and the second, during the ascending orbit. For the Ancona site, PSInSAR data from satellites ERS-1 and ERS-2 of the European Space Agency (ESA) were available for 42 ascending readings (from 1992-08-23 to 2000-12-

13) and 66 descending readings (from 1992-06-11 to 2000-12-10); data from ENVISAT were available for 36 ascending readings (from 2003-02-26 to 2008-10-22) and 28 descending readings (from 2002-12-15 to 2008-11-23).

The relationship between the measured ascending and descending displacements (D_{asc} and D_{des}, respectively) and the "real" vertical and East-West displacements (D_{VT} and D_{EW}, respectively) are given by the trigonometric expressions

$$D_{asc} = D_{VT} \cos \vartheta_{asc} + D_{EW} \sin \vartheta_{asc}$$

$$D_{des} = D_{VT} \cos \vartheta_{des} + D_{EW} \sin \vartheta_{des}$$

in which: θ_{asc} and θ_{des} are the direction cosines of the ascending and descending satellite orbits, respectively.

The above mentioned equations can be reorganized in terms of vertical and East-West displacements as follows:

$$D_{VT} = \frac{D_{asc} \sin \vartheta_{des} - D_{des} \sin \vartheta_{asc}}{\sin \vartheta_{des} \cos \vartheta_{asc} - \sin \vartheta_{asc} \cos \vartheta_{des}}$$

$$D_{EW} = \frac{D_{des} \cos \vartheta_{asc} - D_{asc} \cos \vartheta_{des}}{\sin \vartheta_{des} \cos \vartheta_{asc} - \sin \vartheta_{asc} \cos \vartheta_{des}}$$

For both ERS and ENVISAT, the direction cosines were θ_{asc}=-23° (ascending) and θ_{des}=+23° (descending), respectively. Positive values of D_{VT} indicate uplifts while negative values indicate settlements; positive values of D_{EW} indicate an eastward movement, while negative values indicate a westward movement. These conventions are also valid for calculated velocities. The area of analysis was restricted to the 500 meter-wide buffer offsetting the landslide perimeter given by Cotecchia (2006). A total of 6406 (3811 ascending; 2595 descending) and 6575 (2638 ascending; 3937 descending) Permanent Scatterers were available for ERS and ENVISAT, respectively.

As Permanent Scatterers pertaining to the ascending orbit generally do not correspond to those pertaining to the descending orbit, it is necessary to establish a criterion for merging D_{asc} and D_{des} measurements from distinct Permanent Scatterers and for geo-referencing the resulting values of D_{VT} and D_{EW}. If ascending and descending measurements pertain to spatial locations which are geographically distant, or to readings which are chronologically too distant, results are not likely to be correct or meaningful. As a geographic criterion, couples of conjugate Permanent Scatterers were identified on the basis of a Euclidean distance criterion, the latter being calculated from the available N and E coordinates of the ascending and descending Permanent Scatterers. A maximum distance of 10 m was established. Pseudo-locations were calculated as geographic midpoints of the segment connecting the conjugate ascending and descending Permanent Scatterers.

In a temporal perspective, the maximum acceptable lag between ascending and descending measurement dates was set at 50 days. Pseudo-dates were calculated as average dates between the conjugate dates of ascending and descending measurements.

By the above criteria, a total of 1318 and 1182 pseudo-locations were generated for ERS and ENVISAT, respectively. The associated number of pseudo-dates (and calculated VT and EW velocity components) was 131 for ERS and 58 for ENV.

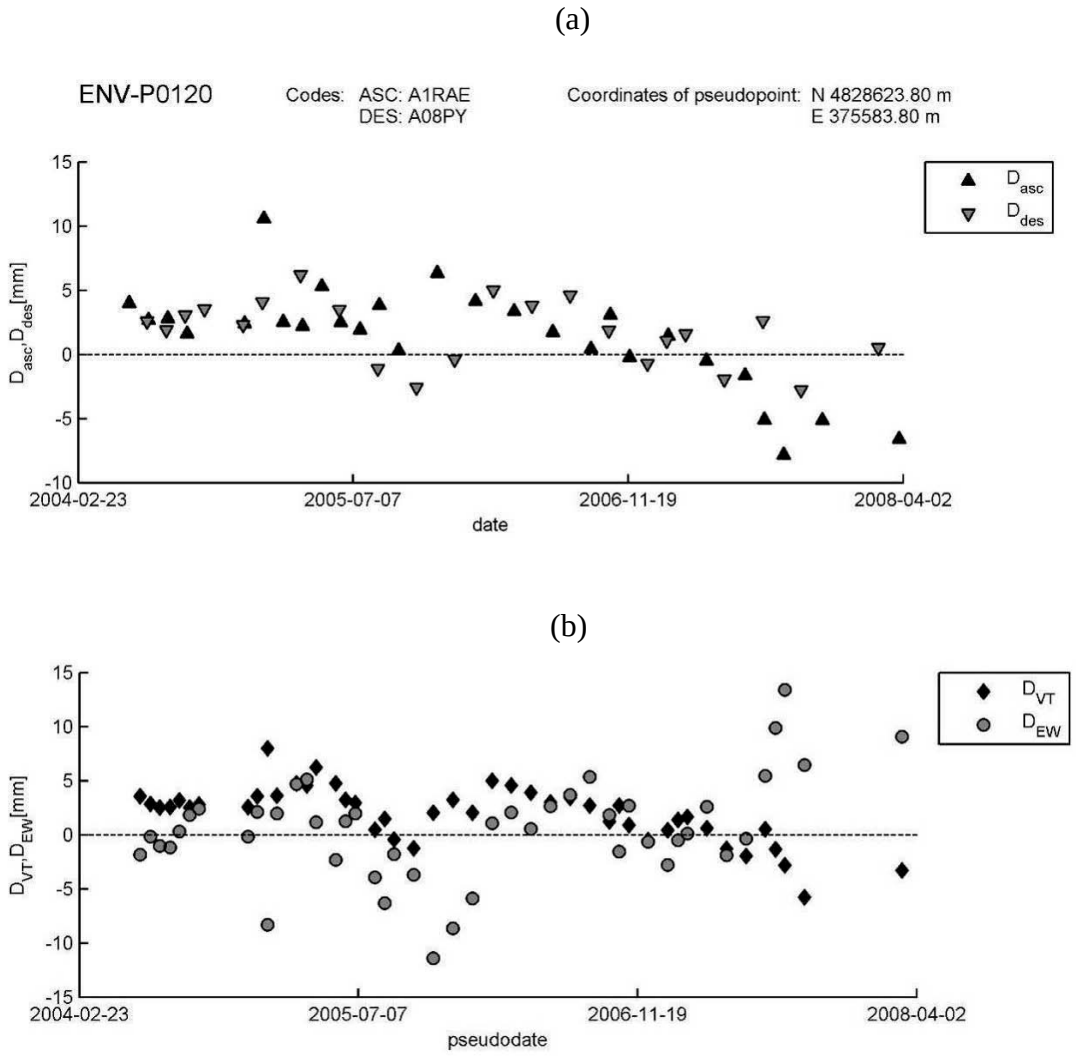

Figure 3.68. Example calculation of vertical and East-West displacements at pseudo-location ENV-P0120.

Figure 3.69 illustrates an example calculation of VT and EW displacements from the ENVISAT dataset. Subplot (a) shows the chronological sequences of ascending and descending measurements D_{asc} and D_{des} taken in distinct dates for the pair of conjugate Permanent Scatterers 'A1RAE' (ascending) and 'A08PY' (descending); subplot (b) plots the resulting NS and EW displacements at the median pseudo-location ENV-PO120. It should be noted that (a) pseudo-dates generally do not coincide with effective reading dates; and (b) one ascending measurement can be associated with more than one descending measurement (or vice versa), as long as the temporal lag does not exceed the present threshold. Hence, a large number of pseudo-dates is identified in comparison with the effective dates of ascending and descending readings.

Average daily VT and EW velocities between consecutive pseudo-dates were calculated by dividing the differential displacements by the time interval between pseudo-dates.

Subsequently, velocities were expressed on a yearly basis by multiplication by 365. The latter parameters, indicated by ξ_{VT} and ξ_{EW} were thus taken as reference parameters for the characterization of slope kinematisms as will be discussed in the following. Figure 3.70 illustrates an example output chrono-plot of ξ_{VT} and ξ_{EW} at pseudo-location ENV-P0120.

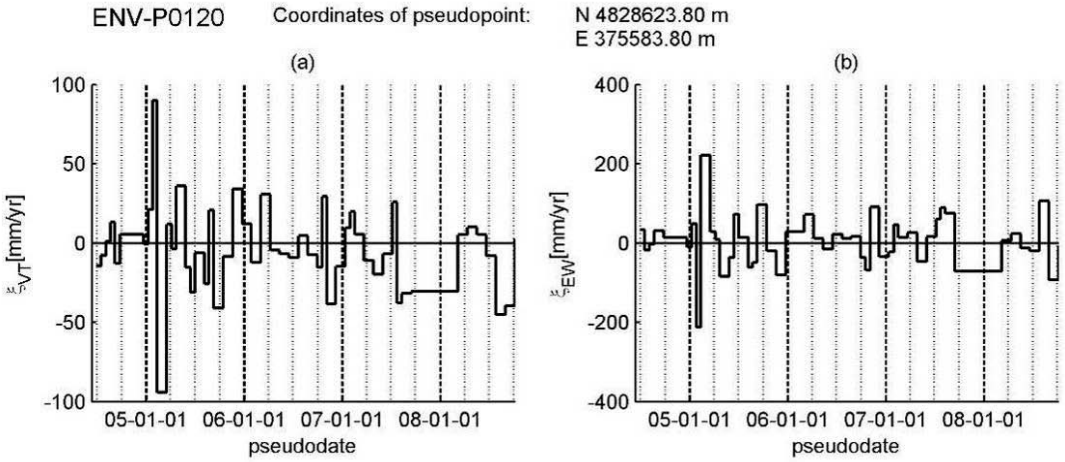

Figure 3.69. Chrono-plot of ξ_{VT} and ξ_{EW} at pseudo-location ENV-P0120.

3.3.2.2 Statistical modeling of PSInSAR data

ECDFs were calculated for samples of VT and EW velocity components from the ERS and ENV data sets at each pseudo-location. An example of cumulative distribution functions for ξ_{VT} and ξ_{EW} is shown in Figure 3.71 for the pseudo-location ENV-P0120. Sample median and characteristic values were retrieved for ξ_{VT} and ξ_{EW} for both ERS and ENV data.

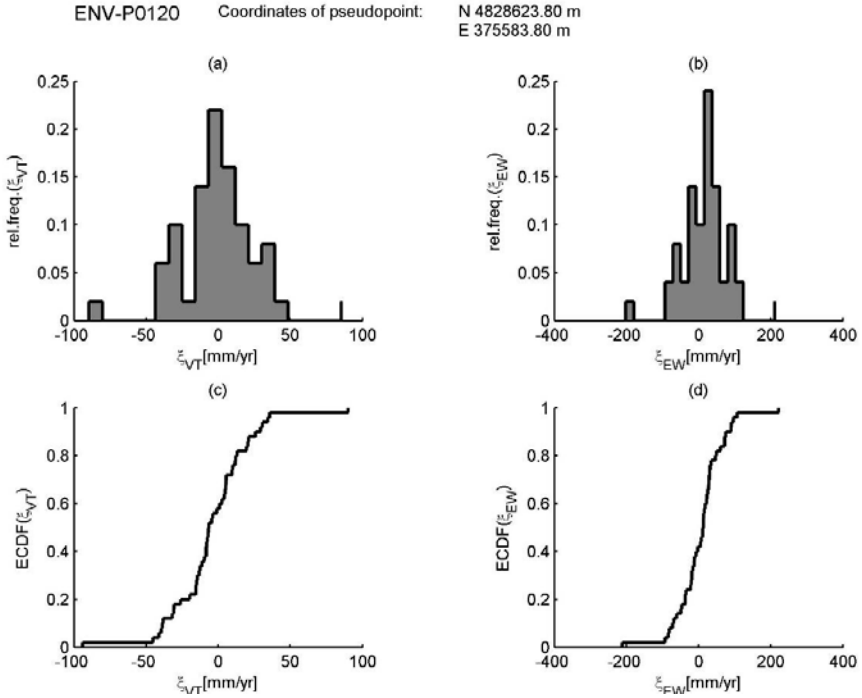

Figure 3.70. Empirical cumulative distribution functions of ξ_{VT} and ξ_{EW} for pseudo-location ENV-P0120

3.3.2.3 Geostatistical interpolation of PSInSAR data

Radial basis functions (RBF) were implemented to interpolate sample median and characteristic values throughout the landslide area. Figures 3.72 to 3.79 plot the RBF interpolations of median and characteristic values of ξ_{VT} and ξ_{EW}, calculated from ERS and ENV data.

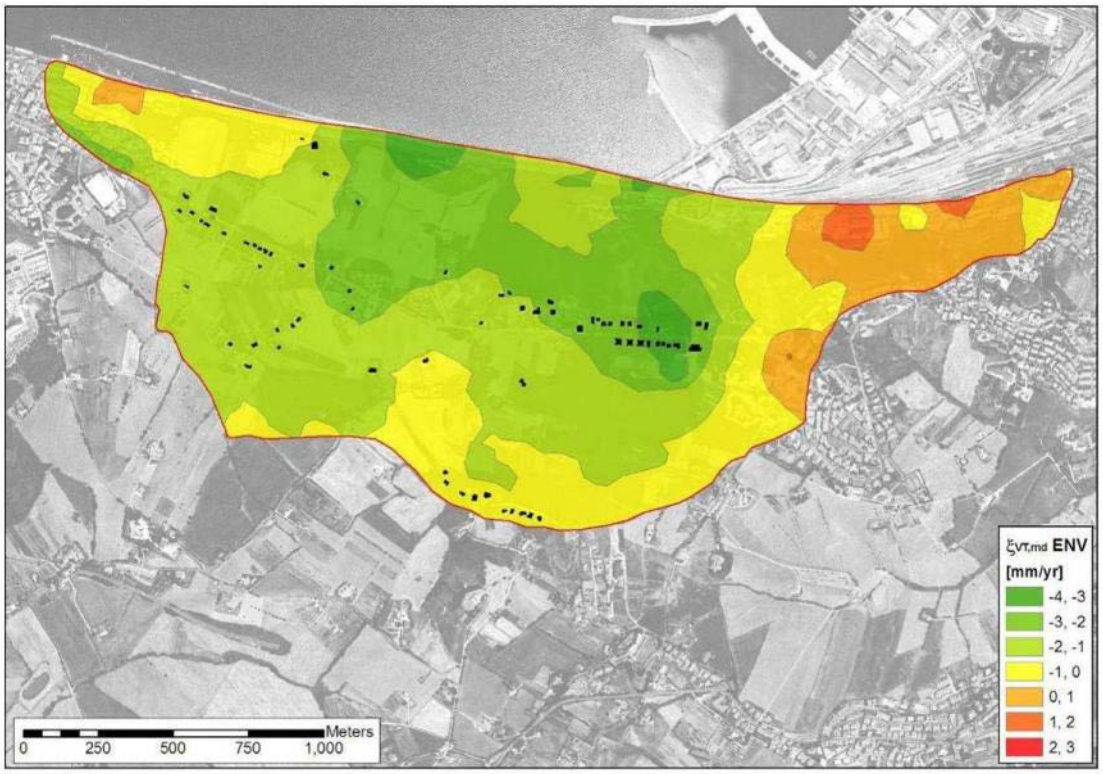

Figure 3.71. RBF interpolations of $\xi_{VT,md}$ from ERS data.

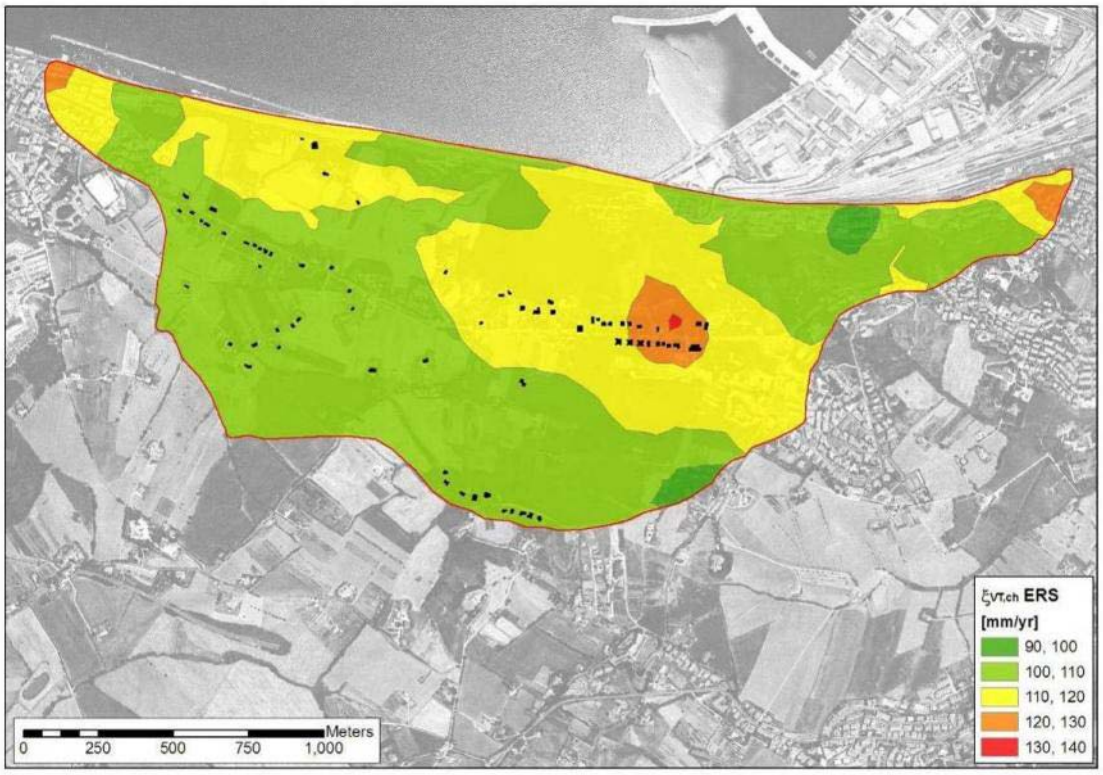

Figure 3.72. RBF interpolations of $\xi_{VT,ch}$ from ERS data.

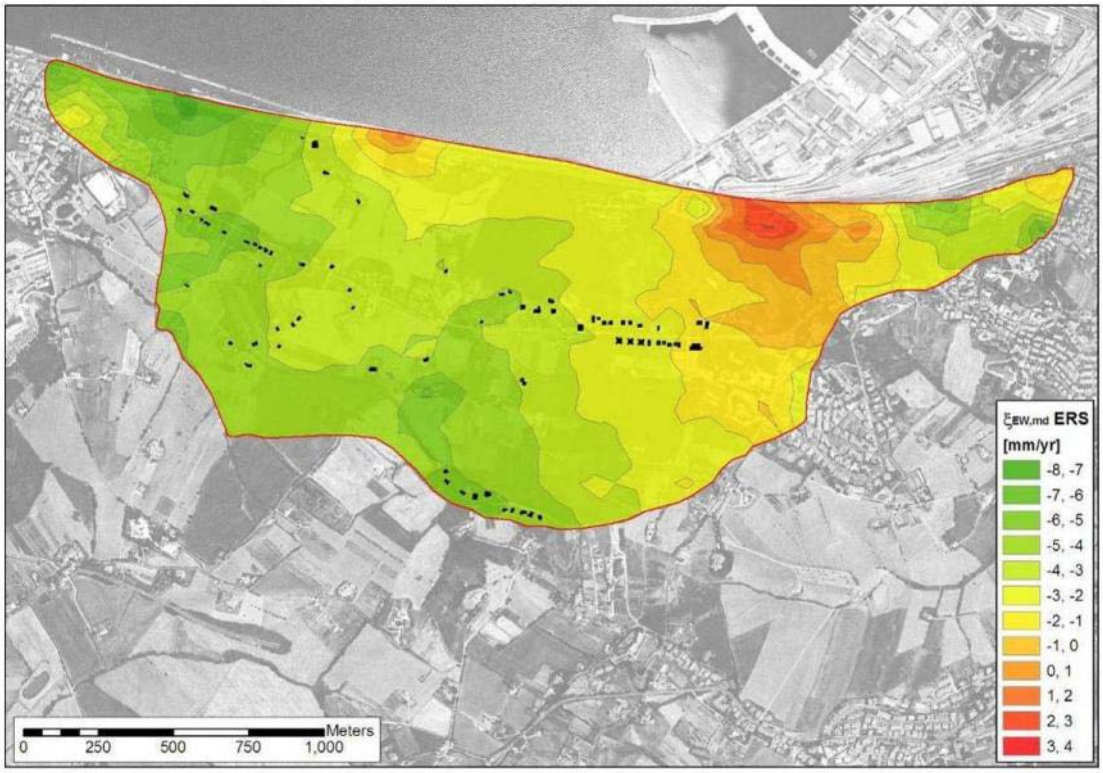

Figure 3.73. RBF interpolations of $\xi_{EW,md}$ from ERS data.

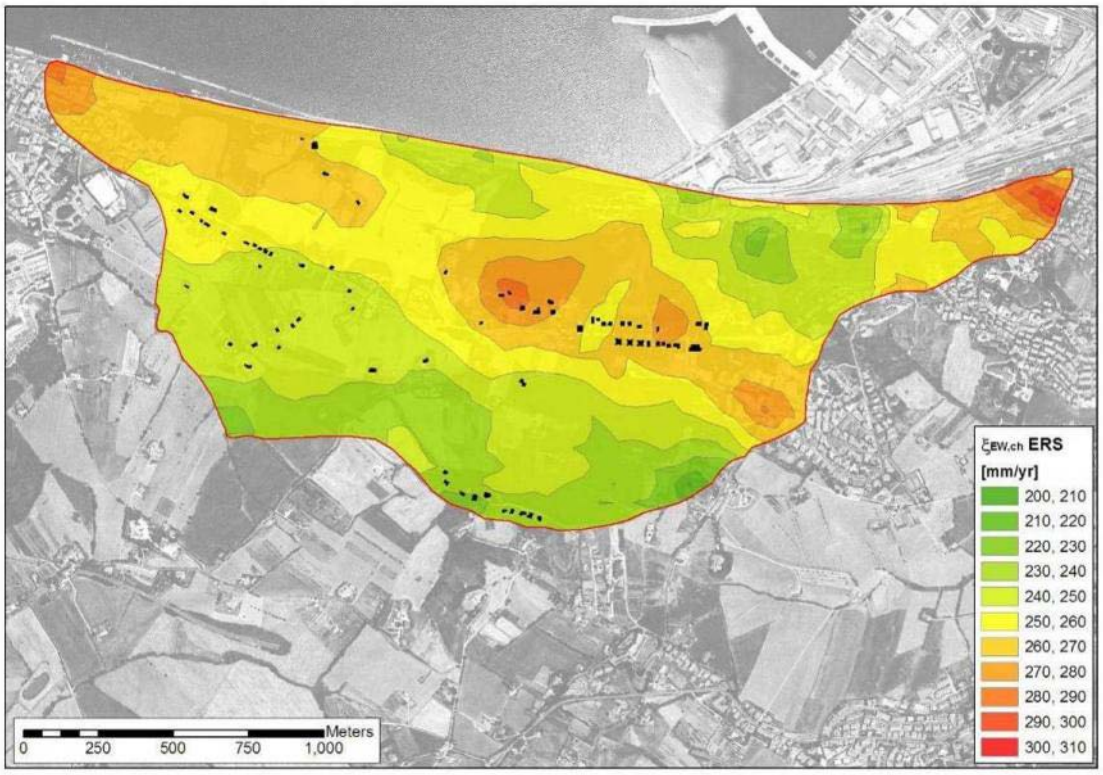

Figure 3.74. RBF interpolations of $\xi_{EW,ch}$ from ERS data.

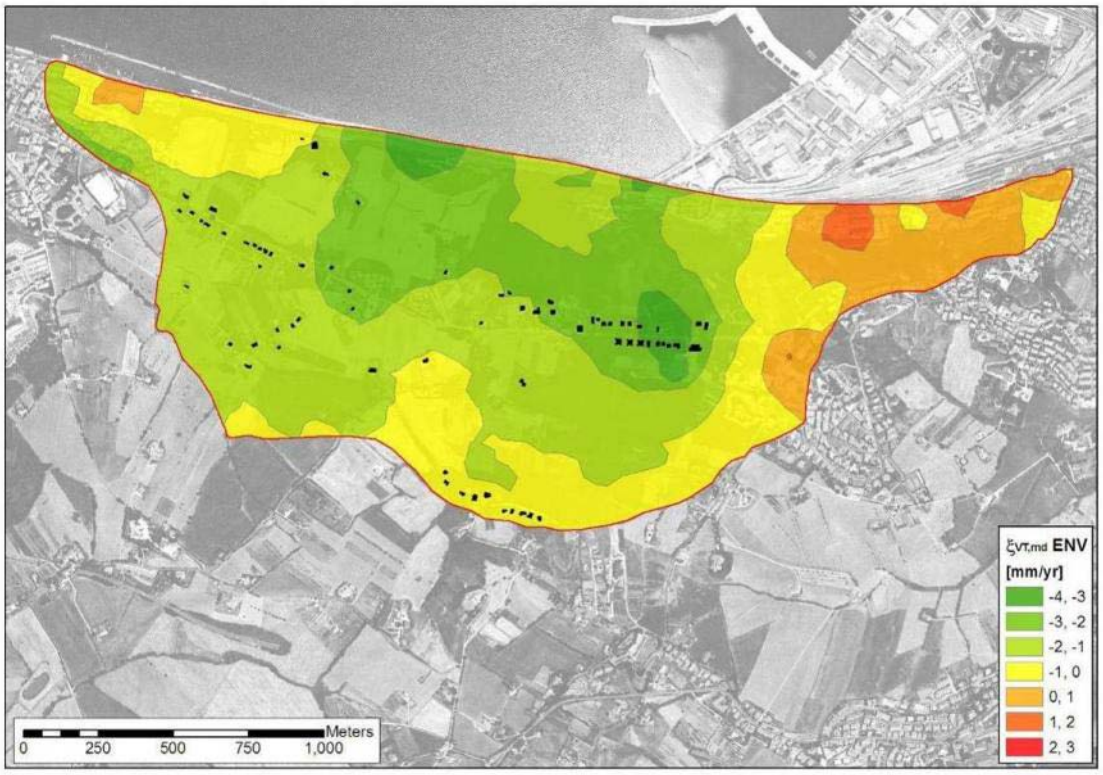

Figure 3.75. RBF interpolations of $\xi_{VT,md}$ from ENV data.

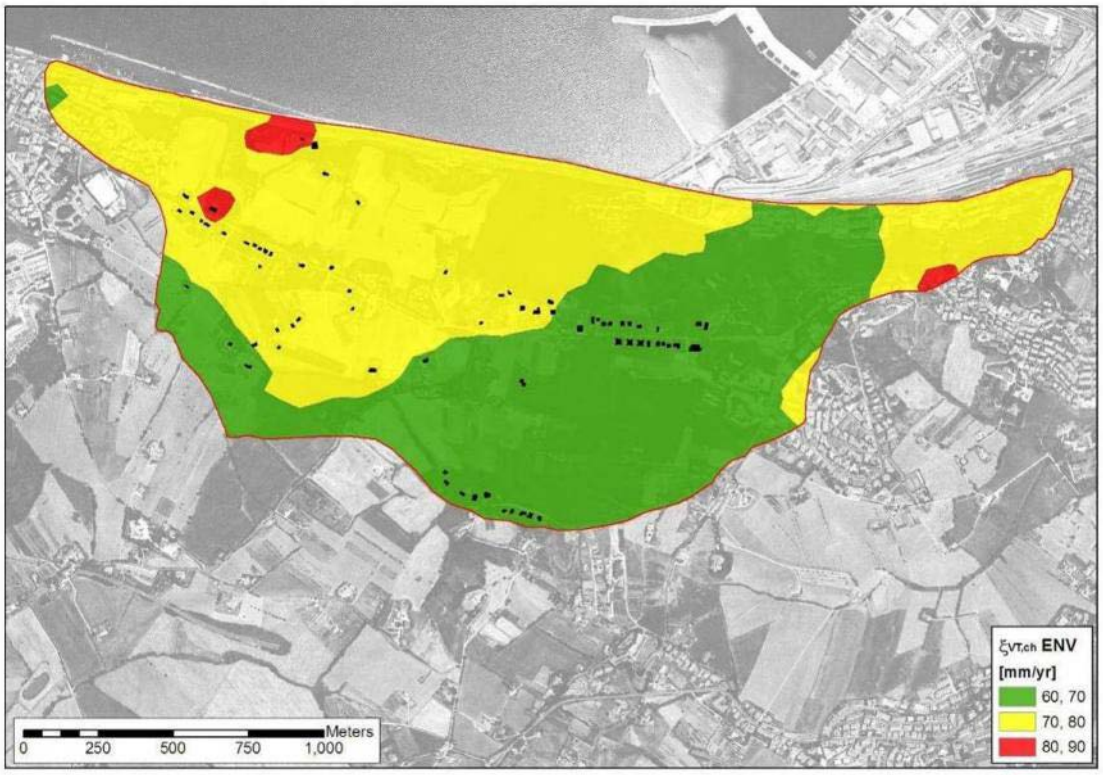

Figure 3.76. RBF interpolations of $\xi_{VT,ch}$ from ENV data.

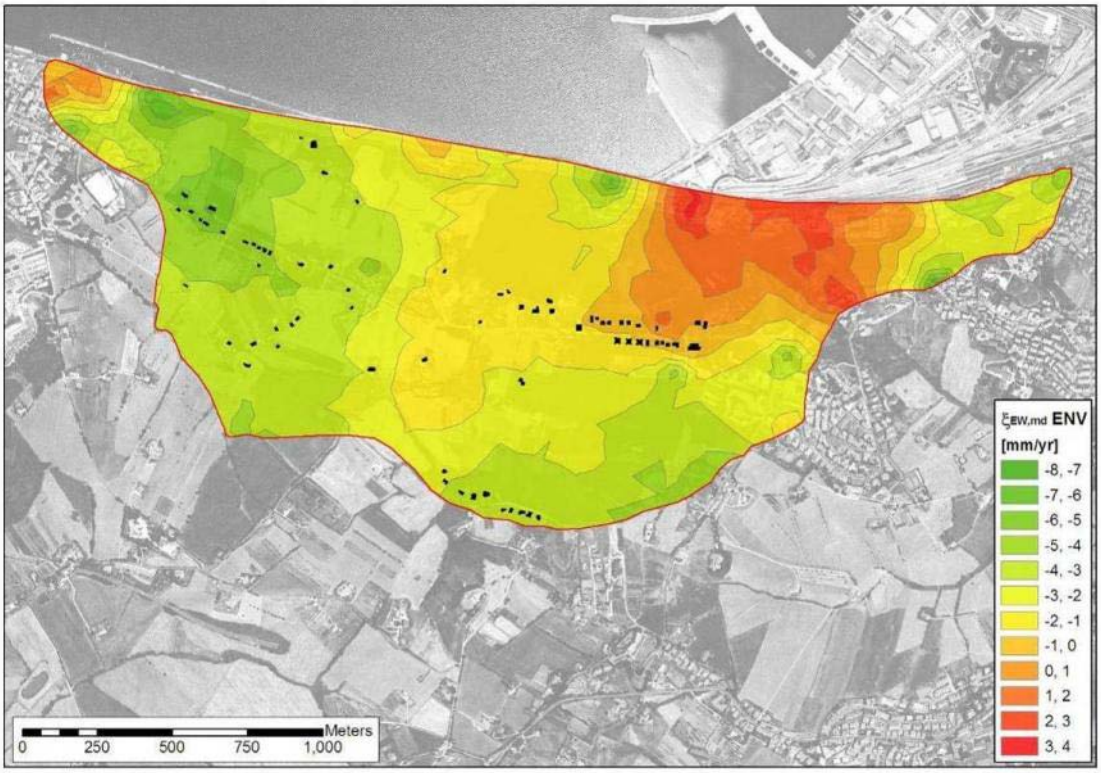

Figure 3.77. RBF interpolations of $\xi_{EW,md}$ from ENV data.

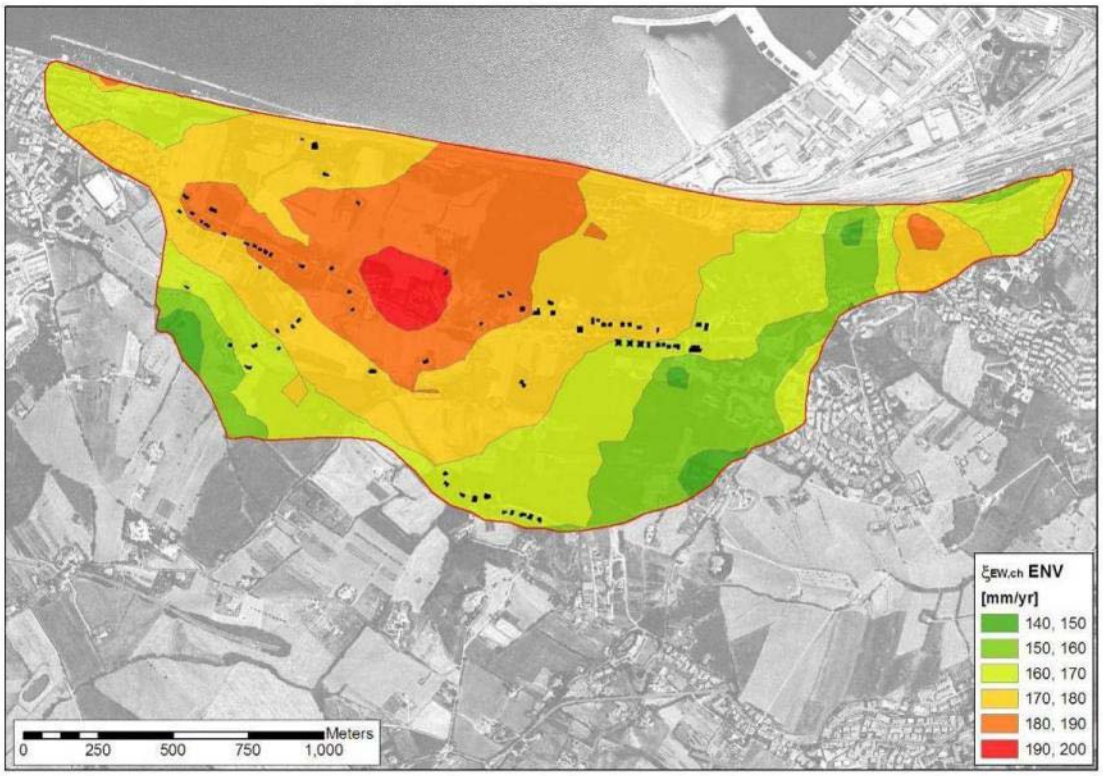

Figure 3.78. RBF interpolations of $\xi_{EW,ch}$ from ENV data.

3.3.2.4 Comparison of ERS and ENVISAT PSInSAR data

The significant differences in ξ_{VT} and ξ_{EW} highlighted by geostatistical interpolation of ERS and ENV data suggest a closer investigation into the relevance of the data for the assessment of current slope kinematics.

ERS data were acquired in the period 1992-2000, i.e. before the remediation and consolidation works, while ENV data refer to the post-remediation period (2002-2008). Cotecchia (2006) attributed the decrease in the magnitudes of monitoring displacement readings from 2001 to present to the activation of the drainage system which was constructed between 1999 and 2000. According to Cotecchia (2006), the implementation of the mitigation measure significantly increased slope stability. The piezometric level inside the landslide area was lowered by "up to some 10 m"; consequently, both shallow and deep-seated sliding kinematisms were greatly reduced. Figure 3.80 plots comparatively the relative frequency histograms of median and characteristic values of ξ_{VT} and ξ_{EW} calculated from ERS and ENV data at the respective sets of pseudo-locations.

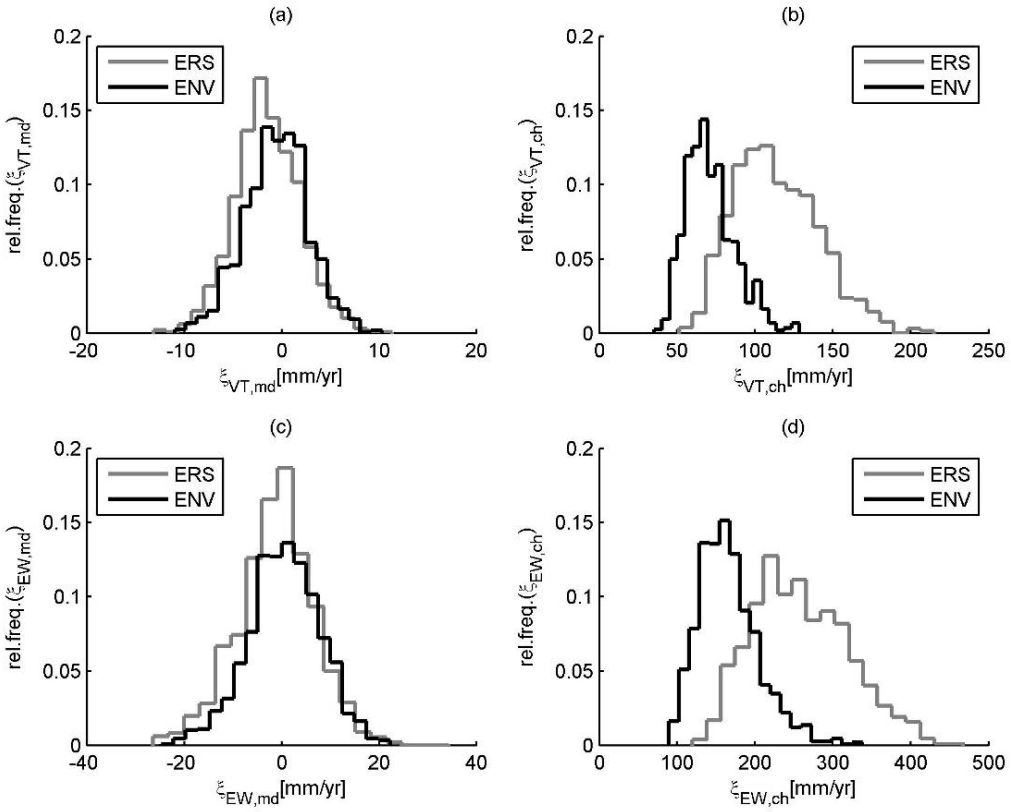

Figure 3.79. Relative frequency histograms of median and characteristic sample values of ξ_{VT} and ξ_{EW}: comparison between ERS and ENV data

Figure 3.80 shows that median values of ξ_{VT} and ξ_{EW} are fairly coincident (relative frequency histograms are approximately superimposed). However, characteristic values of ERS data display considerably larger values than ENV data, indicating the occurrence of more significant "extreme" events in the ERS measurement period. This observation could be related to the effects of the remediation works.

Since the two data sets are not jointly compatible from a quantitative perspective if extreme quantiles are of interest, and since they refer to distinct geotechnical conditions (pre- and post-mitigation, respectively), it is necessary to establish which data set should be referred to for the purpose of meaningful risk estimation. The higher magnitude of ERS statistics with respect to corresponding ENV statistics would suggest the use of the former for sake of conservatism. However, based on the geotechnical reasoning by Cotecchia (2006), it appears that the implementation of slope stabilization measures resulted in an effective change in slope kinematics. The data collected during the pre-implementation period appears to be less than congruent with the present-day scenario. Moreover, available inclinometer measurements range from 2002 to present. Thus, ERS data cannot be examined jointly with inclinometer data. On the basis of the above, ERS data was deemed not representative of current slope behavior, and was thus not used for the forward estimation of specific risk.

3.3.2.5 Gaussian modelling of PSInSAR data

As for inclinometer data, Gaussian distributions were fitted to samples of ξ_{VT} and ξ_{EW} at each pseudo-location by maximum likelihood estimation. A set of distribution statistics was extracted from each fit, namely: $\xi_{IN,05G}$, $\xi_{IN,50G}$ and $\xi_{IN,95G}$, corresponding to the 0.05, 0.50 and 0.95 quantiles of the cumulative Gaussian distribution with parameters μ and σ. Characteristic distribution values, defined as the maximum (in absolute value) between the 0.05 and 0.95 distribution quantiles, were retrieved. An example fit of Gaussian distributions to ECDFs for pseudo-location ENV-P0120 is shown in Figure 3.81.

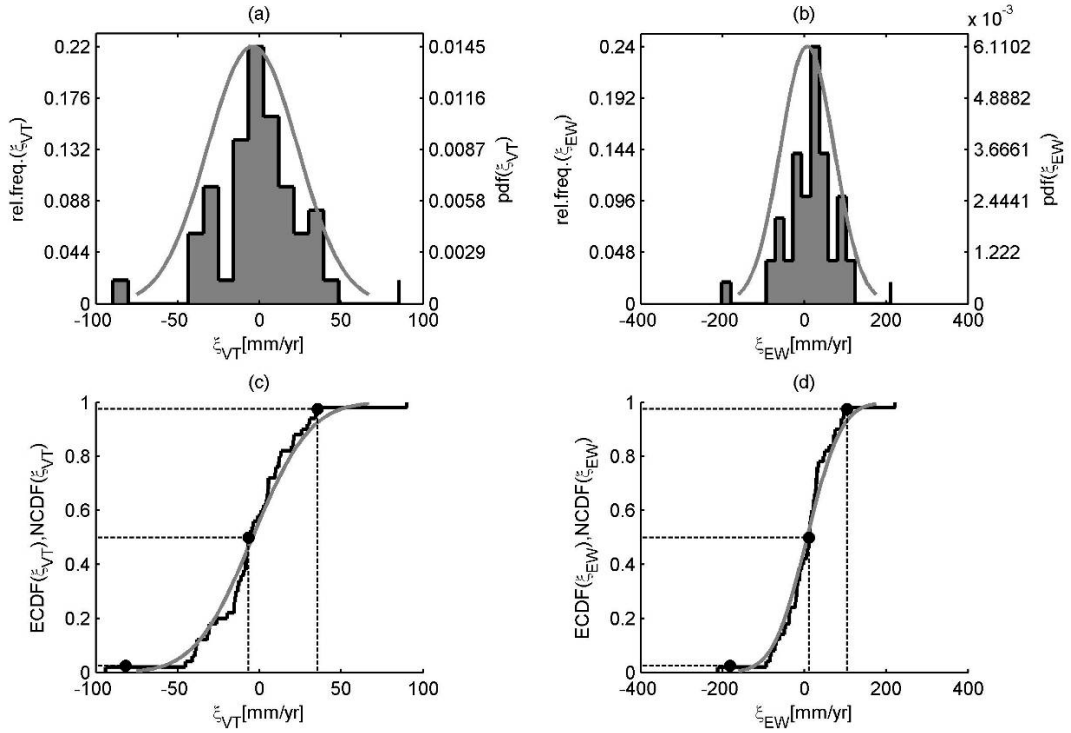

Figure 3.80. Empirical cumulative distribution function of VT and EW velocity for pseudo-location ENV-P0120, and fitted Gaussian distributions

The goodness of fit was assessed at a 0.05 significance level, for each pseudo-location, using the Anderson-Darling test. Out of 1182 ENV pseudo-locations, 1023 samples of ξ_{VT} and 1007 samples of ξ_{EW} were found to be Gaussian at the 0.05 significance level, respectively. These correspond to 86.5% and 85.1% of data sets, respectively. Figures 3.82 and 3.83 plot the assessment of Gaussianity at 0.05 significance level of ξ_{VT} and ξ_{EW} for all ENV pseudo-locations, respectively.

As for inclinometer data, it is of interest to investigate further whether the approximation of empirical distributions by fitted Gaussian distributions is licit from an engineering perspective. Figure 3.84 plots the empirical cumulative distribution functions (from data at pseudo-locations) of the statistic $\Delta\xi_{SG}$ which equals the absolute values of the difference between the absolute values of sample median and sample characteristic quantiles and the corresponding quantiles from the fitted Gaussian distribution in the VT and EW directions.

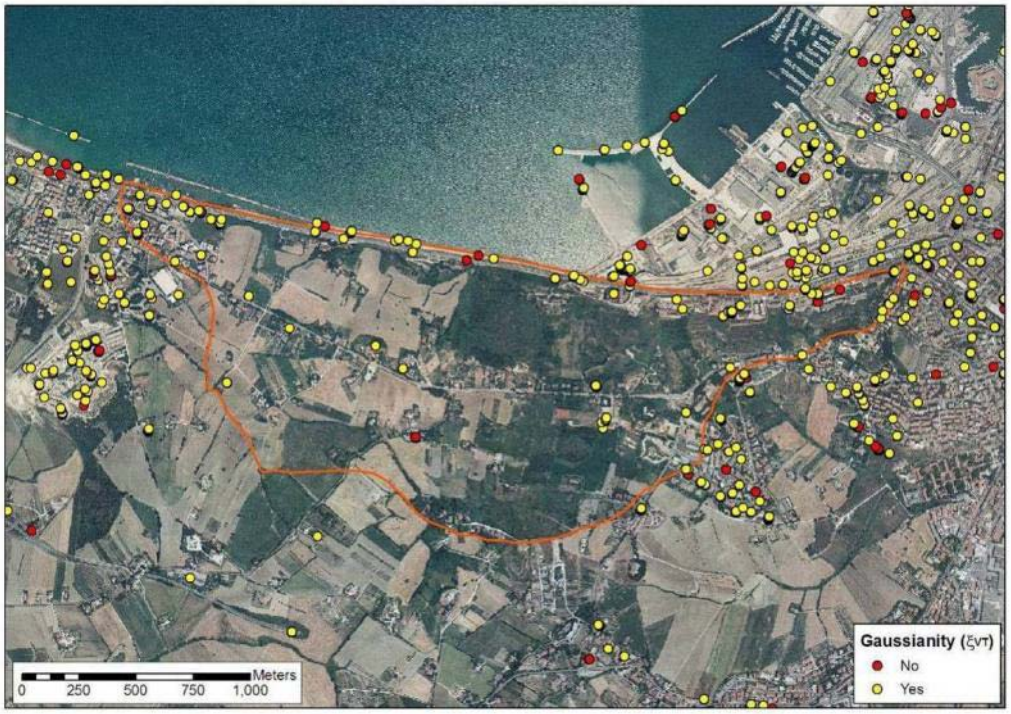

Figure 3.81. Assessment of Gaussianity at the 0.05 significance level of ξ_{VT}.

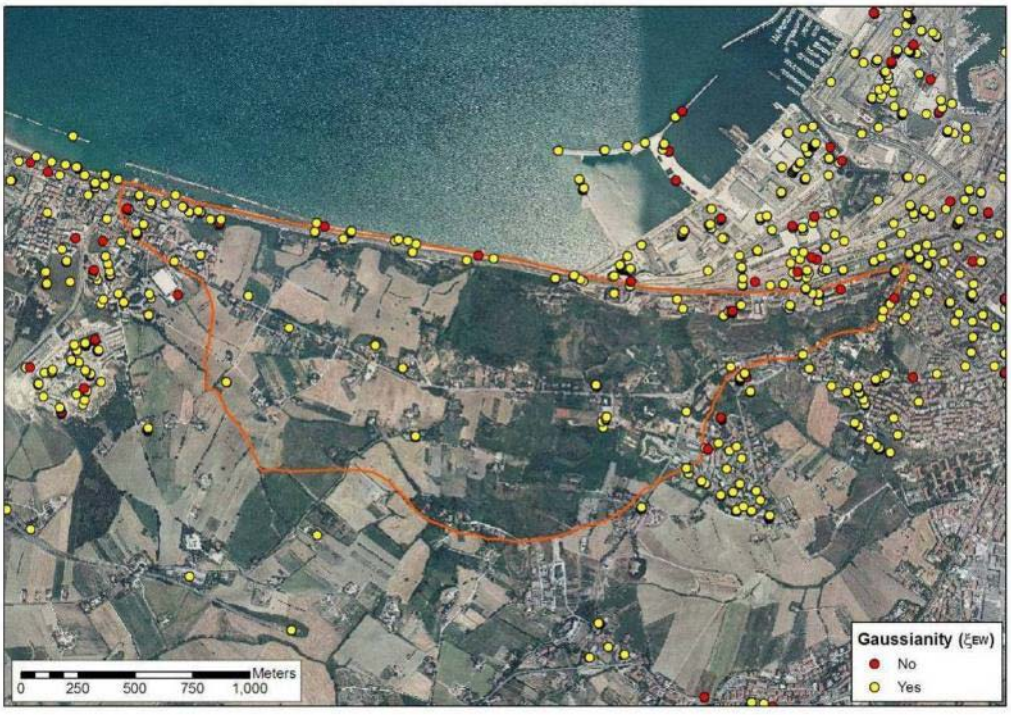

Figure 3.82. Assessment of Gaussianity at the 0.05 significance level of ξ_{EW}.

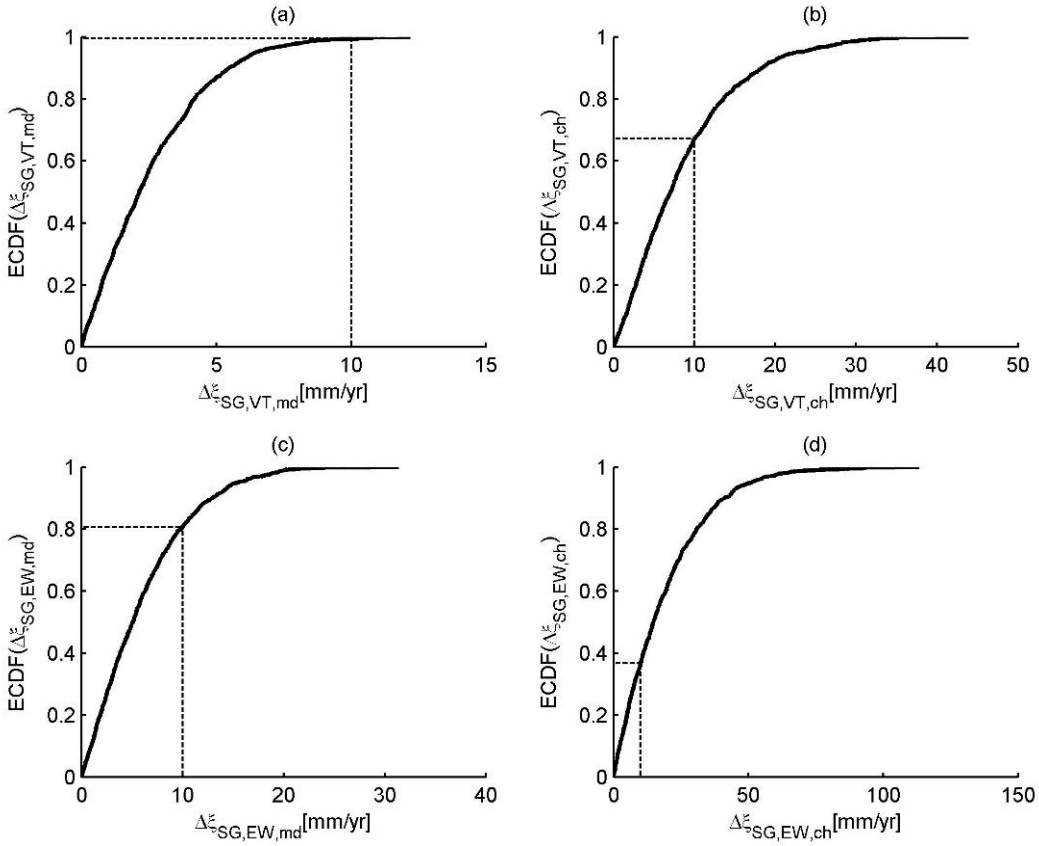

Figure 3.83. Empirical cumulative distribution functions of $\Delta\xi_{SG}$ for samples of ξ_{VT} and ξ_{EW} calculated at ENV pseudo-locations (median and characteristic quantiles)

If the tolerability threshold for $\Delta\xi_{SG}$ is once again set at 10 mm.yr^{-1}, it may be seen in Figure 3.84 that such statistic satisfies the tolerability criterion (i.e. the difference between sample and Gaussian quantiles is less than 10 mm.yr^{-1}) in 99.5% and 80.5% of pseudo-locations for median values of ξ_{VT} and ξ_{EW}, respectively. For characteristic values, the corresponding percentages are 67.2 and 36.7, respectively. With the exception of the median-VT case, the performance of Gaussian distributions in approximating sample values is deemed unsatisfactory. Hence, as for inclinometer data, sample statistics (medians, 0.05 quantiles, 0.95 quantiles and sample characteristic values) of ξ_{VT} and ξ_{EW} are deemed more significant for quantitative analyses.

3.3.3 Assessment of slope kinematics

Inclinometer and PSInSAR observations clearly and consistently show that slope deformation processes are still active, both at shallow and greater depths. Shallow kinematics are significantly greater than deep-seated kinematics. Analysis of vertical kinematic measurements suggests the presence of uplifts at the toe of the slope (along the coast) and settlements in the middle and upper areas of the landslide body. This rotational-type failure is associated with a kinematics by which a South-to-North translation is present in most parts of the landslide area. Lateral rotational-translational kinematics are also identified, both in the Eastern and Western parts of the landslide area (in the Rupe della Palombella/Posatora and Torrette districts, respectively). Such

lateral kinematics are rotationally oriented towards the center of the landslide body, with a West-to-East direction in the eastern part and an East-to West direction in the western part. Rotation-induced uplift movements are evident at the Eastern and Western limits of the landslide area. While highest median values are observed in the Eastern section of "Via della Grotta", the magnitude of characteristic values is especially large in the Rupe della Palombella/ Posatora district and in the "Strada del Carmine" in the South-Western part of the landslide body. The above observations are fully compatible with the description given by Cotecchia (2006) of the Ancona landslide as a "complex, three-dimensional rotational-translational" landslide.

In a quantitative perspective, there is generally a good agreement between inclinometer and PSInSAR observations for median values. PSInSAR characteristic values of East-West velocities often display larger magnitudes than inclinometer-derived velocities. These differences may be explained at least by the following reasons. First, PSInSAR measurements are not always representative of the ground kinematics, since Permanent Scatterers are often man-made objects which movements may depend at least partly on their structural and material properties as well as atmospheric conditions, and may not be significantly related to those of the underlying ground. Second, PSInSAR measurements are (in the most favorable case) taken at ground surface, where surficial kinematics, which may be negligible in the context of risk estimation for buildings, may occur. Third, the calculations of inclinometer-based velocity (ξ_{IN}) and PSInSAR velocities (ξ_{VT} and ξ_{EW}) refer to different conditions in terms of measurement interval (generally 3 months for inclinometer data; one month for PSInSAR data). The higher resolution of Interferometric measurements may include seasonal fluctuations which are not observable in processed inclinometer data, and which reflect statistically in higher extreme quantiles.

For the purpose of the present study, i.e. the estimation of specific risk for buildings, inclinometer data are deemed more meaningful as: (1) they allow the parameterization of landslide kinematics in the North-South direction, which is known to be the principal sliding direction; and (2) they refer to depths at which the interaction between sliding masses and building foundations are relevant to the triggering and development of damage mechanisms.

3.4 ESTIMATION OF SPECIFIC RISK

This section details the quantitative estimation of specific risk for the set of 60 existing buildings located inside the landslide perimeter as shown in Figure 3.85.

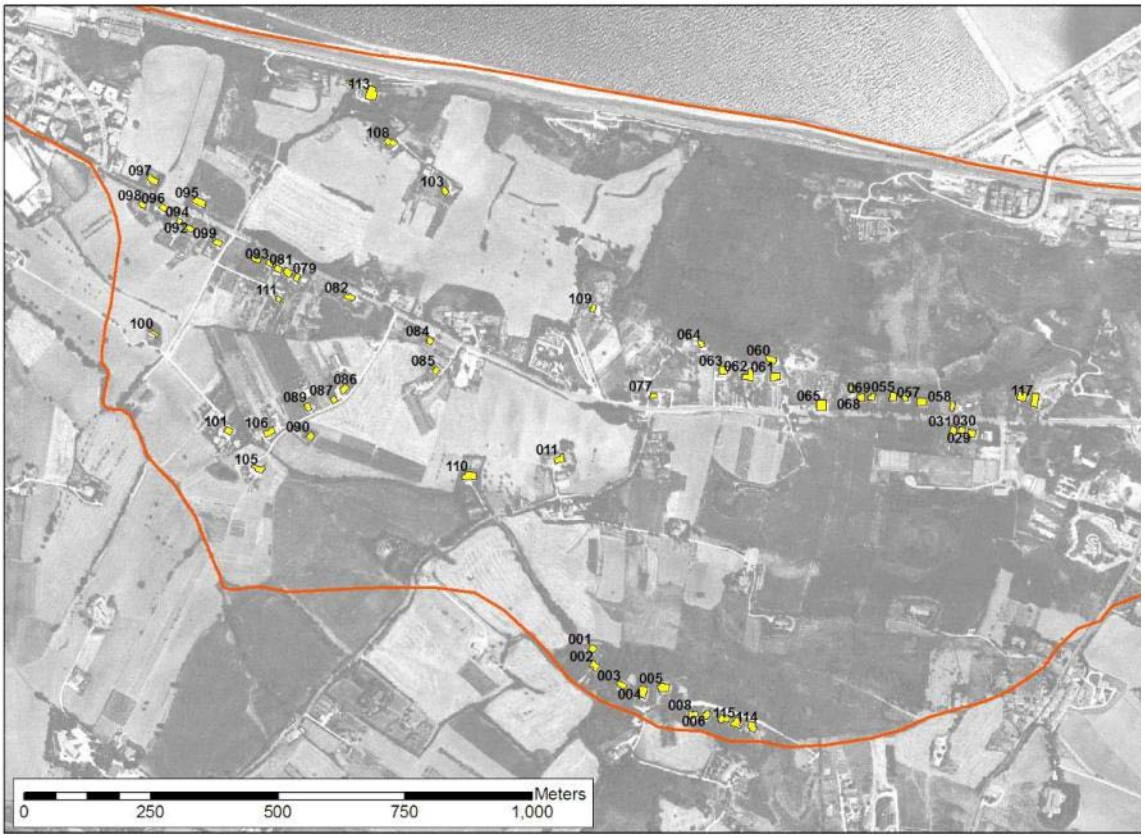

Figure 3.84. Identification of the 60 buildings for which specific risk is estimated

The estimation of specific risk relies on the modeling of hazard and vulnerability as functions of a reference parameter. In the present study, such reference parameter is the ground displacement D_G. Operationally, specific risk is given by the summation of the product of hazard and vulnerability calculated at all "possible" ground displacement levels:

$$R_{s,T} = \sum_{i=1}^{N_{D,T}} H_i\left(D_{G,T}\right) \cdot V_i\left(D_{G,T}\right)$$

This equation highlights the dependence of intensity (and the number of operational displacement levels N_D) on the reference period T. Intensity is parameterized using available inclinometer data, and is calculated for five reference periods: T_{001}=1 year, T_{010}=10 years, T_{025}=25 years, T_{050}=50 years and T_{100}=100 years.

The parameterization of hazard and vulnerability relies on the statistical processing and subsequent probabilistic simulation of the average yearly inclinometer-measured velocity ξ_{IN} defined in Section 3.3.1.2. Hereinafter, the notation ξ_G will be used for risk estimation in place of ξ_{IN}.

The total displacement $D_{G,T}$ measured at one inclinometer location in a reference period T is given by:

$$D_{G,T} = \sum_{j=1}^{T} \left| \xi_{G,j} \right|$$

in which: $\xi_{G,j}$ is the average yearly ground velocity in the j-th year (j=1,…,T).

Probabilistic simulation was employed to estimate $D_{G,T}$). The equation should be regarded as a vector equation in which T vectors $|\xi_{G,j}|$, each of size n_{sim}, are added. Vectors correspond, for each inclinometer and reference period, to sampling distributions of ξ_G. Sampling distributions were generated non-parametrically, i.e. not according to preset distribution types; rather, they were based on the ECDFs of ξ_{IN}. A size n_{sim}=10,000 was established for all sampling distributions. The output of the above mentioned equation is a n_{sim}-sized vector, which corresponds, for a given period T, to a sample of total ground displacement. The presence of absolute values in this equation reflects the conservative hypothesis by which displacement-induced damage is invariant to the direction of ground movement. The inherent conservatism lies in the fact that, by summation of absolute values, $D_{G,T}$ is maximized for any given set of sampled values. The estimation of specific risk for long reference periods implies the hypothesis of temporal stationarity of slope kinematic parameters, i.e. the belief that slope kinematics will not change significantly in time. This hypothesis was verified by checking the absence of temporal trends (iaccelerations or decelerations) in ξ_G through the calculation of Kendall's tau statistic. It was assessed that no significant trends are present in velocity time series. Figure 3.86 plots: (a) the empirical cumulative distribution function of ξ_G for inclinometer GR02; and (b) the cumulative distribution function of the generated size-10,000 sampling distribution of ξ_G.

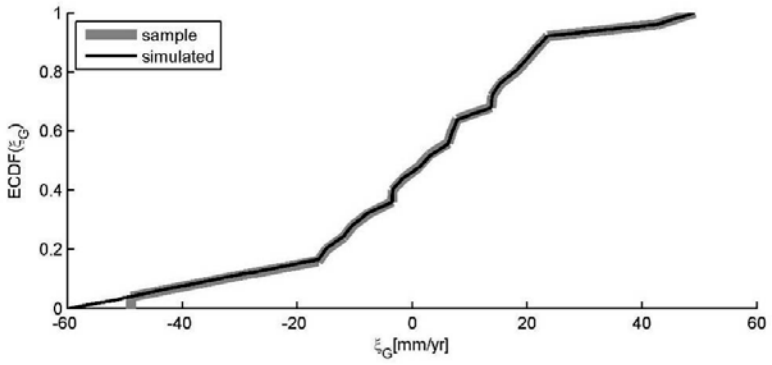

Figure 3.85. (a) empirical cumulative distribution function of ξ_{IN} for inclinometer GR02; and (b) cumulative distribution function of the generated size-10,000 sampling distribution of ξ_G.

Figure 3.87 plots: (a) the relative frequency histogram of the input sampling distribution of ξ_G and the relative frequency histograms of the output samples of D_G for: (b) T001; (c) T010; (d) T025; (e) T050; and (f) T100 for inclinometer GR02. It should be noted that all values of the output distribution are positive because absolute values are considered in risk equation. Also, the distribution of output samples approaches a Gaussian shape with increasing period T in accordance with the central limit theorem,

by which the sum of a large number of random variates (in the present case, the non-parametric sampling distributions) with finite variance approaches a Gaussian distribution.

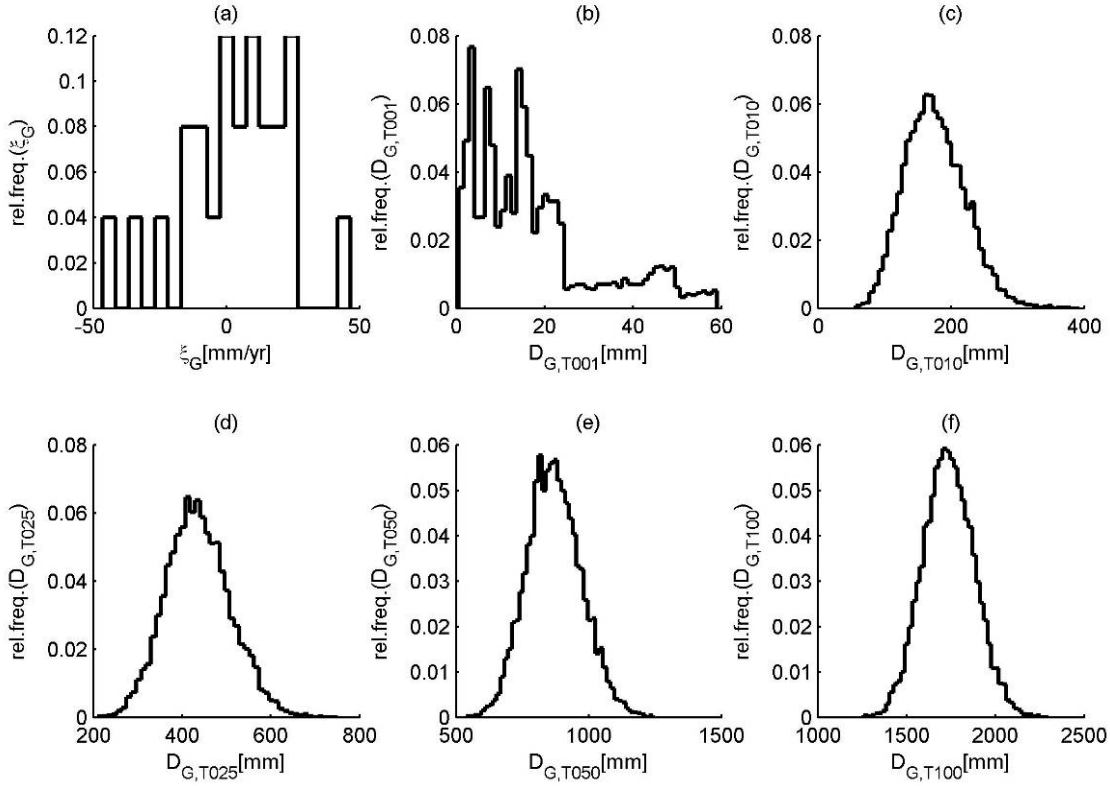

Figure 3.86. Inclinometer GR02: relative frequency histograms of: (a) input sampling distribution of ξ_G and output samples of D_G for: (b) T001; (c) T010; (d) T025; (e) T050; and (f) T100.

Sets of 21 sample quantiles of D_G were retrieved for each inclinometer and for each period T from the simulation output samples of D_G calculated by probabilistic simulation: namely, the 0.005, 0.05, 0.10, 0.15, 0.20, 0.25, 0.30, 0.35, 0.40, 0.45, 0.50, 0.55, 0.60, 0.65, 0.70, 0.75, 0.80,0.85, 0.90. 0.95 and 0.995 quantiles. The above procedure allows the statistical and probabilistic processing of ground displacement data at the inclinometer locations. For risk estimation purposes, it is necessary to estimate the same parameters at building locations. This indirect estimation is pursued by RBF interpolation. All displacement quantiles were interpolated inside the landslide perimeter for all reference periods T001-T100. Figure 3.88 plots the interpolation of the 0.05 quantile of D_G for period T025.

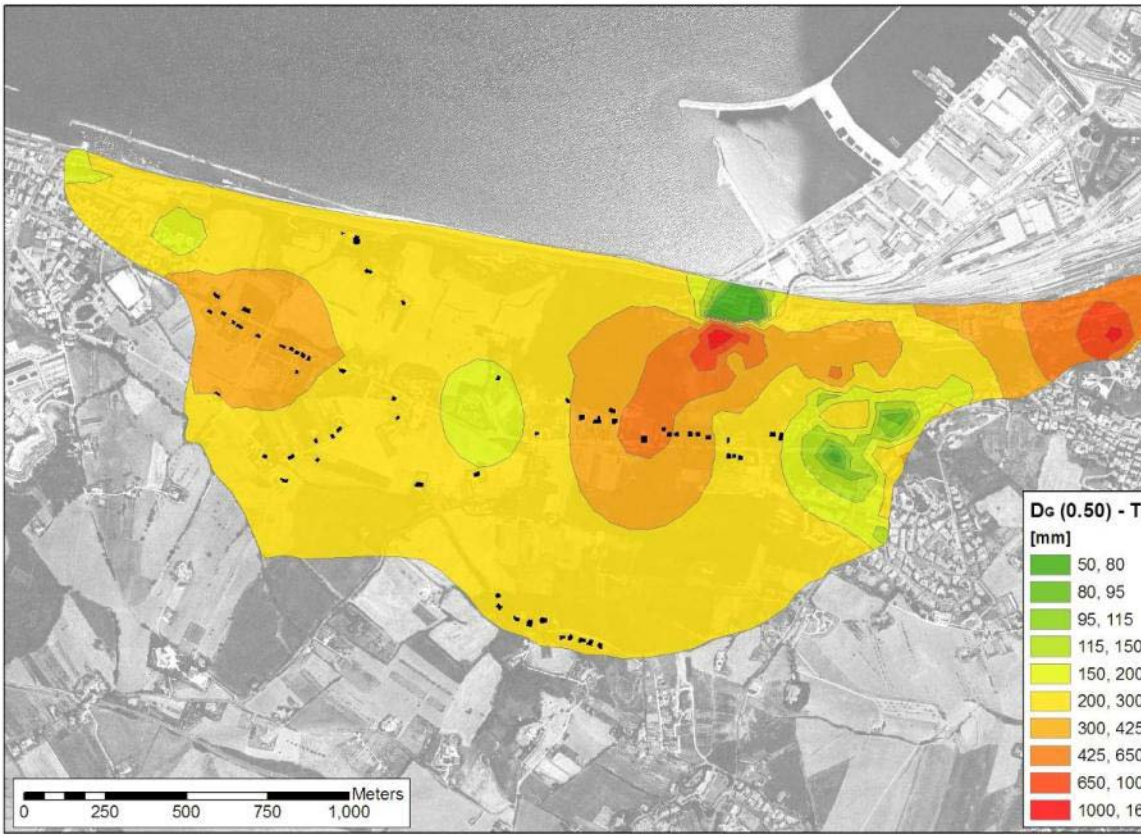

Figure 3.87. RBF interpolation of 0.50 quantile of D_G for reference period T025.

Interpolated values at building locations were extracted. Figure 3.89 plots the displacement quantiles extracted at the location of building 031 for the 5 reference periods.

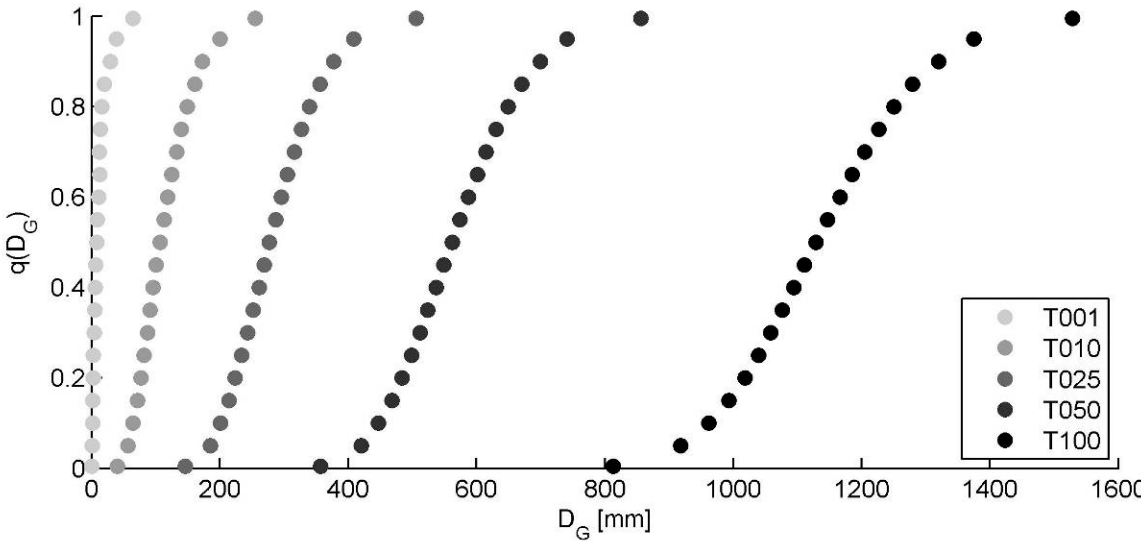

Figure 3.88. Example figure with quantiles of D_G at building 031 for T001-T100.

For each building, the set of quantiles was interpolated linearly between each couple of consecutive quantiles in order to obtain quantile values at step 1 mm. The resulting number N_D of displacement-quantile couples is building-specific. The building-specific set $D_{G1}…D_{G,ND}$ were used to calculated the intensity-specific samples of hazard $H_i(D_{G,T})$ and vulnerability $V_i(D_{G,T})$ (i=1,…,N_D).

3.4.1 Hazard estimation

With reference to the definition given in Section 3.1.1, hazard corresponds to the probability of occurrence, in the reference time period, of a hazardous event of a given magnitude. Hazard descends directly from the outputs of probabilistic simulation of total displacement. Displacement exceedance probability curves were drawn for each building and for each reference period. Figure 3.91 plots the exceedance probability for building 031 by reference period. It should be noted that displacements are considered in discrete sets (i.e. at integer values); hence, the exceedance probability curves are plotted as continuous lines solely for illustrative purposes.

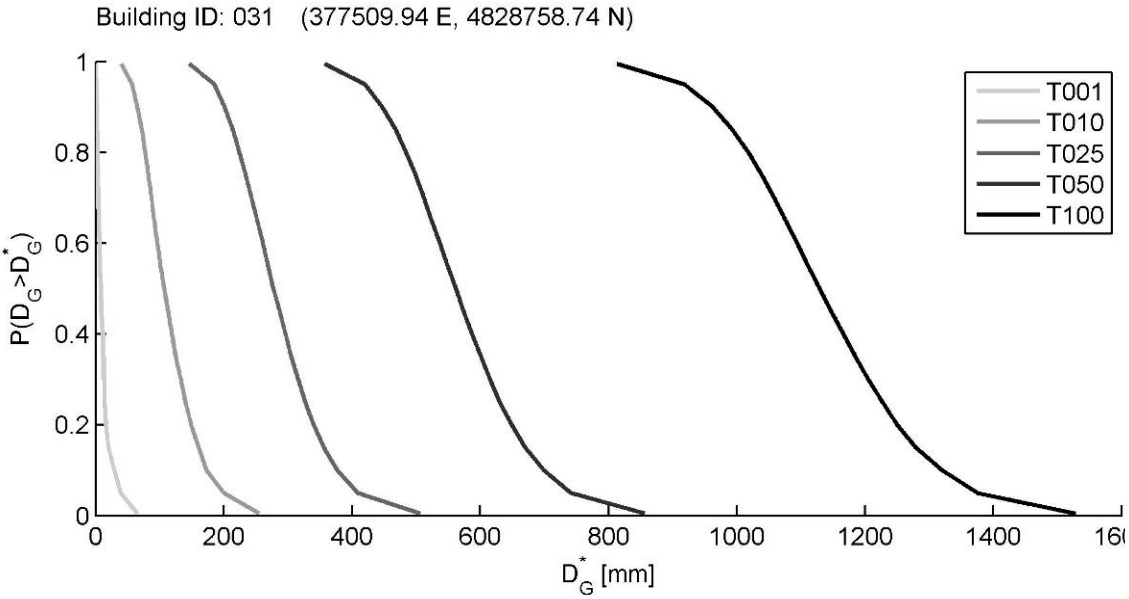

Figure 3.89. Displacement exceedance probability curves for building 031 by reference period

Hazard values were obtained by deconvolution of the cumulative exceedance probability curves, i.e. by calculating the probability that displacement equals a preset magnitude.

3.4.2 Vulnerability estimation

From the general vulnerability model proposed by Uzielli (2012), the vulnerability of a building referred to a return period T is given by:

$$V_T = \begin{cases} \dfrac{2I_T^2}{\Omega_T^2} & \dfrac{I_T}{\Omega_T} < 0.5 \\ 1.0 - \dfrac{2\left(\Omega_T - I_T\right)^2}{\Omega_T^2} & 0.5 \le \dfrac{I_T}{\Omega_T} \le 1.0 \\ 1.0 & \dfrac{I_T}{\Omega_T} > 1.0 \end{cases}$$

in which: $I_{,T}$ is the period-specific intensity parameter and Ω_T is the period-specific resilience of the building. Resilience is effectively period-dependent because the resilience factor for building age decreases with increasing period. The resilience index can be estimated as described in Section 3.2.2. With reference to the upper-bound intensity model developed in Section 3.2.4, the intensity index is given (in terms of ground displacement) by:

$$I_T = 0.24 \cdot \left(D_{G,T}\right)^{0.63}$$

in which: $D_{G,T}$ is the period-specific total ground displacement. The upper-bound intensity model is used for sake of conservatism.

It is important to note that the resilience of the buildings generally does not correspond with the values used in the back-calculation of intensity in Section 3.2.2. There, building resilience was estimated with reference to building conditions at the time of the damage survey (1985-1986). Since then, it is expectable that the resilience factor for building age has decreased. The following model was employed for the resilience factor for building age:

$$\theta_{AGE} = \exp\left(-0.013 \cdot \text{age}\right)$$

where age is expressed in years. Table 3.10 illustrates the variation in the resilience factor for building age Θ_{AGE} for each category of buildings and for each reference period.

Table 3.10 Variation in the resilience factor for building age Θ_{AGE} by category of buildings and reference period.

cat.	survey		T_{001}		T_{010}		T_{025}		T_{050}		T_{100}	
	age	Θ_{AGE}	age	Θ_{AGE}	age	Θ_{AGE}	age	Θ_{AGE}	age	Θ_{AGE}	age	Θ_{AGE}
1	100	0.20	125	0.20	135	0.17	150	0.14	175	0.10	225	0.05
2	80	0.40	105	0.26	115	0.22	130	0.18	155	0.13	205	0.07
3	40	0.70	65	0.43	75	0.38	90	0.31	115	0.22	165	0.12
4	25	0.80	50	0.52	60	0.46	75	0.38	100	0.27	150	0.14
5	15	0.90	40	0.59	50	0.52	65	0.43	90	0.31	140	0.16
6	unkn	0.20	125	0.20	135	0.17	150	0.14	175	0.10	225	0.05

As information regarding possible retrofitting of buildings is not available, it is conservatively assumed that no retrofitting or structural/geotechnical consolidation interventions have been performed since the 1985-1986 survey, nor will they be in the

longest period for which specific risk is estimated (100 years). Consequently, the same values of the resilience factors for structural typology and foundation type used in Section 3.2.2 are adopted for the forward estimation of specific risk. Table 3.11 contains the resilience factors and resilience index by building and reference period used in the estimation of vulnerability.

Table 3.11 Resilience factors and resilience index by building and reference period.

			T_{001}		T_{010}		T_{025}		T_{050}		T_{100}	
ID	Θ_{STR}	Θ_{FND}	Θ_{AGE}	Ω_B	Θ_{AGE}	Ω_B	Θ_{AGE}	Ω_B	Θ_{AGE}	Ω_B	Θ_{AGE}	Ω_B
1	0.70	0.10	0.52	0.45	0.46	0.43	0.38	0.40	0.27	0.37	0.14	0.33
2	0.70	0.30	0.52	0.51	0.46	0.50	0.38	0.47	0.27	0.44	0.14	0.40
3	0.50	0.30	0.52	0.44	0.46	0.42	0.38	0.40	0.27	0.37	0.14	0.33
4	0.70	0.30	0.59	0.54	0.52	0.51	0.43	0.49	0.31	0.45	0.16	0.41
5	0.70	0.30	0.59	0.54	0.52	0.51	0.43	0.49	0.31	0.45	0.16	0.41
6	0.70	0.10	0.59	0.47	0.52	0.45	0.43	0.42	0.31	0.38	0.16	0.34
7	0.70	0.10	0.52	0.45	0.46	0.43	0.38	0.40	0.27	0.37	0.14	0.33
8	0.70	0.10	0.52	0.45	0.46	0.43	0.38	0.40	0.27	0.37	0.14	0.33
11	0.40	0.30	0.20	0.31	0.17	0.30	0.14	0.29	0.10	0.28	0.05	0.26
29	0.30	0.30	0.43	0.34	0.38	0.32	0.31	0.30	0.22	0.28	0.12	0.25
30	0.50	0.50	0.52	0.51	0.46	0.49	0.38	0.46	0.27	0.43	0.14	0.39
31	0.70	0.70	0.52	0.65	0.46	0.63	0.38	0.60	0.27	0.57	0.14	0.53
55	0.70	0.70	0.52	0.65	0.46	0.63	0.38	0.60	0.27	0.57	0.14	0.53
56	0.70	0.70	0.52	0.65	0.46	0.63	0.38	0.60	0.27	0.57	0.14	0.53
57	0.70	0.30	0.52	0.51	0.46	0.50	0.38	0.47	0.27	0.44	0.14	0.40
58	0.40	0.30	0.20	0.31	0.17	0.30	0.14	0.29	0.10	0.28	0.05	0.26
59	0.80	0.30	0.20	0.45	0.17	0.45	0.14	0.44	0.10	0.43	0.05	0.41
60	0.70	0.30	0.59	0.54	0.52	0.51	0.43	0.49	0.31	0.45	0.16	0.41
61	0.70	0.30	0.59	0.54	0.52	0.51	0.43	0.49	0.31	0.45	0.16	0.41
62	0.70	0.30	0.59	0.54	0.52	0.51	0.43	0.49	0.31	0.45	0.16	0.41
63	0.70	0.30	0.59	0.54	0.52	0.51	0.43	0.49	0.31	0.45	0.16	0.41
64	0.70	0.10	0.52	0.45	0.46	0.43	0.38	0.40	0.27	0.37	0.14	0.33
65	0.80	0.50	0.59	0.64	0.52	0.62	0.43	0.59	0.31	0.55	0.16	0.51
67	0.70	0.10	0.52	0.45	0.46	0.43	0.38	0.40	0.27	0.37	0.14	0.33
68	0.70	0.70	0.52	0.65	0.46	0.63	0.38	0.60	0.27	0.57	0.14	0.53
69	0.70	0.70	0.52	0.65	0.46	0.63	0.38	0.60	0.27	0.57	0.14	0.53
77	0.70	0.70	0.59	0.67	0.52	0.65	0.43	0.62	0.31	0.58	0.16	0.54
78	0.70	0.10	0.52	0.45	0.46	0.43	0.38	0.40	0.27	0.37	0.14	0.33
79	0.70	0.10	0.52	0.45	0.46	0.43	0.38	0.40	0.27	0.37	0.14	0.33
81	0.70	0.10	0.52	0.45	0.46	0.43	0.38	0.40	0.27	0.37	0.14	0.33
82	0.30	0.30	0.20	0.27	0.17	0.26	0.14	0.25	0.10	0.24	0.05	0.23
84	0.50	0.30	0.52	0.44	0.46	0.42	0.38	0.40	0.27	0.37	0.14	0.33
85	0.70	0.10	0.52	0.45	0.46	0.43	0.38	0.40	0.27	0.37	0.14	0.33
86	0.50	0.30	0.52	0.44	0.46	0.42	0.38	0.40	0.27	0.37	0.14	0.33
87	0.50	0.30	0.43	0.41	0.38	0.40	0.31	0.38	0.22	0.35	0.12	0.32
89	0.30	0.30	0.43	0.34	0.38	0.32	0.31	0.30	0.22	0.28	0.12	0.25
90	0.70	0.10	0.52	0.45	0.46	0.43	0.38	0.40	0.27	0.37	0.14	0.33
91	0.70	0.50	0.52	0.58	0.46	0.56	0.38	0.54	0.27	0.51	0.14	0.47
92	0.70	0.10	0.59	0.47	0.52	0.45	0.43	0.42	0.31	0.38	0.16	0.34
93	0.70	0.10	0.52	0.45	0.46	0.43	0.38	0.40	0.27	0.37	0.14	0.33
94	0.70	0.10	0.52	0.45	0.46	0.43	0.38	0.40	0.27	0.37	0.14	0.33
95	0.70	0.70	0.52	0.65	0.46	0.63	0.38	0.60	0.27	0.57	0.14	0.53
96	0.40	0.30	0.20	0.31	0.17	0.30	0.14	0.29	0.10	0.28	0.05	0.26
97	0.70	0.30	0.52	0.51	0.46	0.50	0.38	0.47	0.27	0.44	0.14	0.40

98	0.50	0.30	0.26	0.36	0.22	0.35	0.18	0.34	0.13	0.32	0.07	0.31
99	0.70	0.10	0.52	0.45	0.46	0.43	0.38	0.40	0.27	0.37	0.14	0.33
100	0.40	0.30	0.20	0.31	0.17	0.30	0.14	0.29	0.10	0.28	0.05	0.26
101	0.40	0.30	0.20	0.31	0.17	0.30	0.14	0.29	0.10	0.28	0.05	0.26
103	0.40	0.30	0.20	0.31	0.17	0.30	0.14	0.29	0.10	0.28	0.05	0.26
105	0.40	0.30	0.20	0.31	0.17	0.30	0.14	0.29	0.10	0.28	0.05	0.26
106	0.70	0.10	0.59	0.47	0.52	0.45	0.43	0.42	0.31	0.38	0.16	0.34
108	0.70	0.30	0.59	0.54	0.52	0.51	0.43	0.49	0.31	0.45	0.16	0.41
109	0.50	0.30	0.20	0.34	0.17	0.34	0.14	0.33	0.10	0.32	0.05	0.30
110	0.70	0.10	0.59	0.47	0.52	0.45	0.43	0.42	0.31	0.38	0.16	0.34
111	0.70	0.10	0.52	0.45	0.46	0.43	0.38	0.40	0.27	0.37	0.14	0.33
112	0.50	0.30	0.43	0.41	0.38	0.40	0.31	0.38	0.22	0.35	0.12	0.32
113	0.70	0.30	0.59	0.54	0.52	0.51	0.43	0.49	0.31	0.45	0.16	0.41
114	0.70	0.10	0.52	0.45	0.46	0.43	0.38	0.40	0.27	0.37	0.14	0.33
115	0.70	0.10	0.52	0.45	0.46	0.43	0.38	0.40	0.27	0.37	0.14	0.33
117	0.70	0.50	0.59	0.60	0.52	0.58	0.43	0.55	0.31	0.52	0.16	0.47

Figure 3.91 plots the variation in resilience versus reference time period for the set of 60 buildings.

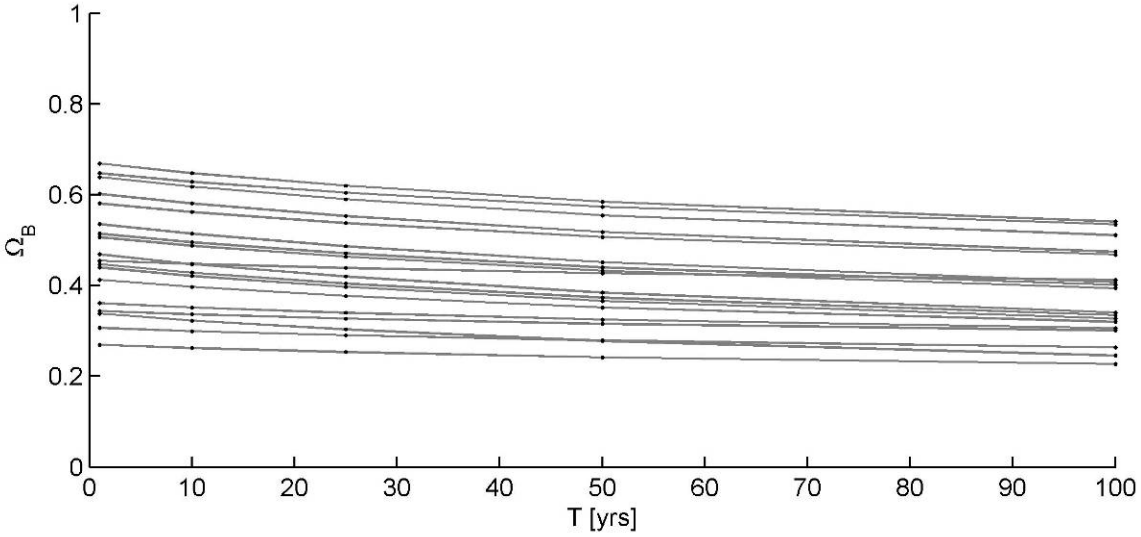

Figure 3.90. Variation of resilience versus reference period for the set of buildings.

3.4.3 Estimation of specific risk

The specific risk model was implemented using the hazard and vulnerability values calculated as described in Sections 3.4.1 and 3.4.2, respectively. Figure 3.92 plots the exceedance probability curves and vulnerability curves for building 031 for each of the 5 reference periods. The sum of the scalar multiplications of the two vectors at each "possible" displacement value for a given reference period yields the single estimate of R_S for the period itself. Specific risk is a useful parameter as it allows the immediate, intuitive prediction of the percentage loss in value of a building in a reference period of time. For instance, a specific risk estimate of 0.15 for attests for T025 is equivalent to the prediction by which 15% of the building's value will be lost in the next 25 years.

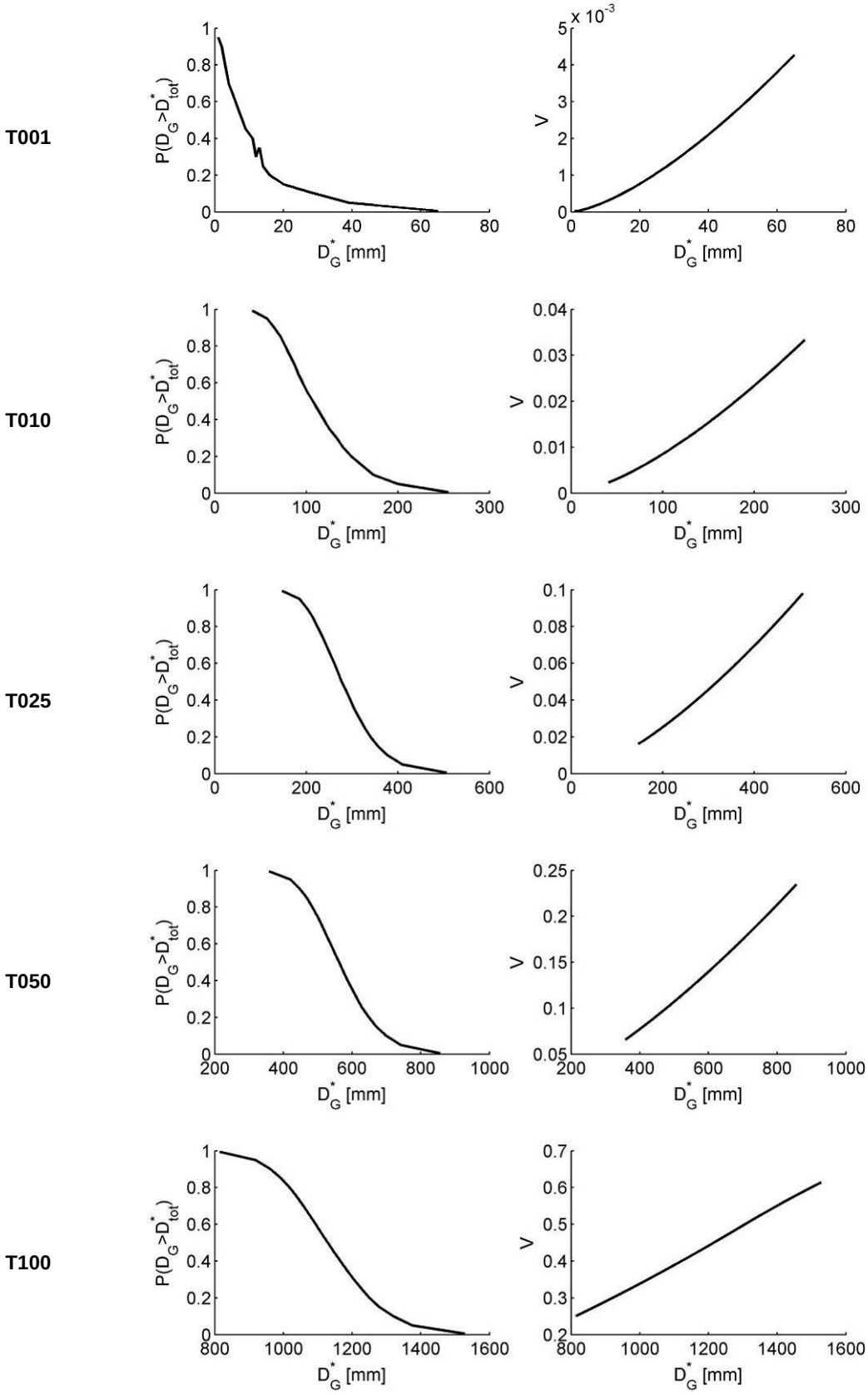

Figure 3.91. Exceedance probability curves and vulnerability curves for building 031.

Table 3.12 contains the estimates of specific risk for each building and for each reference period.

Table 3.12 Estimates of specific risk by building and reference period

ID	$R_{S,T001}$ [$(1\ yr)^{-1}$]	$R_{S,T010}$ [$(10\ yrs)^{-1}$]	$R_{S,T025}$ [$(25\ yrs)^{-1}$]	$R_{S,T050}$ [$(50\ yrs)^{-1}$]	$R_{S,T100}$ [$(100\ yrs)^{-1}$]
1	7.88E-04	1.93E-02	8.05E-02	2.57E-01	7.60E-01
2	6.03E-04	1.46E-02	6.00E-02	1.87E-01	5.97E-01
3	8.23E-04	2.02E-02	8.46E-02	2.72E-01	7.86E-01
4	5.62E-04	1.37E-02	5.66E-02	1.80E-01	5.87E-01
5	5.62E-04	1.37E-02	5.68E-02	1.80E-01	5.88E-01
6	7.34E-04	1.81E-02	7.64E-02	2.49E-01	7.55E-01
7	7.99E-04	1.97E-02	8.22E-02	2.63E-01	7.70E-01
8	7.99E-04	1.97E-02	8.19E-02	2.62E-01	7.68E-01
11	1.43E-03	3.08E-02	1.20E-01	3.52E-01	8.42E-01
29	1.63E-03	3.85E-02	1.60E-01	5.07E-01	9.74E-01
30	7.59E-04	1.75E-02	7.07E-02	2.20E-01	6.72E-01
31	4.72E-04	1.08E-02	4.28E-02	1.29E-01	4.06E-01
55	6.52E-04	1.54E-02	6.16E-02	1.87E-01	5.70E-01
56	6.26E-04	1.46E-02	5.81E-02	1.76E-01	5.41E-01
57	9.00E-04	2.04E-02	8.23E-02	2.56E-01	7.39E-01
58	2.25E-03	4.99E-02	1.93E-01	5.49E-01	9.69E-01
59	7.46E-04	1.59E-02	5.97E-02	1.70E-01	4.94E-01
60	1.03E-03	2.63E-02	1.11E-01	3.53E-01	8.71E-01
61	4.87E-04	1.05E-02	4.20E-02	1.32E-01	4.40E-01
62	1.09E-03	2.81E-02	1.18E-01	3.77E-01	8.92E-01
63	9.32E-04	2.35E-02	9.85E-02	3.14E-01	8.30E-01
64	1.16E-03	2.87E-02	1.20E-01	3.85E-01	9.05E-01
65	4.99E-04	1.20E-02	4.88E-02	1.51E-01	4.83E-01
67	2.48E-03	6.06E-02	2.54E-01	6.95E-01	9.88E-01
68	8.86E-04	2.22E-02	9.08E-02	2.78E-01	7.51E-01
69	7.95E-04	1.98E-02	8.05E-02	2.46E-01	6.97E-01
77	7.20E-04	1.78E-02	7.26E-02	2.24E-01	6.63E-01
78	8.10E-04	1.85E-02	7.64E-02	2.44E-01	7.31E-01
79	1.14E-03	2.88E-02	1.21E-01	3.86E-01	9.17E-01
81	1.13E-03	2.84E-02	1.19E-01	3.80E-01	9.12E-01
82	3.25E-03	8.02E-02	3.22E-01	8.00E-01	9.90E-01
84	9.26E-04	2.37E-02	9.93E-02	3.19E-01	8.55E-01
85	7.59E-04	1.85E-02	7.67E-02	2.45E-01	7.41E-01
86	7.72E-04	1.85E-02	7.68E-02	2.46E-01	7.45E-01
87	9.99E-04	2.53E-02	1.05E-01	3.29E-01	8.55E-01
89	1.50E-03	3.86E-02	1.64E-01	5.29E-01	9.84E-01
90	8.65E-04	2.24E-02	9.45E-02	3.02E-01	8.34E-01
91	5.01E-04	1.26E-02	5.14E-02	1.58E-01	5.07E-01
92	1.14E-03	2.95E-02	1.26E-01	4.10E-01	9.41E-01
93	1.19E-03	3.20E-02	1.36E-01	4.39E-01	9.52E-01
94	1.22E-03	3.10E-02	1.30E-01	4.18E-01	9.39E-01
95	5.43E-04	1.43E-02	5.86E-02	1.79E-01	5.58E-01
96	2.46E-03	6.43E-02	2.59E-01	7.04E-01	9.90E-01
97	7.95E-04	2.14E-02	8.98E-02	2.83E-01	7.92E-01
98	1.54E-03	4.03E-02	1.63E-01	4.89E-01	9.55E-01

99	1.00E-03	2.75E-02	1.17E-01	3.77E-01	9.12E-01
100	2.84E-03	7.41E-02	2.99E-01	7.68E-01	9.90E-01
101	2.01E-03	5.02E-02	2.01E-01	5.80E-01	9.81E-01
103	1.86E-03	4.66E-02	1.85E-01	5.41E-01	9.72E-01
105	1.67E-03	3.89E-02	1.53E-01	4.50E-01	9.28E-01
106	7.71E-04	1.98E-02	8.37E-02	2.72E-01	7.99E-01
108	6.13E-04	1.56E-02	6.53E-02	2.07E-01	6.59E-01
109	1.38E-03	3.27E-02	1.28E-01	3.76E-01	8.65E-01
110	5.06E-04	1.12E-02	4.62E-02	1.49E-01	5.13E-01
111	7.38E-04	1.75E-02	7.23E-02	2.31E-01	7.13E-01
112	1.20E-03	3.13E-02	1.30E-01	4.10E-01	9.27E-01
113	5.70E-04	1.39E-02	5.71E-02	1.81E-01	5.92E-01
114	8.16E-04	2.00E-02	8.30E-02	2.65E-01	7.75E-01
115	8.28E-04	2.02E-02	8.41E-02	2.70E-01	7.80E-01
117	4.59E-04	1.10E-02	4.50E-02	1.40E-01	4.58E-01

Estimates of specific risk for the 5 reference periods T001-T100 are plotted in Figures 3.93 to 3.97.

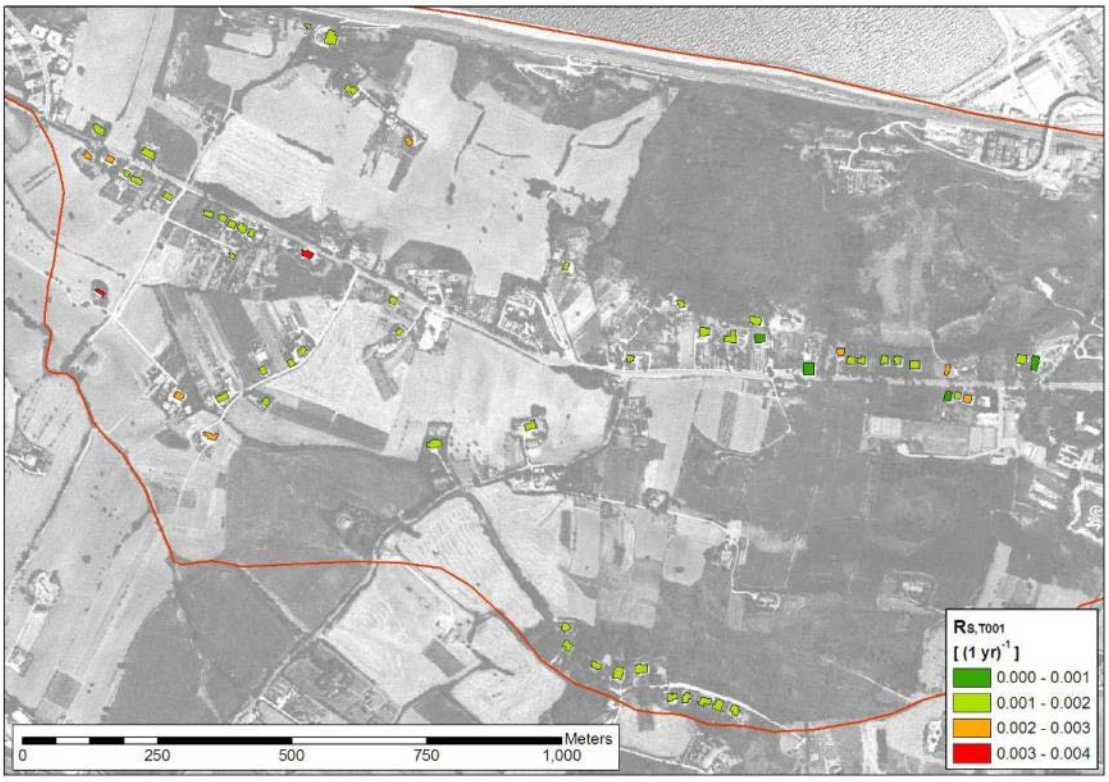

Figure 3.92. Specific risk for T001.

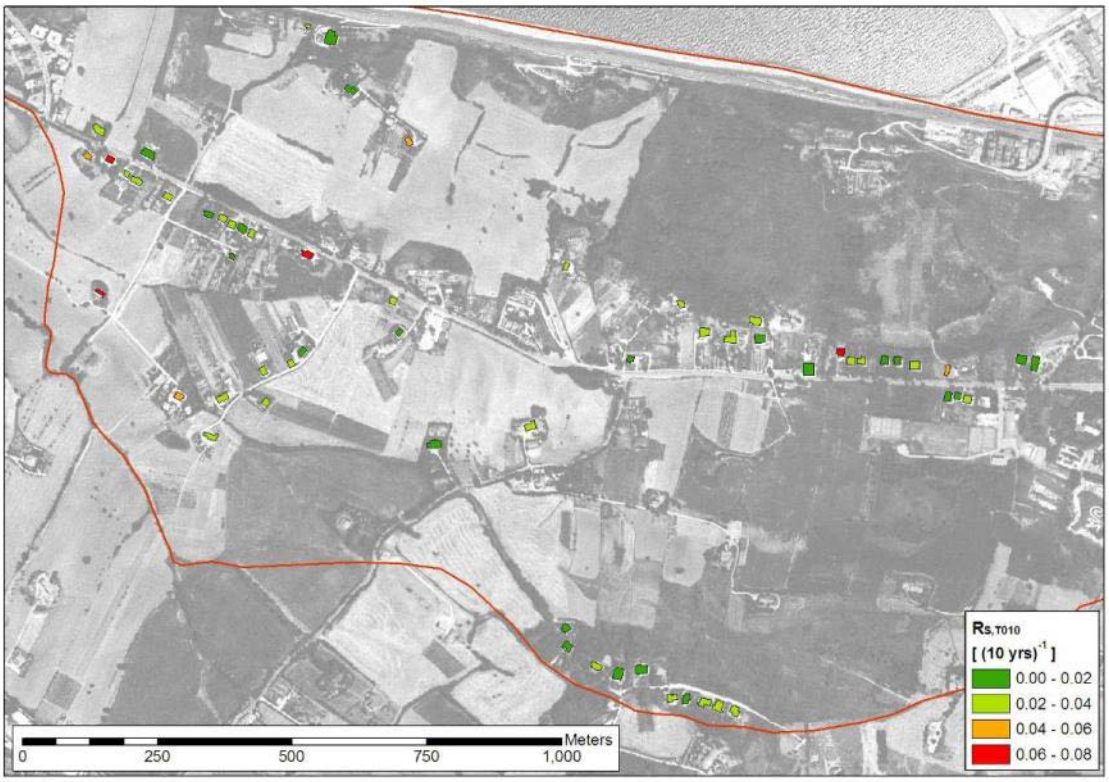

Figure 3.93. Specific risk for T010.

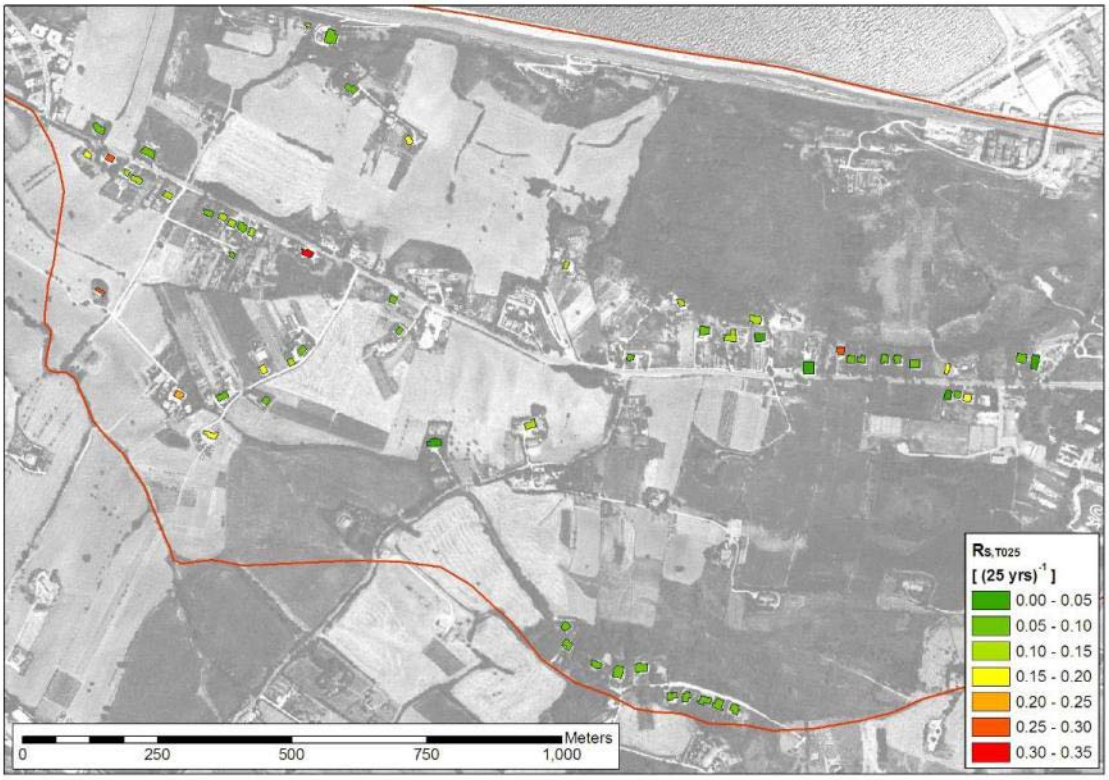

Figure 3.94. Specific risk for T025.

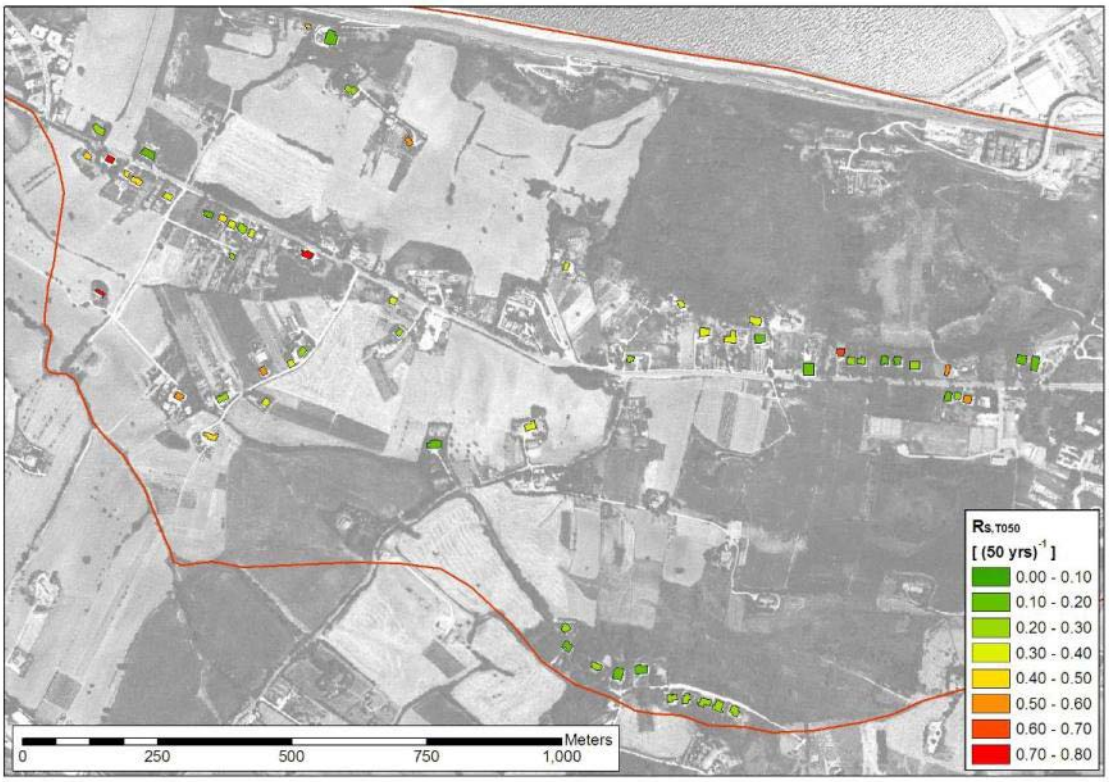

Figure 3.95. Specific risk for T050.

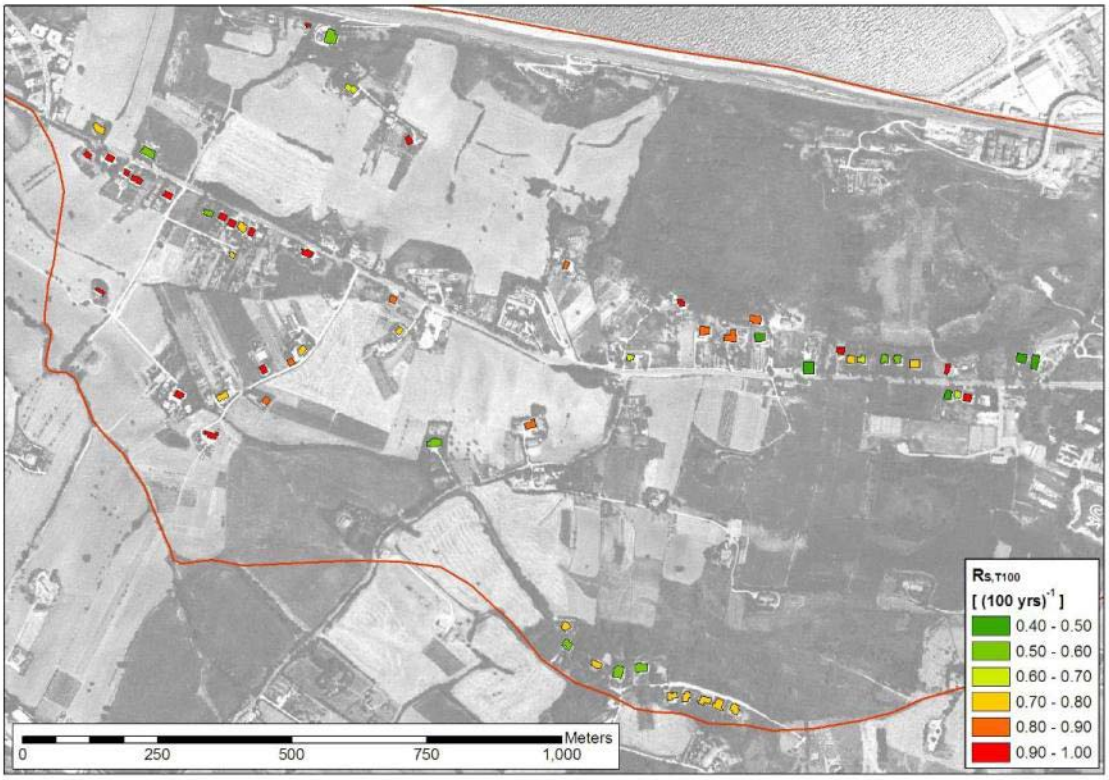

Figure 3.96. Specific risk for T100.

Figure 3.98 plots the variation of specific risk versus reference period for the set of buildings.

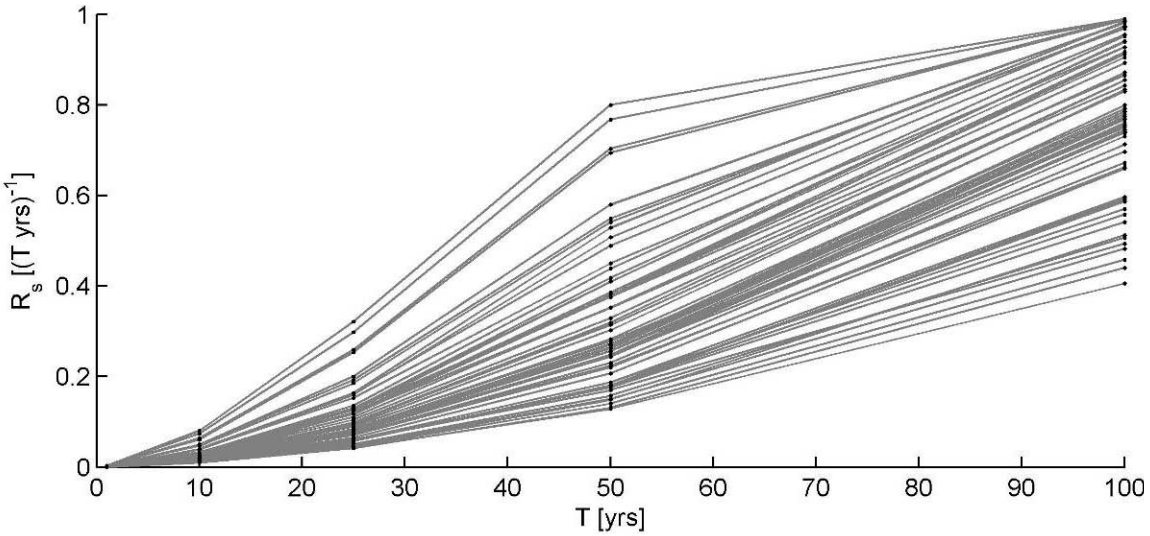

Figure 3.97. Variation of specific risk versus reference period for the set of buildings.

As expectable, specific risk increases significantly with the reference time period, due to the increases both in hazard (due to the larger ground displacements which are more likely to occur during longer periods) and in vulnerability (due to the increase in displacement-related intensity and the decrease in resilience as a consequence of the aging of buildings). Considering the sample of 60 buildings, specific risk could be described overall as "negligible" for T001; "very low" for T010; "low to medium" for T025; "low to high" for T050 and "medium to very high" for T100. The scatter in sample estimates is low for T001 and T010, moderate for T025 and very large for T050 (especially) and T100. Some buildings display greater increase in R_S between T025 and T050; others between T050 and T100. Estimates of specific risk are qualitatively consistent with available building data, slope monitoring data and local knowledge and experience.

3.4.4 From specific risk to risk

Risk can be estimated from specific risk if estimates of the value of vulnerable elements are available. For instance, if the estimated value of a building in a reference time period of 25 years is E=€ 500,000 and the specific risk estimate for T025 is 0.13, the 25-year risk is € 65,000. Similarly to hazard and vulnerability, E is period-specific as it is likely that the value of a building will change in time. As stated previously, estimates of the values of the buildings located in the Ancona landslide body were not available; hence, risk estimation could not be attempted.

3.5 SUMMARY AND CONCLUDING REMARKS

Specific risk as defined in the present study depends, both qualitatively and quantitatively, on the combined effect of the resilience of vulnerable elements and slope

kinematics. Consequently, it is a very complex parameter to estimate. In the analysis presented herein, hazard and vulnerability were addressed quantitatively, though with utmost attention to the practical significance of results and to their compatibility with qualitative observations and experience.

Slope kinematics was investigated quantitatively through the statistical and probabilistic modeling of inclinometer and interferometer data. Results of kinematic slope characterization are qualitatively in very good agreement with the displacements induced by the main 1982-12-13 event. The results of quantitative characterization of slope kinematics by inclinometer and PSInSAR observations are largely compatible even though they cannot be directly compared. Due to the inherent complexity in the estimation of hazard and vulnerability, the estimates of specific risk obtained herein are pervaded by uncertainty.

Uncertainties in specific risk estimates stem from uncertainties in hazard and vulnerability. Uncertainty in hazard is due mainly, but not solely, to: (a) limited number and numerosity of monitoring data samples (inclinometer and PSInSAR data); (b) the uncertainty in displacement statistics at building locations, stemming from the invariably imperfect RBF interpolations. Uncertainties in vulnerability stem at least from: (a) imprecision, inaccuracy and vagueness in damage survey data; (b) uncertainty in resilience model and sub-models; and (c) uncertainty and subjectivity in the empirical intensity model. The reduction of the epistemic components of uncertainty in hazard and vulnerability through additional monitoring data and/or improved vulnerability models is practically unattainable. Moreover, the limited amount of measurement points in the landslide area does not allow confident spatialization of hazard and vulnerability indicators by geostatistical interpolation.

To attempt avoiding unsafe underestimation of specific risk, the upper-bound intensity model was employed in the calculation of vulnerability. As a consequence of the conservatism in the model, specific risk values calculated herein can be expected to "reasonably" overestimate the specific risk. This is a correct approach from an engineering standpoint in presence of non-reducible uncertainty. Overall, quantitative estimates are strongly plausible in terms of consistency with qualitative observations and available information regarding slope kinematics and the characteristics of vulnerable elements.

References

Anderson, T.W., Darling, D.A. (1954). A test of goodness of fit. Journal of the American Statistical Association 49: 765-769.

Anon (1986). La grande frana di Ancona del 13 Dicembre 1982. Special issue of ‘‘Studi geologici Camerti’’, pp 146.

Bally, A.W., Burbi, L., Cooper, C., Ghelardoni, R. (1988). Balanced sections and seismic reflections profiles across thc Central Apennines. Memorie della Società Geologica Italiana 35:257-310.

Cardellini S., Osimani P. (2008). Living with Landslide: the Ancona Case History and Early Warning System. Proc. First World Landslide Forum, Tokyo, 473-476

Cotecchia, V. (1997a). La grande frana di Ancona. Atti del Convegno dell'Accademia Nazionale dei Lincei: "La stabilità del suolo in Italia: zonazione della sismicità – frane", pp 187–259.

Cotecchia, V. (1997b). The vulnerable town and the geological evolution of the middle Adriatic coastal environment. In Proceedings of the IAEG International Symposium "Engineering Geology and Environment", Athens, Greece.

Cotecchia, V. (2006). Experience drawn from the great Ancona landslide of 1982. The Second Hans Cloos Lecture. Bull Eng Geol Env 65: 1–41. DOI 10.1007/s10064-005-0024-z.

Crescenti, U., Nanni, T., Rampoldi, R., Stucchi, M. (1977). Ancona: considerazioni sismotettoniche. Bollettino di Geofisica Teorica e Applicata 73/74:33–48.

Cruden, D.M., Varnes, D.J. (1996). Landslide types and processes. Landslide investigation and mitigation, TRB Special Report 247, National Academy Press, Washington, DC., 36-75.

Hungr, O. (1997). Some methods of landslide intensity mapping. In D.M. Cruden & R. Fell (eds.), Landslide risk assessment - Proceedings of the International Workshop on Landslide Risk Assessment, Honolulu, 19-21 February 1997, Balkema, Rotterdam, 215-226.

Patacca, E., Sartori, R., Scandone, P. (1990). Tyrrhenian basin and Appenninic arcs: kinematic relations since late Tortonian times. Memorie della Società Geologica Italiana 45:425–451.

Tele-Rilevamento Europa (2008). PSInSAR – Manuale d'Uso.

Thode, H.C. (Jr.). (2002). Testing for normality, Marcel Dekker, New York.

UNDRO - United Nations Disaster Relief Organization (1979). Natural disasters and vulnerability analysis. Geneva.

Uzielli, M., Nadim, F., Lacasse, S., Kaynia, A.M. (2008). A conceptual framework for quantitative estimation of physical vulnerability to landslides. Engineering Geology 102:251-256.

Uzielli, M. (2012). Probabilistic vulnerability estimation for geohazards by simulation. Proceedings of Risk Analysis 2012, 19-21 September 2012, Brac, Croatia.

4 HYPERCONCENTRATED FLOW AT NOCERE INFERIORE (ITALY)

(UNISA)

INTRODUCTION

This report summarises the results of the activities carried out by the research group of the University of Salerno (UNISA) with reference to the test site of Monte Albino (Nocera Inferiore, southern Italy). In particular, these activities dealt with the acquisition of the relevant input data and their use within advanced procedures aimed to the quantitative estimation of the risk to life loss posed by the different types of phenomena that could originate from Monte Albino hillslopes (i.e., hyperconcentrated flows, flowslides, landslides on open slopes).

4.1 MONTE ALBINO CASE STUDY

The selected test site of Monte Albino (40°43'N, 14°38'E), located in the municipality of Nocera Inferiore (southern Italy), extends over a total area of about 400 ha, from 890 m a.s.l. to 90 m a.s.l. (Figure 4.1). Along the hillslope 10 catchments can be individuated as well as 10 open slopes (triangular facets), located in the lower portions of the relief (below 330 m a.s.l.). In March 2005, one of these open slopes was affected by a first-failure landslide (Figure 4.2) which caused 3 fatalities and the destruction of some buildings.

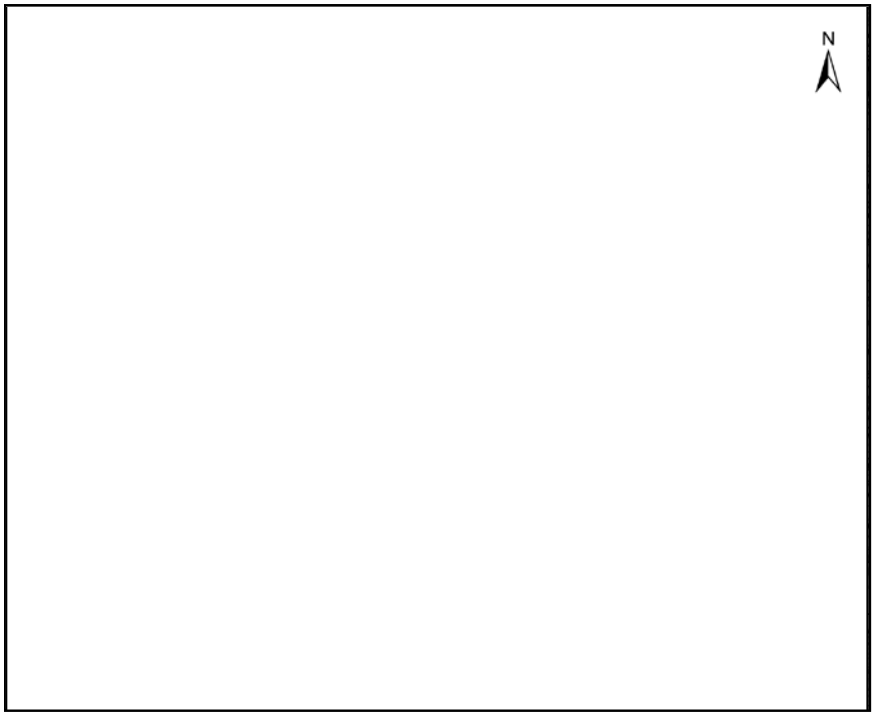

Figure 4.1. Study area.

In order to define the geological setting as well as to deepen the knowledge of the different types of phenomena which can occur on the slopes, in-situ tests, field surveys and studies were firstly carried out following a multidisciplinary approach (involving competences on historical data treatment, geology, geomorphology, hydrogeology, geotechnics, geomatics, geostatistics, etc.). The main results achieved during this preliminary step of the work are presented.

Figure 4.2. Frontal view of the debris avalanche occurred on March 2005.

4.2 ANALYSIS OF HISTORICAL DATA

4.2.1 Documentary sources

For the events preceding the 18th century the documentary sources consisted on historical-literary books (Orlando, 1884; Cimmelli, 1990; Pucci, 1995) and technical reports (Beguinot, 1957; Marciani, 1930; D'Elia, 1994). For the 19th century, historical incident data were recovered in the documents of the "Intendenza del Regno delle Due Sicilie (Sezione Opere Pubbliche)", founded by the Bourbons in 1806, and housed in the State Archive of Salerno. These documents include the correspondence between the "Intendente" and the Mayors of the towns affected by landslides as well as appraisals for the reconstruction works following the catastrophic events. For the 20th century, the main source is the report of the Operative Unit 2.38 (1998) of the University of Salerno, synthesised by Migale e Milone (1998), in which the results of a historical research on first-failure landslides occurred in Campania region in a time period spanning from the end of the 16th century up to now are summarised.

4.2.2 Results of the analyses

From a deep analysis of the contents of the recovered historical documents, it is argued that the events occurred on 18th and 19th centuries can be associated to the occurrence of hyperconcentrated flows (Costa, 1988). On the other hand, the incident data referring to the 20th century (also considering the landslides occurred on March 2005) can be linked to first-failure landslides on open slopes while historical information about flowslide phenomena (Hutchinson, 1988) are lacking.

4.2.2.1 Hyperconcentrated flows

With reference to the hyperconcentrated flows, information furnished by the documentary sources essentially deals with the consequences related to the occurrence of the phenomena at hand. In particular, as far as the incident data of the 18th century are concerned, the described consequences refer to some built-up areas of Nocera de Pagani (i.e. name of the Municipality at that time) and to the site called "Vescovado" (Figure 4.3); furthermore, these consequences seem to have been more severe, in terms of recorded damage, than those caused by the events occurred in the 19th century. In this regard, it can be observed that in the 18th century the described consequence are often due to adverse events originated from the Monte Albino hillslopes (i.e., the hyperconcentrated flows) as well as to flooding phenomena.

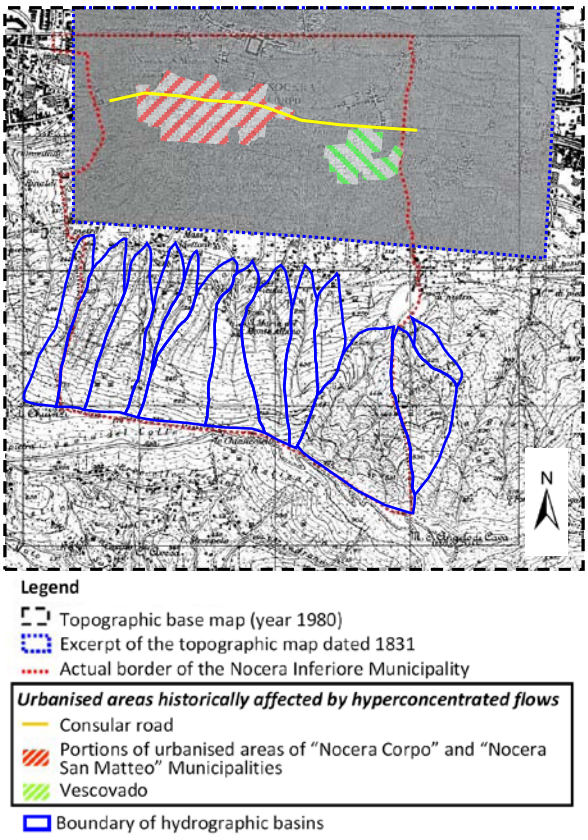

Figure 4.3. Urbanised areas affected by hyperconcentrated flows occurred during the 18th and the 19th centuries.

At the beginning of the 19th century, as required by the King of Bourbons Ferdinand IV who experienced the block of the consular road owing the event of 1804, some hydraulic control works were built in the flat areas (Orlando, 1884; Marciani, 1930; Beguinot, 1957). In the following, thanks also to the existence of these mitigation measures, the consequences related to the occurrence of the hyperconcentrated flows were limited to troubles in accessing some sections of the consular road, near the built-up areas. Finally, it is worth noting that some documents also furnish information about the cost (in ducats) required for the removal of transported sediments on the road.

The cumulative curve of past hyperconcentrated flow events (Figure 4.4) is characterised by a stepped shape during the time period (from 1707 to 1846) for which historical incident data are available.

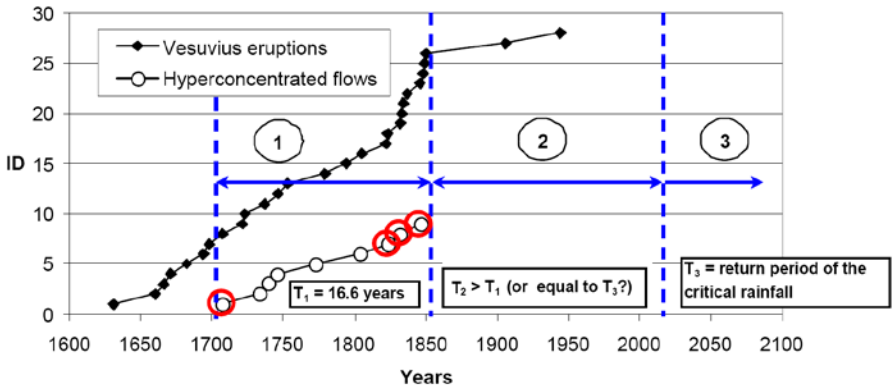

Figure 4.4. **Cumulative distributions of: i) Vesuvius explosive eruptions occurred from 1631 up to now; ii) hyperconcentrated flow incident data (events occurred after the Vesuvius eruptions are circled in red).**

Figure 4.4 also shows that the occurrence of the events may be correlated with the explosive eruptions of the Vesuvius volcano; in particular, between the 1811 and 1848, during a period of intensive strombolian activity of the volcano (Scandone et al., 2008), n. 3 hyperconcentrated flow events were recorded (Table 4.1). With reference to the seasonal distribution of the past events, Figure 5 shows that the recorded incident data concentrate between October and January, with a maximum in November. In this regard, the occurred phenomena can be ascribed to: 1) the availability of pyroclastic soils over the hillslopes (Figure 4.6a), transported by the winds blowing toward the eastern sectors (northeast–southeast) during the Autumn-Winter periods are (Rolandi et al., 2007); 2) the washing operated by rainfall of short duration and high intensity.

Table 4.1. Recorded incident data of hyperconcentrated flows occurred from 1707 to 1846, with indication of the affected areas.

ID	Day	Month	Year	Affected area
1	-	11	1707	All the town(*)
2	11	11	1733	All the town and the consular road
3	24	10	1739	All the town and the “Vescovado”
4	02	12	1745	All the town and the “Vescovado”
5	11	11	1773	All the town and the “Vescovado”

6		1	1804	The consular road
7	24	1	1823	The consular road
8	30	11	1832	The consular road
9	02	10	1846	The consular road

(*) The term "town" indicated the built-up area at the time when the phenomena occurred.

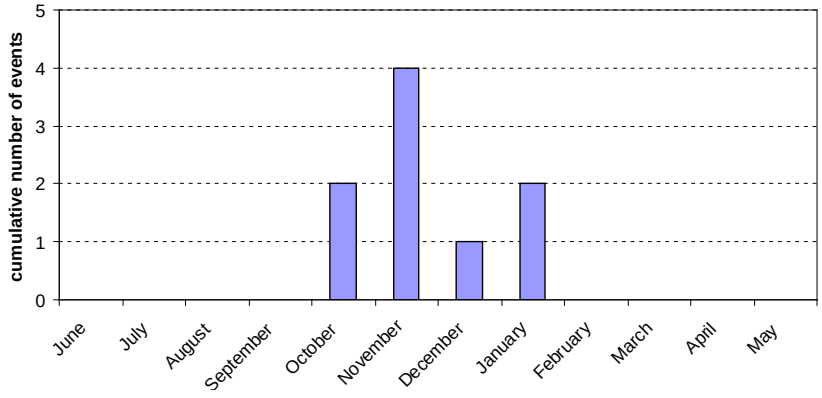

Figure 4.5. Monthly distribution of the hyperconcentrated flows which, in the past, interested the Monte Albino hillslopes.

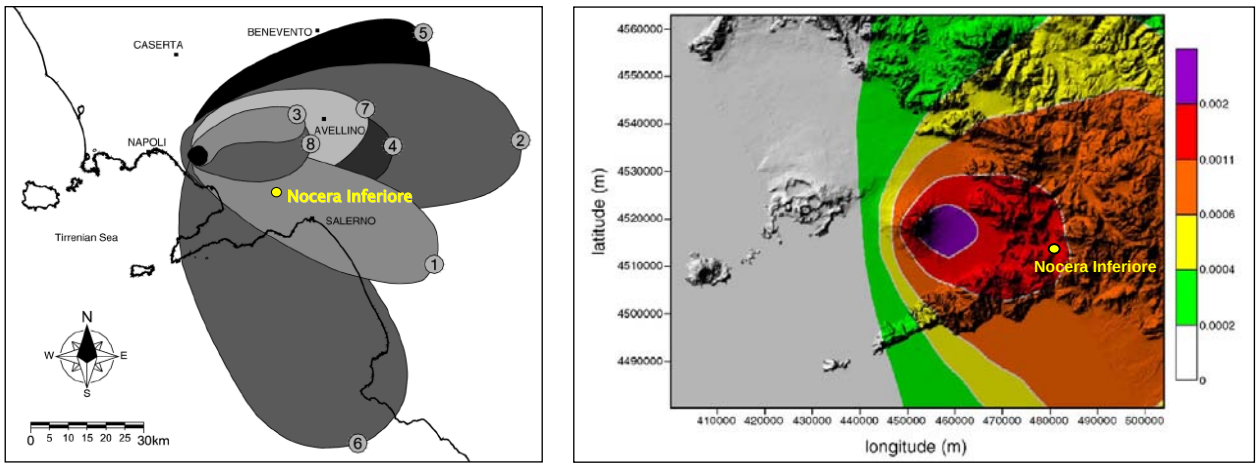

Figure 4.6. a) Distribution map of pyroclastic fall deposits of the Somma-Vesuvius deposited in the last 25 ka BP. Each lobe consists of air fall tephra 10 cm thick from a single Plinian eruption. Numbers are arranged according to the chronological sequence of the eruption. (1) 25.000 anni B.P.; (2) 18.000 anni B.P.; (3) 16020 anni B.P; (4) 8000 anni B.P.; (5) 3550 anni B.P.; (6) A.D. 79; (7) A.D. 472; (8) A.D. 1631 (modified from Rolandi et al., 2007). b) Fall-out hazard map for Vesuvius eruptions. The maps are computed, by several tens thousands of computer simulations, on the basis of the observed wind velocity and direction between 0 and 35 km of height and their relative occurrence, considering all the eruption types with their statistics distributions, according to the volcanological records. The values are the yearly probabilities of a tephra load exceeding 200 kg/m2 (producing the collapse of most roofs) (modified from De Natale et al., 2006).

The previous considerations allow the assumption of some hypotheses on the return period of the hyperconcentrated flow events (Figure 4.4). In particular, with reference to the time period $\Delta T1$ spanning from 1707 to 1846 ($\Delta T1$ = 140 years), it can be assumed that the average return period T1 – in the hypothesis that the database is complete – is equal to 16.6 years (140 years/9 events). If the $\Delta T2$ time period (from 1846 up to now) is considered, owing to the reduced recurrence of strombolian eruptions, the average

return period T2 of the hyperconcentrated flows is greater than T1. Moreover, since their occurrence is related to erosive phenomena rather than washing, it can be assumed that T2 can be equal to the return period T3 of the triggering rainfall events.

Tanking into account the low annual probability that, according to De Natale et al. (2006) can be associated with the occurrence of air-fall pyroclastic deposits (Figure 4.6b), future hyperconcentrated flows will be characterised by a average return period equal to T3, being their occurrence mainly related to erosive phenomena.

4.2.2.2 First-failure landslides on open slopes

With reference to the first-failure landslides on open slopes occurred from 1935 up to now, on the basis of the available data (Table 4.2), it can be observed that the average time period of recurrence equals 18.5 years. This value could be unsafe, being the estimation of T carried out without considering the role played by the anthropogenic factors in predisposing this kind of instability phenomena.

Table 4.2. Recorded incident data of landslides on open slopes occurred from 1935 to 2005, with indication of the consequences to the exposed persons and properties.

ID	Day	Month	Year	Fatalities/Endangered sites
1	-	-	1935	-
2	24	10	1954	-
3	-	-	1958	-
4	4	3	2005	3 fatalities/some houses destroyed

4.3 IN-SITU TESTS

The Monte Albino massif is constituted by a carbonatic bedrock covered by reworked and in-situ pyroclastic deposits originated from the air-fall deposition of the materials produced by the explosive activity of the Somma-Vesuvius volcanic complex. In order to acquire all over the Monte Albino hillslopes the geotechnical dataset (soil cover thickness, soil stratigraphy, physical and mechanical characteristics of the pyroclastic soils, etc.) to be used within the advanced methods useful for QRA purposes (Corominas and Mavrouli, 2011), the following in-situ tests were carried out from November to December 2010:

- n. 68 Seismic field tests;
- n. 40 Dynamic penetration tests (DL030);
- n. 20 Undisturbed soil sampling;
- n. 70 Man-made pits (with detailed soil stratigraphy);
- n. 1,030 Iron-rod drillings;
- n. 54 Suction measurements via quick-draw tensiometers.

Figure 4.7 shows the map of the test sites at the Monte Albino hillslopes.

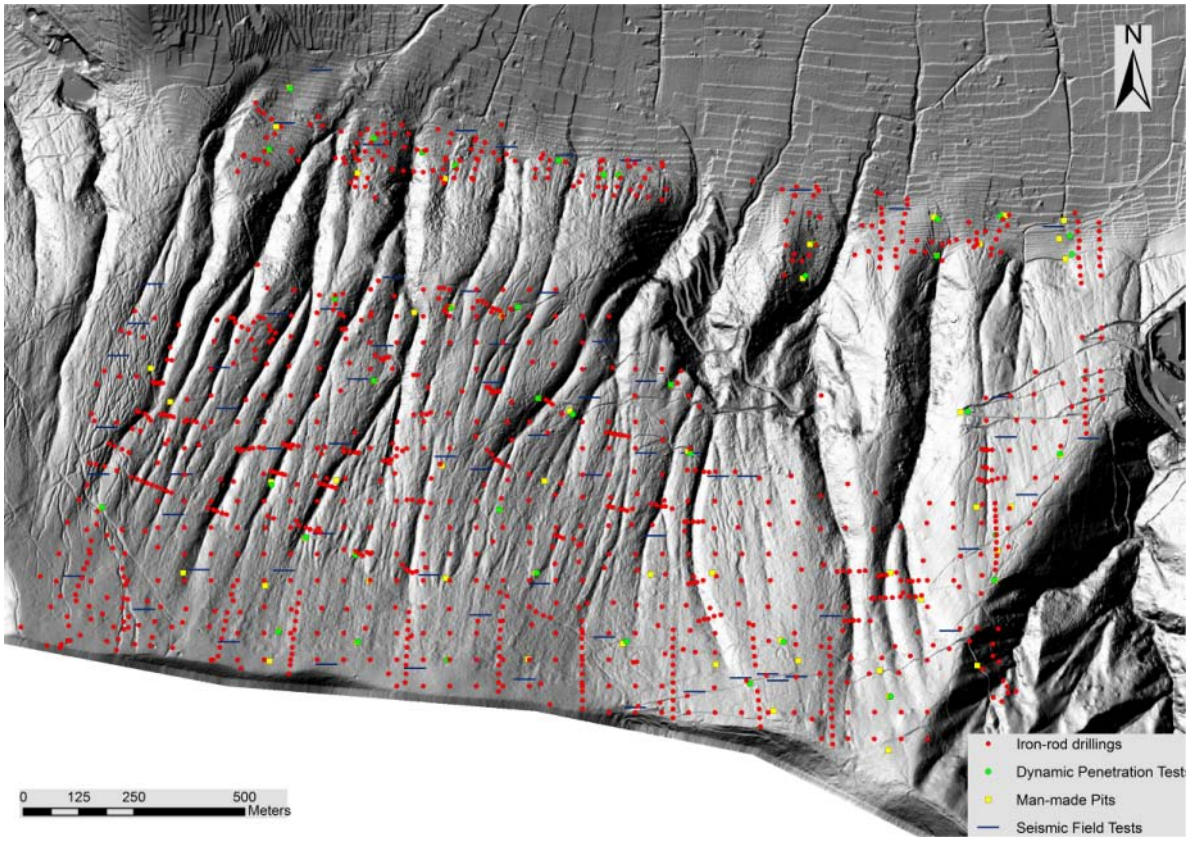

Figure 4.7. DTM obtained on the basis of the data achieved via a LIDAR survey technique (Avioriprese s.r.l., edition of 2005, 1:1,000 scale), with indication of the sites where the in-situ tests were carried out (from the presentation given by Prof. Leonardo Cascini during the 1st meeting of the participatory process in Nocera Inferiore – April 14, 2011).

4.4 GEOLOGICAL SETTING

On the basis of the *in-situ* test results and the field observations on selected areas as well as of the morphological analysis extensively carried out on both topographic maps at different scales and high-detail orthophotos, the thickness distribution of the pyroclastic deposits has been estimated and mapped in the study area. The spatial distribution of the thickness classes is controlled by the morphology of the slope. In particular, the thickness of the pyroclastic deposits reach values of 4 m in the median part of the western sector of the slope where the slope angles range between 20 and 30 degrees; on the contrary, the thickness values do not exceed 1.5 m in the eastern part of the slope where slope angles attain the highest values. Moreover, it must be observed that the main vertical discontinuities of the pyroclastic deposits correspond to: 1) “scarps in calcareous rocks” (usually having a structural control due to the presence of fault scarps or thick strata heads); and 2) “erosion scarps along the gullies” (mainly originated by the erosive processes that grooved the pyroclastic covers and, in some cases, allowed the uncovering of the carbonatic bedrock often in correspondence of the buried tectonic elements).

Moving from the upper part to the toe of the slope, it is possible to recognise – in the western part of the Monte Albino hillslope – the presence of morphological concavities filled by pyroclastic soils and prone to first-failure phenomena. On the contrary, in the

eastern part, streams cutting directly into the carbonatic bedrock are found. In the lateral sectors of the gullies, in the inter-rill areas and along the open slopes there is the presence of morphological elements probably related to landslide and erosive processes. The area at the toe of the slope shows a complex array of fans of different origin, on the top of which lies a part of the urbanized area of the Nocera Inferiore municipality.

Finally, it is worth to observe that the study area corresponds to the northern part of the hydrogeological Unit of the Lattari Mounts, where the groundwater regimen is conditioned by the main tectonic structures originating springs in the lower part of the slope; also ephemeral springs can be found in the upper part of the slope related to suspended groundwaters.

4.5 PREVAILING FLOW-LIKE MASS MOVEMENTS

Owing to the above described geological predisposing factors and taking into account the results of the historical analysis, it can be argued that the Monte Albino hillslopes are prone to different types of rainfall-induced flow-like mass movements (Hutchinson, 2004), namely: hyperconcentrated flows, landslides on open slopes and flowslides. The *hyperconcentrated flows,* as already outlined, essentially relate to erosion processes originated by heavy rains and affect the pyroclastic soils cover along rills as well as on the inter-rills areas. The *landslides on open slopes* affect the triangular facets located at the base of the slope; they have similar characteristics to the phenomenon occurred on March 2005 and are classifiable as “debris avalanches” (Hungr et al., 2001). Finally, in spite of the lack of historical incident data, *flowslides* can be triggered in some areas – e.g., in the so-called “Zero Order Basins” (Dietrich et al., 1986; Cascini et al., 2008) – located in the upper part of Monte Albino massif. The magnitude of the displaced masses could be significantly increased by the materials eventually entrained during the post-failure and propagation stages.

4.6 QUANTITATIVE ASSESSMENT OF THE RISK TO LIFE LOSS

Quantitative Risk Assessment (QRA) has become an indispensable tool for management of landslide hazard and for planning risk mitigation measures at detailed scale (Fell et al. 2008). The framework for the use of QRA for landslides and engineered slopes has been recently reviewed by Fell et al. (2005). In particular, this framework comprises three main components, i.e.: Risk analysis; Risk assessment; Risk management.

Risk analysis includes hazard and consequence analyses. *Hazard analysis* is the process of identification and characterisation of existing and/or potential landslides together with evaluation of their corresponding frequency of occurrence. *Consequence analysis*, in turn, involves:

(a) Identifying and quantifying the elements at risk including property and persons.
(b) Assessing temporal spatial probabilities for the elements at risk;
(c) Assessing vulnerability of the elements at risk.

Risk estimation is the final step of the Risk analysis and essentially consists in the risk calculation through a probabilistic equation. For instance, the annual probability that a

particular person (e.g. the most exposed one to the landslide risk) may lose his/her life $P^i_{(LOL)}$, in general, can be calculated through the formula (Fell et al., 2005):

$$P^i_{(LOL)} = P^i_{(R)} \times P^i_{(T:R)} \times P_{(S:T)} \times V^i_{(D:T)}$$

in which: $P^i_{(R)}$ is the frequency of the landslide events of a given i-magnitude; $P^i_{(T:R)}$ is the probability of the landslide reaching the element at risk; $P_{(S:T)}$ is the temporal spatial probability of the element at risk; $V^i_{(D:T)}$ is the vulnerability of the person with respect to the landslide event.

If the element at risk is exposed to a number of different sizes of landslides of the same classification system, the risks pertaining to each landslide size can be summed in order to obtain the total risk (Corominas et al., 2005). In such a case, the expression (1) can be more conveniently rewritten as:

$$P_{(LOL)} = \sum_{i=1}^{n} \left(P^i_{(R)} \times P^i_{(T:R)} \times P_{(S:T)} \times V^i_{(D:T)} \right)$$

in which: *n* is the number of landslide volume classes.

In the following, with reference to the different kinds of flow-like mass movements that can affect the Monte Albino hillslopes (including flooding phenomena), the adopted procedures and the main results achieved in the quantitative risk – to life loss – assessment and related zoning are briefly summarised.

4.6.1 Risk to life loss posed by the hyperconcentrated flows

As far as the hyperconcentrated flows are concerned, the main purpose of the QRA analyses consisted on the assessment of the risk to life loss posed by the above phenomena to persons living in the urbanised area at the toe of the Monte Albino massif (Nocera Inferiore, Salerno Province). In order to pursue this goal, the methodological approach provided by Fell et al. (2005) and further deepened by Corominas and Mavrouli (2011) was followed.

4.6.1.1. Hazard analysis: danger characterization

For QRA purposes hyperconcentrated flows patterns have been evaluated for each basin via the FLO-2D numerical code (O'Brien et al., 1993), referring to a rainfall event having T = 200 years (namely, the return period to be considered – in Italy – for the design of hydraulic control works) by using a DTM – of squared cells of 5 m x 5 m – obtained via the data achieved by a LIDAR survey .

A synthesis of the input data, in terms of water (Vwater) and sediment (Vsed) volumes, for each of the involved basins, is reported in Table 4.3. It is worth noting that the water volumes were computed on the basis of the VAPI procedure given, for the Campania region, by Rossi and Villani (1995). As far as sediment volumes are concerned, they were estimated thanks to the erosion theory provided by Hungr (1995).

Table 4.3. Input data considered in the analyses dealing with the propagation stage of the hyperconcentrated flows.

Basin	V_{sed} (m^3)	V_{water} (m^3)	V_{tot} (m^3)	V_{sed}/V_{tot}
1	2069.5	3953	6023	0.34
2	2982.5	7052	10035	0.30
3	3119.5	6890	10010	0.31
4	1689.0	3038	4727	0.36
5	705.5	1778	2484	0.28
6	4068.0	7405	11473	0.35
7	2016.0	4918	6934	0.29
8	2964.0	8237	11201	0.26
9	799.0	4586	5385	0.15
10	679.0	2775	3454	0.20

In order to take into account the uncertainties related to rheological properties of the involved mixtures, the following combinations of the parameters τ (shear strength at the base of the propagating flow) and η (dynamic viscosity) were considered:

Scenario 1:

- τ = 1 kPa
- η = 1 Pascal·sec

Scenario 2:

- τ = 1 kPa
- η = 0.1 Pascal·sec

Scenario 3:

- τ = 0.1 kPa
- η = 0.1 Pascal·sec

Areas occupied by the buildings were assumed as “blocked” cells.

Results of FLO-2D numerical code are furnished in terms of depth and velocity of hyperconcentrated flows fronts impacting the exposed houses. In particular, maximum values of both depths and velocities dealing with the cells located around each facility were considered for the analysis purposes. In particular, based on the numerical results, it was estimated that the probability $P_{(T:L)}$ of hyperconcentrated flow phenomena reaching the elements at risks (the houses and their occupants) is equal to:

- 1 if the propagating flows impacts a given house in all the considered scenarios;
- 0.66 if the propagating flows impacts a given house in two scenarios over three;
- 0.33 if the propagating flows impacts a given house in only one scenario.

4.6.1.2. Hazard analysis: frequency analysis

Complete landslide records covering a long time span may be used to perform the probabilistic analyses. According to Corominas and Moya (2008), two probability distributions can be used to assess the annual probability of occurrence of landslides: the binomial distribution and the Poisson distribution. The binomial distribution can be applied for the cases considering discrete time intervals and only one observation for interval (usually a year), as is typically made in flood frequency analysis. The annual probability of a landslide event of a given magnitude which occurs on average one time each T years is:

$P_{(N = 1; t = 1)} = 1/T = P_{(L)}$

in which: T is the return period of the event and $P_{(L)}$ is the expected frequency for future occurrences.

Then, for the problem at hand in which 10 basins may be *potentially* involved by hyperconcentrated flow as a consequence of a rainfall event of return period T = 200 years, the following frequency value results:

$P_{(L),200} = 1/200 \cdot 0.5 = 0.0025$ events/year;

in which: 0.5 the (assumed) probability that a given basin should be really involved by a hyperconcentrated flow during the above rainfall event.

4.6.1.3. Consequence analysis

The $P_{(S:T)}$ terms were computed on the basis of the age of the inhabitants. In particular, the adopted values are reported in the following Table 4.3. It is worth observing that, when information about people living in the impacted houses were lacking, it was safely assumed a $P_{(S:T)}$ value equal to 1.

Table 4.4. Temporal-spatial probability value adopted on the basis of the age of the inhabitants.

Age (years)	**$P_{(S:T)}$**
0 ÷ 5	1
6 ÷ 18	0.75
19 ÷ 65	0.5
66 ÷ 75	0.75
> 75	1

The social vulnerability factors $V_{(D:T)}$ for *persons most at risk living* within the potentially impacted buildings (i.e., having $P_{(T:L)} \neq 0$) have been assessed via a “direct approach” (Wong et al., 1997); the corresponding values are reported in the Table 4.5 as a function of the output data of the FLO-2D numerical code. In particular, these values correspond to the average maximum values of both depth and velocity of

hyperconcentrated flows fronts obtained with reference to the cells surrounding a given house.

Table 4.5. V(D:T) values adopted with reference to the vulnerability of the person most exposed at the hyperconcentrated flow risk.

Case	Flow depth h (m) / velocity v ($m.s^{-1}$)	Adopted $V_{(D:T)}$ value
1. If the building is inundated with sediment-fluid mixture and the person have a high chance to be buried	$h \geq 1$ and $v \geq 5$	0.15
	$h \geq 1$ and $1 \leq v < 5$	0.1
	$0.5 \leq h < 1$ and $v \geq 5$	0.1
2. If the building is inundated with the sediment-fluid mixture and the persons have a low chance to be buried	$h \geq 1$ and $v < 1$	0.08
	$0.5 \leq h < 1$ and $1 \leq v < 5$	0.08
	$h < 0.5$ and $v \geq 5$	0.08
	$0.5 \leq h < 1$ and $v < 1$	0.05
	$h < 0.5$ and $1 \leq v < 5$	0.05
3. If the sediment-fluid mixture strikes the building only	$h < 0.5$ and $v < 1$	0.02

4.6.1.4. Risk estimation

The obtained results, in terms of individual risk to life, were summarised in a map (Figure 4.8) showing, for each of the houses impacted by the hyperconcentrated flows, the corresponding P(LOL) referred to the person most at risk. It is worth noting that some of the most exposed persons have a risk higher than 10^{-4}/annum, namely the risk tolerability threshold established by the Geotechnical Engineering Office (1998) of Hong Kong.

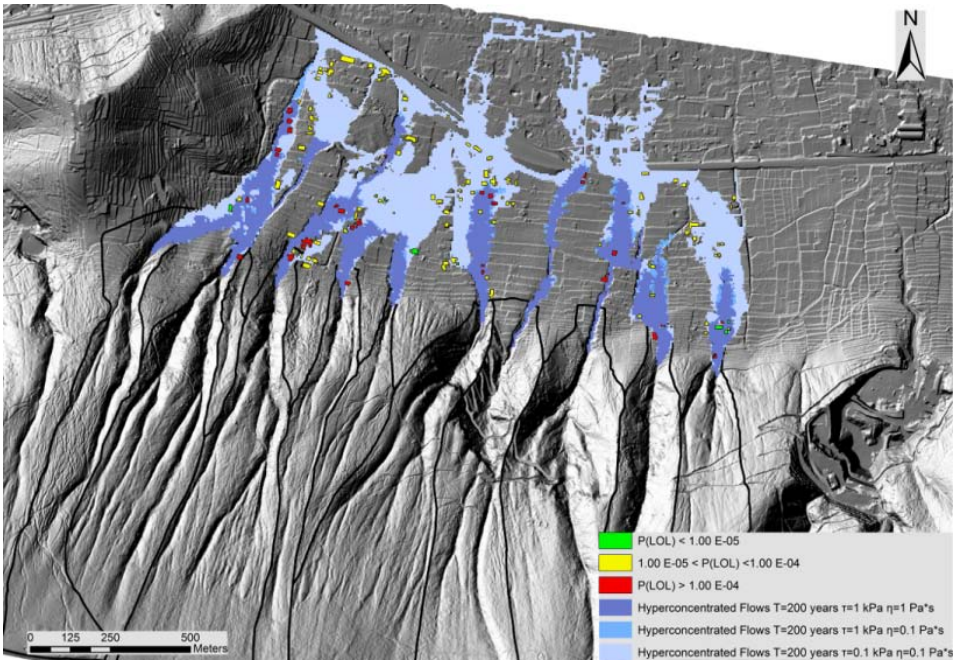

Figure 4.8**. Map of the risk to life loss posed by the hyperconcentrated flows (modified from the presentation given by Prof. Leonardo Cascini during the 3rd meeting of the participatory process in Nocera Inferiore – June 9, 2011).**

4.6.2 Risk to life loss posed by the flowslides

To estimate the risk to life loss from rapid flowslides, the analyses were carried out similarly to those previously described for the hyperconcentrated flows. For rainfall events having a return period T = 200 years, the mobilised soil volumes at the source areas were obtained by using the TRIGRS physically-based model (Baum et al., 2002) as well as the Infinite Slope Model implemented in a GIS environment (Figure 4.9).

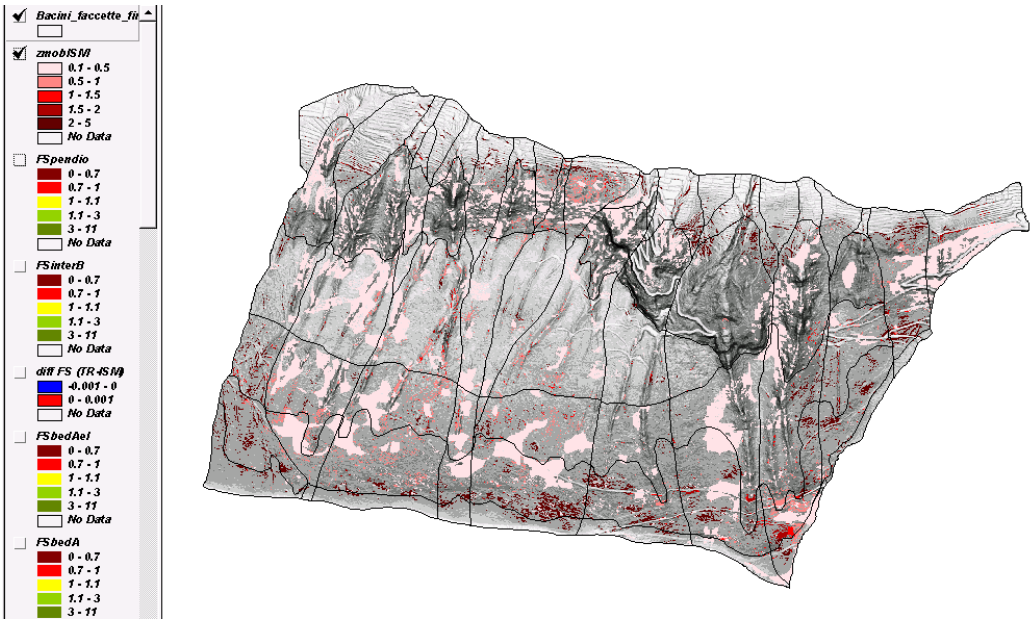

Figure 4.9. Stable (FS > 1) and unstable (FS ≤ 1) areas obtained via the use of the Infinite Slope Model for a rainfall event having a return period T = 200 years.

Then only one scenario of propagation stage (using the FLO-2D numerical code, assuming τ = 1 kPa and η = 2 Pa.s) was considered; the vulnerability values were assumed according to the information provided by the Table 4.6.

Table 4.6. V(D:T) values adopted with reference to the vulnerability of the person most exposed at the flowslide risk.

Case	Flow depth h (m) / velocity v ($m.s^{-1}$)	Adopted $V_{(D:T)}$ value
1. If the building is inundated with debris and the person have a high chance to be buried	$h \geq 1$ and $v \geq 7$	1
	$h \geq 1$ and $3 \leq v < 7$	0.8
	$0.5 \leq h < 1$ and $v \geq 7$	0.8
2. If the building is inundated with debris and the persons have a low chance to be buried	$h \geq 1$ and $v < 3$	0.4
	$0.5 \leq h < 1$ and $3 \leq v < 7$	0.4
	$h < 0.5$ and $v \geq 7$	0.4
	$0.5 \leq h < 1$ and $v < 3$	0.2
	$h < 0.5$ and $3 \leq v < 7$	0.4
5. If the debris strikes the building only	$h < 0.5$ and $v < 3$	0.05

The obtained results, in terms of individual risk to life, were summarised in a map (Figure 4.10) showing, for each of the houses impacted by the flowslides, the corresponding $P_{(LOL)}$ referred to the person the most at risk. Obviously, passing from the hyperconcentrated flow to flowslide phenomena, the number of the most exposed persons having a risk higher than 10^{-4}/annum strongly increases as $V_{(D:T)}$ values increase.

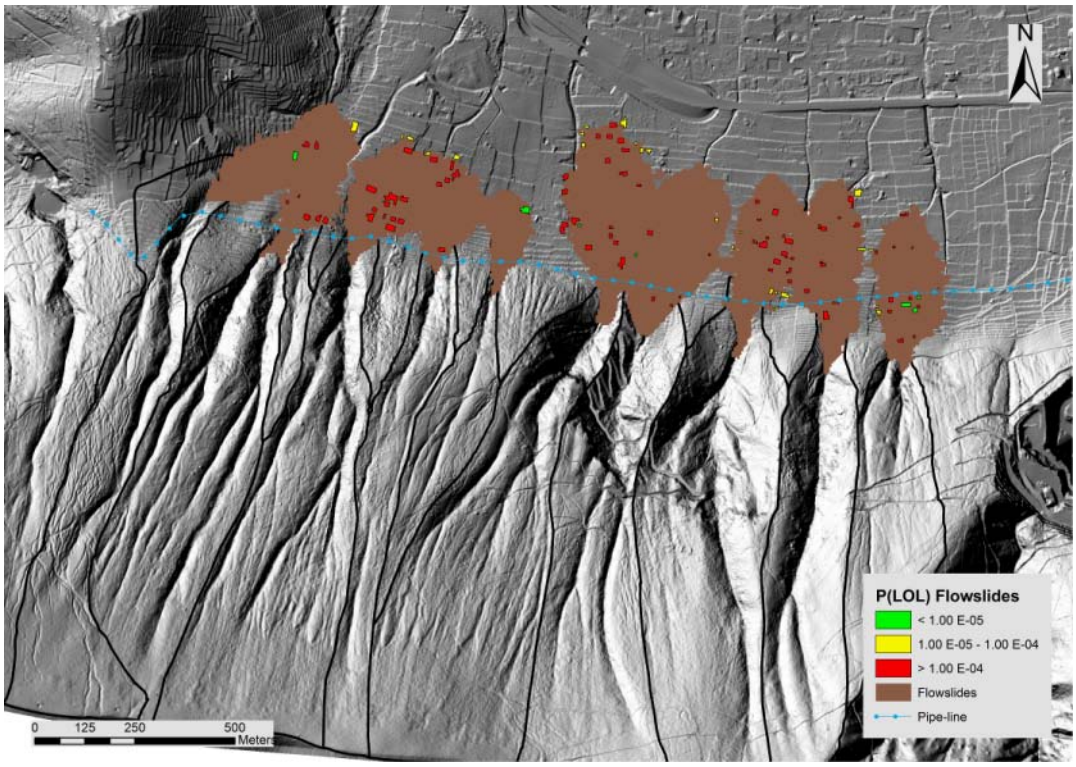

Figure 4.10. Map of the risk to life loss posed by the flowslides (modified from the presentation given by Prof. Leonardo Cascini during the 3rd meeting of the participatory process in Nocera Inferiore – June 9, 2011).

6.3 Risk to life loss posed by the landslides on open slopes

Referring the risk to life loss posed by the landslides on open slopes, the run-out distance was computed by adopting a heuristic criterion, taking into account the shape of the ancient alluvial fans. The landslide frequency $P_{(L)}$ was computed considering that, on the basis of historical information, four events occurred, over a period of 80 years, in a total of 10 open slopes. As a consequence:

$$P_{(L)} = (4/80)\cdot(1/10) = 0.005/\text{annum}$$

The vulnerability $V_{(D:T)}$ was, in turn, estimated considering the criterion explained in Figure 4.11, similar to that proposed by Wong (2005). The obtained results, in terms of individual risk to life, were summarised in a map (Figure 4.12) showing, for each of the houses impacted by the flowslides, the corresponding $P_{(LOL)}$ referred to the person the

most exposed at risk. It is worth to observe that the most exposed persons have, in the case of landslides on open slopes, the highest risk among those obtained for the different kind of flow-like mass movements.

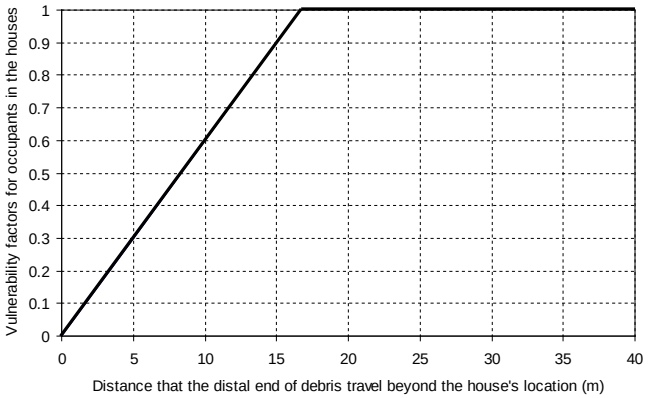

Figure 4.11. Vulnerability factors.

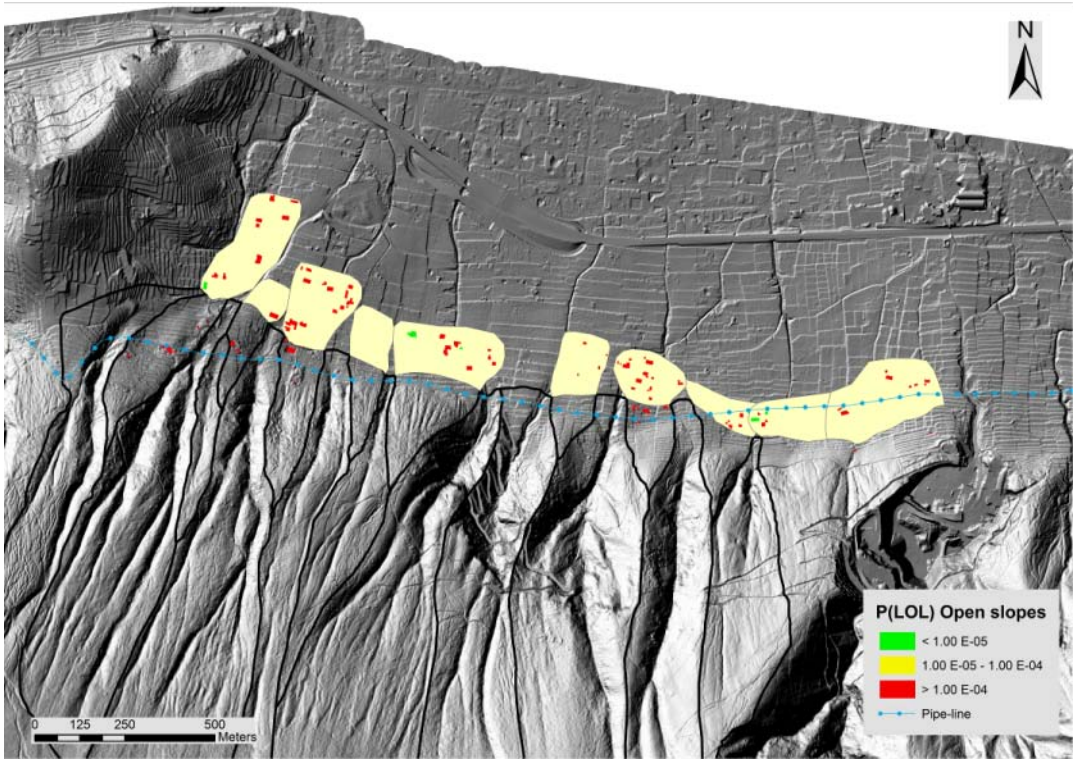

Figure 4.12. Map of the risk to life loss posed by the landslides on open slopes (modified from the presentation given by Prof. Leonardo Cascini during the 3rd meeting of the participatory process in Nocera Inferiore – June 9, 2011).

6.4 Risk posed by the flooding phenomena

To estimate the risk to life loss by flooding, a rainfall event having a return period T = 100 years was considered for the analysis. On the basis of the results obtained via

the FLO-2D numerical code, the vulnerability values were assumed according to the information provided by Table 4.7. The obtained results, in terms of individual risk to life, were summarised in a map (Figure 4.13) showing, for each of the houses impacted by the flood, the corresponding $P_{(LOL)}$ referred to the person most at risk. It is worth noting that the obtained risk values are tolerable for all persons most at risk.

Table 4.7. V(D:T) values adopted with reference to the vulnerability of the person most exposed at the flooding risk.

Case	Flow depth h (m) / velocity v ($m.s^{-1}$)	Adopted $V_{(D:T)}$ value
1. If the building is inundated with the water and the person have a high chance to be buried	$h \geq 1$ and $v \geq 5$	0.1
	$h \geq 1$ and $1 \leq v < 5$	0.05
	$0.5 \leq h < 1$ and $v \geq 5$	0.05
2. If the building is inundated with the water and the persons have a low chance to be buried	$h \geq 1$ and $v < 1$	0.025
	$0.5 \leq h < 1$ and $1 \leq v < 5$	0.025
	$h < 0.5$ and $v \geq 5$	0.025
	$0.5 \leq h < 1$ and $v < 1$	0.01
	$h < 0.5$ and $1 \leq v < 5$	0.01
3. If the water strikes the building only	$h < 0.5$ and $v < 1$	0.005

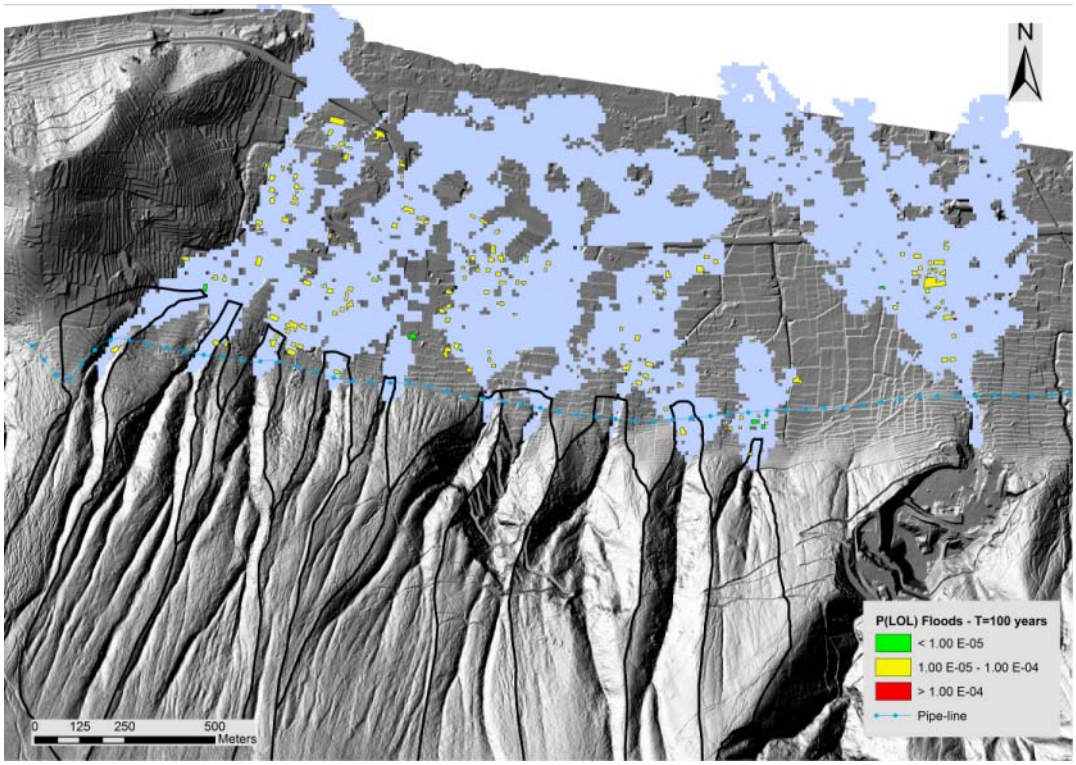

Figure 4.13. Map of the risk to life loss posed by the flooding phenomena (modified from the presentation given by Prof. Leonardo Cascini during the 3rd meeting of the participatory process in Nocera Inferiore – June 9, 2011).

6.5. Societal Risk

The results obtained from QRA analyses can be used also to estimate a "societal risk", i.e. *the risk of widespread or large scale detriment from the realization of a defined risk,*

the implications being that the consequence would be on such a scale as to provoke socio/political response (Leroi et al., 2005). The estimation of the societal risk allows the achievement of different purposes, among which the ranking of the portions of a given urbanised territory at landslide risk and, thus, the prioritization of the areas needing mitigation measures.

In order to pursue this aim, the urbanised area at the toe of the Monte Albino massif was subdivided in six sectors whose shape and size were established on the basis of the calculated run-out distances. Then, on the basis of the QRA results obtained – for all the considered flow-like mass movement risk (excluding floods) scenarios – in terms of annual probability of loss of live for the persons living within the exposed houses, the maximum number of equivalent victims (Wong et al., 1997) to be expected for each of the considered sectors was assessed. This allowed the ranking of the sectors at risk, as shown in Figure 4.14. It is worth noting that the most exposed sectors are those labelled with symbols S2, S5 and S4 where an equivalent number of victims equal to 149, 106 and 78 can be respectively expected.

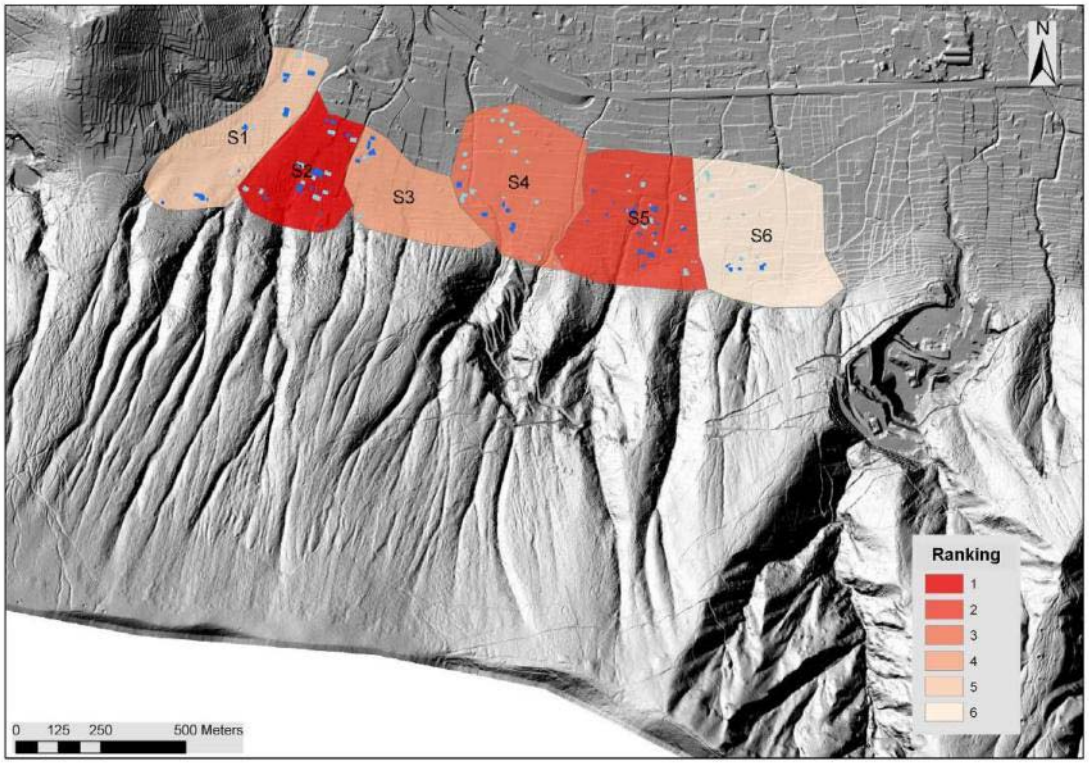

Figure 4.14. Ranking of the sectors at flow-like mass movement risk established for the urbanised area at the toe of the Monte Albino massif. The houses highlighted in blue are those for which the risk to life loss for the person most at risk living inside is the highest.

REFERENCES

Baum, R.L., Savage, W.Z., Godt, J.W. (2002) TRIGRS - a FORTRAN program for transient rainfall infiltration and grid-based regional slope-stability analysis. U. S. Geological Survey Open-File Report 02-0424.

Beguinot, C. (1957) La pianificazione urbanistica della Valle del Sarno: questioni di metodo per la valutazione dell'ambiente, Napoli 1957 (in Italian).

Cascini L., Cuomo S., Guida D. (2008) - Typical source areas of May 1998 flow-like mass movements in the Campania region, Southern Italy. Engineering Geology, 96 (3), p.107-125.

Cimmelli, V. 1990. Università, borghesia e popolo a Nocera dei Pagani nei secoli XVII e XVIII, in "Rassegna storica salernitana", VII, (1990) 2, pp. 93-116 (in Italian).

Corominas, J., Mavrouli, O. (coordinators) (2011) Guidelines for landslide susceptibility, hazard and risk assessment and zoning. Deliverable 2.4 of the Work Package 2.1 - Harmonization and development of procedures for quantifying landslide hazard. SafeLand Project - 7th Framework Programme Cooperation Theme 6 Environment (including climate change) Sub-Activity 6.1.3 Natural Hazards.

Corominas, J., Copons, R., Moya, J., Vilaplana, J.M., Altimir, J., Amigó, J. (2005) Quantitative assessment of the residual risk in a rockfall protected area. Landslides, 2: 343-357.

Corominas, J., Moya, J. (2008) A review of assessing landslide frequency for hazard zoning purposes. Engineering Geology, 102:193-213.

Costa, J.E. (1988) Rheologic, geomorphic, and sedimentologic differentiation of water floods, hyperconcentrated flows, and debris flows. In: V.R. Baker, R.C. Kochel, and P.C. Patton (eds.), Flood Geomorphology, John Wiley and Sons, New York, pp. 113-122.

Dai, F.C., Lee, C.F., Ngai, Y.Y. (2002) Landslide risk assessment and management: an overview. Engineering Geology 64:65-87.

D'Elia, C. 1994. Bonifiche e Stato nel Mezzogiorno (1815-1860), Napoli (in Italian).

Dietrich, W.E., Reneau, S.L., Wilson, C.J.(1986) Hollows, colluvium and landslides in soil-mantled landscapes. In: Abrahamas, A.D. (Ed.), Hillslope processes. Allen and Unwin, pp. 361–388.

De Natale, G., Troise, C., Pingue, F., Mastrolorenzo, G., Pappalardo, L. (2006) The Somma–Vesuvius volcano (Southern Italy): Structure, dynamics and hazard evaluation. Earth-Science Reviews, 74: 73– 111. doi:10.1016/j.earscirev.2005.08.001

Fell, R., Corominas, J., Bonnard, Ch., Cascini, L., Leroi, E., Savage, W.Z. on behalf of the JTC-1 Joint Technical Committee on Landslides and Engineered Slopes (2008) Guidelines for landslide susceptibility, hazard and risk zoning for land use planning. Engineering Geology, 102: 85-98.

Fell, R., Ho, K.K.S., Lacasse, S., Leroi, E. (2005) A framework for landslide risk assessment and management. In: Hungr O., Fell R., Couture R., Eberhardt E. (eds.) Landslide Risk Management. Taylor and Francis, London, pp. 3-26.

Geotechnical Engineering Office (1998) Landslides and Boulder Falls from Natural Terrain: Interim Risk Guidelines. GEO Report No. 75. Geotechnical Engineering Office, The Government of the Hong Kong Special Administrative Region.

Hungr, O. (1995) A model for the runout analysis of rapid flow slides, debris flows and avalanches. Canadian Geotechnical Journal, 32: 610-623.

Hungr, O., Evans, S.G., Bovis, M.J. & Hutchinson J.N. (2001) A review of the classification of landslides of the flow type. Environmental & Engineering Geoscience, VII (3): 221-238.

Hutchinson, J.N. (1988) Morphological and Geotechnical parameters of Landslides in relation to Geology and Hydrogeology. State of the art Report. Proceedings of the V Int. Symposium on Landslides, Lausanne, Vol. 1, pp. 3 – 35.

Hutchinson, J.N. (2004) Review of flow-like mass movements in granular and fine-grained materials. Proceedings of the Int. Workshop "Flows 2003 - Occurrence and Mechanisms of Flows in Natural Slopes and Earthfill", pp. 3 – 16.

Marciani, F. (1930) Per la bonifica integrale dell'Agro Nocerino. Relazione presentata a S.E. il Prefetto di Salerno. 16.3.1930, Salerno 1930 (in "Il Picentino", giugno 1931) [BNN Misc B 42(24] (in Italian).

Migale, L.S., Milone, A. (1998) Colate di fango in terreni piroclastici della Campania. Primi dati della ricerca storica, Rassegna storica salernitana, n.s., XV/2, , n. 30, dicembre, 235-271 (in Italian).

O'Brien, J.S., Julien, P.Y., Fullerton, W.T. (1993) Two-dimensional water flood and mudflow simulation. Journal of Hydraulic Engineering ASCE, 119(2): 244-261.

Operative Unit 2.38. (1998). Ricerca storica sulle colate di fango in terreni piroclastici della Campania. G.N.D.C.I.-C.N.R. Report. University of Salerno, Italy (in Italian).

Orlando, G. (1884) Storia di Nocera de' Pagani, voll. 3, Editore Tocco, Napoli (in Italian).

Pucci, R. 1995. Il Vescovado: il casale, gli abitanti, la chiesa. in Radici nocerine. La storia al servizio del futuro, vol. I, Nocera (1995) pp. 49-67 (in Italian).

Rolandi, G., Paone, A., Di Lascio, M., Stefani, G. (2007) The 79 AD eruption of Somma: The relationship between the date of the eruption and the southeast tephra dispersion. Journal of Volcanology and Geothermal Research 169: 87–98. doi:10.1016/j.jvolgeores.2007.08.020

Rossi, F., Villani, P. (1995) Valutazione delle piene in Campania. Pubbl. n. 1470 del GNDCI-CNR.

Scandone, R., Giacomelli, L., Fattori Speranza, F. (2008) Persistent activity and violent strombolian eruptions at Vesuvius between 1631 and 1944. Journal of Volcanology and Geothermal Research, 170: 167–180. doi:10.1016/j.jvolgeores.2007.09.014

Wong, H.N., Ho, K.K.S., Chan, Y.C. (1997) Assessment of consequence of landslides. Proceedings of the International Workshop on Landslide Risk Assessment, Honolulu, Hawaii, USA, pp. 111-149.

Wong, H.N. (2005) Landslide risk assessment for individual facilities. In: Hungr O., Fell R., Couture R., Eberhardt E. (eds.) Landslide Risk Management. Taylor and Francis, London, pp. 237-296.

5 ROCKFALLS AT THE SOLÀ D'ANDORRA (ANDORRA)

(UPC)

5.1 INTRODUCTION

The objective here is to present a methodology for the quantification of the risk for buildings which are located at the bottom of a slope and are exposed to rockfalls (Corominas and Mavrouli, 2010). The proposed methodology takes into account the fragmental nature of the rockfalls and the structural characteristics of the impacted buildings. It is analytical and it includes individual sub-procedures allowing their refinement according to information available, the scale of work, and the desired degree of the detail. The local conditions are taken into account including the topographical relief and the limits of the built area.

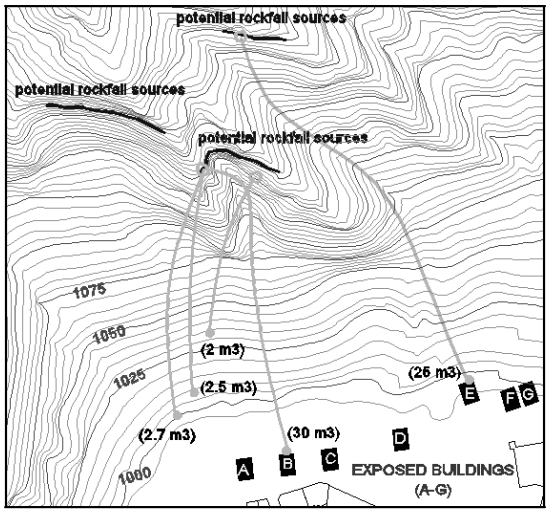

Figure 5.1. Partial view of the study area of Santa Coloma, Principality of Andorra. Potential sources, trajectories, stop points and volumes of some re cent rockfall events are shown.

First of all, the methodology with its sub-procedures is presented through an application example of the Andorra Principality. At the end, a discussion is made on its possibilities and limitations.The study area is a slope situated next to the urban area of Santa Coloma, in the Principality of Andorra, located in the east-central Pyrenees (Figure 5.1). It experiences a relatively high rate of rockfall activity and has been the object of several studies on rockfall hazard during the last years (Copons, 2004; Copons et al., 2005; Corominas et al., 2005). The outcropping rock consists of densely fractured granodiorite and was shaped by Pleistocene glaciers that after their retreat generated the steep slopes of the valley. The intense rockfall activity has produced thick talus deposits which have been partly developed mainly during the 1970s and 1980s.

5.1.1 General procedure

For the QRA of rockfall threatened developed areas, an integrated analytical methodology is proposed here, for application at site-specific scale. The general equation of the rockfall risk is given as follows:

$$R = \lambda(R_i) x P(D:R_i) x P(S:T) x V(E:S) x C$$

in which: R is the expected loss due to rockfall; $\lambda(R_i)$ is the frequency of a rockfall of magnitude I; $P(D:R_i)$ is the probability of a rockfall reaching the element at risk; P(S:T) is the temporal spatial probability of the element at risk; V(E:S) is the vulnerability of the exposed element at risk to impact by a rock fall of magnitude I; and C is the value of the element at risk.

The terms λ (R_i) and $P(D:R_i)$ represent the hazard; the term P(S:T) represents the exposure and the term V(E:S) represents the vulnerability. The previous equation allows the calculation of the risk due to the occurrence of a single rockfall size only. To obtain total risk, all potential rockfall sizes must be considered. In the case that elements at risk consist of buildings, the damage capability of the rockfall is given by its velocity or kinetic energy rather than by its size. Consequently, the above mentionned equation must be substituted by the following equation to obtain the expected annual risk:

$$R_r(P) = \sum_{i=1}^{i} \sum_{j=1}^{j} \left[\lambda(R_i) x P(E_j : R_i) x V(R_{ij}) \right] x C$$

in which: $R_f(P)$ is the expected annual loss to the property due to rockfall, relative to the value of the building; $\lambda(R_i)$ is the annual frequency of a rockfall with a magnitude "i"; $P(E_j:R_i)$ is the probability of a rockfall reaching the building with a kinetic energy. The latter is calculated as a function of the magnitude (volume) "i" and the velocity "j". The kinetic energy levels are those leading to the respective damage states; $V(R_{ij})$ is the vulnerability of the building for a rockfall of magnitude "i" and velocity "j"; and C is the value of the building.

The temporal spatial probability of the element at risk P(S:T) for static elements such as buildings is 1. Consequently, it is not considered here.

5.1.2 Frequency of rockfalls $\lambda(R_i)$

Frequency of rockfalls can be calculated by means of statistical analyses of rockfall records. (Hungr et al., 1999; Dussauge-Peisser et al., 2002; Guzzetti et al., 2003).

Unfortunately, the availability of such records is restricted to a few road and railway maintenance offices and national park services. Historical records are often too short in comparison with the time scale of large rockfall events. In the case of Santa Coloma, the available rockfall record covers a timespan of about 50 years but it is complete only for the last 15 years when the Andorran administration established a systematic inventory of all the rockfall events occurring in the area. This inventory covers exclusively rockfall events larger that 1 m^3 that were noticed by the inhabitants of the area and by

annual surveys with helicopter flights. The rockfall series has been completed by intensive dendrogeomorphological analyses of damaged trees (Moya et al., 2010) and has allowed extending the rockfall record to the last 40 years. The average annual frequency λ_T for all rockfall sizes is 0.5 events per year. This figure must be considered a minimum value because the occurrence of small-size rockfall events without producing impacts on trees cannot be absolutely disregarded.

The magnitude (volume) - frequency relation of the inventoried rockfalls in the entire Santa Coloma area is shown in Table 5.1 and it is assumed to be the same for the study site. $\lambda(Ri)$ is the product of λ_T with the relative frequency of each volume class.The volume corresponds to that measured at the source.

However, the volume to consider in the trajectographic analysis is not an evident issue. A rockfall may involve the displacement of a single or several blocks. It may also begin by the detachment of a more or less coherent rock mass that after the first impact with the slope face splits into several pieces. The latter is the case of a fragmental rockfall which is characterized by the independent movement of individual rock fragments after detachment from a rock face (Evans and Hungr, 1993). The fragmentation mechanism is not currently included in trajectographic models and may strongly affect the reliability and validity of the results. The detachment of large rock masses without considering their fragmentation after the first impacts on the ground will give unrealistic travel distances in excess of what should be expected. The important effect of the number and mean size of fragmented rocks on the hazard due to a single event has been discussed by Jaboyedoff et al. (2005) who proposed the empirical evaluation of the latter.

Table 5.2 shows the average distribution of block sizes from several rockfall events of the Santa Coloma area inventoried during the last decade. Both the number and size of the blocks increase with the volume of the detached rock mass. The assumption made in the methodology presented here is that the frequency of falling blocks of a given size has to be increased by adding the frequency of the blocks of the same size produced by fragmentation of larger rockfall events. Thus the frequency of rockfalls of a defined block size “s” is given by the following expression:

$$\lambda(Rs) = \sum_{i=1}^{i} [\lambda(R_i) x P(R_s : R_i)] x \lambda_t$$

in which:λ (R_s) is the frequency of blocks of “s” size; $\lambda(R_i)$ is the frequency of rockfalls of “i” volume; $P(R_s:R_i)$: the percentage of blocks of size “s” per every rockfall of volume “i” ; λ_t the annual frequency of rockfalls in the area.

Table 5.3 shows the annual frequency of each block class in Santa Coloma area.

Table 5.1 Rockfall events observed in Santa Colo ma area. $\lambda(Vi)$ is the relative frequency of each volume class and $\lambda(R_i)$ its annual frequency.

Source volume (m^3)	Number of events	$\lambda(V_i)$	$\lambda(R_i)$
≤ 5	14	0.667	0.333
10	4	0.19	0.095
25	2	0.095	0.047
150	1	0.048	0.024

Table 5.2 Number of fragmented blocks of each size class for different volumes of the rock mass detached at the source area.

Block size (m^3)	Volume of the rock mass detached at the source area (m^3)			
	5	10	25	150
1	1	2	4	12
2.5	1	1	1	8
10	0	0	1	2
30	0	0	0	1

Table 5.3 Frequency of different block sizes in the area of Santa Coloma area.

Block size (m^3)	λ(R)
1	1.000
2.5	0.667
10	0.095
30	0.024

5.1.3 Trajectory analysis $P(E_j:R_s)$

For each range of block volume, a three-dimensional probabilistic trajectory analysis has been performed with ROTOMAP32 to define the percentage of possible rockfall paths reaching each exposed building with a given level of kinetic energy. This level is defined by the potential damage states caused to the buildings (Mavrouli and Corominas, 2010a) which are: non-structural damage, local damage, partial collapse or extensive to total collapse. The thresholds of E that distinguish between the damage states are calculated by the analysis of the response of the exposed structure to the block impact.

ROTOMAP32 code provides different rockfall paths from different initial velocities, respective directions and exact locations of the rockfall sources. Some rockfall sources produce paths that have higher probability of affecting some buildings than others and this is taken into account in the analysis. The potential range of kinetic energy E of the rock blocks reaching the buildings is also calculated. The blocks that reach a particular building are classified into groups with respect to their E, and the probability of each group is evaluated.

The model was calibrated to comply with past rockfall events data. The results were considered acceptable when the stop points from the simulation approximated those of the real events. In the case of the blocks of 30 m^3 size, the velocity of impact onto the buildings is not known and the restitution coefficients and limit angles were calibrated through successive trials to reproduce the path of the block. However, the obtained velocities from the calibration indicate extremely high levels of E, the reliability of which should be validated with a back-analysis of future rockfall events.

After the calibration, the trajectory analysis was performed. Given the detailed work scale, the risk in this example is evaluated using the following equation and the probability of reaching directly a target building with a certain E was obtained by:

$$P(E_j:R_i)= \frac{n_E}{n_T}$$

in which: n_E is the number of block paths reaching any particular building with a certain E; and n_T is the total number of block paths.

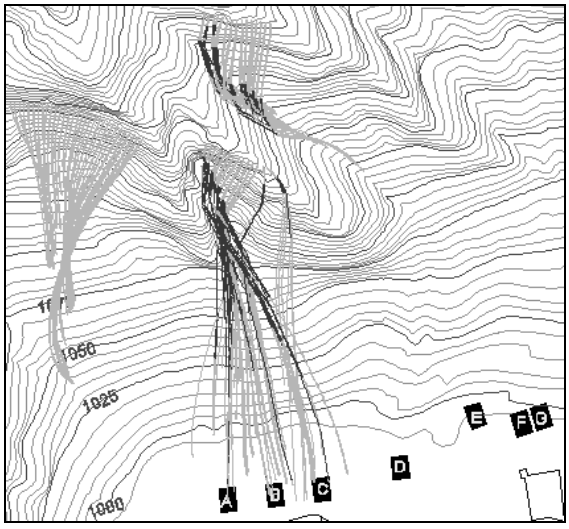

Figure 5.2. Rockfall paths for blocks of 2.5 m^3 size.

The obtained values for the $P(E_j:R_i)$ are shown in Table 5.4. Additionally, Figure 5.2 presents an example of all the potential paths produced by a block of 2.5 m^3, their associated rockfall sources and the potentially affected buildings. The total number of simulations for every magnitude class was 1500.

Table 5.4 Probability of reaching the building with an energy $P(Ej:R_s)$ as calculated in the trajectory analysis.

Building	Block volume (m^3)	Kinetic Energy (KJ)		
		<14	14-28	>28
A	1	0.003	0.008	0.008
	2.5	0	0	0.013
	10	0	0	0.020
	30	0	0	0.104
B	1	0.001	0.003	0.002
	2.5	0	0	0.004
	10	0	0	0.001
	30	0	0	0.037
C	1	0.003	0	0.004
	2.5	0	0	0.011
	10	0	0	0.029
	30	0	0	0.060
D	1	0	0	0
	2.5	0	0	0
	10	0	0	0
	30	0	0	0
E	1	0	0	0

	2.5	0	0	0
	10	0	0	0
	30	0	0	0.015
F	1	0	0	0
	2.5	0	0	0
	10	0	0	0
	30	0	0	0.033
G	1	0	0	0
	2.5	0	0	0
	10	0	0	0
	30	0	0	0.017

The used thresholds that may lead to different damage states that, for this example, were obtained during the sub-procedure that is described in section 5.4 (Table 5.6). They are: < 14 kJ for non-structural damage, 14 – 28 kJ for local or partial structural damage and > 28 kJ for extensive to total collapse.

5.1.4 Vulnerability of the exposed buildings

The exposed elements here are considered to be the buildings which are situated at the bottom of the slope. A single structural typology is considered: a 2-story frame reinforced-concrete frame (RC) structure.

The vulnerability is quantified considering the potential repair cost of the building, with respect to its reconstruction value. To evaluate it, the step-by-step procedure for the response of RC buildings to single rock impacts on their basement column(s), proposed by Mavrouli and Corominas (2010a), is used. It is an analytical methodology that can be adapted to various structural typologies, for the assessment of the physical damage in case of loss of structural and non-structural elements of a building, taking into consideration the potential of a cascade of failures (progressive collapse) which extends to a part or to the entire building, due to the initial loss of the element.

For simple regular frame RC buildings, the damage extent and the potential of progressive collapse depends on the number and damage of the struck element(s) for a rockfall impact of a given E, and their importance for the overall stability of the building. Potential damage can be classified into four damage states: a.) non-structural damage of the infill walls, b.) local structural damage, c.) partial collapse and d.) extensive to total collapse.

In the worked example, it is considered the same building typology as used in Corominas and Mavrouli (2010b) and is shown in Figure 5.3. The results of the analysis for the considered building, which is composed by two frames (three columns) at its exposed façade, 3 frames perpendicularly to it, along its length, and 5 m infill walls in-between the columns, indicate the conditions that lead to the proposed damage states. The four following initial damage scenarios are investigated: loss of a central column, of a corner column, an infill wall and two or more central or corner columns perpendicularly to the exposed façade, depending on the impact location and the kinetic energy that determines the capacity of a block to destroy one or more columns. The considered scenarios are unfavourable regarding the direction of the rock blocks perpendicularly to the exposed façade and are considered here from the safety side.

The proposed vulnerability is calculated as the sum of the products of the probability of encounter of the rock block with a structural or non-structural element and the associated RRC:

$$V(R_{ij}) = \sum_{k=1}^{k} (P_{e,k} \text{ x } RRC_k)$$

in which: V(R ij) is the vulnerability for a rock block with a magnitude i" and velocity "j"; Pe,k is the encounter probability of a rock with a possible structural and non-structural element of the building " k" that may be struck by a rock block of magnitude "i"; RRCk is the relative recovery cost that corresponds to the damage of one or more structural and/or non-structural element(s) of the building "k" by a rock block of magnitude "i" and velocity "j". To calculate the probability of each impact location, the following equations are used:

$$P_{ec} = \frac{l_c + d}{a \sin\psi}$$

$$P_s = \frac{1}{n}\frac{l_c + d}{a \sin\psi}$$

$$P_w = \frac{1}{n}\frac{l_w + d}{a \sin\psi}$$

in which: P_{ec} is the probability of encounter with any exposed column; P_s is the probability of encounter with a specific column; P_w is the probability of encounter with an infill wall; n is the number of projected columns on a line vertical to the rock path; l_c is the column width; l_w is the infill-wall width; a is the distance between centers of columns; d is the rock block diameter; ψ is the angle between the rock path and the façade plane.

For the given building, the probability of encounter with a non-structural or a structural member is given by Table 5.5. The impact location is expected to occur exclusively in the structural elements present at the first level of the building.

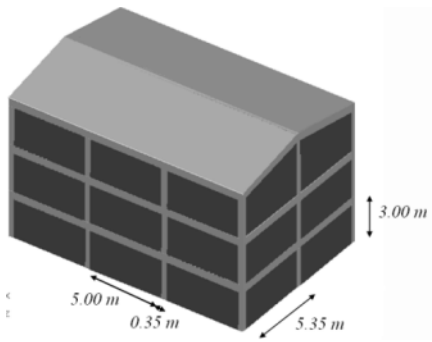

Figure 5.3. Typical structural typology of the area.

Table 5.5 Probability of encounter with a non-structural or a structural member.

Building	m^3	Central column	Corner column	Any column
A, B, C, D, E, F, G	1	9.91E-02	1.98E-01	2.97E-01
	2.5	1.27E-01	2.53E-01	3.80E-01
	10	1.88E-01	3.77E-01	5.65E-01
	30	2.62E-01	5.24E-01	7.86E-01

The RRC expresses the cost of the repair in relation to the value of the building. It is calculated in function of the physical structural and non-structural damage, translated into economical cost, for every potential location of the impact (Mavrouli and Corominas 2010b).

For the considered building, the RRC is provided by Table 5.6, for every scenario (impact location and kinetic energy sufficient to cause the loss of one or more elements)

Table 5.6 Conditions leading to every damage state and associated RRC

Damage state	Damaged element	E (kJ)	RRC
No damage	Any column	< 14	0
Non-structural damage	External infill wall		0.01
Local structural damage	Central column	14 - 28	0.2
Partial structural collapse	Corner column	14 - 28	0.4
Generalised damage	Two or more columns	> 28	1

Considering these, the vulnerability is calculated in function of the block diameter and kinetic energy as shown in Table 5.7.

Table 5.7 Vulnerability $V(R_{ij})$ for every possible impact energy

Building	m	E (kJ)		
		< 14	14 - 28	> 28
A, B, C, D, E, F, G	1	1.00E-02	1.09E-01	3.07E-01
	2.5	1.00E-02	1.37E-01	3.90E-01
	10	1.00E-02	1.98E-01	5.75E-01
	30	1.00E-02	2.72E-01	7.96E-01

5.1.5 Calculation of the relative risk

For every building, the relative risk to its value is calculated by substituting the rockfall frequency $\lambda(R_i)$ by the block size frequency $\lambda(R_s)$ as discussed previously. The results are presented in Table 5.8.

Table 5.8 Relative risk for every building $R_r(P)$

Building	m^3	$R_r(P)$ for every magnitude i	Total $R_r(P)$ for the building
A	1	1.32E-03	7.86E-03
	2.5	3.46E-03	
	10	1.09E-03	
	30	1.99E-03	
B	1	9.12E-04	2.69E-03
	2.5	1.04E-03	
	10	3.64E-05	
	30	7.01E-04	
C	1	1.26E-03	6.78E-03
	2.5	2.78E-03	
	10	1.60E-03	
	30	1.15E-03	
D	1	0.00E+00	0.00E+00
	2.5	0.00E+00	
	10	0.00E+00	
	30	0.00E+00	
E	1	0.00E+00	2.92E-04
	2.5	0.00E+00	
	10	0.00E+00	
	30	2.92E-04	
F	1	0.00E+00	6.36E-04
	2.5	0.00E+00	
	10	0.00E+00	
	30	6.36E-04	
G	1	0.00E+00	3.31E-04
	2.5	0.00E+00	
	10	0.00E+00	
	30	3.31E-04	

The global risk for an area is then evaluated by summing up the products of the relative risk for all the exposed buildings with their values:

$$R(P) = \sum (R_r(P) * C)$$

in which: R(P) is the global risk for an area; Rr(P) is the relative risk for a building; and C is the value of the building.

The total relative risk for the entire area is the sum of the relative risk for all buildings and equal to $2.16x10^{-2}$. In buildings A, B, and C, the risk is higher for small rock sizes (1 and 2.5 m^3). This is due to the higher frequency associated to them. Instead, buildings E, F, G are affected by the largest blocks only. This is because, for these particular cases, only blocks of 30 m^3 are able to reach the building locations with the required energy level to produce damage (Table 5.4). It has to be taken into account that these are results of a simulation and they should be validated with real cases. Building D has no risk because none of the modelled trajectories passes through the building location.

5.1.6 Conclusions

The calculation of risk using the proposed methodology is quantitative and may be expressed in terms of annual loss. The proposed procedure takes into account the fragmentation on the detached rock masses which otherwise would have produced longer runout distances and higher impact energies in the trajec- tographic analyses. The increase of the number of blocks of small size caused by the fragmentation of the detached rock mass has been included in the assessment of the frequency of the different block sizes. However, this may not prevent an underestimation of their kinetic energy and runout distance. It is thus necessary a validation with further rockfall events.

In what concerns the vulnerability the methodology includes a weighted vulnerability that takes into account the encounter probability of the block with key structural and non-structural ele- ments and the subsequent damage. Thus, the vulnerability can be integrated into the risk equation. The worked example includes only a particular structural building typology and it is necessary to add other typologies before generalizing the procedure.

The methodology may be used for the calculation of the risk for a building that is impacted at its basement by a single block fragmented rockfall, as well as for the calculation of the global risk for a built area, by aggregation. The application example was carried out at site-specific scale. This analysis indicated that not all the exposed buildings have the same impact probability; instead rockfalls follow preferential paths towards some of them. As a result the risk for each building is different even though the vulnerability and their location with reference to the topographic elevation under the rockfall source are the same. This can be useful for the optimiza- tion of the cost/benefit relationship of protection measures.

References

Agliardi, F., Crosta, G.B., Fratini, P. (2009): Integrating rockfall risk assessment and countermeasure design by 3D modelling techniques. Natural Haz-ards and Earth System Sciences, 9, 1059–1073

Bell, R. and Glade, T. (2004): Quantitative risk analysis for landslides - Examples from Bvldudalur, NW-Iceland. Natural Hazards and Earth System Scien-ces, 4(1): 117-131

Copons, R. (2004): Avaluació de la perillositat de caigudes de blocs a Andorra la Vella (Princi-pat d'Andorra), PhD Thesis, UB, Barcelona, 244pp.

Copons, R., Vilaplana, J.M., Corominas, J., Alitmir, J. Amigo, J. (2005): Rockfall hazard management policy in urban areas: the Andorran ex-perience. In: T. Glade, M. Anderson and M. Crozier, Editors, Landslide Hazard and Risk, John Wiley & Sons, Chichester, 675–698.

Corominas, J., Copons, R., Moya, J., Vilaplana, J.M Alitmir, J. Amigó, J. (2005): Quantita-tive assessment of the residual risk in a rock fall pro-tected area. Landslides, 2: 343–357, 2005.

Corominas, J. and Mavrouli, O. (2010). Method-ology for the Quantitative Risk Assessment for Rock-falls at Site-Specific Scale. In J-P Malet, T. Glade & N. Casagli (editors). Mountain Risks: Bringing Science to Society. CERG Editions, Strasbourg, 343-350.

Dussauge-Peisser, .A., Helmstetter, C., Grasso, J.R., Hantz, D., Desvareux P., Jeannin, M. & Giraud, A. (2002).:Probabilistic approach to rockfall hazard assessment: potential of historical data analysis. Natural Hazards and Earth Systems Sciences 2, 15-26.

Guzzetti, F., Reichenbach, P. & Wieczorek, G.F. (2003): Rockfall hazard and risk assessment in the Yosemite Valley, California, USA. Natural Hazards and Earth System Sciences 3, 491-503.

Evans, S.G. and Hungr, O. (1993). The assessment of rockfall hazard at the base of talus slopes. Canadian Geotechnical Journal, 30: 620-636

Hungr, O., Evans, S.G., & Hazzard, J (1999).: Magnitude and frequency of rock falls and rock slides along the main transportation corridors of south-western British Columbia. Canadian Geotechnical Journal 36, 224-238, 1999.

Jaboyedoff, M.,Dudt, J.P. & Labiouse, V. (2005). An attempt to refine rockfall hazard zoning based on the kinetic energy, frequency and fragmenta-tion degree. Natural Hazards and Earth System Sciences, 5, 621–632

Li, Z.H, Huang, H.W, Xue, Y.D., & YIN, J.(2009): Risk assessment of rockfall hazards on high-ways, Georisk, 3 (3): 147 – 154.

Mavrouli O. and Corominas, J. (2010a): Vul-nerability of simple reinforced concrete buildings in front of the rockfall impact. Landslides, 7 (2): 169-180, 2010a.

Mavrouli O. & Crorominas, J. (2010b): Rock-fall vulnerability assessment for reinforced concrete buildings. Natural Hazards and Earth System Sciences, 10: 2055-2066,

Moya, J., Corominas, J., Perez-Arcas, J. and Baeza, C. (2010). Tree-ring based assessment of rockfall frequency on talus slopes at Solà d'Andorra, Eastern Pyrenees. Geomorphology, 118: 393-408

Roberds, W.J. (2005): Estimating temporal and spatial variability and vulnerability. In: O. Hungr, R. Fell, R. Couture and E. Eberhardt, Editors, Landslide risk management, Proceedings of the International Conference on Landslide Risk Management, Vancou-ver, 31 May–3 June 2005, Taylor & Francis, London, 129–157.

6 ROCKFALLS AT FIUMELATTE (ITALY)

(UNIMIB)

6.1 SPECIFIC ASPECTS OF ROCKFALL RISK

Quantitative risk analysis for all types of natural hazards require the ability of accounting for the probability of specific scenarios of potentially damaging events, and the resulting costs/damage depending on the vulnerability and value of exposed elements (Straub and Schubert, 2008; Uzielli et al., 2008). When dealing with rapidly evolving, long runout landslide types such as fragmental rockfalls (i.e. rockfalls characterised by negligible interaction among falling blocks), the task becomes more difficult. In fact, rockfalls are rare and strongly spatially distributed processes, characterised by complex dynamics and interaction with structures.

In this case, risk analysis requires evaluating: (1) a serie of rockfall hazard scenario over the affected area; (2) the distribution and intensity of impacts on exposed structures; (3) the vulnerability of impacted structures; and (4) the expected cost of specific risk scenarios. A Quantitative Risk Analysis (QRA; Corominas et al., 2005; Fell et al., 2005) for rockfalls should thus be based on sound modelling of rockfall processes, especially when risk analysis is undertaken in order to design and evaluate rockfall protection measures (Bunce et al, 1997; Hungr et al., 1999; Corominas et al., 2005; Straub and Schubert, 2008; Agliardi et al., 2009).

Nevertheless, standard procedures for rockfall risk analysis are still not available, probably because of the difficult assessment of hazard and vulnerability components. The simplest form of rockfall risk analysis consists of a distribution count of elements at risk with different assumed vulnerability falling in different hazard zones. However, this approach does not account quantitatively for the probability of rockfall impact and the vulnerability and value of exposed elements. GEO (1998) proposed guidelines for rockfall QRA based on rockfall inventory in Hong Kong, whereas Straub and Schubert (2008) combined probability theory and 2D numerical modelling in order to improve risk analysis for the design of individual protection structures. Bunce et al. (1997) and Hungr et al. (1999) provide QRA estimates along highways in British Columbia, based on inventories of rockfall events. They provided theoretically sound assessment frameworks, but did not include an evaluation of the probability of impact since they assumed no significant runout from detachment points. QRA for rockfalls in spatially distributed contexts (e.g. urban areas; Corominas et al., 2005), characterised by long runout and complex interactions between rockfall and individual elements at risk, thus requires a quantitative assessment of both rockfall runout and vulnerability (Mavrouli and Corominas, 2010).

In this perspective, Agliardi et al. (2009) have proposed a quantitative risk assessment framework exploiting the advantages of 3D numerical modelling to integrate several risk components, namely: temporal probability of rockfall events, spatial probability and intensity of impacts, vulnerability of elements at risk, and expected costs for different scenarios.

Following the cited work, we present a case study illustrating the entire process of QRA, which has been set up to support and evaluate the design of rockfall risk mitigation structures after a damaging event occurred in 2004 at Fiumelatte, near the village of Varenna, along the world-famous eastern shore of the Como Lake.

6.2 ROCKFALL DISASTER AT FIUMELATTER (VARENNA, ITALY)

The village of Fiumelatte is located on the eastern shore of the Lake of Como, just south of Varenna (Figure 6.1). Rocky cliffs up to 300 m high, with slope inclination locally exceeding 70 degrees, impend the area. They are made of massive or thick-bedded Middle Triassic dolostones of the Esino formation (Carnian), belonging to the upper structural unit of the Grigne massif (i.e. Northern Grigna-Coltignone Unit; Schönborn, 1992). The rock mass is cut by bedding planes gently dipping to the WNW, and steep, NNE trending fractures.

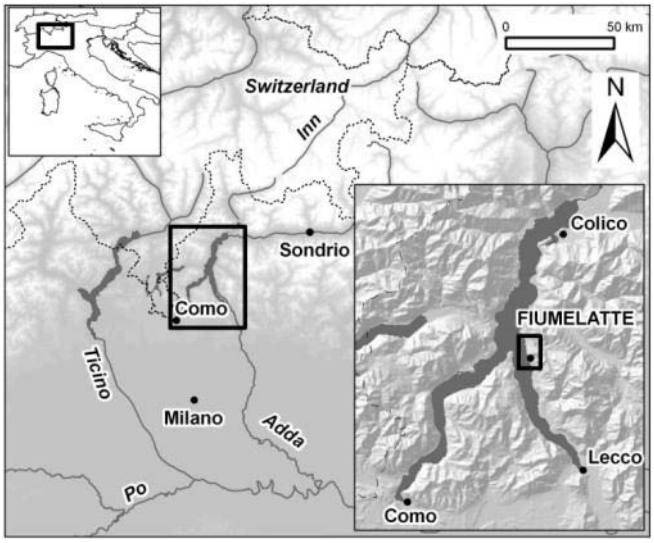

Figure 6.1. Location map of the Fiumelatte case study area (Agliardi et al., 2009).

Between 270 and 500 m a.s.l., the slope consist of discontinuous, partly cemented and forested or bush-covered talus deposits, inclinations in the range 33-38°. Below 270 m a.s.l., colluvial deposits, extensively reworked by artificial terraces, cover the slope toe, with slope inclination varying between 20 and 25°. Most buildings and infrastructures are located in this part of the slope. In particular, the area is crossed by regionally important transportation corridors, including the Lecco-Colico railway, the State Road 36 freeway, and the SP72 road.

The entire area has been historically affected by rockfalls of different size and runout potential, frequently causing damage and fatalities in the context of a moderate to high hazard area (Crosta and Agliardi, 2003). In this specific sector, rockfall events occasionally caused fatalities (e.g. May 1987, 2 casualties in a car on SP72 road) or traffic interruptions, thus requiring the construction of extensive countermeasures (flexible barriers, rock face cleaning and reveting). Nevertheless, no systematic record of rockfall events is available for this area.

On 13 November 2004, about 4-5000 m^3 of rock detached by toppling from a rocky cliff at 650 m a.s.l. above Fiumelatte (Figure 6.2a, b), and fragmented soon at impact upon a rocky bench immediately downslope. Resulting blocks, up to 100 m^3 in volume, bounced and rolled down through a channelled sector of the talus, reaching the lower part of the slope, and then spread over the terraced slope and reached the built area

below. Maximum rockfall runout distance attained about 500 m. Significant lateral dispersion of rockfall trajectories, with a width/length ratio of the runout area up to 0.34 (Crosta and Agliardi, 2004), resulted in a larger affected area and associated damage. Most blocks bounced close to the terraced ground.

Figure 6.2.The 2004 Fiumelatte rockfall event. (a) NW view of the affected area; (b) source area; (c) impacted area; (d) railway station, damaged by the impact of a 30 m3 block; (e) roof of building damaged by a 8 m3 block; (f) three-storey building destroyed by a 96 m3 block (2 casualties occurred here; (g) damaged railway section; (h) building downslope of building in (F), severely damaged by the same 96 m3 block (Agliardi et al., 2009).

6.3 METHODOLOGY

6.3.1 Theoretical framework

The risk assessment methodology illustrated by this case study has been developed with specific reference to the risk posed by fragmental rockfalls to buildings and people inside buildings, and does not account for risk to people outside buildings or to non-static elements at risk (i.e. vehicle traffic).

Rockfall risk is here defined as the annual expected cost due to the impact of rockfall events, and can be regarded as a simple product of three conditional probabilities, vulnerability and value, summed up for all the considered rockfall magnitude scenarios and elements at risk and, according to the following equation (Hungr et al., 1999; Fell et al., 2005):

$$R = \sum_{i=1}^{I} \sum_{j=1}^{J} P(L)_j \cdot P(T|L)_{ij} \cdot P(I|T)_i \cdot V_{ij} \cdot W_i$$

in which: $P(L)_j$ is the "probability of occurrence" of events in the magnitude (i.e. volume) class j; $P(T|L)_{ij}$ is the"probability of reach" (i.e. for block in the volume class j to reach the element i); $P(I|T)_i$ is theprobability that a given element at risk is at the impact location at the time of impact (i.e. temporal spatial probability or exposure); V_{ij} is the vulnerability (i.e. expected degree of loss) of a given element at risk i to the impact of a block in the magnitude class j; and W_i economic value of the element at risk i (building and people inside).

The "probability of impact" of a rock fall in the magnitude class j on the element at risk i can be defined as:

$$P(I)_{ij} = P(L)_j \cdot P(T|L)_{ij} \cdot P(I|T)_i$$

allowing the former equation to be rewritten as:

$$R = \sum_{i=1}^{I} \sum_{j=1}^{J} P(I)_{ij} \cdot V_{ij} \cdot W_i$$

Considering rockfall events as Bernoulli trials (i.e. simple experiments with a random binary outcome as "failure" or "success", the probability that any impact of a rockfall in the volume class j occur on the element at risk i can thus be expressed as (Hungr and Beckie, 1998):

$$P(I)_{ij} = 1 - \left[1 - P(I|L)_{ij}\right]^{N_j}$$

in which: $P(I|L)_{ij} = P(T|L)_{ij} \cdot P(I|T)_i$ is the probability of impact of rockfall on the element at risk i, given that a rockfall event in the volume class j occurs; N_j is the annual frequency of rockfall events in the volume class j.

For $P(I|L)_{ij}$ less than 10^{-3}, and Nj less than 100, Hungr and Beckie (1998) demonstrated that the former equation can be approximated in practice by:

$$P(I)_{ij} = N_j \cdot P(I|L)_{ij}$$

and that the numerical difference between the two is < 5%. The following expression for total rockfall risk can therefore be defined:

$$R = \sum_{i=1}^{I} \sum_{j=1}^{J} N_j \cdot P(T|L)_{ij} \cdot P(I|T)_i \cdot V_{ij} \cdot W_i$$

In the approach of Agliardi et al. (2009), the annual frequency of rockfall events in a given volume class j (i.e. probability of occurrence) is evaluated using magnitude-cumulative frequency (MCF) curves (e.g. Hungr et al., 1999; Dussauge et al., 2003), whereas the probability of reach was derived from the results of 3D numerical modelling. The vulnerability of the elements at risk was evaluated using a site-specific function, obtained by the authors obtained by combining numerical modelling results and field data for buildings.

6.3.2 3D runout modelling approach

As introduced above, the risk variables depending on rockfall dynamics (i.e. the probability of impact and impact energy) were evaluated with the support of 3D numerical modelling performed through the code Hy_Stone (Agliardi and Crosta, 2003; Crosta et al., 2004; Frattini et al., 2008). This code is able to simulate rockfall trajectories in 3D with a multi-scale stochastic approach, and exploits the high-resolution descriptions of 3D topography provided by increasingly available remote sensing techniques (airborne LIDAR, Terrestrial Laser Scanner, Terrestrial Digital Photogrammetry). The code incorporates a hybrid algorithm, allowing to model free fall, impact and rolling with different damping relationships available to simulate energy loss. Slope topography is provided to the code as a raster DEM, and all the relevant parameters are spatially distributed. The stochastic nature of rockfall processes and the variability of the relevant parameters are accounted for by topographic accuracy and by the random sampling of most parameters from different probability density distributions (e.g. uniform, normal, exponential). The model accounts for the interactions between blocks and countermeasures or structures by introducing their

geometry and energy absorption capacity. Input data are spatially distributed and include: source cell locations, number, shape and mass of simulated blocks, initial conditions and values of impact restitution a rolling friction coefficients. Results (in raster and vector formats) include rockfall frequency, bounce height, rotational and translational velocity and kinetic energy, as well as information about motion types and impacts evaluated at each point along fall paths.

6.4 RISK ANALYSIS

6.4.1 Rockfall protection scenarios and elements at risk

Immediately after the event, the Civil Protection authority of the Regione Lombardia enforced a series of emergency-stage measures to reduce rockfall hazard by trimming unstable blocks on the rocky cliff face, and built a provisional, 180 m long embankment. This was completed and raised in height up to 4 m. This protected only the already damaged area (Figure 6.3). After the emergency, the design and construction (now completed) of three larger embankments, up to 8 m high and 500 m long, was planned to ensure long-term protection and risk mitigation of the entire exposed area (Figure 6.3).

Risk analysis has been performed in order to provide a quantitative measure of the expected technical performance of the different rockfall protection solutions. Agliardi et al. (2009) thus considered three separate rockfall protection scenarios, i.e. situations accounting for different (actual or planned) countermeasures to protect the same set of elements at risk.

Protection scenarios included (Figure 6.3):

1) S0: reference scenario without countermeasures, corresponding to the unprotected area after the 2004 event;
2) S1: scenario protected by the provisional embankment built in the emergency stage;
3) S2: long-term protection scenario including three large embankments.

For each protection scenarios, the entire quantitative risk analysis has been carried out considering the following elements at risk:

1) buildings existing in the Fiumelatte area after the 2004 disaster (i.e. building completely lost or demolished after the events have not been considered). A building database (i = 86) was collected using available documentation and field surveys and set up in GIS, including housing, commercial, and other buildings (e.g. railway station). For each building, several attributes relevant to risk analysis were surveyed, namely:
    a) structural type (e.g. masonry walls, reinforced concrete frame);
    b) building height, plan area, and number of storeys, derived by field surveys, 1:2000 topographic maps and comparison between DTM and DSM models derived by aerial LiDAR surveys (Courtesy of Regione Lombardia);
    c) reference commercial value estimate per unit area (from real estate market information and reports of losses suffered in 2004).

2) people inside buildings, based on estimates of average annual people occupancy for different types of buildings. An economic value of 10^6 Euro was assumed for human life using a human capital approach according to the literature (GEO, 1998; Fuchs and McAlpin, 2005; Porter et al., 2006; Jonkman, 2007).

The spatial temporal probability (i.e. exposure) of the elements at risk was evaluated by simple assumptions about their mobility, and set to 1 for buildings (i.e. static elements) and 0.5 for people inside buildings (conservative estimate of average daily occupancy of 12 hours).

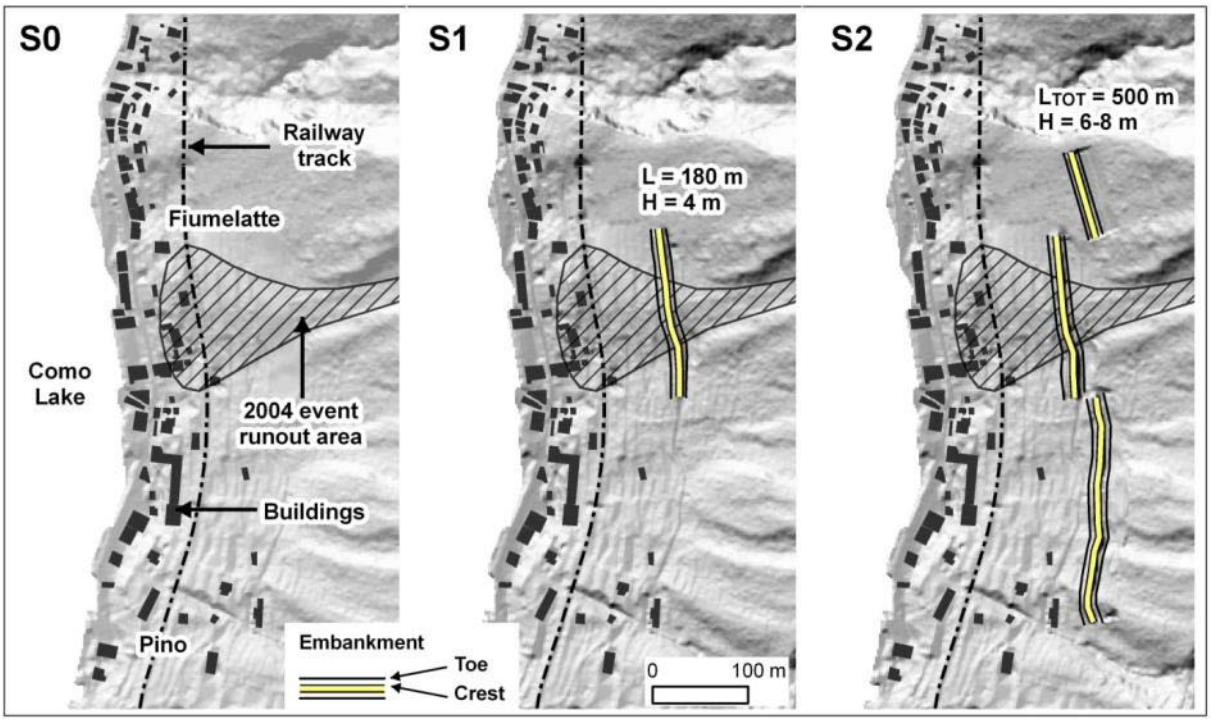

Figure 6.3. Rockfall protection scenarios. (a) Reference scenario S0 (unprotected post-event); (b) Scenario S1, protected by a provisional embankment; (c) Scenario S2, with larger embankments designed for long-term rockfall protection of the area (Agliardi et al., 2009).

6.4.2 Rockfall event scenarios

Any type of quantitative risk analysis should account for the contribution of different "event scenarios" (i.e. modes of occurrence of the considered processes), depending on the probability of occurrence of each scenario. In the case of rockfall processes, event scenario definition is usually based on block volume, representing the initial "magnitude" of a rockfall event, as for earthquake hazards. Estimating the annual frequency of rockfall events, Nj (i.e. a proxy of rockfall onset temporal probability), characterised by block volume falling into a given magnitude - i.e. volume - class, thus requires knowing or assuming the magnitude-frequency distribution of rockfall events in a given area characterised by specific geological and geomorphological features. For rockfalls, several authors (Hungr et al., 1999; Dussauge et al., 2003; Malamud et al.,

2004) showed that the magnitude-cumulative frequency (MCF) distribution of events in a given volume class j can be described by a power law in the form:

$$\log N(V) = N_0 + b \cdot \log V$$

in which: $N(V)$ is the cumulative annual frequency of rockfall events exceeding a given volume; N_0 is the total annual number of rockfall events; and b is the power law exponent.

The power-law exponent b has no general significance, although it has been suggested to vary in a quite narrow range, i.e. -0.7<b<-0.4 (Hungr et al., 1999; Dussauge et al., 2003). The knowledge of b and N_0 should be based on statistically complete, site-specific rockfall inventories/catalogues. In this case a site-specific catalogue was lacking, then the authors selected a value b= -0.41 based on the literature (i.e. value for carbonate rocks proposed by Dussauge et al., 2003). A conservative estimate of N_0=10 (events.yr^{-1}) was derived from available historical and geomorphological information for the entire 800 m long cliff span. Five rockfall volume classes j were selected (Table 6.1) to cover the observed volume range 0.001-100 m^3. Larger individual block volumes can also occur in rock masses in the area, but they are most prone to fragmentation soon after detachment, as suggested by the 2004 event dynamics. Thus they were not considered for the definition of event scenarios.

Table 6.1. Definition of magnitude scenarios for risk analysis: block volume classes and related frequencies, derived by the assumed magnitude-frequency relationship.

Magnitude class, j [-]	Block volume range [m^3]	Incremental frequency of events, Nj [year^{-1}]	Return period [year]
1	0.001 ÷ 0.01	6.11	0.16
2	0.01 ÷ 0.1	2.38	0.42
3	0.1 ÷ 1	0.92	1.09
4	1 ÷ 10	0.36	2.78
5	10 ÷ 100	0.14	7.14

6.4.3 3D rockfall runout modelling

Mathematical modelling of rockfall runout was carried out over an area of about 0.52 km^2 including the whole Fiumelatte village and the impending rocky cliffs for a total cliff length of about 800 m. The model was based on LIDAR topography with 2 m spatial resolution (courtesy of Regione Lombardia), and rockfall sources, surface lithology and vegetation were mapped in the field. The trajectory and maximum runout of single blocks and the related damages to structures had also been mapped in detail soon after the 2004 event, thus providing a reliable calibration/validation dataset.

Information about surface lithology and vegetation allowed to define 9 classes of slope units to be assigned initial values for the impact energy restitution and rolling friction coefficients. These were initially assumed by previous experience (Agliardi and Crosta, 2003; Frattini et al., 2008) and then calibrated using site specific observations. Steep bedrock outcrops mapped in the field, evidence of past failure, rockfall accumulations,

and available geomechanical and historical data allowed to map and characterise potential rockfall sources (21463 raster cells over 85852 m^2, about 16% of the model area).

Model parameters have been calibrated by back analysis of the 2004 rockfall event, for which the source area and the paths and arrest points of individual blocks were well known (Figure 6.4). The trajectories of 2,750 spherical blocks, with block radius varying between 0.5 and 3 m (volumes in the range 0.5-113 m^3) according to an exponential probability density function were simulated. Parameter calibration exploited detailed event data mapped in the field soon after the event, namely: block trajectories and runout, extent of the impacted area, impact and rolling scours, and block-structure interactions (Figure 6.4).

For each considered "protection scenario" (S0, S1, S2) and for each "event scenario" (i.e. volume class; Table 1), 3D rockfall numerical modelling was then performed over the entire exposed area by simulating the trajectories of 10 blocks falling from each source cell (total: 214,630). In order to account for protection scenarios S1 and S2, the geometry of embankments was accounted for by generating specific DEM starting from detail information extracted from design plans. These were generated as TIN (Triangular Irregular Networks) and then merged into the available LIDAR after conversion to raster at the same resolution. At embankment locations, the restitution and rolling friction coefficients were also modified accordingly.

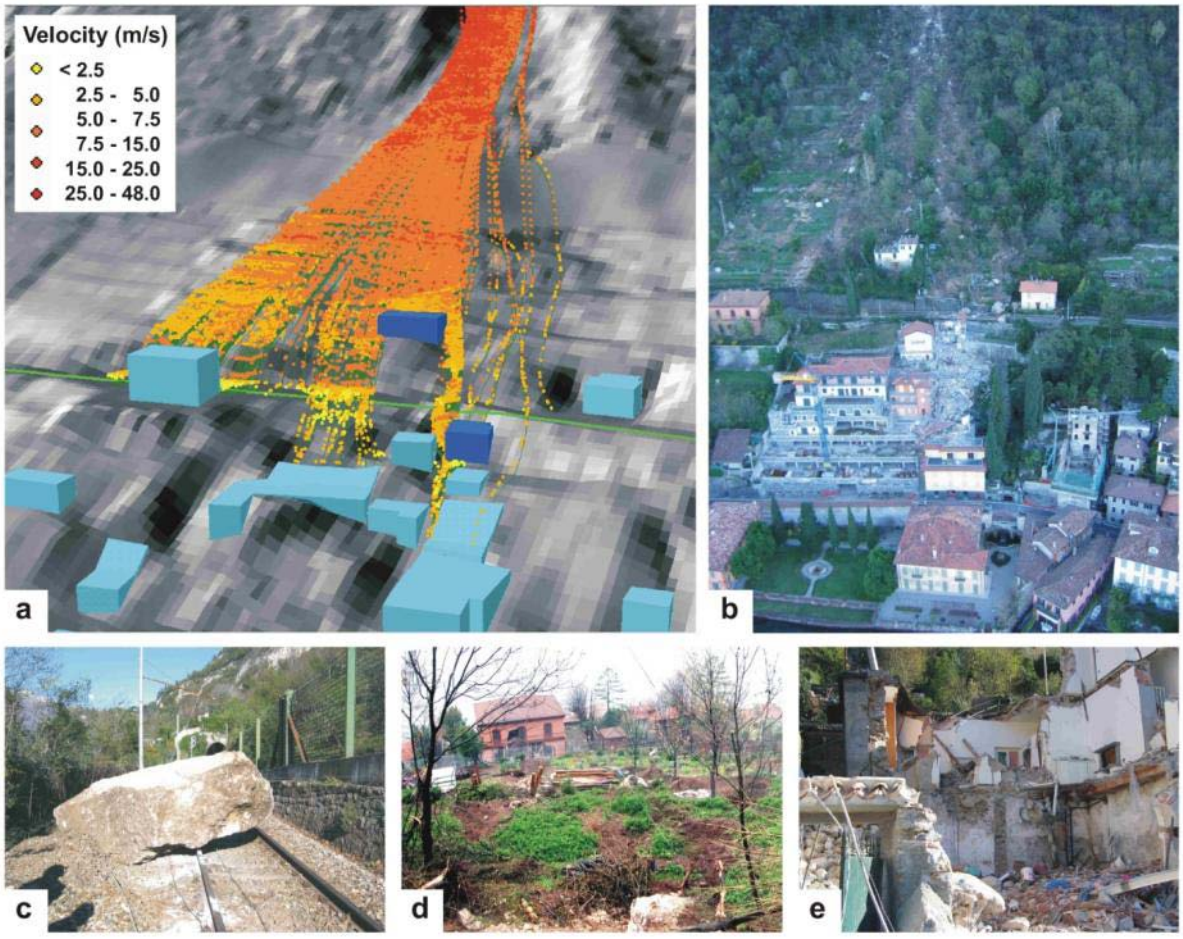

Figure 6.4. Back-analysis simulation of the 2004 event. (a) Simulated trajectories (points classified by block velocity); (b) mapped block paths; (c) block stopping locations; (d) impact and rolling scours; (e) damage to structures (Agliardi et al., 2009).

6.4.4 Probability of rockfall impact

The results of 3D rockfall models were queried in order to extract the information required by QRA, namely: the frequency (i.e. number of passages or stops) and the kinetic energy of blocks reaching each 2x2 m model cell.

For each element at risk and block volume class, the probability of reach was evaluated as the ratio of the total number of blocks reaching each building i and the total number of trajectories simulated by the model (Figure 6.5), assuming a constant rockfall susceptibility over the entire cliff.

Finally, the probability of impact of a block in the volume class j on the building i is given by multiplying the annual frequency of events in the volume class j by the reach probability (Figure 6.7). For persons inside buildings, the impact probability was scaled according to a spatial temporal probability of 0.5.

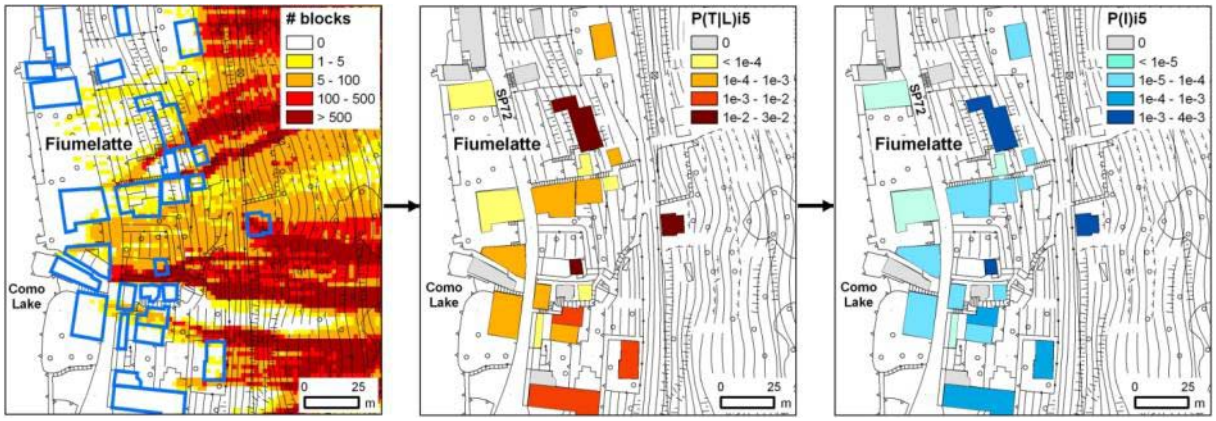

Figure 6.5. Calculation of the probability of rockfall impact on buildings, by combining the "probability of reach" with the annual frequency of rockfall events in each volume class j. Reported example is for protection scenario S0 and volume class j=5 (Agliardi et al., 2009).

6.4.5 Vulnerability

Quantitative risk assessment for rockfalls requires evaluating the physical vulnerability of individual elements at risk, which is a scenario-specific parameter (Uzielli et al., 2008). Although well-established methods for the estimation of physical vulnerability have been developed for earthquake and flood risks, a quantitative assessment of vulnerability to landslides is still hampered by: a) lack of statistically sound databases of damage data, and b) by the inherent complexity of landslide-structure interactions (Glade, 2003).

For rockfalls, physical vulnerability of elements at risk or protection structures is a function of the kinetic energy of rockfall impacts (Straub and Schubert, 2008). Although attempts have been made to evaluate vulnerability through the numerical modelling of building response to impact (Mavrouli and Corominas, 2010), statistically

reliable vulnerability curves are not currently available in the rockfall literature. In the Fiumelatte case study, an empirical, site-specific quantitative assessment of physical vulnerability has been made. In particular, the analysis of detailed event data collected soon after the 2004 disaster allowed to link the impact energy values of individual observed blocks (derived by 3D runout modelling), with the damages caused by the same blocks (characterised in the field).

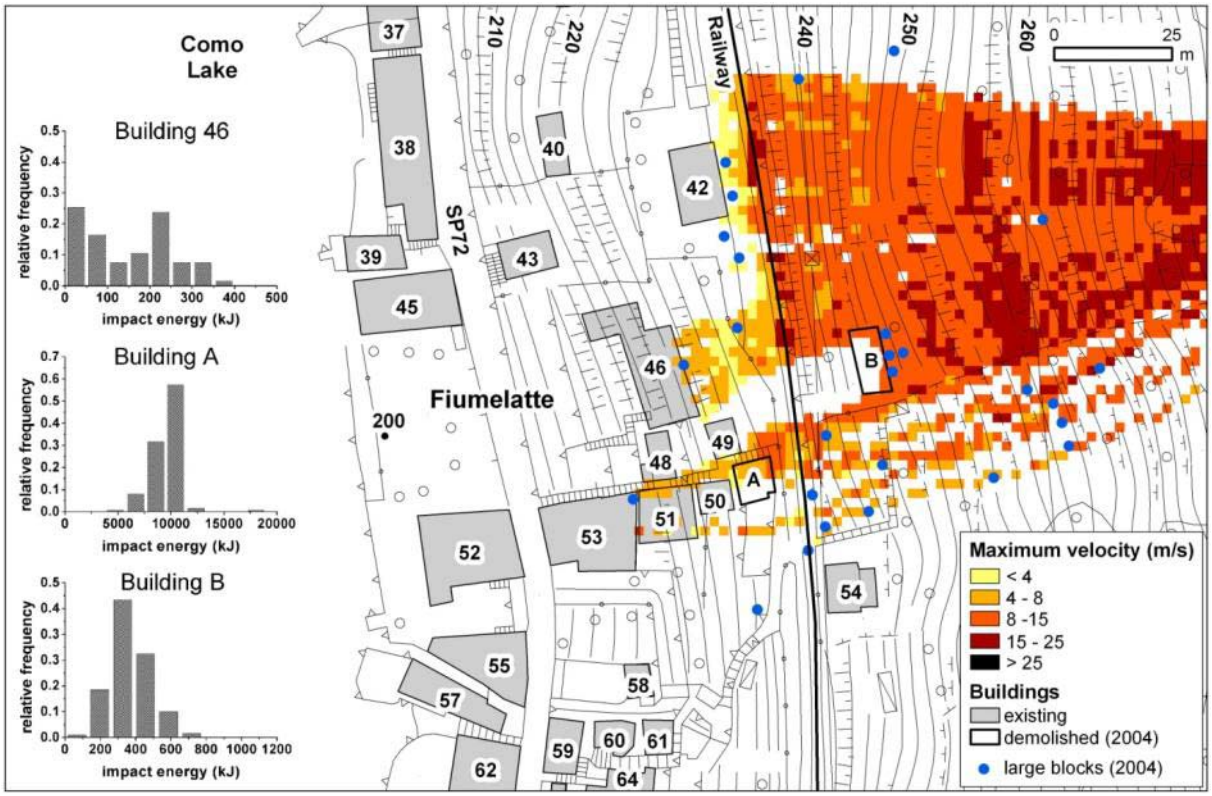

Figure 6.6. Spatial distribution of block velocity derived from the numerical back analysis of the 2004 rockfall event (Agliardi et al., 2009).

To characterise the vulnerability, the energy of blocks impacting each building damaged in 2004 were back-calculated from simulated velocity (Figure 6.6), considering the mass of blocks causing damage. The degree of loss suffered by each building was reasonably estimated through an engineering evaluation of structure type (e.g. masonry or reinforced concrete frame), damaged structural elements (e.g. concrete bearing frame, bearing or partition walls), functional damage and repairability (Figure 6.7). A site-specific empirical vulnerability function was obtained by fitting a sigmoidal function (Figure 6.9) to damage and impact energy values:

$$V(E) = 1 - \frac{1.358}{1 + e^{\frac{E - 129000}{120300}}}$$

in which: V is the fractional degree of loss (0 to 1); and Eis the impact energy (in J).

Physical vulnerability of human life to rockfalls is very difficult to estimate, and none of the few published studies expressed it in the form of vulnerability curves (Hungr et al., 1999; Corominas et al., 2005). According to a simplified approach, the vulnerability of persons inside buildings (i.e. the degree of loss in terms of injury or death suffered by an occupant if a block impacts a building) has been assumed to show the same dependence on impact energy.

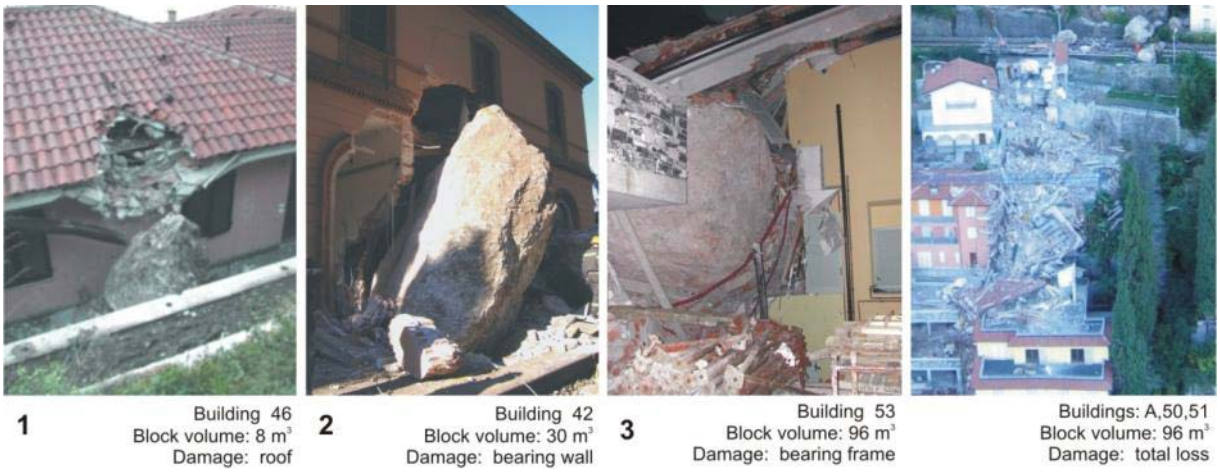

Figure 6.7. Examples of structural damage evaluation for empirical vulnerability assessment (after Agliardi et al., 2009)

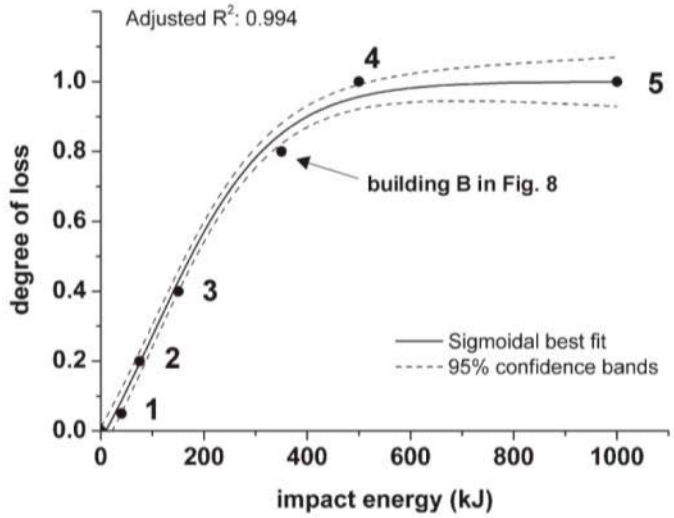

Figure 6.8. Empirical, site-specific rockfall vulnerability curve (after Agliardi et al., 2009).

6.4.6 Risk

Knowing the impact energies computed by numerical modelling for each "event scenario" (volume class j), the degree of loss associated to each element at risk has been

computed using the empirical vulnerability curve (Figure 6.8). The combination of the degree of loss, the probability of impact, and the value of the elements at risk allowed to compute the risk to buildings (and persons inside) in terms of annual expected costs (in Euro; Figure 6.9). The analysis has been repeated for all the considered "event scenarios" and "protection scenarios".

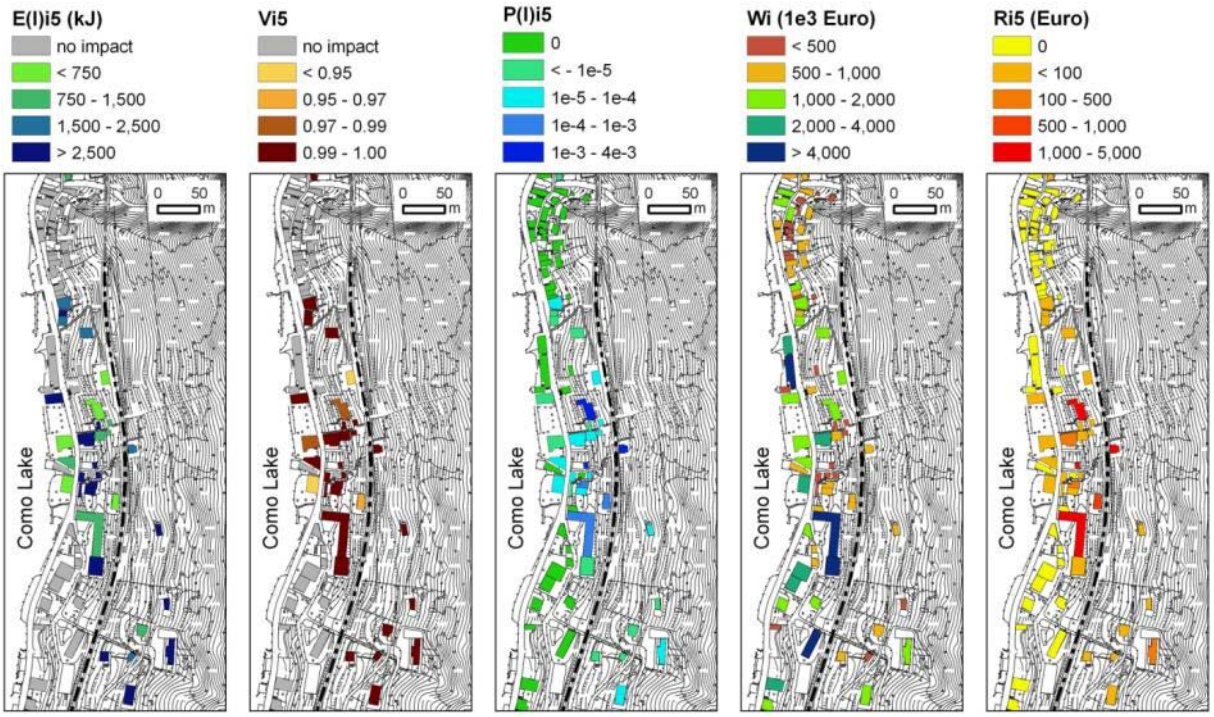

Figure 6.9. Risk computation for buildings (i.e. annual expected cost in Euro) by combination of degree of loss (i.e. function of vulnerability and impact energy on each building i), probability of impact and value. Reported example is for protection scenario S0, volume class j=5 (Table 2) and average computed impact energies (Agliardi et al., 2009).

Finally, the total risk R (i.e. the total annual expected cost, accounting for the contribution of all "event scenarios") has been computed for each of the three protection scenarios (Figure 6.10) as the sum of expected costs due to each block volume class and element at risk. The statistical variability of simulated energy of impact on each building was accounted for by providing lower and upper bound risk estimates considering the minimum, average and maximum computed impact energies, respectively.

QRA results in terms of total annual expected costs, including risk to buildings and persons inside, showed that in the unprotected scenario (S0) a 250 m wide corridor (including the sector impacted in 2004) and the southern area (Figure 6.10) would have been exposed to a total annual risk of about 98,000 Euro (average value) and up to 428,000 Euro (maximum). Moreover, the estimated annual probability of loss of life (PLL), i.e. the annual probability for an individual to suffer complete loss, would have reached $7.5*10^{-3}$, exceeding the limit value of 10^{-4} suggested by the Hong Kong rockfall risk acceptability guidelines (GEO, 1998). Construction of the provisional embankment (S1) reduced total annual risk in the area hit by the 2004 event, with a total annual expected cost lowered of about 43,000 Euro (average) and 130,000 Euro (maximum).

Nevertheless, in this scenario the southern part of the area was still unprotected, with estimated annual PLL up to $8*10^{-4}$. Long-term protection embankments of scenario S2 provide the highest degree of protection, with some residual risk affecting the area south of Fiumelatte and an estimated annual PLL below 10^{-4} for all the exposed individuals.

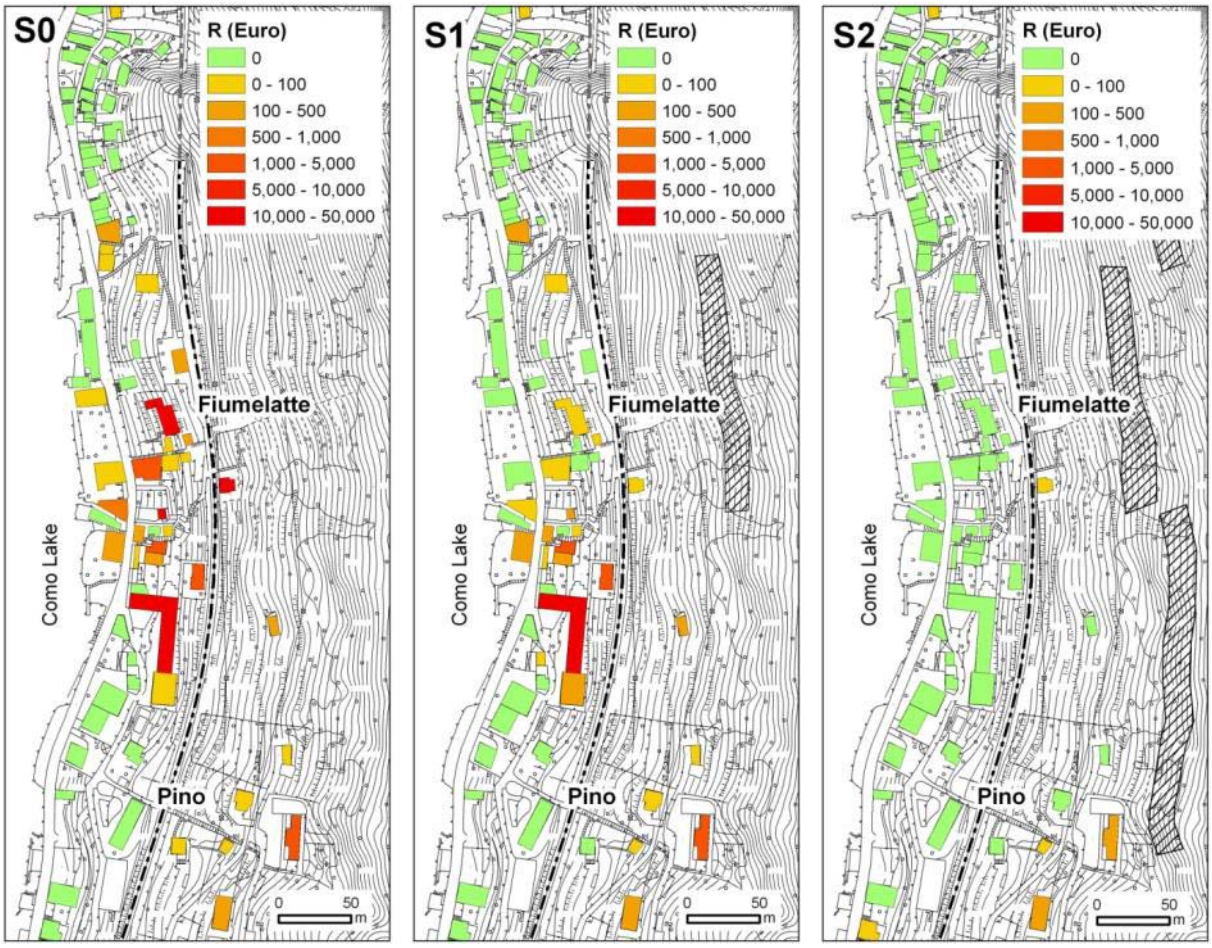

Figure 6.10. Total risk for single buildings (and persons inside), including the contribution of all the considered volume classes, for all the considered "protection scenarios". Maps show the spatial distribution of risk and the degree of risk reduction. Risk values in the reported example are obtained using average values of impact energy (Agliardi et al., 2009).

Table 6.2. Residual / initial risk ratio of considered protection scenarios S1.

	Risk:	Buildings	Persons	Total
S1-S0	Minimum	0.44	0.53	0.50
	Average	0.39	0.46	0.44
	Max	0.27	0.32	0.31
S2-S0	Minimum	0.01	0.02	0.02
	Average	0.01	0.01	0.01
	Max	0.01	0.01	0.01

S2-S1	Minimum	0.03	0.03	0.03
	Average	0.02	0.02	0.02
	Max	0.02	0.02	0.02

The technical performance of the different rockfall protection options in reducing rockfall risk at Fiumelatte was further evaluated by evaluating the ratio of the residual risk (i.e. the annual expected cost estimated in a given protected scenario) to the initial risk, corresponding to the (reference) unprotected scenario S0. This ratio, computed with respect to the minimum, average and maximum estimated risks (Table 6.2), outline the very good expected performance of the S2 option (long-term scenario) with respect to the one of S1 (provisional embankment).

REFERENCES

Agliardi, F., and Crosta, G. (2003). High resolution three-dimensional numerical modelling of rockfalls. International Journal of Rock Mechanics and Mining Sciences, 40, 455–471.

Agliardi F., Crosta G.B., Frattini, P. (2009). Integrating rockfall risk assessment and countermeasure design by 3D modelling techniques. Natural Hazards and Earth System Sciences, 9, 1059–1073.

Bunce, C.M., Cruden D.M., and Morgenstern N.R (1997). Assessment of the hazard from rock fall on a highway. Canadian Geotechnical Journal, 34, 344-356.

Corominas, J., Copons, R., Moya, J, Vilaplana, J.M., Altimir, J, and Amigò, J. (2005). Quantitative assessment of the residual risk in a rockfall protected area. Landslides, 2, 343-357.

Crosta, G.B., and Agliardi, F. (2003). A methodology for physically-based rockfall hazard assessment. Natural Hazards and Earth System Sciences, 3, 407-422.

Crosta, G.B., and Agliardi, F. (2004). Parametric evaluation of 3D dispersion of rockfall trajectories. Natural Hazards and Earth System Sciences, 4, 583-598.

Crosta, G.B., Agliardi, F., Frattini, P., and Imposimato, S. (2004). A three-dimensional hybrid numerical model for rockfall simulation. Geophysical Research Abstracts, 6, 04502.

Dussauge, C., Grasso, J.R., and Helmstetter, A. (2003). Statistical analysis of rockfall volume distributions: implications for rockfall dynamics. Journal of Geophysical Research, 108, B6, 2286.

Fell, R., Ho, K.K.S., Lacasse, S., and Leroi, E. (2005). A framework for landslide risk assessment and management. In: Hungr, O., Fell, R., Couture, R., Eberhardt, E. (Eds.), Landslide Risk Management. Taylor and Francis, London, 3–26.

Frattini, P., Crosta, G., Carrara, A., and Agliardi, F. (2008). Assessment of rockfall susceptibility by integrating statistical and physically-based approaches. Geomorphology, 94, 419-437.

Fuchs, S., and McAlpin, M.C. (2005). The net benefit of public expenditures on avalanche defence structures in the municipality of Davos, Switzerland. Natural Hazards and Earth System Sciences, 5, 319–330.

GEO (1998). Landslides and boulder falls from natural terrains: interim risk guidelines. GEO Report 75. Geotechnical Engineering Office, Civil Engineering Department, Honk Kong, 183 pp..

Glade, T. (2003). Vulnerability assessment in landslide risk analysis. Die Erde, 134, 121-138.

Hungr., O., and Beckie, R.D. (1998). Assessment of the hazard from rock fall on a highway: Discussion. Canadian Geotechnical Journal, 35, 409.

Hungr, O., Evans, S.G., and Hazzard, J. (1999). Magnitude and frequency of rockfalls and rock slides along the main transportation corridors of south-western British Columbia. Canadian Geotechnical Journal, 36, 224-238.

Jonkman, S.N. (2007). Loss of life estimation in flood risk assessment. Theory and applications. PhD Thesis, Technical University of Delft, Delft, Netherlands, 354 pp.

Malamud, B.D., Turcotte, D.L., Guzzetti, F., and Reichenbach, P. (2004). Landslide inventories and their statistical properties. Earth Surface Processes and Landforms, 29, 687-711.

Mavrouli, O. and Corominas, J. (2010). Vulnerability of simple reinforced concrete buildings to damage by rockfalls. Landslides, 7, 169–180.

Porter, K.A., Shoaf, K., and Seligson, H. (2006). Value of injuries in the Northridge Earthquake. Earthquake Spectra, 22 (2), 555-563.

Schönborn G. (1992). Alpine tectonics and kinematic model of the Central Southern Alps. Mem. Sci. Geol Univ. Padova, 44, 229-393.

Straub, D., and Schubert, M. (2008). Modelling and managing uncertainties in rock-fall hazards. Georisk, 2, 1-15.

Uzielli, M., Nadim, F., Lacasse, S., and Kaynia, A.M.. (2008). A conceptual framework for quantitative estimation of physical vulnerability to landslides. Engineering Geology, 102, 251-253.

7 CONCLUSIONS

The methodologies for the QRA may vary significantly depending on the landslide type, the scale of the analysis, the considered exposed elements and the techniques used for the acquirement of input data. Quantitative estimates provide more objective and comparable risk results in comparison with the quantitative ones.

The cases presented in this report are good examples of the progress experienced in QRA of landslides during the last few years. The advance has been evident in the consideration of the magnitude of the events, the intensity of the phenomena at selected locations and in the vulnerability assessment. Despite of this, further research is still required before QRA could become a routine and standardized tool. Determining the size of the potential failure is still a challenge. Magnitude-frequency relations are fundamental input data for quantitative hazard and risk analysis, however the scarcity of good quality historical data in many regions restrict its construction. The approach used in Castellammare di Stabia (Section 2) aims to overcome this difficulty by first identifying landslide susceptible spots and then using empirical relations linking the height of the failure-transportation zone and the area of the mobilized slide mass. These type of approaches although valuable are far from being applicable to other contexts and need to be validated.

In existing landslides (either active or dormant) both the magnitude and the extent is usually known, such as in the Ancona case study (Section 3). In active landslides, the probability of occurrence is not the parameter that better characterizes hazard. Instead, a probabilistic simulation was employed to estimate total displacement or displacement rates.

Landslide magnitude-frequency analyses assume the existence of steady conditions for both triggers and slopes. This assumption is, however, arguable in some geological contexts because the conditions responsible for a given landslide frequency in the past might no longer exist. This is nicely demonstrated in the case of flow-slides in Nocera Inferiore (Section 4) where historical records show than main instability events followed the refill of the slopes with pyroclastic material from Vesuvius eruptions.

Significant progress has been produced in the evaluation of the vulnerability of the exposed elements, particularly in front of fragmental rockfalls. The cases of Andorra (Section 5) and Fiumelatte (Section 6) are appropriate examples. In the former, an analytical approach has been followed. The advantage of such approach is the objectivity and the incorporation of the uncertainty of the impact location on key structural elements and the response of the whole structural system. The vulnerability obtained can be directly integrated in the risk equation. However, this approach requires the consideration on a large variety of structural typologies and arrays which analysis has not been yet finished. The latter, is based on empirical observations of the past damages of buildings. This provides a realistic evaluation of the response of the buildings. Again, this procedure requires the analysis of a representative set of cases and different building typologies. The analysis of the impact produced by rapid landslides (i.e. debris slides) as shown in Castellammare di Stabia (Section 2) highlights the importance of features such as the openings on the vulnerability of the buildings. It may be reasonably expected that all these analyses could be completed in the years to come.

The development of fragility curves (Section 2 and 6) is one of the main recent achievements in the landslide risk analysis. These type of curves are well known in other natural hazard domains such as earthquake risk. They may be prepared based on

empirical or analytical data. The main contribution is that they allow the assessment of the vulnerability in terms of intensity of the landslide event, which is more realistic. Intensity expresses the damaging capability of the landslide events. A distinct characteristic of the landslide hazard and risk is that intensity can not be defined with a single descriptor. The cases presented have shown that landslide intensity must take into account both the landslide mechanism and the nature of the exposed element. In Castellammare di Stabia (Section 2) impact pressure and burial by debris mass has to be considered while in Nocera Inferiore (Section 4), the flow depth and velocity are the selected parameters for intensity. In Andorra (section 4) and Fiumelatte (Section 5) is the kinetic energy of the falling blocks what determines the damaging capability. An analytical intensity model was constructed in Ancona (Section 3) by comparing landslide-induced ground displacements and the effects on the set of buildings for which post-landslide damage was surveyed

Seggregating the risk equation has highlighted the role of the exposure of the elements at risk (spatio-temporal probability of the elements at risk) which has received little attention so far. Traditional approaches used in risk analysis tend to simplify risk in two main components: hazard and vulnerability. Nevertheless, practical application of QRA has shown that exposure, particularly for mobile elements at risk (cars, trains, persons) has a strong influence in risk results and on the probability of loss of life. The consideration of exposure within vulnerability is not an appropriate way to address this issue because vulnerability is an intrinsic property of the element at risk while exposure may be a transient attribute even for buildings which exposure to landslide hazards is conditioned by the presence of other (future) buildings within the landslide track. Simplified approaches are often required for evaluating the exposure, such as for instance, assuming the same exposure for all buildings in a neighborhood. This type of approaches may be acceptable for small scale anlyses but the must be refined when working at either local or site specific scale. To overcome this restriction, in the example of Nocera Inferiore (section 4), the calculation of vulnerability of the persons has taken into account the extent of debris end lobe beyond the building location.

Finally, the incorporation of the performance of landslide mitigation measures in QRA is an issue that is seldom considered but it is necessary for risk management purposes. The difficulty of considering mitigation measures has been highligthed in the example of Ancona (section 3). Since the two data sets of displacements measured with PSInSAR are not jointly compatible from a quantitative perspective if extreme quantiles are of interest, and since they refer to distinct geotechnical conditions (pre- and post-mitigation, respectively) it is necessary to develop criteria for deciding which data set should be referred to for the purpose of meaningful risk estimation.